UNIVERSITY of CALIFORNIA

Santa Barbara

Insights into the Rational Design of Multi-Functional Fullerene Systems

for Application in Blended Heterojunction Organic Solar Cells

A dissertation submitted in partial satisfaction of the requirements for the degree

Doctor of Philosophy

in

Chemistry

by

John S. Cowart Jr.

Committee in charge:

Professor Michael L. Chabinyc, Chair

Professor Craig J. Hawker

Professor Fred Wudl

Professor Luke Theogarajan

Professor Javier Read De Alaniz

December 2014

The dissertation of John S. Cowart Jr. is approved.

_____

Professor Craig J. Hawker

_____

Professor Fred Wudl

_____

Professor Luke Theogarajan

_____

Professor Javier Read De Alaniz

_____

Professor Michael L. Chabinyc, Committee Chair

December 2014

Insights Into the Rational Design of Multi-Functional Fullerene Systems

for Application in Blended Heterojunction Organic Solar Cell Devices

To my Father and Mother for their undying love and support

Acknowledgements

I would like to take this opportunity to express my profound appreciation to the individuals whose collective contributions to my personal and scientific growth ultimately created the conditions which allowed me to obtain my Ph.D. These individuals have left a lasting imprint on my life, and this thesis would not have been possible without their help.

First and foremost, I would like to thank my parents: John S. Cowart Sr. and Jannette E. Cowart. Their guidance, support, and love throughout my lifetime have been the foundation of my development. Any past, present, or future successes that I experience are soundly rooted in the many sacrifices that they have made on my behalf. I have the best parents in the world – quite possibly the galaxy. Mom and Dad, thank you for believing in me even when I forgot to believe in myself. Your support means more than words could ever hope to describe. I love you to the moon and back.

To my Ph.D. advisors: Michael L. Chabinyc, Craig J. Hawker, and Fred Wudl, it has been a true honor and a profound privilege to learn from each of you during my tenure in graduate school. Thank you for challenging me to develop my critical thinking and creating an environment abound with opportunities to advance my intellectual growth and professional development. Although I have decided that a pivot away from chemistry towards music is the best personal decision for my future, I am sure the multidisciplinary approach to tackling problems and executing projects that you've helped me to cultivate as a member of your research groups will play an important role in my professional career.

I would also like to express my sincere appreciation to my undergraduate research advisor Professor John Reynolds; for seeing more than just an 18 year old kid with a huge

afro and taking a chance with me, by allowing me an opportunity to work in his polymer chemistry laboratory. His role in my personal and professional development is undeniable. He opened doors for me that I couldn't possibly have opened by myself and his fingerprint on my life could never be washed away. I wish him and his family the very best.

I would also like to thank Professor Pierre Audebert of ENS Cachan. I first became acquainted with Pierre in his capacity as my secondary research supervisor during three summers of undergraduate research in France. However, in the eleven years that I have known Pierre we've developed a meaningful friendship that extends far beyond the perimeters of academic research. Pierre has been a tremendous ally and a great mentor. No doubt we'll be life-long friends.

To my beautiful girlfriend Oura Neak: your timing was impeccable! You were a true friend to me when I needed one the most. I could search the world 1,000 years and never find another you. From the bottom of my heart - I love you so, so much. Also, thank you for preparing many delicious home cooked meals (especially the seafood pasta!) and not allowing me to eat that stuff they make at McDonald's. You kept me alive while writing my thesis. Won't soon forget it. Moreover, your companionship brought a long needed balance to my life and put a silver lining around graduate school.

I would also like to thank my sisters Jalanna and Jabrianna for their support and friendship. We're all graduating/job hunting around the same time and I'm excited to see what the future has in store for the Cowart siblings. I sincerely hope we can make a positive impact on the world around us. I would also like to thank my mom's identical twin sister Auntie Net Net (Annette) for being my mom #2. And gotta say what up to my father's sister

Auntie Mary for being such a great aunt and always keeping it 100. To the rest of my aunts, uncles, and cousins I would also like thank you for your support over the years.

To the friends I've gained during my time in Santa Barbara, thank you for contributing to my growth as a scientist and human being. In no particular order, I'd like to give each of you shout outs. To my 1519 San Pascual housemates past and present: Damian Monternal, Daniel Klinger, William Harroch, Sigga the pitbull, and Max Steifel - boy did we have a lot of fun??!! I'll never forget our legendary dinners, drinking, and more drinking. I thank you and my liver thanks you. To the most excellent Dr. Damian Monternal: many thanks for the epic chess matches and countless White Russians. I never knew there were so many different kinds of cheese! Ça ce passe dans l'espace! To the infamous Herr Dr. Daniel Klinger: duderino, thanks for keeping it real and being a great friend. Present JJ predicts Future JJ and Future Daniel will have many more late nights of drinking and pontification! Looking forward to staying connected with you for many years to come. Giggidy! To William "Frenchy" Harroch: merci bien for the French lessons and keeping an eye on Sigga. The road doesn't end for us here brother. We still have a lot of damage to do in France together! To the first dog to successfully complete a moonwalk, ladies and gentlemen, give it up for my pitbull – Sigga "Budge" Cowart!! Listen Sigga, I know that you will never read this since you are dog, but real talk - you my dawg! Now that I'm finally done with the thesis, we'll go on lots of walks buddy. Would you like to "eat a treat outside"??

To my comrade Dr. Nabil Laachi: ça vas mon gars! Many thanks for our countless conversations, early morning runs, and late nights out on the town. It's rare that people click on the level that we did. Looking forward to a life-long friendship with you brother. Do your best to navigate away from the scallywags and swizzle-backs! I believe you can do it! To the

dread-lock rasta Mahadar Tesfai: what up my ninja!! Really glad our time-space collided at the bus stop that day and that we've grown to be friends. No doubt in my mind I've had the great fortune of walking with one of the best artists of our time. I'm excited to see how your career launches off. Also looking forward to future opportunities for collaboration. Let's get this paper! To the one and only Dr. Eric "Professor" Pressly: a veritable renegade and incredible friend. F%$& the well-trodden path broseph! Your courage to go against the grain, live by your own rules, and contort life into your own personal rubix cube has been a true inspiration for me. Thanks for saving that bottle of Cab Franc to help me celebrate finishing the thesis. Looking forward to seeing all of the beautiful women in the world using your hair products! Let's make the trip to Machu Pichu happen! No excuses, be a champion! To mi hermano Teddy: who woulda thought? Should one ever have the foresight to make friends with a mechanic, they should be so lucky to encounter one with as solid a character as yours. Not many people on this planet we call earth are as genuine as you my man. Moreover, thank you so much for reviving my truck from the pits of eternal damnation well over 30 times. Incidentally, I never knew it was possible for a truck to die in so many ways…By the way, congratulations on the birth of your new son! To my homeboi from the "dirty south" Dr. Justin Poelma: I truly appreciate the friendship that we've forged over the past 5 years. I knew we'd be life-long buddies the moment you first threw on that J. Dilla album. Donuts Baby!! To my main man with the sharpest blade on this side of the Mississippi, Big Serg: thanks for the hair cuts, conversations, and chess games. Keep practicing piano brother, you'll get there. To my good friend Dr. Will Gutekunst: glad you chose Santa Barbara as your post-doctoral destination. Haven't known you long, but the connective vibrations are there. Thanks for your help solving that p-tosyl-hydrazides problem that was kicking my

butt. Not sure if I could have wrapped up those loose ends without your contributions to deciphering the riddle. To my good friend Dr. Velu Sivanandan: bhaiya, so glad you were the first Hawker group member I came to know. A real brother through and through. No amount of time or distance will ever change that. To the indelible Dr. Johannes Sprafke: Ya Ya, Du bist ein hinder loader! Just kidding...or am I?! Thanks for our many conversations scientific and otherwise. Authentic rock star! Looking forward to crashing on your couch in Germany!

To all members of the Hawker, Chabinyc, and Wudl groups past and present: thanks guys for the many scientific conversations that we've had in lab, and out of lab – over coffee, lunch, and pig roasts. Our interactions over the years have left lasting impressions on my life. Best of luck to all of you in the future.

To the staff members of the MRL, Materials, CNSI, and Chemistry Departments: thank you so much. These are the unsung heroes of our research. Without their contributions, the work described in my thesis would not have been possible. A special thank you to Dr. Krystyna Brzezinska, Dr. Tom Mates, Maureen Evans, Janet Shalhoob, Dr. Jerry Hu, Richard Bock, Dr. Amanda Strom, Dr. Rachel Behrens, and Jaya Nolt for all of their help!

Few other people I'd like to quickly mention, before I have to meet this December 19, 2014 12:00 am deadline to upload my thesis, Dr. Herbert Peeples II, Dr. Jerrod Williams, Marco Belloso, Lo Bonaby, Xavier Murry, Wallace Murry, Robert Henderson II, Jade Bonaby, Frank McRae, T. Coop, Dr. Nadir Matringe, Dr. Ousmanne "le faible", Dr. Rachid – thanks guys. All of my teachers K-12 and beyond: Mrs. Hunt, Mrs. Geistorf, Mrs. Hurd, Mrs. Sexton, Mrs. Gailey, Mrs. Fowler, Mrs. Watkins, Mrs. Atria, Dr. Poe, Mrs. Taylor, Señora Journey, Mr. Fraizer, Mrs. Geizler, and Dr. Jimenez. To my first piano teacher Mr. Powell – thanks for getting me started. Not sure where I'd be if you hadn't always spent that extra 30

mins overtime each week helping me sharpen my piano skills. To the members of AFCC: thanks to all of you for your support these years. If I've forgotten to mention anyone by name, please excuse my cognitive dissonance. I currently have less than 1 hour before I have to submit the final draft of my thesis and any lapses in memory are attributed to temporal pressures, not a lack of appreciation.

Again, to everyone who has contributed to my scientific, personal, and professional growth over the years, please except my profound gratitude. I would not be the man that I am without you.

Peace be tha journey,

John S. Cowart Jr. Ph.D.

Abstract

Insights into the Rational Design of Multi-Functional Fullerene Systems for Application in

Blended Heterojunction Organic Solar Cells

John S. Cowart Jr.

Elucidating the structure-function relationships of organic semiconductors has been central to the advancement of organic photovoltaics (OPVs). In particular, enhancing the performance of *p-type* materials in disordered heterojunctions is broadly acknowledged as the principal factor leading to current trends of improved power conversion efficiencies (PCEs). However, two additional factors are crucially important for the next step forward in improving PCEs. First, investigating the influence, design and synthesis of new *n-type* materials, specifically fullerene acceptors, is of high importance. Second, because fullerene performance is often compromised by the morphological disorder of bulk heterojunctions, developing fullerenes systems that retain fidelity within disordered blends is also of broad interest. In light of these challenges, the field has witnessed a notable shift towards developing a comprehensive understanding of the design rules needed to advance the performance of fullerene acceptors in bulk heterojunctions.

This work spotlights two multi-functional fullerene systems designed for blended heterojunctions. First, the synthesis of several novel fullerene-dye adducts with enhanced photon absorption will be presented. The ability of these adducts to absorb visible light in their pure state was evaluated and systematically examined versus their capacity to

complement the absorption of low band gap donors and mediate charge transport in bulk heterojunctions. Second, mixed fullerene ternary blends were introduced as a strategy to stabilize the morphology in bulk heterojunctions and prolong operational lifetimes of OPV devices. Combined, these two systems offer unique insight into the rational design of fullerenes for their application in blended systems.

Table of Contents

Chapter 1: Introduction

Chapter 2: Synthesis and Characterization of Fullerene-Dye Adducts

Chapter 3: Investigation of Fullerene-Dye Adduct Blends

Chapter 4: Investigation of P3HT:PC$_{61}$BM:PCB-F Ternary Blends

List of Figures

Chapter 4

List of Tables

List of Schemes

Chapter 1

Introduction

1.1 Motivation for Solar Energy Alternatives

The beginning of the 21st century has witnessed an unprecedented push for the development of fossil fuel alternatives.[1] Motivation for this change has largely been fueled by knowledge of limited global oil reserves and a desire to reduce carbon emissions. Accelerated population growth, higher energy consumption from developing countries, and the consequent raise in gasoline prices, as fossil fuels become an increasingly precious commodity, also factor into the desire to develop new fuel sources. The environmental and economic implications of this problem have highlighted renewable energy sources as a long-term solution. The science community has therefore been challenged with the development of green-energy technologies with the hope that they will eventually overtake existing carbon and nuclear based technologies in efficiency, lifetime, and cost.

One particularly interesting candidate for renewable energy has been solar energy, as the sun already sustains the majority of life on earth. Every hour, 1050 W/m^2 of solar radiation reach the earth's surface.[2] 31% of that energy is reflected back to space by clouds, air, and the polar ice caps; 19% of the energy is absorbed by dust, ozone, and water vapor in the stratosphere; 4% is absorbed by clouds in the troposphere; and 47% reaches the earth. Ultimately, the entire planet receives approximately 84 Terrawatts of power from the sun each day, while the current worldwide consumption of energy is only 12 Terrawatts/day. This fact highlights that the sun has more than enough energy to supplement global fuel consumption. Efforts to make better use of the sun's radiation is therefore of great interest.

Today, technological advancements in solar energy have led to solar power conversion efficiencies (PCE's) of 20% in commercial solar modules.[3] The majority of these commercially viable solar cells are fabricated using amorphous silicon semiconductors. Silicon based solar modules can be found on rooftops, calculators, solar fields, and even spacecraft. Although their use is increasing integrated into today's society, there are still a few unavoidable drawbacks associated with their use.

In particular, silicon solar cells depend on ultra high levels of purity of silicon for these semiconductors to operate properly. To achieve high purity silicon, energy intensive, high-temperature processing steps are required. These processing constraints render the production of silicon solar cells an expensive enterprise. Moreover, these factors also limit the production of high surface area silicon solar panels do to cost. In addition, the high temperatures required for silicon fabrication are generally incompatible with the use of plastic substrates. As a result, flexible silicon solar modules are uncommon. In addition, silicon solar cells are heavy and highly brittle, factors that limit their use in portable applications. The inherent deficiencies limiting silicon based solar cells have left room open for the development of solar energy alternatives.[4]

1.2 Brief History of Organic Solar Cells

The groundbreaking discovery of polyacetylene in 1971 demonstrated for the first time plastics could be used to generate electricity, launching the field of organic electronics.[5] The paradigm shift in the concept of organic semiconductors led to the development of novel technologies such as organic light emitting diodes (OLEDs), organic field effect transistors (OFETs), and OSCs.[6] In comparison to their inorganic counterparts OFETs, OLEDs, and

OSCs share a common advantage in that they can be prepared from solution processable organic semiconducting inks. This feature makes them prime for inexpensive fabrication techniques such as roll-to-roll printing, which allow them to be prepared at low temperatures, over large surface areas, and on plastic substrates.[7] Moreover, because organic semiconductors are plastics that can be processed on plastic substrates, the mechanical features that one would typically associate with plastics are extended to most organic electronic devices. Therefore, on the basis of their potential to reduce fabrication costs and afford flexible, lightweight alternatives to silicon solar cells, OSCs have gained unique attention as a promising 21st century green technology.[8]

Although the first literature precedent of an OSC was reported in the early 1980's, progress in organic solar cells over the next decade was limited.[9] However, several important breakthroughs in materials chemistry would be central to the future of this field.

The 1985 discovery of the carbon allotrope C_{60} buckminsterfullerene by Smalley and coworkers was an important milestone in organic electronics and would ultimately have a direct impact on OPVs.[10] C_{60} is an aromatic 60 atom, spherical patchwork of hexagons and pentagons with icosahedral symmetry: a structure analogous to a soccer ball (**Figure 1.1**). Importantly, C_{60} has a low lying, triply degenerate LUMO which registers -4.0 eV relative to vacuum.[11] This molecular property makes C_{60} a highly efficient electron transporter or acceptor. Moreover, due to its near spherical geometry, C_{60} is able to efficiently transport charge in all three dimensions. Because the only functional handles of C_{60} are 30 stereochemically identical olefins, synthetic modification of its structure is generally limited to addition and cylcoaddition reactions which impart functionality via chemical pendants.[12] Interest in exploiting the unique properties of fullerenes, and the synthetic challenges

required to do so, led numerous research efforts to participate in C_{60} chemistry. Notably, these pursuits were largely enabled by improved arcing techniques, which allowed C_{60} fullerene to be prepared on a multigram scale and sold as a commercial commodity.[13]

Figure 1.1: C_{60} Fullerene

The advent of solution processable conducting polymers such as poly 3-hexylthiophene, made it possible to prepare materials that were soluble in common solvents through simple modification to the polymer backbone with side chains.[14] While this discovery allowed high molecular weight thiophenes to become more processable, the polymerizations utilized for its preparation, also yielded materials with head-to-head, tail-to-head, and tail-to-tail couplings. A consequence of these atactic polymers were chain defects, which disrupted pi-orbital overlap of the repeat units, limiting intramolecular charge transport, and reduced self assembly of ordered crystalline domains, limiting intermolecular charge transport. The discovery of Grignard metathesis by McCullough et al, afforded high molecular weight regioregular P3HT (rr-P3HT).[15] This synthetic improvement allowed soluble, syndiotactic P3HT to absorb more light and transport charge more efficiently.
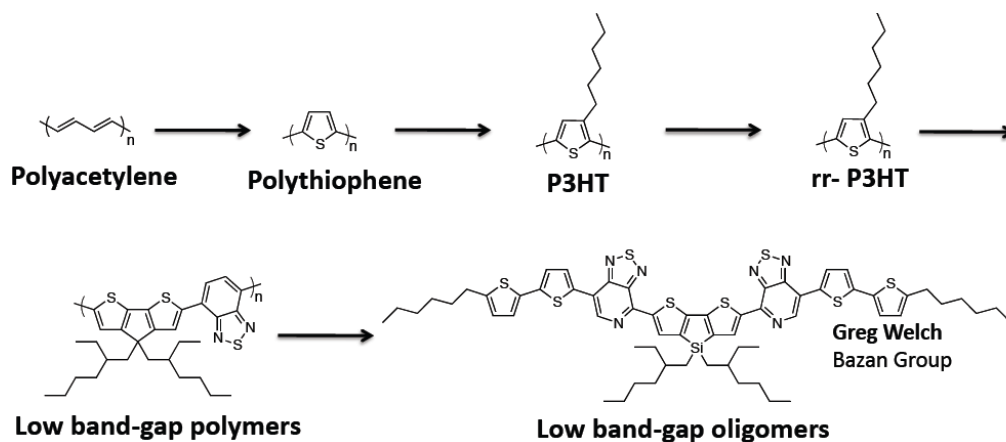
Figure 1.2: Progress in the development of organic donors

Another important contribution was the development of Phenyl C_{61} butyric acid methylester [**PC$_{61}$BM**], which was first introduced in 1995 by the Wudl group as a soluble derivative of C_{60} with potential for biological compatibility.[16] Although its use was not originally intended for OSCs, PC$_{61}$BM gained notoriety as the 1st acceptor used in a bulk heterojunction (**BHJ**) OSC.[17] The bulk heterojunction refers to an active layer prepared by the simultaneous solution deposition of an electron donor (hole transporter) and electron acceptor (electron transporter), such as rr-P3HT and PC$_{61}$BM.[18] In addition, the commercial availability of rr-P3HT and PC$_{61}$BM allowed materials and device engineering groups to develop new processing techniques and device structures which led to dramatic improvements in the efficiencies of these blends. Moreover, the unprecedented access to P3HT and PC$_{61}$BM allowed thousands of fundamental studies to be performed on these materials, the result of which dramatically advanced the collective understanding of the OPV field. Today, P3HT:PC$_{61}$BM devices are the most studied blend in OPVs and are almost unanimously used as the control device in organic solar cell studies.

Subsequent interest in conducting polymers with better overlap with the solar spectrum, led synthetic efforts in the development of soluble low band gap polymers.[19] The ability to synthetically modify molecular functionality to yield organic *donors* whose absorption features could be fine-tuned to various regions of the visible spectrum was a substantial step forward. Continued efforts in the synthesis of organic *donors* also led to the development of low band gap oligomers, which demonstrate comparable absorption, but are easier to purify and have lower batch-to-batch variation than their polymer counterparts (**Figure 1.2**).[20]

On account of the synthetic and engineering progress in OPVs, today's organic semiconductors are highly efficient at photon absorption and charge generation. As a result, the field of OPVs has seen PCE's breach the 10% PCE widely accepted as their threshold for commercial viability.[21] As OSCs have surpassed 10% PCE with only 30 years of research development, they are currently on pace to match the progress of their inorganic counterparts. Moreover, several operations centered on the commercial production of materials for OSCs and industrial scale fabrication of OSCs ensure that this field will have a future with commercial implications beyond academic the academic setting. Nevertheless, there are still important fundamental aspects of OSCs to address.[22]

1.3 Organic Solar Cell Architecture and Device Principles

Typically, an OSC uses a transparent conducting electrode such as indium tin oxide (**ITO**) to collect holes. The ITO is generally bound to a glass substrate. An electron blocking layer such as Polyethylenedioxythiophene:Polystyrene sulfanate (PEDOT:PSS) is generally solution deposited onto ITO and annealed to remove excess water. The semiconducting active layer is subsequently deposited onto the layer of PEDOT:PSS. The active layer is

typically solution-deposited via spin-coating, drop-casting, or blade-coating, although some materials can also be vapor deposited. The active layer usually undergoes a thermal processing step to remove excess solvent. Following annealing, a metal cathode is such as aluminum is vapor deposited onto the active layer through a mask. The final device architecture of an OSC is typically Glass/ITO/PEDOT:PSS/Active layer/Ca.[23]

OSCs require an organic semiconducting *active layer* to absorb photons and convert them into electricity. There are three fundamental architectures utilized for active layers in an OSC; single junction, bi-layer heterojunction and a bulk heterojunction. Due to the high energy needed to separate excitons (bound electron-hole pair), most OSCs typically utilize heterojunction architectures because they provide a stronger driving force for charge separation.[24]

Bi-layer heterojunctions are prepared by a two-step sequential deposition of a donor layer and an acceptor layer. In principle, the primary advantage of a bi-layer heterojunction originates from its contiguous, unobstructed pathways to the electrode. The key limitation of a bi-layer heterojunction is the reduced *donor/acceptor* interfacial surface area consequent of the planar interface between the two layers, limiting the possibility of charge transfer events as a result. In practice, however, it is especially difficult to fabricate a completely planar bi-layer without disrupting the interface of at least one layer. Therefore, the moniker bi-layer heterojunction is frequently a misnomer; the term quasi bi-layer heterojunction or quasi bulk-heterojunction provides a more accurate description of the *donor/acceptor* interface that truly exists in the system.

Bulk heterojunctions are prepared via the simultaneous solution deposition of the *donor* and *acceptor*. The principle advantage of a BHJ is the bicontinuous, interpenetrating

donor:*acceptor* network that forms from this deposition technique, affording high *donor*:*acceptor* interfacial surface area that allows more charges to be separated. The chief disadvantage of a bulk heterojunction is lack of contiguous defect-free pathways for the separated free-charge carriers, which limits charge transport.

In a heterojunction active layer, free-charge carriers are generated through a four-step process, illustrated below in (**Figure 1.3**).[25] First, *photon absorption* occurs, generating a bound electron-hole pair known as an exciton. Although the process of absorption is typically depicted as a phenomenon which occurs in the *donor*, it should be noted that absorption can also take place in the *acceptor*. Following absorption, *exciton diffusion* to a *donor*:*acceptor* interface. Exciton diffusion is believed to occur in a random walk process and can generally cover a distance of 10 - 100 nm before it is either separated or recombined. If an exciton is able to reach a *donor*:*acceptor* interface charge transfer occurs, generating a charge-separated state wherein the electron and hole are pair are physically separated but their wavefunctions maintain a degree of overlap. This charge-separated state has a low energy, low intensity absorption that can be monitored with certain sensitive absorption characterization techniques. Finally, *charge separation* occurs once the electron and hole have completely separated, generating a free-charge carrier for the electron on the *acceptor* and a free-charge carrier for the hole on the *donor*. If these charges are able to diffuse to their electrodes charge collection will take place.
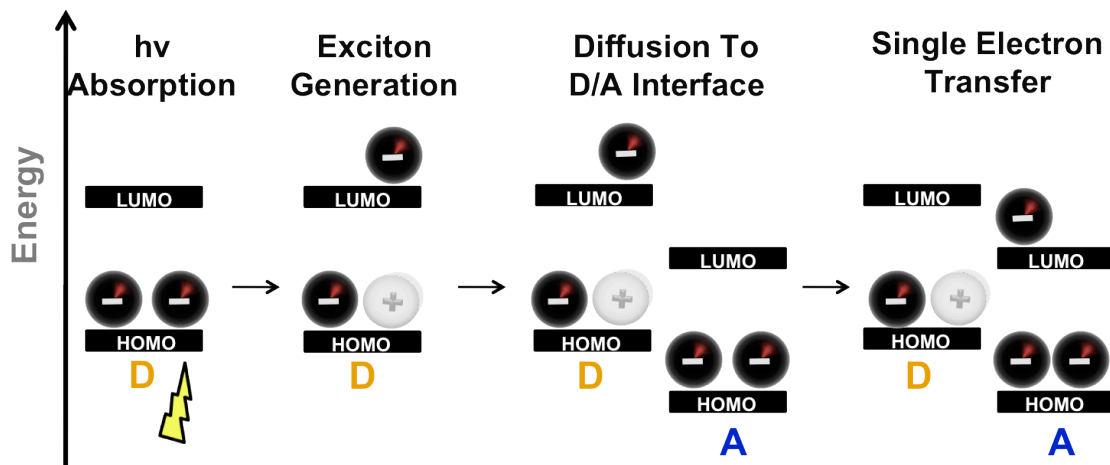
Figure 1.3: Process of Charge Separation in an OSC

$$FF = \frac{(J_m)(V_m)}{(J_{SC})(V_{OC})}$$

$$\eta = \frac{(FF)(J_{SC})(V_{OC})}{P_{in}} = \boxed{\frac{P_{out}}{P_{in}}}$$
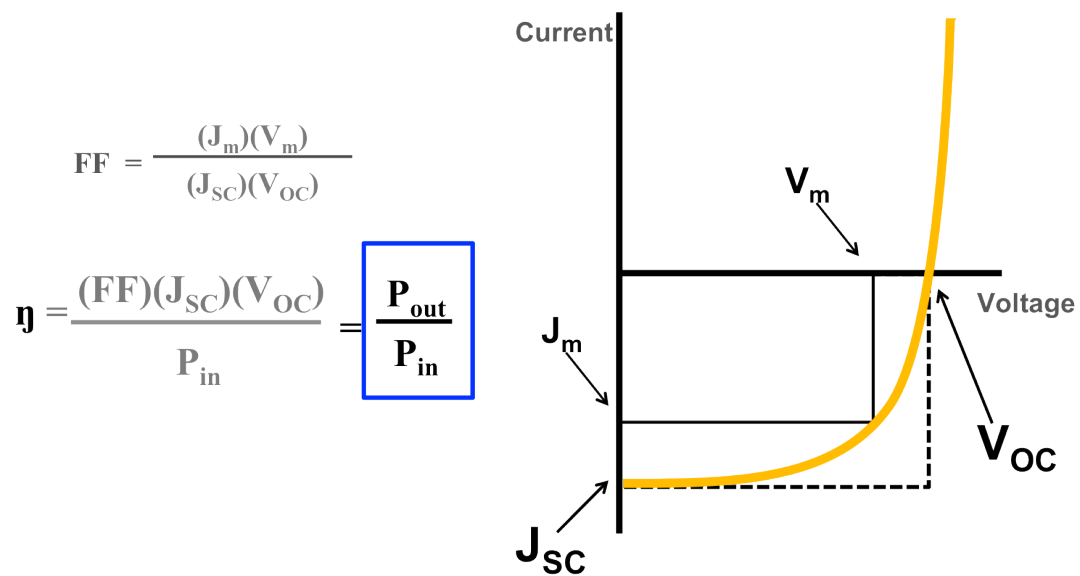
Figure 1.4: Calculation of PCE

1.5 Summary of Thesis

1.5.1 Current Challenges in OPVs

9

Elucidating the structure-function relationships of organic semiconductors has been central to the advancement of organic photovoltaics (OPVs). In particular, enhancing the performance of *p-type* materials in disordered heterojunctions is broadly acknowledged as the principal factor leading to current trends of improved power conversion efficiencies (PCEs).[26] However, two additional factors are crucially important for the next step forward in improving PCEs. First, investigating the influence, design and synthesis of new *n-type* materials, specifically fullerene acceptors, is of high importance.[27] Second, because fullerene performance is often compromised by the morphological disorder of bulk heterojunctions, developing fullerenes systems that retain fidelity within disordered blends is also of broad interest.[28] In light of these challenges, the field has witnessed a notable shift towards developing a comprehensive understanding of the design rules needed to advance the performance of fullerene acceptors in bulk heterojunctions.[29]

This work spotlights two multi-functional fullerene systems designed for blended heterojunctions. First, the synthesis of several novel fullerene-dye adducts with enhanced photon absorption will be presented. The ability of these adducts to absorb visible light in their pure state was evaluated and systematically examined versus their capacity to complement the absorption of low band gap donors and mediate charge transport in bulk heterojunctions. Second, mixed fullerene ternary blends were introduced as a strategy to stabilize the morphology in bulk heterojunctions and prolong operational lifetimes of OPV devices. Combined, these two systems offer unique insight into the rational design of fullerenes for their application in blended systems. A brief introduction to each thesis chapter is provided below.

1.5.2 Synthesis and Characterization of Fullerene-Dye Adducts

Amongst the numerous scientific contributions which have helped propel OPVs forward, efforts in elucidating the structure-function relationships of organic semiconductors have been central to advancing the field. In particular, an improved understanding of the design rules needed to enhance visible light absorption in *p-type* materials is broadly acknowledged as the principal factor leading to trends of improved PCEs thus far.[30] Today, it is possible to design *p-type* materials that satisfy the performance requirements of OPV systems with a high degree of fidelity, targeting strong absorption behavior at specified wavelengths, in addition to other desired materials properties. However, in spite of this progress, continued development of novel *p-type* materials has begun to yield diminishing returns.

Synthetic techniques utilized to enhance the absorption of low energy photons may ultimately limit the absorption of higher energy photons. For example, it is not uncommon for an optical window between 350 - 550 nm to emerge as the absorption profiles of low band-gap *p-type* materials shift toward the near infrared (IR).[31] As a result of this limitation, attention has recently pivoted in favor of strategies which take advantage of all components in blended heterojunctions to improve upon an OSC's ability to harness the full visible spectrum. Notably, reports describing methods for tuning the absorption of *n-type* materials to more effectively complement the absorption profiles of *p-type* materials have shown potential to improve the PCE of BHJs.[32] In general, however, photovoltaic research of *n-type* organic semiconductors is underdeveloped relative to that of *p-type* materials. Accordingly, the design rules of these systems are less well understood.[33]

PC$_{61}$BM, the most widely utilized *n-type* material in OPVs, has a strong absorption in the ultraviolet (UV) (λ_{max} = 283 nm, ε = 5.13 x 10^4 M^{-1}cm^{-1}) (**Figure 1.5**). However, before most UV photons can reach the semiconducting active layer of an OSC, they have already been absorbed by the earth's ozone layer and the indium tin oxide (ITO) transparent conducting electrode.[34] Because OSCs are intrinsically incapable of harvesting UV radiation, the high extinction coefficient of PC$_{61}$BM's UV absorption is of limited practical use. Moreover, PC$_{61}$BM is characterized by relatively poor absorption in the visible region (λ = 400 - 900 nm, ε < 5.00 x 10^3 M^{-1} cm^{-1}). The especially low molar extinction coefficient for visible light absorption is chiefly accredited to the high symmetry of C$_{60}$'s core and its lack of lone pair electrons. These factors reduce C$_{60}$'s dipole moment and preclude lower energy n-π* absorption transitions, therein reducing its ability to absorb visible light.[35]

Figure 1.5: Solution Absorption of PC$_{61}$BM and PC$_{71}$BM in Toluene

One synthetic strategy that has seen moderate success for enhancing the absorption of C$_{60}$ fullerene has been the covalent attachment of organic chromophores onto the fullerene

core.[36] Nominally, most reports of such modifications detail either the photophysical properties of these systems or their capacity for control over the phase-segregation behavior of heterojunction blends.[37] There are only several examples which specifically explore the potential for fullerene-dye adducts to boost photocurrent in OSCs through improved photon harvesting. Even less common are reports where the covalent anchor is systematically examined to determine its effect on PCE. Nevertheless, the prospects for enhancing OPV spectral absorption offered by fullerene-dye adducts warrant continued investigation of these systems.

Chapter 2 will present the synthesis of a family of fullerene-dye adducts and a study of their molecular and electronic properties. To begin, a description of the materials criteria informing the selection of organic dyes and their methods of attachment onto C_{60} will be discussed. The modular synthetic method developed to investigate multiple fullerene anchoring strategies will also be described. In consideration of their unique structures, chemical properties, and functional group tolerance, several modifications to reaction conditions typically used for synthesis of fullerene derivatives were ultimately employed to obtain the fullerene-dye adducts; the details of these considerations will be discussed. Finally, comparisons and contrasts between the optical, electronic, and thermal properties of the fullerene-dye adducts will be presented to evaluate their structure-function relationships. The global objective of this study is to develop a series of fullerene-dye adducts that will facilitate systematic examination of their utility in OSCs. This investigation will shed light on how the individual molecular properties of fullerene-dye adducts ultimately influence the collective opto-electronic behavior of their heterojunctions. It is anticipated that the results of this study will offer additional insight into the structure-function interplay of fullerenes,

which may improve upon the ability to rationally design fullerenes that complement blended photovoltaic systems more effectively.

1.5.3   Investigation of Fullerene-Dye Adduct Blends

Investigations of donor:fullerene-dye adduct thin films are instrumental for elucidating the potential of this class of fullerenes to perform as *n-type* materials with enhanced photon absorption relative to $PC_{61}BM$.[38] Chapter 3 will build upon the study of fullerene-dye adducts (**Figure 1.6**) through examination of their optoelectronic and morphological behavior in blended systems. The fullerene-dye adducts were blended with the organic donors: P3HT, PDPP2FT, and Benzoporphyrin (**Figure 1.7**). These three donors are distinguished by contrasting optical, electronic, and morphological features and are therefore expected to interact differently with each of the fullerene-dye adducts. This broad collection of blends will allow the influence of fullerene-dye adduct structure on bulk behavior to be thoroughly surveyed across different materials systems. To assess their influence on the collective properties of the blends, interpretation of their bulk behavior in mixed material assemblies will be based upon the prior analysis of their pristine molecular behavior.
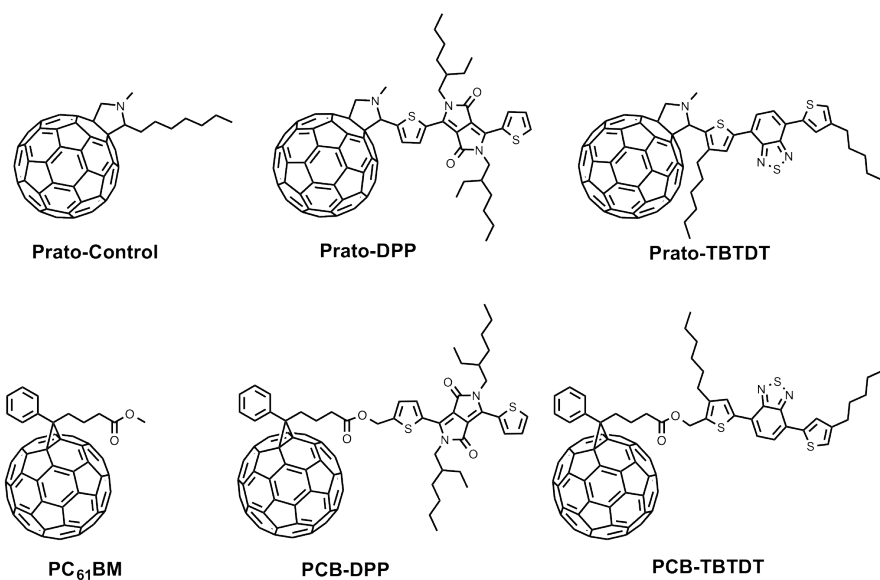
Figure 1.6: Chemical Structures of the Fullerene-Dye Adducts and Their Controls
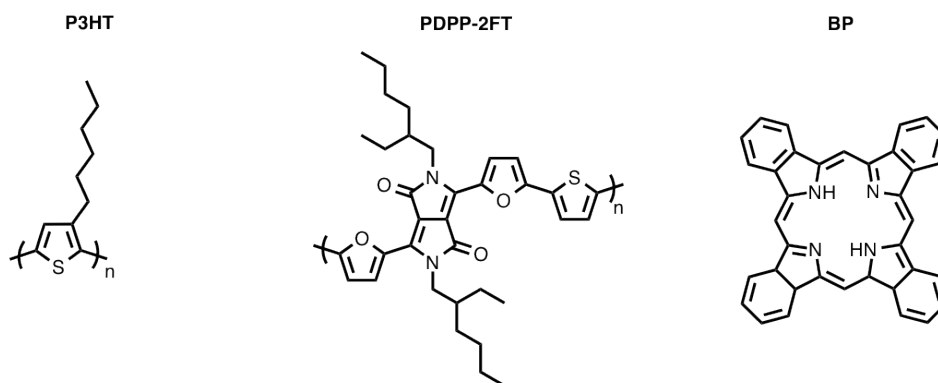
Figure 1.7: Chemical Structures of P3HT, PDPP2FT, and BP

Chapter 3 will present a study of the thin films prepared from fullerene-dye adducts blended with donors P3HT, PDPP2FT, and BP; with each donor:acceptor system analyzed independently in the order described. To begin, the optical behavior of each donor:fullerene-dye adduct system will be examined to assess their potential as optical complements. The frontier orbital energies of each blend will then be outlined to illustrate the electronic

alignment of these systems and their capacity for cascade charge transfer. Following, the processing conditions of these blends will be described, and the consequent morphologies of their thin films will be discussed. The electronic behavior of the *donor*:fullerene-dye adduct blends will then be analyzed via examination of the current-voltage (IV) plots and device parameters obtained from their OSCs. To investigate the general effectiveness of covalently anchoring dyes onto fullerene as a strategy for enhancing photon absorption, the external quantum efficiency (EQE) measurements performed on each *donor*:fullerene-dye adduct blend will also be presented and evaluated. Subsequently, the opto-electronic and morphological behavior of each blend will be summarized to help identify the global trends present in these systems. The results of these experiments are expected to clarify the structure-function relationships of fullerene-dye adducts as pristine materials and in blends, and are ultimately intended to improve upon the ability to rationally design fullerenes for blended systems with application in organic photovoltaic devices.

1.5.4 Investigation of P3HT:PC$_{61}$BM:PCB-F Mixed Fullerene Ternary Blends

Recent progress in OPVs has led the field to a notable shift in focus beyond simply improving PCE, towards exploring deeper issues in OPVs which pose additional barriers to market entry.[39] Notably, challenges associated with extending the operational lifetime of OSCs have received particular attention because of their commercial implications. A solar cell which experiences a rapid decline from 10% PCE after only several hours of operation would be impractical for use in consumer products. The importance of overcoming this obstacle cannot be undervalued, and it remains a principle topic for the organic electronics community to tackle moving forward.[40] Therefore, efforts in pursuit of clarifying the root

causes of device instability and improving upon the ability to rationally prolong the lifespan of OSCs are paramount.

It is especially well documented that changes within the active layer's microstructure, which evolve over time, play a central role in observations of reduced efficiency as OSCs age.[41] Numerous investigations exploring the relationship between PCE degradation and morphology changes have identified fullerene acceptors as a primary antagonist.[42] A general observation emerging from several independent studies is that fullerenes are prone to diffuse over time, leading to growth of large fullerene crystallites; a physical phenomenon that tends to coincide with decreased device performance.[43] OPV processing protocols typically limit annealing to five minutes at 150 °C to avoid fullerene crystallization and its associated drawbacks.[44]

There are several rational reasons for this crystallization behavior. X-ray analysis of unannealed thin films prepared from binary polymer/fullerene blends confirm that upon deposition, these blends typically assemble into morphologies where fullerenes reside within disordered, amorphous regions.[45] These initial morphologies are not necessarily permanent, however. In comparison to conjugated polymers, the small size of fullerenes affords them molecular mobility throughout disordered bulk systems. On account of their capacity for diffusion through amorphous domains, thermal treatment of these thin films may accelerate transformations in fullerene assembly within the bulk.[46] These structural evolutions may also occur at lower temperatures; although the timescale for said changes would be longer.[47] A general correlation can therefore be drawn between fullerene diffusion and the microstructural evolution of the active layer.

Recently, several novel OPV studies have emerged which exploit the behavior of fullerenes to address problems associated with morphological instability. In general, these studies used mixed fullerene ternary blends to suppress of fullerene crystallization. However, these demonstrations of the advantages of ternary blends in extending OSC operational stability have chiefly employed fullerenes that were similar in chemical structure and behavior; yielding marginal influence over bulk morphology beyond suppression of fullerene crystallization. Although this strategy has its merits, it is also of interest to explore systems which program additional handles of control over molecular self-assembly.

Numerous reports of organic semiconducting systems incorporating perfluorinated materials have highlighted the general utility of their inclusion as a vehicle for enhancing self-assembly.[48] The basis for this behavior can be traced to the propensity of perfluorinated groups to migrate towards the air interface, on account of fluorine's characteristically low surface energy with air. The subsequent influence of this migration on the anisotropy of bulk molecular assemblies has proven beneficial in a number of cases.[49] In particular, the incorporation of perfluorinated fullerenes (PCB-F) into standard solar cell architectures has also been explored as an approach for inducing self-assembled, de-facto electron transporting layers.[50] Evidence of favorable bulk morphologies stemming from perfluorinated phase-segregation is generally noted via tangible benefits to charge transport and extraction; empirically observed as statistically significant improvements in J_{sc}, FF, and R_s. The use of fullerenes modified with perfluorinated groups therefore presents a viable approach for screening the affects of enhanced self-assembly on the operational lifetime of OSCs prepared from ternary blends.

To investigate the morphological and electronic stability of ternary blend devices utilizing two chemically distinct fullerenes with enhanced phase-segregation, a series of ternary blends based on P3HT:PC$_{61}$BM:PCB-F were prepared (**Figure 1.8**). The absolute ratio of P3HT:fullerene was held constant in these devices, while the relative ratios of each fullerene were systematically varied. As indicated above, reports detailing the tendency of perfluorinated fullerenes to phase-segregate from PC$_{61}$BM suggested PCB-F would be an optimal material for introducing greater influence over the bulk morphology of ternary blends.[51] Moreover, because PCB-F has identical frontier orbital energies as PC$_{61}$BM, its use presented a control for molecular electron affinity. In principle, this feature would allow the interpretation of emerging trends in the electronic behavior of the blends to be simplified and unambiguously attributed to the chemical identity of the perfluorinated tail rather than the LUMO of the fullerene core itself. It was therefore of interest to explore the general applicability of ternary blends for prolonging the morphological stability and device lifetime of OSCs through use of a blending strategy where enhancements in self-assembly could be rationally dialed-in.
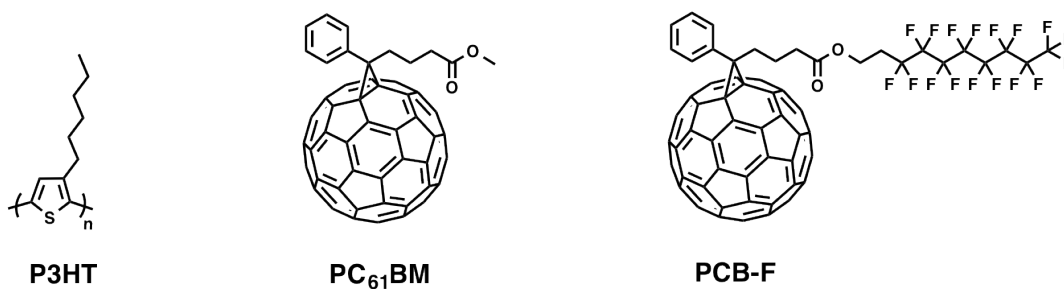
Figure 1.8: Chemical Structures of P3HT, PC$_{61}$BM, and PCB-F

Chapter 4 will investigate the thermal behavior and self-assembly of P3HT:PC_{61}BM:PCB-F ternary blends, systematically varying the relative ratios of PC_{61}BM:PCB-F to rationalize the influence of their chemical identity and blending properties on trends observed in the morphological stability and operational lifetime of their corresponding OSCs. First, a study contrasting the thermal behavior of PC_{61}BM:PCB-F binary blends with P3HT:PC_{61}BM:PCB-F ternary blends will be presented. Analysis of these two systems will clarify the chemical origin of thermal trends emerging from the introduction of perfluorinated pendants. The effects of thermal processing on the self-assembly of P3HT:PC_{61}BM:PCB-F blends will then be described through analysis of their thin film morphologies via optical microscopy and GIWAXS measurements. This behavior will in turn be discussed through the context of DSIMS measurements collected to analyze their vertical molecular profiles. Finally, a device study of these ternary blends will be presented to rationalize the influence of blend composition, self-assembly, and thermal processing on the electrical behavior and operational lifetime of OSCs. The results of this investigation are anticipated to shed light on the potential for ternary blends with enhanced self-assembly to extend morphological and electronic stability to OPV devices. The global objectives of this study are to add clarity to future decisions in choice of fullerenes for ternary blends, and to further improve upon the ability to rationally design fullerenes which target desirable materials properties in blended bulk systems.

Chapter 2

Synthesis and Characterization of Fullerene-Dye Adducts

2.1 Introduction

Organic photovoltaics (OPVs) have received widespread interest over the past decade due to their promise as a renewable source of energy with application in flexible, lightweight solar modules.[1] In addition, OPVs demonstrate potential to reduce the expense associated with energy-intensive industrial scale fabrication because they can be solution-deposited at low temperatures over large surface areas, similar to techniques utilized for printing newspapers.[2] Notably, solar power conversion efficiencies (PCEs) for OPVs have increased steadily over the past ten years, with multiple examples of solar cells demonstrating efficiencies greater than 10%.[3] Therefore, on account of their attractive properties and prospects for broad applicability, green technologies incorporating organic solar cells (OSCs) are anticipated to reach the consumer market in the near future.

Amongst the numerous scientific contributions which have helped propel OPVs forward, efforts elucidating the structure-function relationships of organic semiconductors have been central to advancing the field. In particular, an improved understanding of the design rules needed to enhance visible light absorption in *p-type* materials is broadly acknowledged as the principal factor leading to trends of improved PCEs thus far.[4] Today, it is possible to design *p-type* materials that satisfy the performance requirements of OPV systems with a high degree of fidelity, targeting strong absorption behavior at specified wavelengths, in addition to other desired materials properties. However, in spite of this

progress, continued development of novel *p-type* materials has begun to yield diminishing returns.

Synthetic techniques utilized to enhance the absorption of low energy photons may ultimately limit the absorption of higher energy photons. For example, it is not uncommon for an optical window between 350 - 550 nm to emerge as the absorption profiles of low band-gap *p-type* materials shift toward the near infrared (IR).[5] As a result of this limitation, attention has recently pivoted in favor of strategies which take advantage of all components in blended heterojunctions to improve upon an OSC's ability to harness the full visible spectrum. Notably, reports describing methods for tuning the absorption of *n-type* materials to more effectively complement the absorption profiles of *p-type* materials have shown potential to improve the PCE of BHJs.[6] In general, however, photovoltaic research of *n-type* organic semiconductors is underdeveloped relative to that of *p-type* materials. Accordingly, the design rules of these systems are less well understood.[7]

$PC_{61}BM$, the most widely utilized *n-type* material in OPVs, has a strong absorption in the ultraviolet (UV) (λ_{max} = 283 nm, ε = 5.13 x 10^4 $M^{-1}cm^{-1}$). However, before most UV photons can reach the semiconducting active layer of an OSC, they have already been absorbed by the earth's ozone layer and the indium tin oxide (ITO) transparent conducting electrode.[8] Because OSCs are intrinsically incapable of harvesting UV radiation, the high extinction coefficient of $PC_{61}BM$'s UV absorption is of limited practical use. Moreover, $PC_{61}BM$ is characterized by relatively poor absorption in the visible region (λ = 400 - 900 nm, ε < 5.00 x 10^3 M^{-1} cm^{-1}). The especially low molar extinction coefficient for visible light absorption is chiefly accredited to the high symmetry of C_{60}'s core and its lack of lone pair

electrons. These factors reduce C_{60}'s dipole moment and preclude lower energy n-π* absorption transitions, therein reducing its ability to absorb visible light. [9]

Figure 2.1: Solution Absorption of $PC_{61}BM$ and $PC_{71}BM$ in Toluene

$PC_{71}BM$, the C_{70} analogue of $PC_{61}BM$, was developed as a fullerene alternative to $PC_{61}BM$ with improved absorption.[10] The absorption profiles of $PC_{61}BM$ and $PC_{71}BM$ are shown above in **Figure 2.1**. Due to the reduced symmetry of its oblong core, $PC_{71}BM$ demonstrates enhanced visible absorption relative to $PC_{61}BM$ (λ_{max} = 282 nm, ε = 7.3 x 10^4 $M^{-1}cm^{-1}$; λ = 465 nm, ε = 2.5 x 10^4 $M^{-1}cm^{-1}$). Challenges associated with the isolation of pristine C_{70} from other fullerene isomers, however, have led to the higher costs associated with commercially sourced $PC_{71}BM$.[11] Even so, most high performance OPVs have been fabricated using $PC_{71}BM$ blends; with improvements in performance largely tracing their

origin to the additional visible absorption of C_{70}. This observation signals that enhancing fullerene's absorption may offer a viable course for improving the spectral absorption of OSCs and their PCEs as a consequence.

One synthetic strategy that has seen moderate success for enhancing the absorption of C_{60} fullerene has been the covalent attachment of organic chromophores onto the fullerene core.[12] Nominally, most reports of such modifications detail either the photophysical properties of these systems or their capacity for control over the phase-segregation behavior of heterojunction blends.[13] There are only several examples which specifically explore the potential for fullerene-dye adducts to boost photocurrent in OSCs through improved photon harvesting. Even less common are reports where the covalent anchor is systematically examined to determine its effect on PCE. Nevertheless, the prospects for enhancing OPV spectral absorption offered by fullerene-dye adducts warrant continued investigation of these systems.

This chapter will present the synthesis of a family of fullerene-dye adducts and a study of their molecular and electronic properties. To begin, a description of the materials criteria informing the selection of organic dyes and their methods of attachment onto C_{60} will be discussed. The modular synthetic method developed to investigate multiple fullerene anchoring strategies will also be described. In consideration of their unique structures, chemical properties, and functional group tolerance, several modifications to reaction conditions typically used for synthesis of fullerene derivatives were ultimately employed to obtain the fullerene-dye adducts; the details of these considerations will be discussed. Finally, comparisons and contrasts between the optical, electronic, and thermal properties of the fullerene-dye adducts will be presented to evaluate their structure-function relationships.

The global objective of this study is to develop a series of fullerene-dye adducts that will facilitate systematic examination of their utility in OSCs. This investigation will shed light on how the individual molecular properties of fullerene-dye adducts ultimately influence the collective opto-electronic behavior of their heterojunctions. It is anticipated that the results of this study will offer additional insight into the structure-function interplay of fullerenes, which may improve upon the ability to rationally design fullerenes that complement blended photovoltaic systems more effectively.

2.2 Materials Selection

The oligomers chosen to be anchored onto C_{60} were selected on the basis of several criteria. First, the organic chromophores would require a strong optical absorption in the 350 – 600 nm spectral window. Second, the materials would need frontier orbital energies that could promote cascade electron transfer. Third, highly soluble analogues of the oligomers would need to be relatively simple to access synthetically.

The most important of the materials attributes described above is the molar extinction coefficient of the 350 – 600 nm window. To harness low energy photons, high performance OSCs typically incorporate low band-gap *p-type* materials in their blends.[14] However, the methods utilized to synthesize conjugated materials which absorb low energy photons, commonly sacrifice high absorption coefficients in the 350 – 600 nm optical window as a result.

The design rules for low band-gap conjugated materials typically employ the use of three techniques. First, these materials feature extended pi-conjugated networks. As the extent of conjugation increases, electron repulsion drives the HOMO to higher energies,

while the ability to delocalize electrons in the excited state simultaneously lowers the LUMO. This feature leads to a reduced band-gap that scales with the extent of conjugation.[15] Second, these materials call for synthetic strategies that allow donor acceptor units to be alternated along the molecular backbone. Alternating higher HOMO/LUMO moieties with a lower HOMO/LUMO moiety along the backbone facilitates frontier orbital mixing, allowing lower band-gaps to be accessed.[16] Third, many of these materials utilize moieties which are aromatic in their excited state. This feature reduces the energetic penalty for promoting an electron into the excited state by yielding a structure that gains energetic stability through aromaticity; ultimately lowering the energy of the LUMO and the band gap as a result.[17]

The combination of these three features leads to low band-gap materials that are able to absorb more low energy photons; but there is a tradeoff. As the n-π* transitions of these materials move deeper into the near IR, their π - π* transitions remain stationary. A general consequence of this process is the opening of an optical gap in the 350 - 600 nm region of the visible spectrum. Due to $PC_{61}BM$'s characteristically small extinction coefficient in this region, it is also unable to capture these photons and they typically go unharnessed by the organic semiconducting active layer. For this reason, organic dyes for the fullerene adducts were selected based on the ability of their extinction coefficient in the 350 nm – 600 nm optical range to complement the optical absorption of low band-gap *p-type* materials.

The second most important attribute was for the dye to have HOMO/LUMO values that facilitated cascade electron transfer from the polymer donor to the fullerene acceptor vis-à-vis the dye. The absence of proper electronic alignment would increase the likelihood of energetic environments that could inhibit the transport of free-charge carries.[18] Disruptions to carrier transport promote charge trapping, a feature which can reduce PCEs.[19] For example,

single electron charge transfer from an electron promoted to a -4.0 eV LUMO into the empty -3.8 eV LUMO of a neighboring molecule would represent a forbidden transition because it is uphill in energy. Therefore, electrons promoted to -4.0 eV excited states would reach nominal potential wells if surrounded by molecular states of -3.8 eV, effectively trapping their charges. Selecting dyes with orbital energies that provide a driving force for cascade charge transfer minimizes the possibility of charge trapping resulting from improper energetic alignment.

The third materials criterion was that the soluble conjugated oligomers be obtained from simple synthetic procedures. For this reason, dyes were targeted which could be synthetically accessed in two steps or less. Excessively long synthetic procedures would be less practical for screening multiple attachment strategies to the fullerene core. Moreover, incorporation of conjugated oligomers with low solubility would likely reduce the ability of fullerene-dye adducts to be solution processed.

Ultimately, Diketopyrrolopyrrole (**DPP**) and Thiophene Benzothiadiazole Thiophene (**TBTDT**) were the organic chromophores selected for attachment onto C_{60} in this study, as they fulfilled the criteria described above. Their structures are shown below in **Figure 2.2**. DPP has its main absorption between 420 nm – 580 nm with $\varepsilon = 2.62$ x 10^4 $M^{-1}cm^{-1}$ at a local maximum of $\lambda = 551$ nm. TBTDT has its main absorption between 365 - 535 nm with $\varepsilon = 1.31$ x 10^4 $M^{-1}cm^{-1}$ at a local maximum of $\lambda = 455$ nm (**Figure 2.3**). In addition, DPP has a HOMO of -5.6 eV and a LUMO of -3.5 eV and TBTDT has a HOMO of -6.1 eV and a LUMO of -3.8 eV (**Table 2.1**). In
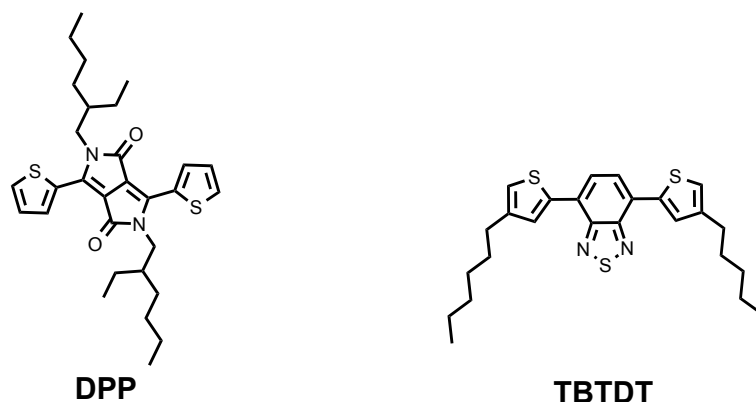
Figure 2.2: Chemical Structures of DPP and TBTDT

principle, the frontier orbitals of these organic dyes should facilitate single electron transfer between P3HT, which has a HOMO of -5.2 eV and a LUMO of -3.0 eV, and $PC_{61}BM$, which has a HOMO of -6.4 eV and a LUMO of -4.1 eV. Moreover, both dyes are relatively simple to access synthetically. Soluble analogues of DPP and TBTDT oligomers can be obtained within two steps from commercially sourced starting materials. These three factors presented DPP and TBTDT as strong candidates for attachment onto the fullerene core.

Compound	HOMO (eV)	LUMO (eV)	Main Absorption (nm)	λ_{max} (nm)	ε ($M^{-1}cm^{-1}$)	E_g (ev)
DPP	-5.6	-3.5	420 - 580	551	26,200	2.1
TBTDT	-6.1	-3.8	365 - 535	455	13,100	2.3
P3HT	-5.2	-3.0	300 - 550	450	7,910	2.2
$PC_{61}BM$	-6.4	-4.1	275 - 390	283	51,300	2.3

Table 2.1: Solution Absorbance Properties and Frontier Orbital Energies of

DPP, TBTDT, P3HT, $PC_{61}BM$, and $PC_{71}BM$
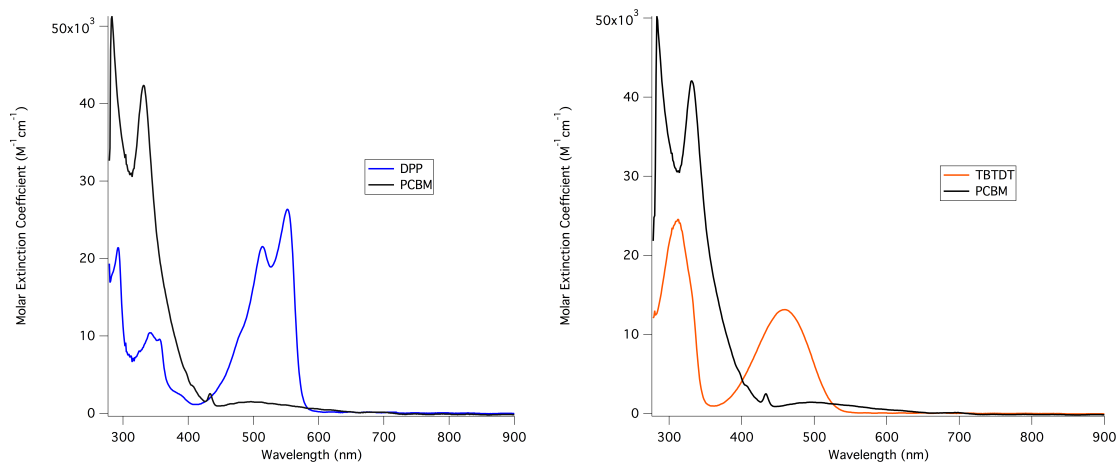
Figure 2.3: Solution Absorption Spectra of Organic Dyes in Toluene **a.** DPP **b.** TBTDT

2.3 Attachment Strategy

Functionalization of C_{60} fullerene presents several unique considerations for design of synthetic routes. First, the only synthetic handle of C_{60} is an olefin. With thirty equivalent olefins, monoaddition onto any of C_{60}'s double bonds yields stereochemically identical mono adducts. Bisaddition of C_{60}, however, yields a multiplicity of stereoisomers (sixteen for a perfectly symmetric adduct and many more for asymmetric adducts).[20] Second, C_{60} molecules agglomerate into nanoclusters in solution. Meaning, even when dissolved, fullerenes rarely exist as singular molecular entities. This issue confounds accurate calculations of reaction stoichiometry because the actual number of unobstructed C_{60}'s available for reaction cannot be accurately estimated. As a result, 1:1 molar ratios of reactants to fullerene result in higher instances of bisadditions than would be statistically anticipated. Notably, isolation of monoadducts from bisadducts can complicate purification and significantly lower yields. Therefore, when possible, measures should be taken to limit the production of bisadducts if monoadducts are the compounds of interest.

Because C_{60}'s sole functional handle is an olefin, synthetic modifications of pristine C_{60} are limited to addition and cycloaddition reactions, several of which find common use in C_{60} chemistry.[21] Among these, 1,3-dipolar cycloadditions have proven especially practical.[22] In particular, the Prato reaction has seen broad utility in C_{60} functionalization due to its simplicity and robust tolerance of sensitive functional groups.[23] The Prato reaction relies on the formation of a reactive ylide from an aldehyde and N-Methyl glycine. Loss of CO_2 generates the ylide, which adds across the double bond of C_{60} in a concerted fashion. One unique feature of the Prato reaction is the resulting pyrrolidine heterocycle anchored onto C_{60}. Studies utilizing fullerenes containing this nitrogen heterocycle are generally characterized by lower PCEs, however. It has been speculated that trace acids present in the chlorinated deposition solvents may quarternize the pyrrolidine nitrogen's lone pair, yielding electronic traps which inhibit efficient transport of free-charge carriers in OPVs. For this reason, a nitrogen-free anchoring strategy was sought in parallel as an alternative to the Prato reaction.

Attachment strategies utilizing the cyclopropyl anchor of methanofullerenes were also of interest. In particular, $PC_{61}BM$'s structure proved an attractive option because its consistent performance in bulk heterojunctions demonstrates broad tolerance across a range of *p-type* materials. The methano structure of $PC_{61}BM$ is obtained following addition of the reactive diazo species across a C_{60} double bond, formed via basic treatment of a p-tosyl hydrazone. Following addition of the diazo species to C_{60}, loss of N_2 yields a methano attachment in either the [5,6] or [6,6] positions. $PC_{61}BM$ with the [6,6] closed position has been noted to yield solar cells with higher power conversion efficiencies.[24]
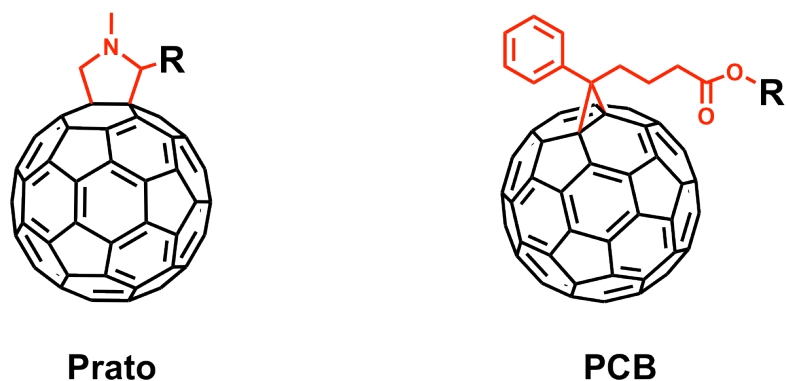
Figure 2.4: General C_{60} Anchoring Platforms

This study will therefore compare and contrast fullerene-dye adducts which utilize the Prato reaction's pyrrolidine attachment and the $PC_{61}BM$-like methano anchor (**Figure 2.4**). Analysis of the molecular and electronic properties of fullerene-dye adducts within these two systems of covalent anchors will allow the influence of the anchor to be decoupled from the structure-function properties of the fullerene-dye adducts and assessed independently.

2.4 Synthesis

To simplify investigation of the selected organic dyes against different C_{60} anchors, it was useful to develop a modular synthetic target that would allow facile access to multiple structures. In this light, the terminal mono-aldehyde of each given dye was selected as the target synthon. Though several synthetic methods exist for formylation of aryl compounds, the Vilsmeier-Haack formylation was identified as the best candidate because this electrophilic aromatic substitution utilizes mild reaction conditions which afford broad functional group tolerance.[25] Upon obtaining the terminal aldehyde, the dye may be attached directly onto C_{60} via the Prato reaction. Alternatively, the aldehyde may be reduced to a primary alcohol, a modification which would allow for attachment onto C_{60} as an analogue of

PC$_{61}$BM's methyl ester. The syntheses of the four fullerene-dye adducts outlined below were based upon these targets.

2.4.1   Synthesis of Prato-TBTDT

The synthesis of TBTDT was modeled on a report detailed by Yamashita and coworkers of a series of low band-gap conjugated oligomers incorporating the ortho-quinoidal acceptor unit benzothiadiazole.[26] The synthesis of Prato-TBTDT is shown below in **Scheme 2.1**. To ensure solubility of the final products, however, 3-hexylthiophene was utilized as the starting point instead of thiophene. This choice necessitated a slight modification to reaction conditions because the less hindered 5 position of thiophene also has a slightly higher pka.[27] A strong kinetic base such as nBuLi favors removal of the more accessible proton at the 5 position, although removal of the proton at the 2 position is thermodynamically favored. For this reason, a dilute solution with excess 3-hexyl thiophene relative to nBuLi was used to mitigate the formation of 2-stannyl-3-hexylthiophene over the desired 2-stannyl-4-hexylthiophene, in addition to reaction at -78 ˚C. The desired product was obtained following fractional distillation with 82% yield. Subsequently, a Stille biaryl cross-coupling was performed to obtain TBTDT by treating 3 eq of the stannylated thiophene with 1 eq of 4,7-dibromobenzothiadiazole in the presence of Pd$_2$(dba)$_3$. The desired compound was obtained in near quantitative yields. The TBTDT unit was then treated under Vilsmeier-Haack conditions to obtain the mono-formylated product TBTDT-CHO in 72% yield. A Prato reaction was later used to obtain the title product by treating TBTDT-CHO with sarcosine in refluxing toluene. To favor the formation of the mono adduct, the reaction was performed at high dilution with a large excess of C$_{60}$. The title compound was purified

via flash column chromatography on silica gel and collected as a shinny black granular solid with an isolated yield of 25%. Notably, after extensive efforts to purify the title compound, carbon disulfide was the only solvent system found to reliably separate the mono Prato-TBTDT from its bis adducts.
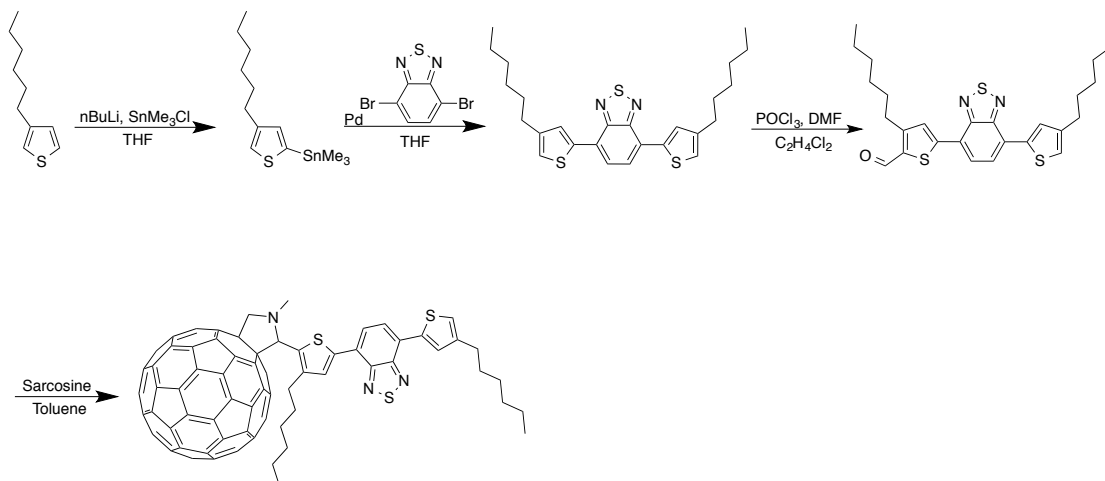
Scheme 2.1: Synthesis of Prato-TBTDT

2.4.2 Synthesis of PCB-TBTDT

The synthesis of PCB-TBTDT is outlined below in **Scheme 2.2**. As described in the section above, TBTDT-CHO was obtained under Vilsmeier-Haack conditions. Subsequently, the aldehyde was reduced to a primary alcohol with NaBH$_4$ in 89% yield. Next, a DCC coupling was employed to form the TBTDT-benzyl ketoester. A large excess of 4-benzylbutyric acid was needed to push the reaction to completion. The TBTDT-ketoester was isolated with 68% yield. Notably, efforts to obtain the hydrazone using protocols typically employed for the p-tosylhrazone analogue of the PC$_{61}$BM precursor[28] led to complete loss of the starting material and no formation of the desired product. In particular, reaction

conditions utilizing temperatures high enough to vigorously reflux benzene and azeotrope water into a dean stark trap led to formation of unwanted polymerized side products. The desired TBTDT-hydrazone was eventually accessed following optimization of the molar concentrations and reaction temperatures. A highly concentrated solution of the ketoester treated with p-tosylhydrazide in benzene at 70°C for 3 hours was ultimately used to obtain the TBTDT-hydrazone with 50% yield. The title compound, PCB-TBTDT was afforded via slight modification of the procedure used to obtain $PC_{61}BM$.[29] Traditionally, this reaction is accomplished by treating the p-tosyl hydrazone with sodium methoxide in pyridine to form the reactive diazo intermediate. The resulting diazo compound is then transferred dropwise into a solution of C_{60} in toluene. Attempts to obtain the title compound using this standard protocol consistently failed, with neither product nor starting material ever recovered. It was later reasoned the reactive diazo intermediate likely cannibalized the thiadiazole ring. A modification to the standard reaction conditions preventing the diazo species from being formed in a thiadiazole-rich environment proved successful. A highly dilute solution of the TBTDT-hydrazone was added dropwise, extremely slowly, to a solution of toluene, pyridine, sodium methoxide, and excess C_{60}. This modification favored addition of the diazo to C_{60} by reducing the probability a diazo species would encounter a thiadiazole. The title compound was isolated via column chromatography on silica gel in toluene as a maroon solid with 36 % yield.
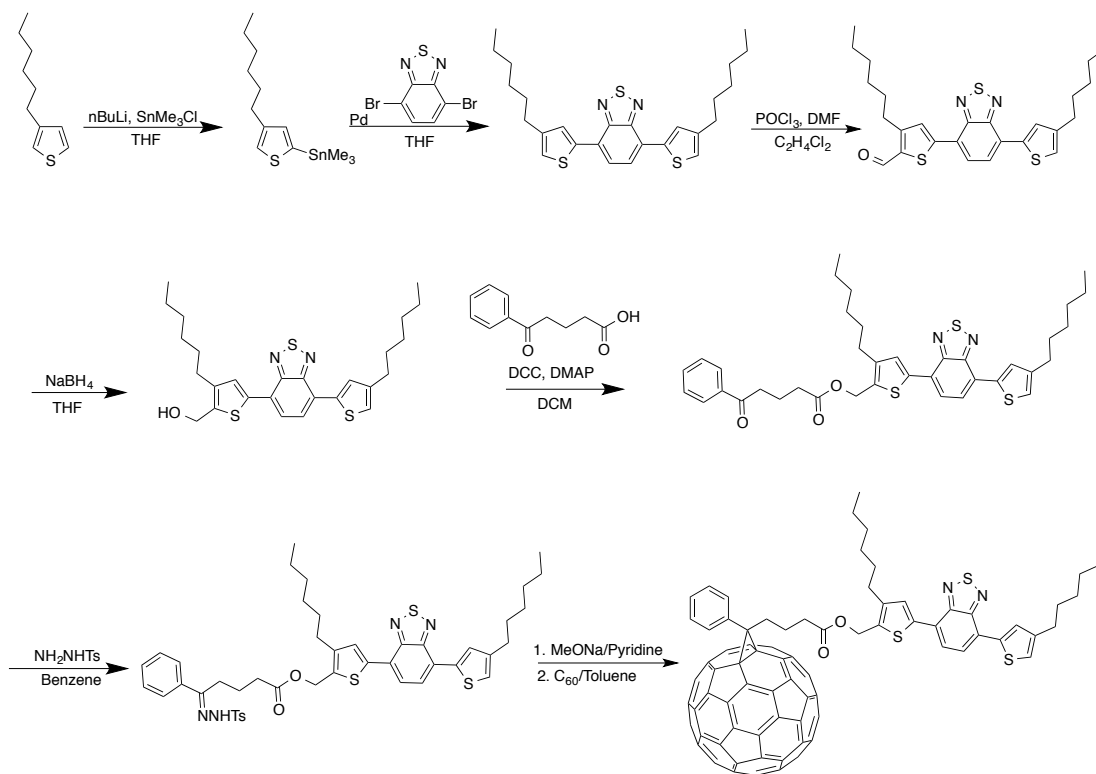
Scheme 2.2: Synthesis of PCB-TBTDT

2.4.3 Synthesis of Prato-DPP

The synthesis of Prato-DPP is outlined below in **Scheme 2.3**. The DPP oligomer was obtained following literature protocols.[30] Attempts to mono-formylate DPP under traditional Vilsmeier-Haack conditions were largely unsuccessful. Reaction conditions utilizing a large excess of the Vilsmeier-Haack reagents were only slightly more successful, with 10% isolated yield following purification. It was reasoned that both phosphoryl chloride and the Vilsmeier-Haack reagent formed in-situ reacted with the lactam rings of DPP to form undesired side products. Several literature reports detail side reactions of lactams and amides under Vilsmeier-Haack conditions which bypass formation of an aldehyde.[31] Investigations of alternative formylation strategies ultimately led to a Vilsmeier-Haack formylation

modified by use of pyrophosphoryl chloride and N-methyl formanilide.[32] These conditions enhance the electrophilicity of the Vilsmeier-Haack reagent while avoiding the equilibrium that favors formation of the lower energy N,N-dimethylchloromethyleneiminium chloride salt produced with phosphoryl chloride. This chloride salt is noted as the principle antagonist for rearrangements in lactam rings.[33] In avoiding formation of the chloride salt, no ring rearrangements or side products were observed. Furthermore, use of the bulkier N-methyl formanilide enhanced the reagent's regioselectivity; guiding reaction away from the lactam carbonyls towards the thiophene alpha position. This modification allowed DPP-CHO to be obtained in 72% isolated yields, a significant improvement over the traditional route. Subsequently, a Prato reaction was employed to obtain the title compound Prato-DPP. The product was purified via flash column chromatography in toluene and isolated as a purple solid in 36% yield.
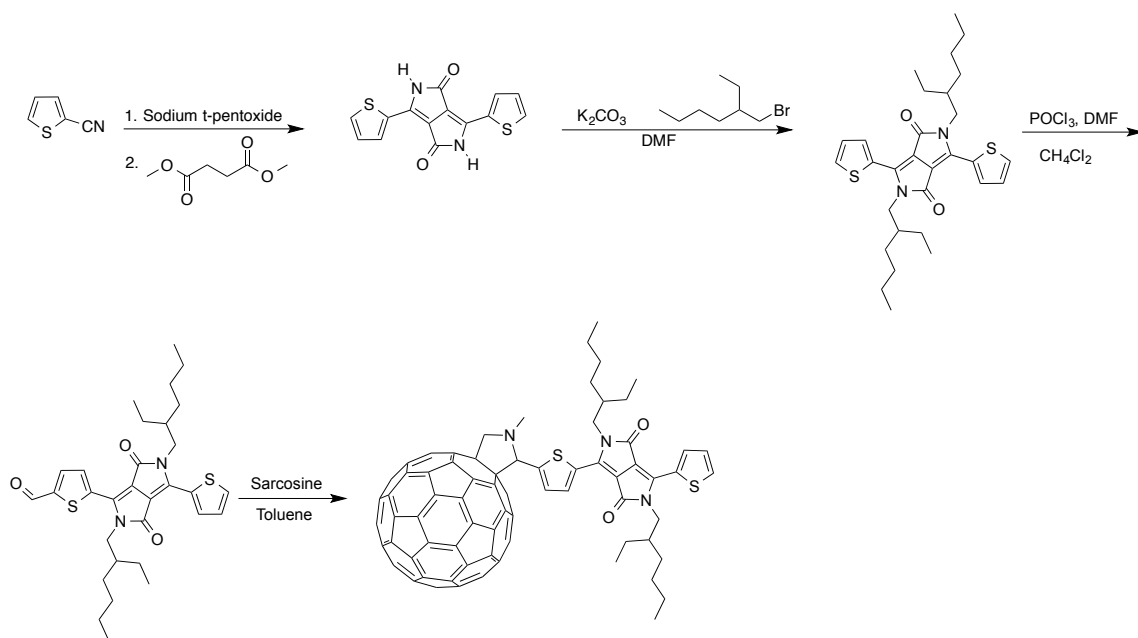
2.4.4 Synthesis of PCB-DPP

The synthesis of PCB-DPP is outlined in **Scheme 2.4** below. DPP-CHO was obtained as described above. The mono-aldehyde was then reduced to a primary alcohol with NaBH$_4$ to afford DPP-CH$_2$OH in 26% yield. Subsequently, a DCC coupling of DPP-CH$_2$OH with 4-benzylbutyric acid was employed and the DPP-benzyl ketoester was isolated in 69% yield. The ketoester was then treated with p-tosyl hydrazide to afford the DPP-hydrazone in 91% yield. The modified reaction conditions utilized for preparation of the TBTDT-hydrazone analogue were also employed for this reaction. To obtain the title compound, the DPP-hydrazone was diluted in toluene, added dropwise to a solution of C$_{60}$, sodium methoxide, pyridine, and toluene, and heated to reflux over night. Following purification via flash column chromatography on silica gel with toluene, the desired product was isolated as a purple solid with 24% yield.
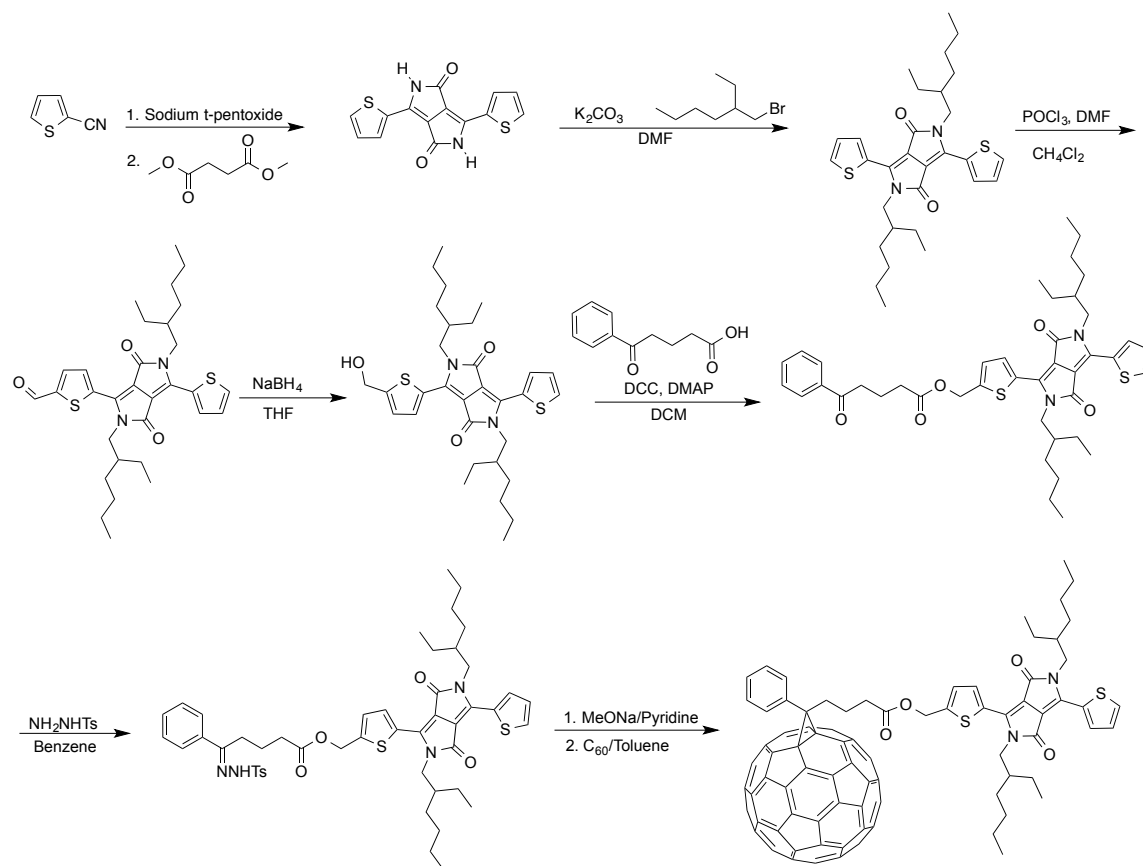
Scheme 2.4: Synthesis of PCB-DPP

2.4.5 Synthesis of Prato-Control

The synthesis of Prato-Control is outlined below in **Scheme 2.5**. The title compound was obtained via the Prato reaction by reacting dodecyl aldehyde with a solution of sarcosine and C_{60} in toluene and refluxing overnight. The product was purified via flash column chromatography in toluene and isolated as a brown solid with 32% yield.
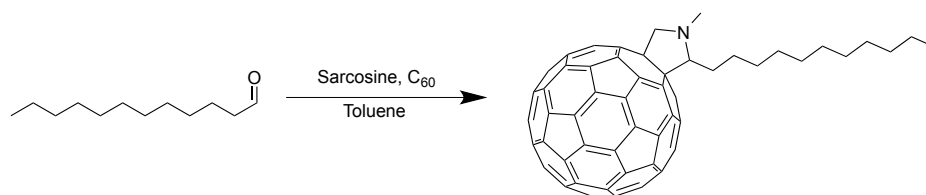
Scheme 2.5: Synthesis of Prato-Control

2.5 Electronic Characterization of Fullerene-Dye Adducts

2.5.1 Solution UV-Vis

The four fullerene-dye adducts were analyzed via solution UV-vis in toluene and compared to their oligomer controls. The Prato-Control is a strong UV-absorber with ε = 5.28 x 10^4 $M^{-1}cm^{-1}$ at λ_{max} = 284 nm, but shows negligible visible light absorption between 400 nm and 900 nm (ε < 5.00 x 10^3 $M^{-1}cm^{-1}$). The pristine TBTDT unit has its main absorption between 360 nm - 530 nm with ε = 1.31 x 10^4 $M^{-1}cm^{-1}$ at its local maximum λ = 460 nm. Interestingly, the absorption profile of Prato-TBTDT is an effective hybrid of the Prato-Control and TBTDT's optical absorptions (**Figure 2.5**). Prato-TBTDT is also a strong UV absorber with its π-π* transition located at λ_{max} = 322 nm with ε = 6.49 x 10^4 $M^{-1}cm^{-1}$. However, in contrast to the Prato-Control, Prato-TBTDT has significantly enhanced absorption between 400 nm and 550 nm with a local maximum at λ = 466 nm with ε = 1.96 x 10^4 $M^{-1}cm^{-1}$. A 6 nm red shift is noted between Prato-TBTDT and the corresponding local maximum of pristine TBTDT. This Stokes shift suggests attachment of TBTDT onto C_{60} lowers the dipole moment of the dye's n-π* transition.
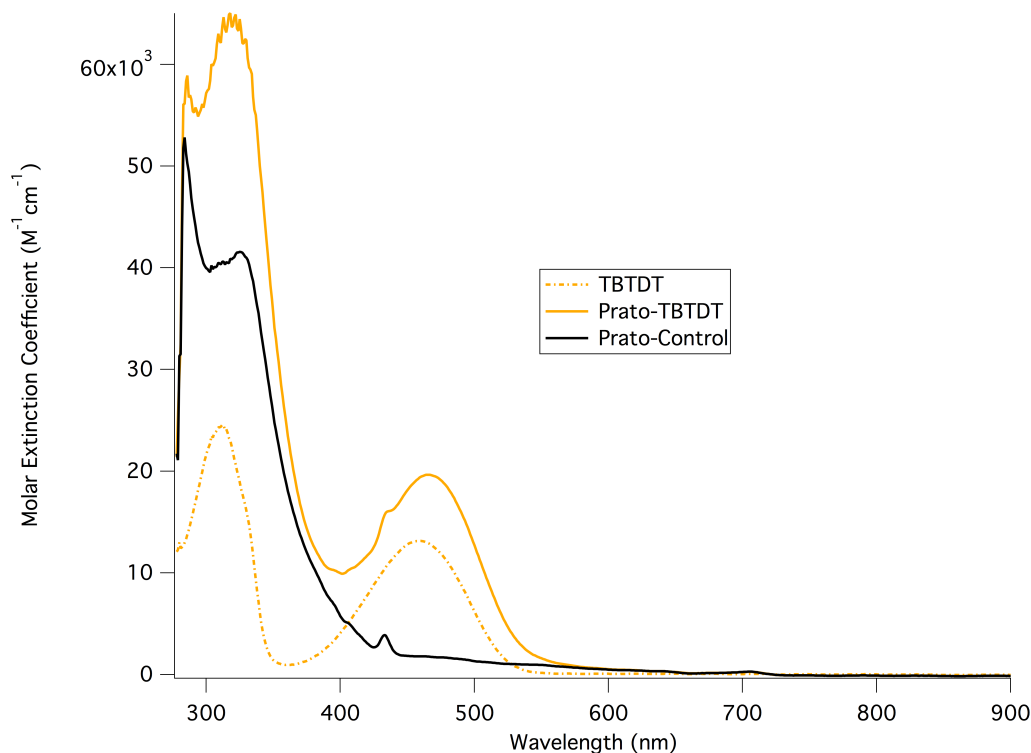
Figure 2.5: Solution Absorption of Prato-TBTDT and Controls in Toluene

The pristine DPP oligomer has a strong visible absorption between 430 nm and 585 nm with $\varepsilon = 2.63 \times 10^4$ M^{-1}cm^{-1} at $\lambda_{max} = 552$ nm. Prato-DPP, similar to Prato-TBTDT and Prato-Control, is also a strong absorber of UV radiation, with $\varepsilon = 6.72 \times 10^4$ M^{-1}cm^{-1} at $\lambda_{max} = 283$ nm. Enhanced absorption between 450 nm and 600 nm is attributed to the presence of the DPP dye, as Prato-DPP has a $\varepsilon = 3.53 \times 10^4$ M^{-1}cm^{-1} at its local maximum $\lambda = 563$ nm (**Figure 2.6**). A 20 nm red shift in the absorption onset relative to the pristine oligomer is observed for the Prato adduct. The molar extinction coefficients in the visible region for Prato-TBTDT and Prato-DPP were both larger than those of their respective parent oligomers TBTDT and DPP. In addition, the observed red-shifts in visible transitions suggest that

attachment of these dyes to C_{60} via the pyrrolidine anchor lowers the dipole moments of these electronic states.
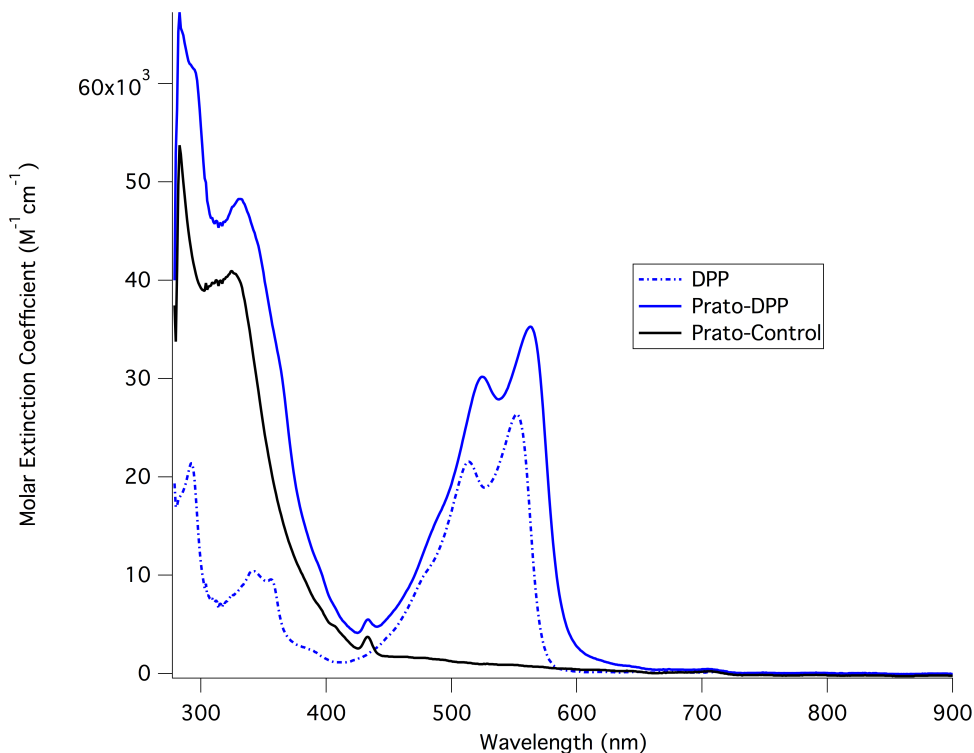
Figure 2.6: Solution Absorption of Prato-DPP and Controls in Toluene

$PC_{61}BM$, similar to the Prato-Control, is a strong absorber of UV radiation with $\varepsilon =$ 5.13 x 10^4 $M^{-1}cm^{-1}$ at $\lambda_{max} = 283$ nm, but shows negligible absorption of visible light ($\lambda = 400 - 900$ nm, $\varepsilon < 5.00$ x 10^3 $M^{-1}cm^{-1}$). PCB-TBTDT is also a strong UV absorber with its π-π* transition having a molar extinction coefficient of $\varepsilon = 6.48$ x 10^4 $M^{-1}cm^{-1}$ at $\lambda_{max} = 282$ nm (**Figure 2.7**). In contrast to $PC_{61}BM$, however, PCB-TBTDT has significantly enhanced absorption between 400 nm and 535 nm with $\varepsilon = 1.53$ x 10^4 $M^{-1}cm^{-1}$ at its local $\lambda_{max} = 464$ nm. A 10 nm red-shift is observed in the local maximum of PCB-TBTDT's n-π* transition

relative to the analogous peak on pristine TBTDT. This Stokes shift suggests attachment to C_{60} lowers the dipole moment of the attached dye's n-π* transition.
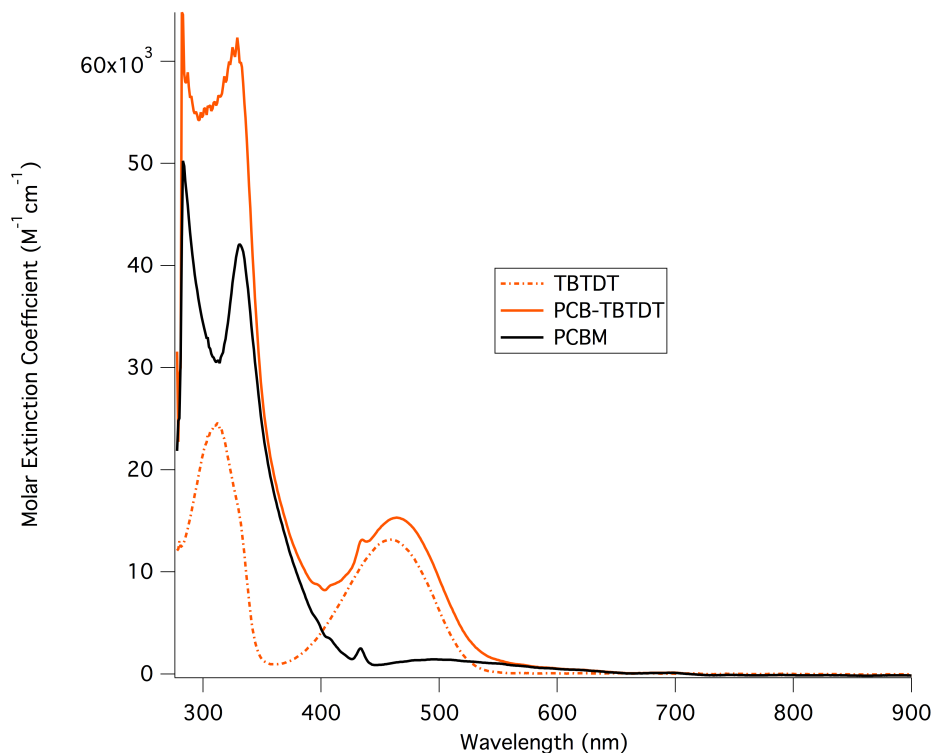
Figure 2.7: Solution Absorption of PCB-TBTDT in Toluene

PCB-DPP, like Prato-TBTDT and Prato-Control, is also a strong UV absorber with ε = 7.38 x 10^4 $M^{-1}cm^{-1}$ at λ_{max} = 284 nm. Enhanced absorption between 440 nm and 590 nm is again attributed to the presence of the dye, and PCB-DPP has ε = 2.95 x 10^4 $M^{-1}cm^{-1}$ at its local maximum λ = 559 nm (**Figure 2.8**). A 7 nm red-shift is observed in the local maximum of PCB-DPP in comparison to that of pristine DPP. The molar extinction coefficients in the visible region for PCB-TBTDT and PCB-DPP were both larger than those of their respective parent oligomers TBTDT and DPP. This suggests, that attachment of these dyes to C_{60} via the PCB linker raises the oscillator strength of these electronic transitions.
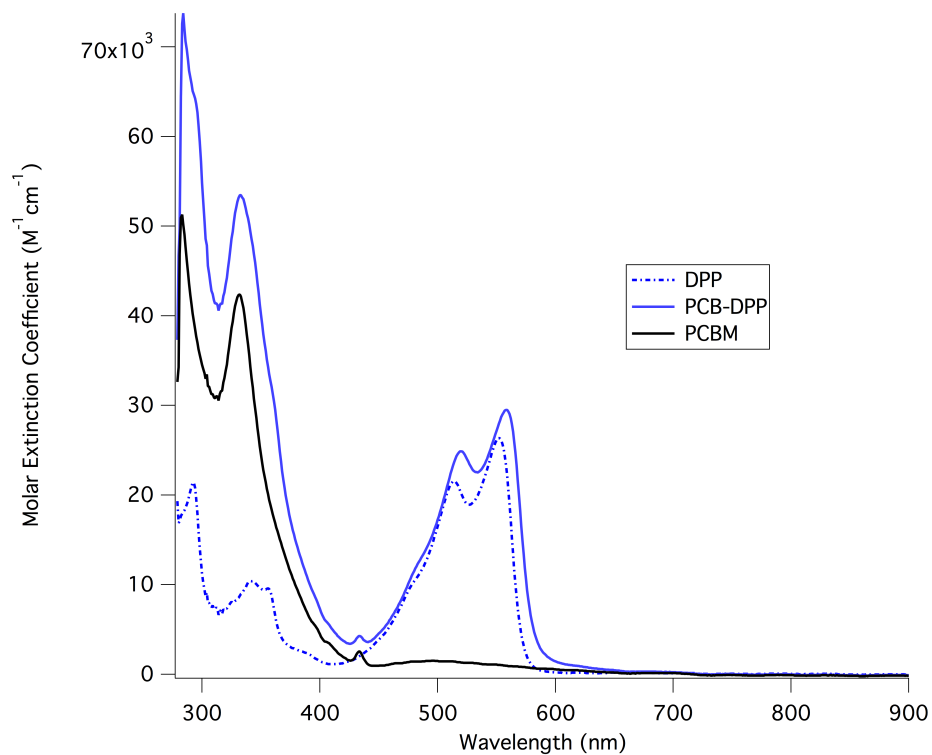
Figure 2.8: Solution absorption of PCB-DPP and controls in toluene
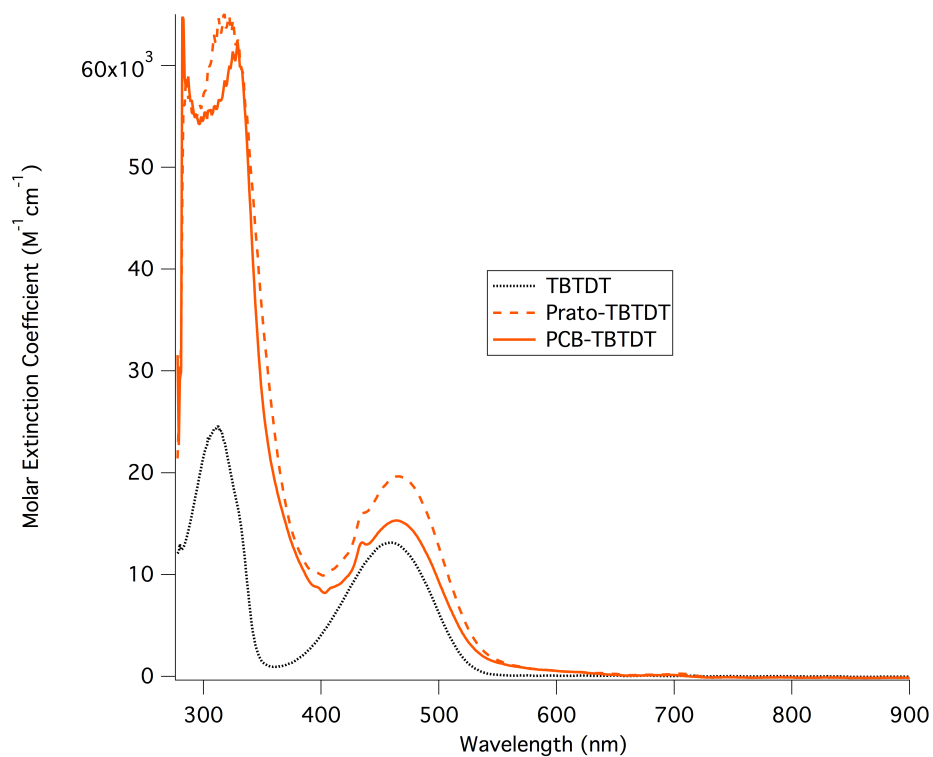
Figure 2.9: Comparison of the Solution Absorption of the TBTDT Analogues in Toluene

Comparison of Prato-TBTDT with PCB-TBTDT highlights the fact that these particular fullerene-dye adducts share the same local maximums and absorption onsets (λ = 464 nm and λ = 530 nm, respectively) (**Figure 2.9**). These values are both red-shifted 4 nm relative to pristine TBTDT. Nevertheless, the Prato adduct is a stronger absorber with the molar extinction coefficient of its local maximum (ε = 1.96 x 10^4 $M^{-1}cm^{-1}$) 28% more intense than that of the PCB analogue (ε = 1.53 x 10^4 $M^{-1}cm^{-1}$), and 49% more intense than pristine TBTDT (ε = 1.31 x 10^4 $M^{-1}cm^{-1}$). These observations suggest that while the anchors equally reduce the energetic cost of promoting an electron to the LUMO, the Prato adduct raises the intensity of this transition.

48
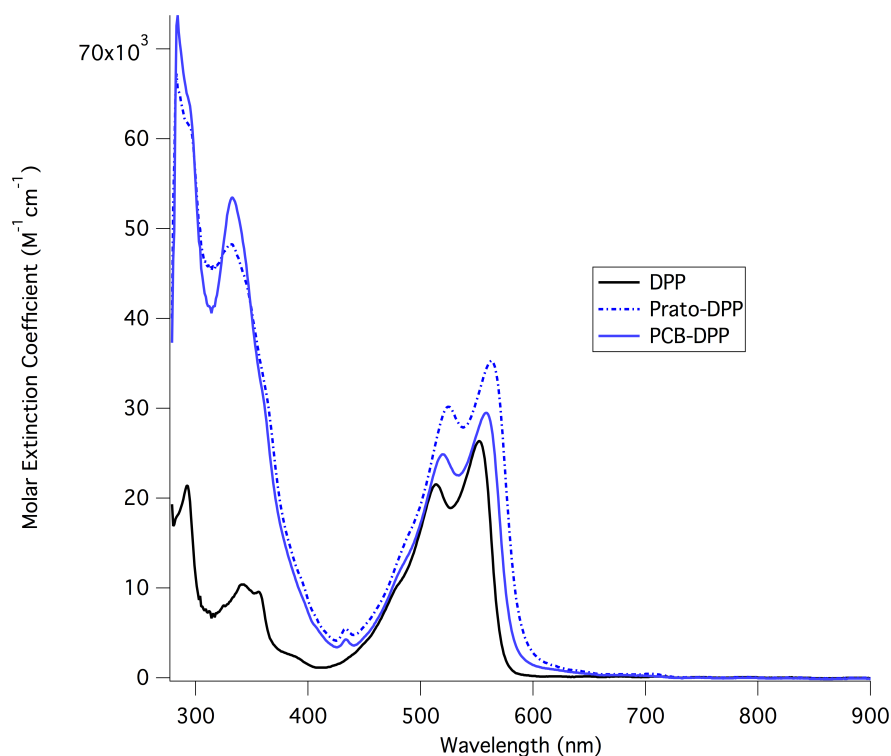
Figure 2.10: Comparison of the Solution Absorption of the DPP Analogues in Toluene

In contrast, comparison of Prato-DPP, PCB-DPP, and DPP shows that the Prato adduct's local maximum and absorption onset ($\lambda = 563$ nm and $\lambda = 592$ nm, respectively) are red-shifted relative to PCB-DPP ($\lambda = 559$ nm and $\lambda = 582$ nm, respectively) and additionally red-shifted relative to DPP ($\lambda_{max} = 552$, $\lambda = 572$ nm) (**Figure 2.10**). In addition, observations of the molar extinction coefficient at their respective local maximums indicate Prato-DPP's transition ($\varepsilon = 3.53 \times 10^4$ M^{-1}cm^{-1}) is 19% larger than that of PCB-DPP ($\varepsilon = 2.95 \times 10^4$ M^{-1}cm^{-1}) and 34% larger than that of pristine DPP. This trend in extinction coefficients parallels that of the TBTDT adducts. However, a divergence between the two systems of adducts is noted with respect to the wavelengths of their absorption onsets and local maximums. The molecular identity of the covalent anchor is observed to influence these two parameters for the DPP analogues to different degrees, though no such difference is found in the TBTDT analogues. The source of this discrepancy is currently unknown.

2.5.2   Cyclic Voltammetry

Cyclic voltammetry was performed to further probe the electronic properties of these materials. Measurements were carried out using a three-electrode configuration; with a platinum button working electrode, a platinum wire counter electrode, and a Ag/Ag$^+$ reference electrode. The reference electrode was prepared with 0.01 M AgNO$_3$/0.1 M TBAPF$_6$/4:1 Acetonitrile:Chlorobenzene. Measurements were recorded at scan rates of 100 mV/s in 0.1 M TBAPF$_6$/4:1 Acetonitrile:Chlorobenzene and are shown below in **Figure 2.11**.

49

C$_{60}$ fullerene has been documented to possess a triply degenerate LUMO.[34] Meaning, in principle, its LUMO can support up to six electrons. In practice, however, the addition of the first electron into C$_{60}$'s LUMO alters the energies of the five remaining states. Nevertheless, under certain conditions C$_{60}$ can be reduced by up to six electrons,[35] the first three of which may be observed in a standard electrochemical window at room temperature. This study's analysis of C$_{60}$ as a control confirmed this finding, with three chemically and electrochemically reversible red/ox couples observed at -4.1 eV, -3.7 eV, and -3.3 eV (LUMO = -4.1 eV). PC$_{61}$BM demonstrated similar electrochemical behavior with three electrochemically and chemically reversible peaks observed at -4.0 eV, -3.6 eV, and -3.1 eV (LUMO = -4.0 eV). The Prato-Control also showed three electrochemically and chemically reversible peaks at -4.0 eV, -3.6 eV, and -3.1 eV (LUMO = -4.0 eV). A single chemically and electrochemically reversible peak was observed for TBTDT at -3.3 eV. DPP also had only one reduction peak at -3.4 eV that was chemically and electrochemically reversible.

The four fullerene-dye adducts were found to display electrochemical behavior that essentially superimposed the pendant dye's reduction peak onto that of its respective fullerene anchor. This behavior indicates that the fullerene and dye, in principle, remain largely electrochemically decoupled, in spite of their spatial proximity. Therefore, for the purpose of aligning frontier orbital energies, the dye and the fullerene may be considered to coexist as independent electronic entities.

Interestingly, however, there are several important distinctions to note within these four fullerene-dye adducts. Prato-TBTDT has four chemically and electrochemically reversible peaks at -4.0 eV, -3.6 eV, -3.3 eV, and -3.0 eV. The third of these red/ox couples residing at -3.3 eV directly correlates to the reduction peak of TBTDT and has similar shape to the peaks

attributed to the Prato-Control. PCB-TBTDT, in contrast, displays different behavior. PCB-TBTDT has four reversible peaks at -4.1 eV, -3.7 eV, -3.4 eV and -3.1 eV, but only the peaks at -4.1 eV, -3.7 eV, and -3.1 eV are electrochemically and chemically reversible. These three peaks happen to correlate directly to the first three reductions of $PC_{61}BM$. The third reduction of PCB-TBTDT's four red/ox couples, located at -3.4 eV, is chemically reversible since multiple scans leave the red/ox couple unmolested, but the broadened appearance of this red/ox couple renders it non electrochemically reversible as it falls outside of the 75 mV limit of the Nernst equation.

Prato-DPP, akin to Prato-TBTDT, has four chemically and electrochemically reversible peaks. These four peaks reside at -4.0 eV, -3.6 eV, -3.4 eV, and -3.0 eV (LUMO = -4.0 eV). The third of these peaks at -3.4 eV correlates directly to the reversible reduction of the pendant DPP oligomer. PCB-DPP, like PCB-TBTDT, has only three electrochemically and chemically reversible peaks at -4.1 eV, -3.7 eV, and -3.1 eV. The peak corresponding to DPP's reduction is neither chemically reversible nor electrochemically reversible. When the potential is scanned to the third peak, the onset of reduction is noted with a slight shoulder. This peak is not neutralized on the reverse scan, however. This observation suggests insertion of the electron into DPP's LUMO destabilizes the adduct, resulting in detachment of the pendant dye from its anchor. As previously described, PCB-TBTDT showed broadening of its pendant dye's red/ox couple, indicating this reduction was mildly destabilized as well. The extent of this destabilization is amplified in the case of PCB-DPP, however. Despite these observations, this non-reversible behavior is not expected to have a significant impact in solar cells because it is rare for a fullerene to house three electrons simultaneously.[36] The global observation of these fullerene-dye adducts is that, within experimental error, their

LUMOs are equivalent to that of PC$_{61}$BM. A summary of these results are provided below in **Table 2.2**.

Molecule	Red$_1$(eV) vs. vac	Red$_2$(eV) vs. vac	Red$_3$(eV) vs. vac	Red$_4$(eV) vs. vac	Red$_1$(eV) vs. Fc/Fc$^+$	Red$_2$(eV) vs. Fc/Fc$^+$	Red$_3$(eV) vs. Fc/Fc$^+$	Red$_4$(eV) vs. Fc/Fc$^+$
C$_{60}$	-4.1	-3.7	-3.3	-	-1.0	-1.4	-1.8	-
TBTDT	-3.3	-	-	-	-1.8	-	-	-
DPP	-3.4	-	-	-	-1.7	-	-	-
Prato-Control	-4.0	-3.6	-3.0	-	-1.1	-1.5	-2.1	-
Prato-TBTDT	-4.0	-3.6	-3.3	-3.0	-1.1	-1.5	-1.8	-2.1
Prato-DPP	-4.0	-3.6	-3.4	-3.0	-1.1	-1.5	-1.7	-2.1
PC$_{61}$BM	-4.0	-3.6	-3.0	-	-1.1	-1.5	-2.1	-
PCB-TBTDT	-4.1	-3.7	-3.4	-3.1	-1.0	-1.4	-1.7	-2.0
PCB-DPP	-4.1	-3.7	-	-3.1	-1.0	-1.4	-	-2.0

Table 2.2: Summary of Frontier Orbital Energies of the Fullerene-Dye Adducts and Their Component Subunits Registered to Vacuum and Fc/Fc$^+$

a.

b.

d.

e.

f.

g.

h.

i.

52
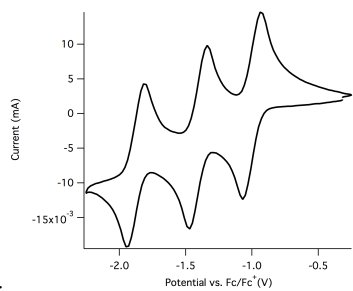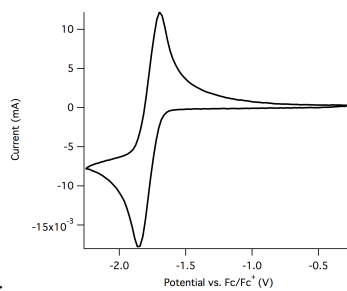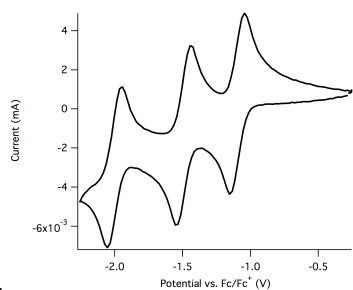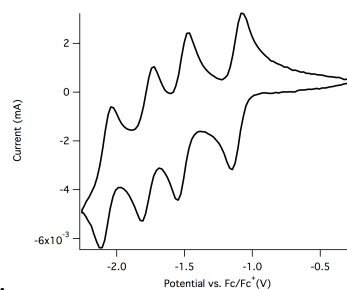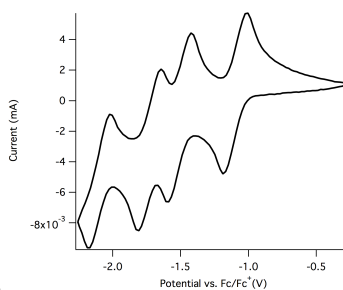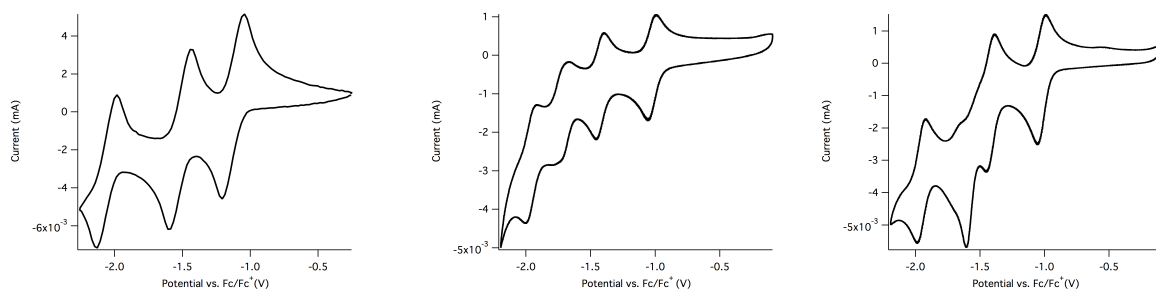
Figure 2.11: Cyclic Voltammagrams of the Fullerene-Dye Adducts and Their Controls.

a. C_{60} **b.** TBTDT **c.** DPP **d.** Prato-Control **e.** Prato-TBTDT **f.** Prato-DPP

g. $PC_{61}BM$ **h.** PCB-TBTDT **i.** PCB-DPP

2.6 Thermal Characterization of Fullerene-Dye Adducts

2.6.1 Thermal Gravimetric Analysis

Thermal decomposition profiles of the fullerene-dye adducts and their component controls were collected via thermal gravimetric analysis (TGA). Measurements were performed under a nitrogen atmosphere with a temperature ramp of 10 ˚C per minute. A general observation within the four fullerene-dye adducts is their enhanced thermal stability relative to their pristine dye subunits, with an average weight loss of < 1% until 305 ˚C. Beyond 310 ˚C the thermal decomposition of the DPP adducts is accelerated. Relative to the DPP adducts, the TBTDT adducts demonstrate moderate enhancements in their thermal stability, as their mass loss doesn't exceed 1% until beyond 330 ˚C. In both cases, thermal decomposition of the PCB adducts is accelerated in comparison to their Prato analogues. At 600 ˚C the fullerene core comprises the majority of the remaining mass, as the pendant dyes of each adduct have decomposed. The results of this analysis are provided below in **Figure 2.12**.
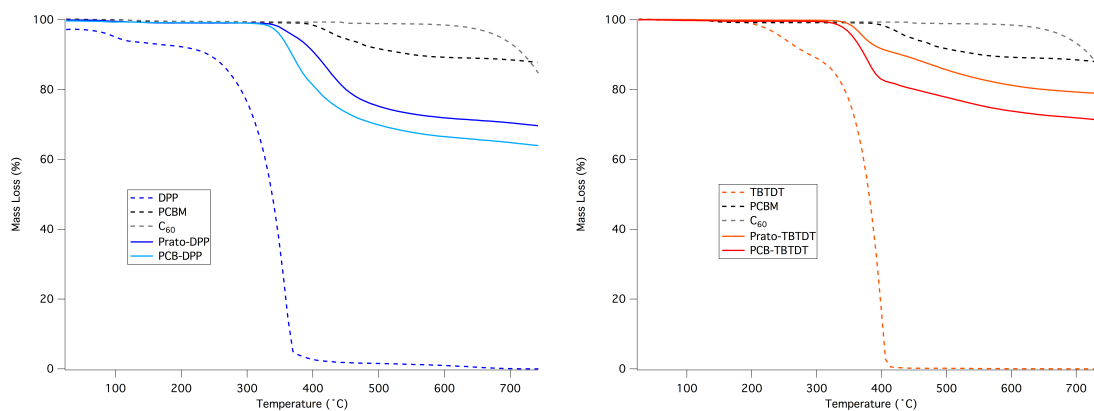
Figure 2.12: Thermal Decomposition of Fullerene-Dye Adducts

a. DPP derivatives **b.** TBTDT derivatives

2.6.2 Differential Scanning Calorimetry

Differential Scanning Calorimetry was performed on the fullerene-dye adducts to examine their thermal transitions. Measurements were recorded under a helium/nitrogen atmosphere from 0 - 330 ˚C with a thermal ramp of 10 ˚C/min, using powder samples of 5-7 mg. Three Heat/Cool cycles were collected in total, the second of which is provided below in **Figure 2.13**.

PC$_{61}$BM shows a cold crystallization[37] and melt on its heating cycle at 185 ˚C and 285 ˚C, respectively. In contrast, no thermal transitions were observed for any of the four fullerene-dye adducts or Prato-Control, and each material appears to be amorphous. No thermal transitions were noted on the cooling cycles, and all of the materials retain their amorphous behavior as they are cooled.

54
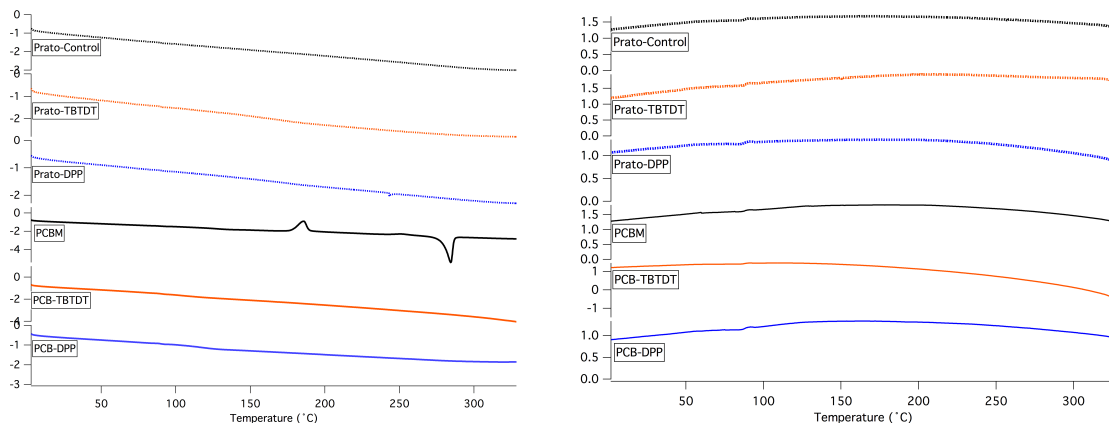
Figure 2.13: Differential Scanning Calorimetry of Fullerene-Dye Adducts

a. heating scan **b.** cooling scan

2.7 Conclusion

The synthesis of four fullerene-dye adducts and the Prato-Control was presented along with a rational for their development. Analysis of their opto-electronic and thermal behavior was also described. Although small variances in the optical behavior of each fullerene-dye adduct were found, overall, the adducts were observed to show enhanced optical absorption between 350 nm - 600 nm relative to their pristine fullerene and organic dye subunits. This improvement in absorption is anticipated to produce a measurable enhancement in the photocurrent of OSCs utilizing these materials as acceptors within their blends. In addition, investigations of the photoluminesence of the adducts show quenching of the pendant dye's fluorescence. This observation suggests single-electron transfer from the dye to the fullerene is the primary relaxation pathway following optical excitation to the LUMO, further strengthening the premise that attaching dyes onto fullerene will contribute to the photogenerated current. Moreover, the orbital energies of the adducts were observed to mimic those of $PC_{61}BM$, with the presence of the dye having no noticeable affect on the

LUMO of the fullerene. While differences in the anchoring units did appear to vary the stability of the pendant dye, the dye and fullerene were still observed to operate semi-independently of one another and are not anticipated to be problematic in that solid state. Furthermore, analysis of the thermal behavior of these materials shows they form amorphous assemblies with thermal stabilities that are compatible with temperatures used for processing plastics. The collective effect of these features suggests the four fullerene dye-adducts have the appropriate combination of properties to be successfully integrated as *n-type* materials in donor/acceptor blends for OSCs, and in principle, should lead to noticeable enhancements in the photocurrent when blended with complimentary p-type materials.

2.8 Experimentals
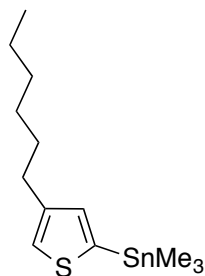
(4-hexylthiophen-2-yl)trimethylstannane

A dry 500 mL 3-neck RBF equipped with a stir bar, condenser, addition funnel, rubber septa, and outfitted with an argon atmosphere was charged with 3-hexylthiophene (14.92 mL, 83.33 mmol) and anhydrous THF (200 mL). The solution mixture was cooled to -78 ˚C. n-BuLi

(36.60 mL, 2.5 M, 91.66 mmol) was then cannulated into the addition funnel and added dropwise to the solution mixture over 1 hour. The reaction mixture stirred at -78 ˚C for 1 additional hour and was then gradually warmed to room temperature, where it stirred for an additional 2 hours. The reaction mixture was then cooled to -78 ˚C, and trimethyltin chloride (100 mL, 1M, 100 mmol) was added via syringe. The reaction mixture gradually warmed to room temperature and left to stir overnight. Upon completion, the reaction mixture was quenched with sodium bicarbonate (200mL) and extracted with ether (3 x 150 mL). The organic fractions were combined, rinsed with sodium bicarbonate (200 mL), rinsed with brine (2 x 200 mL), dried over sodium sulfate, filtered to remove solids, and condensed under reduced pressure to yield 31.39 g of a crude light brown oil. The crude product was purified via fractional distillation (47 mtorr, 76 ˚C, 140˚C oil bath) to yield a clear, colorless oil (22.74 g, 82.4%). ^{1}H NMR (500 MHz, CDCl$_3$): δ 7.21 (at, J = 0.9 Hz, 1H), 7.03 (at, J = 0.9 Hz, 1H), 2.67 (t, J = 8.0 Hz, 2H), 1.65 (p, J = 7.8, 7.3 Hz, 1H), 1.42 – 1.27 (m, 6H), 0.96 – 0.85 (m, 3H), 0.51 – 0.21 (m, 9H); ^{13}C NMR (125 MHz, CDCl$_3$): δ 144.82, 137.44, 136.86, 125.86, 31.93, 30.94, 30.21, 29.40, 22.85, 14.33, -8.07; HRMS (FI): Calcd for C$_{13}$H$_{24}$SSn (M$^+$), 332.0621, found m/z, 332.04.
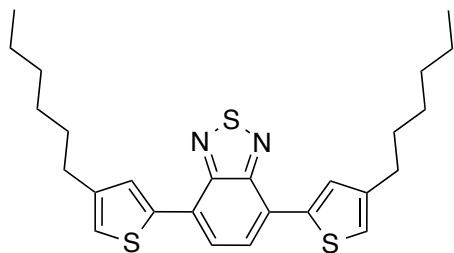
4,7-bis(4-hexylthiophen-2-yl)benzo[c][1,2,5]thiadiazole

A dry 500 mL 3-neck RBF equipped with a stir bar, 2 rubber septa, condenser, and argon atmosphere was charged with (4-hexylthiophen-2-yl)trimethylstannane (22.737 g, 68.67 mmol), 4,7-dibromobenzothiadiazole (6.73 g, 22.89 mmol), $Pd_2(dba)_3$ (1.04 g, 1.14 mmol), and tri-o-tolylphosphine (1.05 g, 3.45 mmol). The contents of the flask was evacuated and flushed with argon 3 times. Anydrous THF (250 mL) was cannulated into the flask, and the solution mixture was sparged with argon for 1hour while stirring. The reaction mixture was then heated to reflux and allowed to stir overnight. Upon completion, the reaction mixture was quenched with water and extracted with Et_2O (3 x 100mL). The organic fractions were combined, washed with brine (2 x 100 mL), dried over magnesium sulfate, filtered to remove solids, and condensed under reduced pressure to yield a crude orange brown semi-solid. The crude product was adsorbed onto silica gel and purified via flash column chromatography on silica gel in 49:1 Hexanes:Ethyl Acetate. The title compound was isolated as a bright orange solid (10.17 g, 94.9%). TLC R_f = 0.35 (Silica Gel, 49:1 Hexanes:Ethyl Acetate); ^{1}H NMR (500 MHz, $CDCl_3$): δ 7.98 (d, J = 1.4 Hz, 1H), 7.83 (s, 1H), 7.04 (d, J = 1.3 Hz, 1H), 2.70 (t, J = 7.9 Hz, 2H), 1.71 (p, J = 7.7 Hz, 2H), 1.46 – 1.26 (m, 6H), 0.97 – 0.85 (m, 3H); ^{13}C NMR (125 MHz, $CDCl_3$): δ 152.88, 144.58, 139.23, 129.23, 126.27, 125.76, 121.74, 31.94, 30.90, 30.71, 29.28, 22.87, 14.34; HRMS (FI): Calcd for $C_{36}H_{32}N_2S_3$ (M^+), 468.1728, found *m/z*, 468.1734.
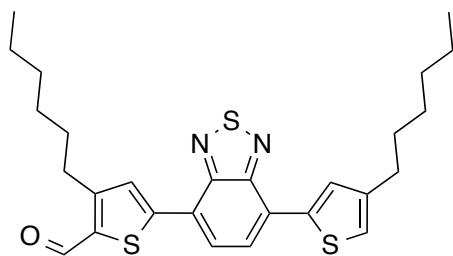
3-hexyl-5-(7-(4-hexylthiophen-2-yl)benzo[*c*][1,2,5]thiadiazol-4-yl)thiophene-2-carbaldehyde

A 500 mL RBF equipped with a stir bar, condenser, and argon atmosphere was charged with 4,7-bis(4-hexylthiophen-2-yl)benzo[*c*][1,2,5]thiadiazole (5.82 g, 12.42 mmol), anhydrous DMF (2.896 mL, 37.25 mmol), and anhydrous dichloroethane (200 mL). Phosphoryl chloride (1.215 mL, 13.04 mmol) was then added dropwise to the solution mixture as it stirred at room temperature. The reaction mixture was held at room temperature for 2 hours and was then warmed to 80 ˚C and allowed to stir overnight. Upon completion, the majority of dichloroethane was distilled off. The reaction mixture was then cooled to 60 ˚C and DI water (200 mL) was poured into the flask. The reaction stirred at 60 ˚C for an additional 2 hours and was then cooled to room temperature. The reaction mixture was extracted with dichloromethane (3 x 50 mL). The organic fractions were combined, washed with brine (2 x 100 mL), dried over sodium sulfate, filtered to remove solids, and condensed under reduced pressure to yield a crude dark red oil. A silica gel slurry of the crude product was prepared and purified via flash column chromatography in 19:1 Hexanes:Ethyl Acetate. The title compound was isolated as a red solid (4.43 g, 72.0%).   (Silica gel, 19:1 Hexanes:Ethyl Acetate); ^{1}H NMR (500 MHz, CDCl$_3$): δ 10.10 (s, 1H), 8.06 (s, 1H), 8.04 (d, *J* = 1.4 Hz, 1H), 7.96 (d, *J* = 7.7 Hz, 1H), 7.87 (d, *J* = 7.7 Hz, 1H), 7.09 (d, *J* = 1.2 Hz, 1H), 3.04 (t, 2H),

2.70 (t, 2H), 1.86 – 1.60 (m, 4H), 1.48 – 1.29 (m, 12H), 0.94 – 0.85 (m, 6H); ^{13}C NMR (125 MHz, CDCl$_3$): δ 182.15, 182.10, 153.44, 152.42, 147.51, 144.65, 138.62, 137.44, 130.47, 129.94, 128.08, 127.24, 124.89, 124.11, 122.66, 31.87, 31.76, 31.61, 30.77, 30.60, 29.24, 28.83, 22.82, 22.76, 14.29, 14.25.; HRMS (EI): Calcd for C$_{27}$H$_{32}$N$_2$S$_3$O (M$^+$), 496.1677, found m/z, 496.1685.
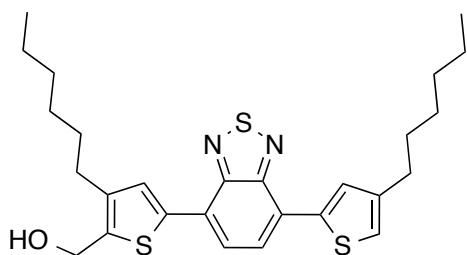
(3-hexyl-5-(7-(4-hexylthiophen-2-yl)benzo[*c*][1,2,5]thiadiazol-4-yl)thiophen-2-yl)methanol

A dry 100 mL RBF equipped with a stirbar and argon atmosphere was charged with 3-hexyl-5-(7-(4-hexylthiophen-2-yl) benzo[*c*][1,2,5] thiadiazol-4-yl) thiophene -2- carbalde-hyde (1.75 g, 3.51 mmol) and anhydrous THF (50 mL). The solution mixture was cooled to 0 ˚C and NaBH$_4$ (0.140 g, 3.69 mmol) was added in small portions. The reaction mixture stirred at 0 ˚C for 3 hours and was then slowly warmed to room temperature. Upon completion, the reaction mixture was quenched with DI water (40 mL) and extracted with Et$_2$O (3 x 50 mL). The organic fractions were combined, washed with brine (2 x 100 mL), dried over magnesium sulfate, filtered to remove solids, and condensed under reduced pressure to yield a crude red-orange solid. The crude material was preadsorbed onto silica gel and purified via

flash column chromatography on silica gel with 9:1 Hexanes:Ethyl Acetate. The title compound was isolated as an orange solid (1.55 g, 88.7%). (Silica Gel, 9:1 Hexanes:Ethyl Acetate); ^{1}H NMR (500 MHz, CDCl$_3$): δ 7.98 (s, 1H), 7.89 (s, 1H), 7.85 – 7.77 (m, 2H), 7.04 (s, 1H), 4.84 (d, J = 5.4 Hz, 2H), 2.68 (dt, J = 11.4, 7.7 Hz, 4H), 1.78 – 1.60 (m, 5H), 1.47 – 1.22 (m, 12H), 0.97 – 0.81 (m, 6H); ^{13}C NMR (125 MHz, CDCl$_3$): δ 152.84, 144.60, 141.60, 139.18, 138.51, 137.74, 129.91, 129.28, 126.37, 125.93, 125.71, 121.82, 58.17, 31.94, 31.27, 30.89, 30.71, 29.42, 29.28, 28.70, 22.87, 14.33; HRMS (EI$^+$): Calcd for C$_{27}$H$_{34}$N$_2$S$_3$O (M$^+$), 498.1833, found m/z, 498.1850.
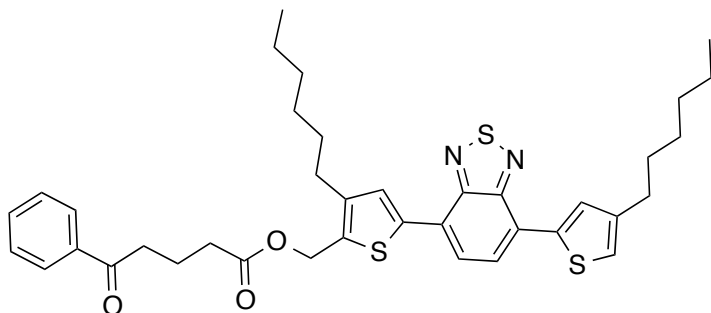
(3-hexyl-5-(7-(4-hexylthiophen-2-yl)benzo[*c*][1,2,5]thiadiazol-4-yl)thiophen-2-yl)methyl 5-oxo-5-phenylpentanoate

A 250 mL RBF equipped with a stir bar and outfitted with an argon atmosphere was charged with (3-hexyl-5-(7-(4-hexylthiophen-2-yl)benzo[*c*][1,2,5]thiadiazol-4-yl)thiophen-2-yl)methanol (1.15 g, 2.31 mmol), 4-Benzoyl Butyric Acid (1.33 g, 6.93 mmol), DMAP

(0.056 g, 0.46 mmol) and Chloroform (150 mL). DCC (1.43 g, 6.93 mmol) was added in small portions to the stirring solution. The reaction mixture was warmed to 50 ˚C and left to stir overnight. Upon completion, the reaction mixture was filtered to remove solids, condensed under reduced pressure to ~ 10 mL, and refiltered to removed additional solids. The reaction mixture was then poured into DI water (100 mL) and extracted with DCM (3 x 50 mL). The organic fractions were combined, washed with brine (2 x 100 mL), dried over sodium sulfate, filtered to remove solids, and condensed under reduced pressure to yield a crude orange solid. A silica gel slurry was prepared with the crude compound and purified via flash column chromatography on silica gel with 9:1 Hexanes:Ethyl Acetate. The title compound was isolated as an orange solid (1.05 g, 68.3%). (Silica Gel, 9:1 Hexanes:Ethyl Acetate); ^{1}H NMR (500 MHz, CDCl$_3$): δ 7.98 (s, 1H), 7.94 – 7.86 (m, 3H), 7.79 (aq, J = 7.6 Hz, 2H), 7.48 (t, J = 7.4 Hz, 1H), 7.38 (t, J = 7.6 Hz, 2H), 7.05 (s, 1H), 5.30 (s, 2H), 3.05 (t, J = 7.2 Hz, 2H), 2.69 (q, J = 7.7 Hz, 4H), 2.51 (t, J = 7.1 Hz, 2H), 2.11 (p, J = 7.1 Hz, 2H), 1.76 – 1.59 (m, 4H), 1.46 – 1.23 (m, 12H), 0.90 (q, J = 6.9 Hz, 6H); ^{13}C NMR (125 MHz, CDCl$_3$): δ 173.21, 152.81, 152.78, 144.62, 143.68, 139.13, 138.94, 137.01, 133.18, 132.67, 129.49, 129.35, 128.73, 128.20, 126.56, 125.84, 125.67, 125.63, 121.91, 58.78, 37.58, 33.60, 31.92, 31.22, 30.88, 30.70, 29.36, 29.27, 28.74, 22.85, 19.59, 14.32.; HRMS (ESI): Calcd for C$_{38}$H$_{44}$S$_3$N$_2$O (M+Na$^+$), 672.2514, found m/z, 695.2390.
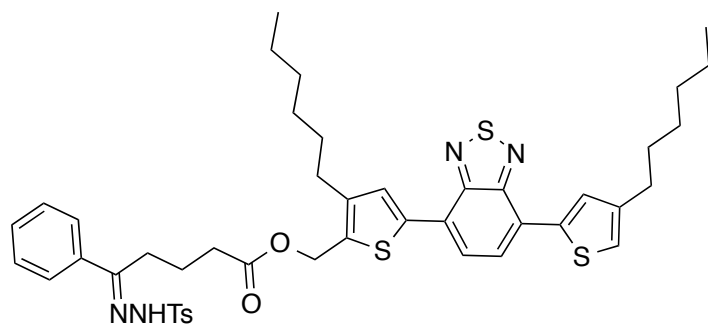
(3-hexyl-5-(7-(4-hexylthiophen-2-yl)benzo[*c*][1,2,5]thiadiazol-4-yl)thiophen-2-yl)methyl (*E*)-5-phenyl-5-(2-tosylhydrazono)pentanoate

A 20 mL scintillation vial equipped with a stir bar was charged with (3-hexyl-5-(7-(4-hexylthiophen-2-yl)benzo[*c*][1,2,5]thiadiazol-4-yl)thiophen-2-yl)methyl-5-oxo-5-phenylpentan-oate (0.60 g, 0.89 mmol), p-tosylhydrazide (0.33 g, 1.78), and benzene (10 mL). The solution mixture stirred at room temperature for 2 hours and was then warmed to 80 ˚C for an additional 2 hours. Upon completion, the reaction mixture was cooled to room temperature and condensed under reduced pressure to yield a crude red aerogel. A silica gel slurry was prepared from the crude solid and purified via flash column chromatography on silica gel with 4:1 Hexanes:Ethyl Acetate. The title compound was isolated as a red aerogel (0.37 g, 49.7%). TLC R_f = 0.26 (silica gel, 4:1 Hexanes:Ethyl Acetate); ^{1}H NMR (500 MHz, CDCl$_3$): δ 9.28 (s, 1H), 8.02 – 7.65 (m, 7H), 7.53 – 7.04 (m, 7H), 5.36 (d, *J* = 63.6 Hz, 2H), 2.79 – 2.29 (m, 11H), 1.94 – 1.57 (m, 6H), 1.51 – 1.31 (m, 12H), 1.01 – 0.86 (m, 6H); ^{13}C NMR (125 MHz, CDCl$_3$): δ 174.29, 172.96, 156.93, 153.84, 152.63, 152.60, 144.47, 144.15, 143.95, 143.80, 143.48, 139.15, 138.98, 138.81, 136.31, 136.20, 135.45, 132.77, 132.55, 131.97, 129.97, 129.73, 129.70, 129.60, 129.57, 129.32, 129.25, 128.54, 128.09, 128.04, 126.78, 126.45, 126.40, 126.34, 125.80, 125.68, 125.45, 125.36, 121.86, 59.48, 58.68, 37.25,

33.35, 32.53, 31.87, 31.84, 31.18, 31.11, 30.77, 30.59, 29.27, 29.18, 28.66, 28.62, 26.00, 22.77, 21.70, 21.68, 21.26, 21.08, 14.26; HRMS (ESI): Calcd for $C_{45}H_{52}N_4O_4S_4$ (M+Na$^+$), 840.2871, found m/z, 863.2750
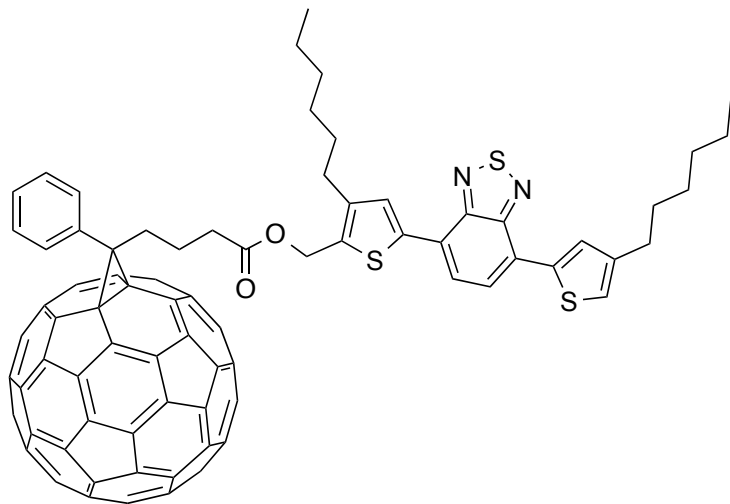
PCB-TBTDT

A dry 1L 3-neck RBF equipped with a stir bar, condenser, 200 mL addition funnel, argon atmosphere, and 2 rubber septa, was charged with a solution of C_{60} fullerene (0.39 g, 0.54 mmol) in anhydrous, O_2 free toluene. The solution mixture stirred at RT for 20 mins and was then sonicated for 20 mins. The solution mixture was then charged with dry pyridine (50 mL), and sodium methoxide (0.029 g, 0.54 mmol). A solution of (3-hexyl-5-(7-(4-hexylthiophen-2-yl)benzo[*c*][1,2,5]thiadiazol-4-yl)thiophen-2-yl)methyl(*E*)-5-phenyl-5-(2-tosylhydrazono)pent-anoate (0.23 g, 0.27 mmol) in dry toluene (150 mL) was added to the septa capped addition funnel via syringe. This solution was added dropwise to the reaction

mixture over 1.5 hours. The reaction mixture stirred at RT for 1 hour and was then warmed to a rolling reflux and left to stir overnight. After 12 hours, an additional portion of sodium methoxide (0.029 g, 0.54 mmol) was added to push the reaction to completion. Upon completion, the reaction mixture was cooled to room temperature and condensed to ~10 mL under reduced pressure. This 10 mL crude solution was precipitated dropwise into a 125 mL Erlenmeyer flask equipped with a long stir bar and vigorously stirring methanol (75 mL). The solution stirred for 20 mins and was filtered via osmonics filtration with a 0.2 micron nylon filter to collect solids. The solids were dried under high vacuum to yield 0.547 g of a crude red-brown solid. The crude solid was dissolved in 20 mL of CS_2 and preadsorbed onto silica gel under reduced pressure. The silica gel slurry was purified via gravity column chromatography on silica gel. CS_2 was used as the first eluent to remove unreacted C_{60}. Following removal of C_{60}, the title compound was eluted with toluene. The organic fractions were combined and condensed to ~10 mL under reduced pressure. The solution was then precipitated dropwise into a solution of vigorously stirring MeOH (75 mL) and allowed to stir for 20 mins. The solids were collected via osmonics filtration and dried under high vacuum to yield the title compound as a red-brown solid (0.135 g, 36.2%). TLC R_f = (Silica Gel, Toluene); ^{1}H NMR (500 MHz, CDCl$_3$); HRMS (FD): Calcd for $C_{98}H_{44}N_2O_2S_3$ (M$^+$), 1376.2565, found m/z, 1376.21.
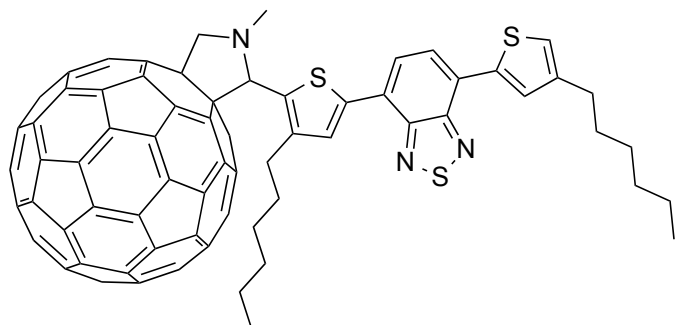
Prato-TBTDT

A dry 1 L RBF equipped with a stir bar, condenser, and argon atmosphere was charged with C_{60} (1.730 g, 241 mmol), sarcosine (0.430 g, 4.83 mmol), 3-hexyl-5-(7-(4-hexylthiophen-2-yl)benzo[c][1,2,5]thiadiazol-4-yl)thiophene-2-carbaldehyde (0.800 g, 1.610 mmol), and anhydrous toluene (500 mL). The solution mixture stirred for 20 minutes and was then sonicated for an additional 20 minutes. Following sonication, the reaction mixture was brought to a rolling reflux and left to stir overnight under argon. Upon completion, the reaction mixture was cooled to room temperature and condensed to ~10 mL under reduced pressure. This 10 mL crude solution was precipitated dropwise into vigorously stirring methanol (75 mL). The solution stirred for 20 mins and was filtered via osmonics filtration with a 0.2 um nylon filter to collect solids. The solids were dried under high vacuum to yield 2.374 g of a crude black solid. The solid was dissolved into 20 mL of CS_2 and adsorbed onto silica gel under reduced pressure. The silica gel slurry was purified via gravity column chromatography on silica gel with CS_2. The organic fractions were combined and condensed to ~10 mL under reduced pressure. The solution was then precipitated dropwise into vigorously stirring MeOH (75 mL) and allowed to stir for 20 mins. The solids were collected via osmonics filtration and dried under high vacuum to yield the title compound as a black-crystalline solid (0.498 g, 24.9 %). (Silica Gel, CS_2); ^{1}H NMR (500 MHz, $CDCl_3$); HRMS (FD$^+$): Calcd for $C_{89}H_{37}N_3S_3$ (M$^+$), 1243.2150, found *m/z*, 1243.20.

Procedure adapted from: Downie, I. M.; Earle, M. J.; Shuhaibar, K. F.; *Tetrahedron* **1993** , *49*, 4015-4034
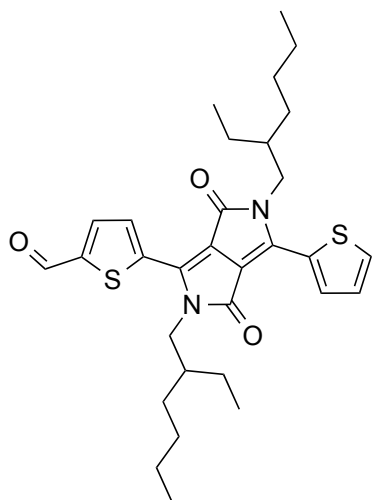
5-(2,5-bis(2-ethylhexyl)-3,6-dioxo-4-(thiophen-2-yl)-2,3,5,6-tetrahydropyrrolo[3,4-c]pyrrol-1-yl)thiophene-2-carbaldehyde

A 250 mL RBF equipped with a stir bar, condenser, and argon atmosphere was charged with 3,6-di(thiophen-2-yl)-2,5-dihydropyrrolo[3,4-c]pyrrole-1,4-dione, N-methylformanilide, and anhydrous dichloroethane (125 mL). The solution mixture was cooled to 0 ˚C and Pyrophosphoryl chloride was added dropwise to the stirring mixture. The reaction mixture gradually warmed to room temperature, and was then heated to 80 ˚C and left to stir overnight. Upon completion, the reaction was cooled to room temperature, quenched with 1M NaOH (100 mL), and extracted with dichloromethane (3 x 100 mL). The organic fractions were combined, washed with brine (2 x 100 mL), dried over sodium sulfate, filtered

to remove solids, and condensed under reduced pressure to yield a crude dark purple oil. The crude product was lyophilized overnight to remove excess N-methylformanilide, dissolved in DCM (10 mL), and preadsorbed onto silica gel. The silica gel slurry was purified via flash column chromatography in 9:1 Hexanes:Ethyl Acetate to yield the title compound as a dark purple solid (71%). (Silica Gel, 9:1 Hexanes:Ethyl Acetate); ^{1}H NMR (500 MHz, CDCl$_3$): δ 9.98 (s, 1H), 9.03 (dd, ^3J = 3.9 Hz, ^4J = 1.1 Hz, 1H), 8.91 (d, ^3J = 4.2 Hz, 1H), 7.82 (d, ^3J = 4.2 Hz, 1H), 7.69 (dd, ^3J = 5.0 Hz, ^4J = 1.1 Hz, 1H), 7.28 Hz (dd, ^3J = 5.0 Hz, ^3J = 3.9 Hz, 1H), 4.07 - 3.95 (m, 4H), 1.90 - 1.76 (m, 2H), 1.43 - 1.13 (m, 16H), 0.90 - 0.77 (m, 12H); ^{13}C NMR (125 MHz, CDCl$_3$): δ 182.86, 161.36, 161.96, 145.68, 143.03, 138.06, 137.63, 136.96, 136.18, 135.04, 132.17, 129.60, 128.89, 111.01, 108.24, 46.18, 39.45, 39.23, 30.35, 30.29, 29.87, 28.47, 23.69, 23.21, 23.18, 14.16, 10.63, 10.62; HRMS (ESI): Calcd for C$_{31}$H$_{40}$N$_2$O$_3$S$_2$ (M+Na$^+$), 552.2480, found m/z, 575.2357.
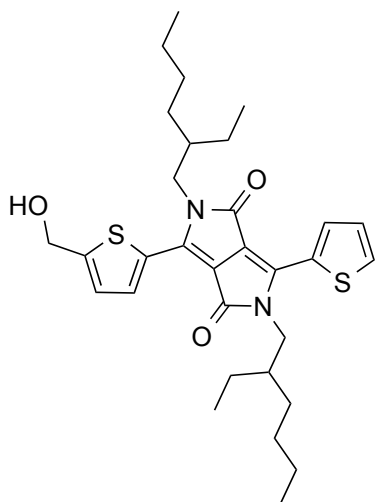
2,5-bis(2-ethylhexyl)-3-(5-(hydroxymethyl)thiophen-2-yl)-6-(thiophen-2-yl)-2,5-dihydropyrrolo[3,4-*c*]pyrrole-1,4-dione

A dry 100 mL RBF equipped with a stir bar and argon atmosphere was charged with 5-(2,5-bis(2-ethylhexyl)-3,6-dioxo-4-(thiophen-2-yl)-2,3,5,6-tetrahydropyrrolo[3,4-*c*]pyrrol-1-yl)thio-phene-2-carbaldehyde (1.250 g, 2.26 mmol) and anhydrous THF (500mL). The solution mixture was cooled to 0°C and NaBH$_4$ (0.0942 g, 2.49 mmol) was slowly added over 30 mins. The reaction was allowed to slowly warm to room temperature and left to stir overnight. The reaction mixture was quenched via slow addition of DI water, and extracted with Et$_2$O (3 x 50mL). The organic fractions were combined, washed with brine (2 x 50mL), dried over sodium sulfate, filtered to remove solids, and condensed under reduced pressure to yield a crude purple oil (0.422 g). The crude oil was preadsorbed onto a silica gel slurry and purified via flash column chromatography in 4:1 Hexanes:Ethyl Acetate to yield a dark purple solid (0.325 g, 26%). TLC R_f = 0.15 (Silica Gel, 4:1 Hexanes:Ethyl Acetate); ^{1}H NMR (500 MHz, CDCl$_3$): δ 8.86 (dd, ^3J = 3.9 Hz, ^4J = 1.2 Hz, 1H), 8.74 (d, ^3J = 3.9 Hz, 1H), 7.62 (dd, ^3J = 5.0 Hz, ^4J = 1.2 Hz, 1H), 7.26 (dd, ^3J = 5.0 Hz, ^4J = 1.2 Hz, 1H), 7.10 (d, ^3J = 3.9 Hz, 1H), 4.91 (s, 2H), 4.08 – 3.93 (m, 4H), 2.28 (s, 1H), 1.90 - 1.80 (m, 2H), 1.40 – 1.15 (m, 16H), 0.90 – 0.78 (m, 12H); ^{13}C NMR (125 MHz, CDCl$_3$): δ 161.93, 161.86, 150.63, 140.63, 140.50, 135.67, 135.40, 130.72, 130.03, 129.49, 128.60, 126.29, 108.18, 108.08, 60.31, 46.11, 46.08, 39.26, 39.23, 30.45, 30.38, 28.57, 28.54, 23.77, 23.24, 14.21, 10.70; HRMS (ESI): Calcd for C$_{31}$H$_{42}$N$_2$O$_3$S$_2$ (M+Na$^+$), 554.2637, found *m/z*, 577.2521
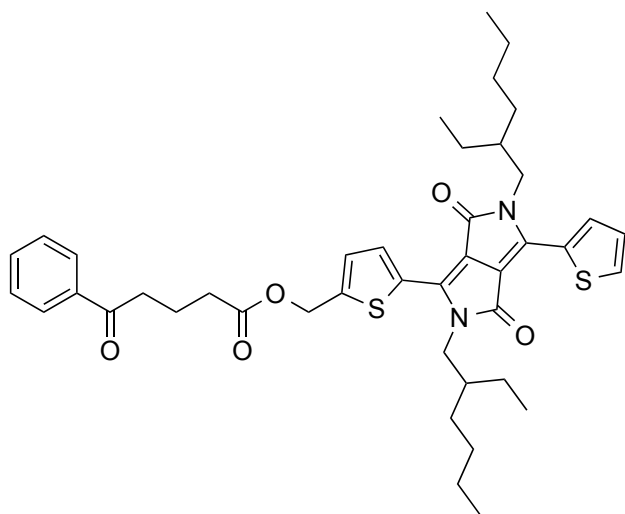
(5-(2,5-bis(2-ethylhexyl)-3,6-dioxo-4-(thiophen-2-yl)-2,3,5,6-tetrahydropyrrolo[3,4-*c*]pyrrol-1-yl)thiophen-2-yl)methyl 5-oxo-5-phenylpentanoate

A 100 mL RBF outfitted with a stir bar was charged with 2,5-bis(2-ethylhexyl)-3-(5-(hydroxymethyl)thiophen-2-yl)-6-(thiophen-2-yl)-2,5-dihydropyrrolo[3,4-*c*]pyrrole-1,4-dione (0.325 g, 0.59 mmol), 4-Benzoyl Butyric Acid (0.338 g, 1.76 mmol), DMAP (0.00715 g, 0.059 mmol), and Chloroform (50 mL). After stirring for 1 min, DCC (0.363 g, 1.76 mmol) was added to the solution mixture. The reaction mixture stirred at RT for 1 hr and was then heated to 50 ˚C and left to stir overnight. Upon completion, the reaction mixture was filtered to remove solids, condensed under reduced pressure to ~10 mL and refiltered to removed additional solids. The solution was then poured into DI water (50 mL) and extracted with CH$_2$Cl$_2$ (3 x 50mL). The organic fractions were combined, washed with brine (2 x 50mL), dried over sodium sulfate, filtered to remove solids, and condensed under reduced pressure to yield 0.804 g of a crude red solid. The crude solid was preadsorbed onto a silica

gel slurry and purified via flash column chromatography on silica gel with 4:1 Hexanes:Ethyl Acetate. The title compound was isolated as a dark purple solid (0.295 g, 69.2%). TLC R_f = 0.38 (Silica Gel, 4:1 Hexanes:Ethyl Acetate); ^{1}H NMR (500 MHz, CDCl$_3$): δ 8.82 (dd, ^{3}J = 3.9 Hz, ^{4}J = 1.2 Hz, 1H), 8.66 (d, ^{3}J = 3.9 Hz, 1H), 7.86 – 7.82 (m, 2H), 7.55 (dd, ^{3}J = 5.0 Hz, ^{4}J = 1.2 Hz, 1H), 7.45 (tt, J = 6.9, 1.1 Hz, 2H), 7.37 – 7.32 (at, 2H), 7.20 – 7.17 (m, 1H), 7.13 (d, ^{3}J = 3.9 Hz, 1H), 5.25 (s, 2H), 4.04 – 3.76 (m, 4H), 2.96 (t, ^{3}J = 7.1 Hz, 2H), 2.42 (t, ^{3}J = 7.2 Hz, 2H), 2.02 (p, ^{3}J = 7.1, 2H), 1.82 – 1.70 (m, 2H), 1.35 – 1.07 (m, 16H), 0.84 – 0.72 (m, 12H); ^{13}C NMR (125 MHz, CDCl$_3$): δ 172.87, 161.85, 161.76, 143.46, 140.82, 140.05, 136.91, 135.60, 135.12, 133.23, 130.88, 130.86, 129.93, 129.18, 128.73, 128.60, 128.12, 108.45, 108.07, 60.35, 46.04, 46.01, 39.29, 39.23, 37.40, 33.35, 30.36, 28.51, 23.72, 23.20, 19.41, 14.17, 10.65; HRMS (ESI): Calcd for C$_{42}$H$_{52}$N$_2$O$_5$S$_2$ (M+Na$^+$), 728.3318, found m/z, 751.3207

(5-(2,5-bis(2-ethylhexyl)-3,6-dioxo-4-(thiophen-2-yl)-2,3,5,6-tetrahydropyrrolo[3,4-c]pyrrol-1-yl)thiophen-2-yl)methyl (*E*)-5-phenyl-5-(2-tosylhydrazono)pentanoate

A 20 mL scintillation vial equipped with a stir bar was charged with (5-(2,5-bis(2-ethylhexyl)-3,6-dioxo-4-(thiophen-2-yl)-2,3,5,6-tetrahydropyrrolo[3,4-c]pyrrol-1-yl)thiophen-2-yl)methyl-5-oxo-5-phenylpentan-oate (0.258 g, 0.354 mmol), p-tosyl hydrazide (0.132 g, 0.708 mmol), and Benzene (4 mL). The reaction mixture stirred at RT for 2 hours and was then warmed to 70˚C and allowed to stir for an additional 2 hours. Upon completion, the reaction mixture was cooled to RT and condensed under reduced pressure to a crude purple aerogel. The crude solid was preadsorbed onto a silica gel slurry and purified via flash column chromatography using a biotage. A solvent gradient was gradually applied from 9:1 Hexanes:Ethyl Acetate to 4:1 Hexanes:Ethyl Acetate. The title compound was isolated as dark purple aerogel-like solid (0.290 g, 91.4%). TLC R_f = 0.13 (Silica Gel, 4:1 Hexanes:Ethyl Acetate); ^{1}H NMR (500 MHz, CDCl$_3$); ^{13}C NMR (125 MHz, CDCl$_3$): δ 173.84, 172.69, 161.78, 161.76, 161.66, 156.74, 153.98, 144.12, 143.88, 143.38, 142.67, 140.93, 140.83, 139.89, 139.80, 136.24, 136.04, 135.62, 135.57, 135.45, 134.94, 134.80, 132.72, 131.05, 130.95, 130.79, 129.98, 129.80, 129.70, 129.66, 129.61, 129.56, 129.10, 128.55, 128.52, 128.03, 127.96, 126.75, 126.30, 108.51, 108.41, 107.95, 60.91, 60.46, 60.23, 45.95, 39.18, 39.14, 37.11, 33.10, 32.50, 30.31, 30.28, 30.25, 28.43, 25.95, 23.67, 23.64, 23.13, 23.10, 21.69, 21.65, 21.12, 20.95, 14.29, 14.11, 10.60, 10.57; HRMS (ESI): Calcd for C$_{49}$H$_{60}$N$_4$O$_6$S$_3$ (M+Na$^+$), 896.3675, found m/z, 919.3560
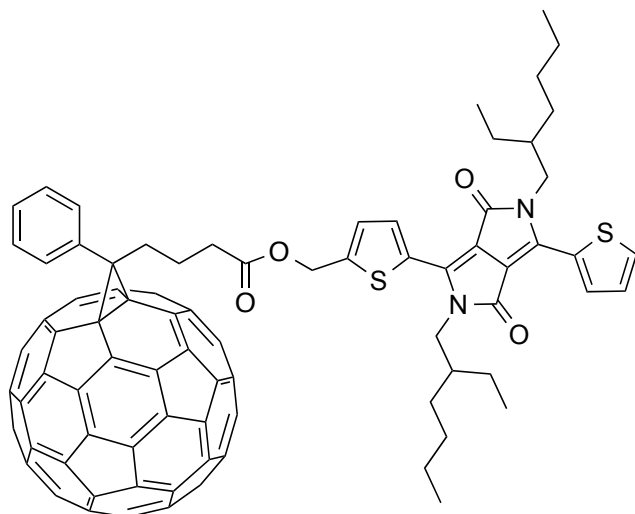
PCB-DPP

A dry 1L 3-neck RBF equipped with a stir bar, condenser, 200 mL addition funnel, argon atmosphere, and 2 rubber septa, was charged with a solution of C_{60} fullerene (0.401 g, 0.557 mmol) in anhydrous, O_2 free toluene. The solution mixture stirred at RT for 20 mins and was afterwards sonicated for 20 mins. The solution mixture was then charged with dry pyridine (50 mL), and sodium methoxide (0.030 g, 0.557 mmol). A solution of (5-(2,5-bis(2-ethylhexyl)-3,6-dioxo-4-(thiophen-2-yl)-2,3,5,6-tetrahydropyrrolo[3,4-*c*]pyrrol-1-yl)thiophen-2-yl)methyl (*E*)-5-phenyl -5-(2-tosylhydrazono)pentanoate (0.250 g, 0.278 mmol) in 150 mL of dry toluene was added to the septa capped addition funnel via syringe. This solution was slowly added dropwise to the reaction mixture over 1.5 hours. The reaction mixture stirred at RT for 1 hour and was then warmed to a rolling reflux at 120 °C and left to stir overnight. After 12 hours, an additional portion of sodium methoxide (0.030 g, 0.557 mmol) was added to push the reaction to completion. Upon completion, the reaction mixture was cooled to RT and condensed to ~10 mL under reduced pressure. This 10 mL crude

solution was precipitated dropwise into vigorously stirring methanol (75 mL). The solution stirred for 20 mins and was filtered via osmonics filtration with a 0.2 um nylon filter to collect solids. The solids were dried under high vac to yield 0.480 g of a crude purple solid. The crude solid was dissolved into 20 mL of CS_2, and preadsorbed onto silica gel under reduced pressure. The silica gel slurry was purified via gravity column chromatography on silica gel. CS_2 was used as the first eluent to remove unreacted C_{60}. Following removal of C_{60}, the title compound was eluted with toluene. The organic fractions were combined and condensed to ~10 mL under reduced pressure. The solution was then precipitated into a solution of vigorously stirring MeOH (75 mL) and allowed to stir for 20 mins. The solids were collected via osmonics filtration and dried under high vacuum to yield the title compound as a purple solid (0.0942 g, 23.6%). (Silica Gel, Toluene); ^{1}H NMR (500 MHz, CDCl$_3$); ^{13}C NMR (125 MHz, CDCl$_3$); HRMS (FD$^+$): Calcd for $C_{102}H_{52}N_2O_4S_2$ (M$^+$), 1432.3368, found m/z, 1433.19.
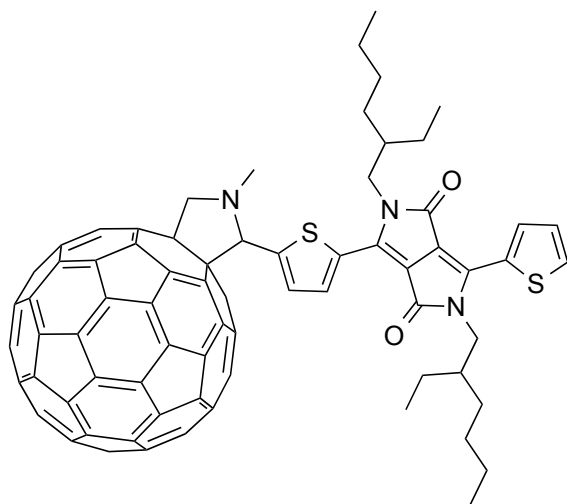
Prato-DPP

A dry 1 L RBF equipped with a stir bar, condenser, and argon atmosphere was charged with C$_{60}$ (1.172 g, 1.628 mmol), sarcosine (0.290 g, 3.25 mmol), 5-(2,5-bis(2-ethylhexyl)-3,6-dioxo-4-(thiophen-2-yl)-2,3,5,6-tetrahydropyrrolo[3,4-c]pyrrol-1-yl)thiophene-2-carbalde-hyde (0.600 g, 1.085 mmol), and anhydrous toluene (500 mL). The solution mixture stirred for 20 minutes and was then sonicated for an additional 20 minutes. Following sonication, the reaction mixture was brought to a rolling reflux and left to stir under argon overnight. Upon completion, the reaction mixture was cooled to room temperature and condensed to ~10 mL under reduced pressure. This 10 mL solution was precipitated dropwise into vigorously stirring methanol (75 mL). The solution stirred for 20 mins and was filtered to collect solids via osmonics filtration with a 0.2 um nylon filter. The solids were dried under high vacuum to yield 1.609 g of a crude purple solid. The solid was dissolved into 20 mL of CS$_2$ and preadsorbed onto a silica gel slurry under reduced pressure. The silica gel slurry was purified via gravity column chromatography on silica gel. CS$_2$ was used as the first eluent to remove unreacted C$_{60}$. Following removal of C$_{60}$ the title compound was eluted with toluene. The organic fractions were combined and condensed to ~10 mL under reduced pressure. The solution was then precipitated dropwise into vigorously stirring MeOH (75 mL) and allowed to stir for 20 mins. The solids were collected via osmonics filtration and dried under high vacuum to yield the title compound as a purple solid (0.511 g, 36.2%). (Silica Gel, Toluene); ^{1}H NMR (500 MHz, CDCl$_3$); ^{13}C NMR (125 MHz, CDCl$_3$); HRMS (FD): Calcd for C$_{93}$H$_{45}$N$_3$O$_2$S$_2$ (M$^+$), 1299.2953, found m/z, 1299.27
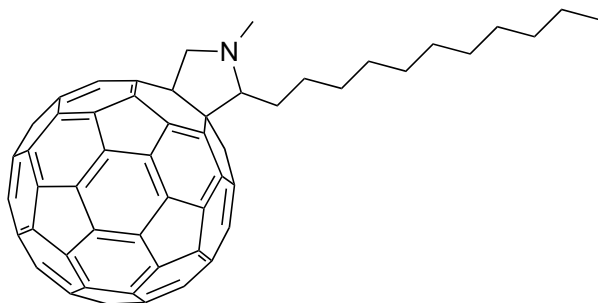
Prato-Control

A dry 1 L RBF equipped with a stir bar, condenser, and argon atmosphere was charged with C_{60} (0.500 g, 0.69 mmol), sarcosine (0.123 g, 1.39 mmol), decyl aldehyde (0.087 mL, 0.46 mmol), and anhydrous toluene (500 mL). The solution mixture stirred for 20 minutes and was then sonicated for an additional 20 minutes. Following sonication, the reaction mixture was brought to a rolling reflux and left to stir under argon overnight. Upon completion, the reaction mixture was cooled to room temperature and condensed to ~10 mL under reduced pressure. The 10 mL crude solution was precipitated dropwise into vigorously stirring methanol (75 mL). The solution stirred for 20 mins and was filtered to collect solids via osmonics filtration with a 0.2 um nylon filter. The solids were dried under high vacuum to yield 0.528 g of a crude brown solid. The solid was dissolved into 20 mL of CS_2 and preadsorbed onto a silica gel slurry under reduced pressure. The silica gel slurry was purified via gravity column chromatography on silica gel. CS_2 was used as the first eluent to remove unreacted C_{60}. Following removal of C_{60} the title compound was eluted with toluene. The

organic fractions were combined and condensed to ~10 mL under reduced pressure. The solution was precipitated dropwise into vigorously stirring MeOH (75 mL) and allowed to stir for 20 mins. The solids were collected via osmonics filtration and dried under high vacuum to yield the title compound as a brown solid (0.202 g, 32.2 %). (Silica Gel, Toluene); ^{1}H NMR (300 MHz, CDCl$_3$); ^{13}C NMR (75 MHz, CDCl$_3$); HRMS (FI): Calcd for C$_{72}$H$_{25}$N$_1$ (M+), 903.1987, found *m/z*, 903.15.

2.9 References

1.
Thompson, B. C.; Frechet, J. M. J. *Angew. Chem. Int. Ed.* **2008**, *47*, 58

2.
Koidis, C.; Logothetidis, S.; Kassavetis, S.; Kapnopoulos, C.; Karagiannidis, P.G.; Georgiou, D.; Laskarakis, A. *Solar Energy Materials & Solar Cells*, **2013**, *112*, 36

Yang, J.; Vak, D. ; Clark, N.; Subbiah, J.; Wong, W. W. H.; Jones, D. J.; Watkins, S. E.; Wilson, G. *Solar Energy Materials & Solar Cells*, **2013**, *109*, 47

3.
Brady, M. A.; Su, G. M.; Chabinyc, M. L. *Soft Matter*, **2011**, *7*, 11065

4.
Hudhomme, P. *E.P.J. Photovoltaics*, **2013,** *4*, 40401

6.
Wang, M.; Chesnut, E.; Sun, Y.; Tong, M.; Guide, M.; Zhang, Y.; Treat, N. D.; Varotto, A.; Mayer, A.; Chabinyc, M. L.; Nguyen, T.-Q.; Wudl, F. *J. Phys. Chem. C* **2012**, *116*, 1313

Saravanan, C.; Liu, C.-L.; Chang, Y.-M.; Lu, J.-D.; Hsieh, H.-J.; Rwei, S.-P.; Wang, L. *ACS Appl. Mater. Interfaces* **2012**, *4*, 6133

9.
Harigaya, K.; Abe, S. *Phys Rev. B.* **1994**, *49*, 16746

10.
Wienk, M.; Kroon, J. M.; Verhees, W. J. H.; Knol, J.; Hummelen, J. C.; Hal, P.A.; Janssen, R. A. J. *Angew. Chem. Int. Ed.* **2003**, *42*, 3371

12.
Banerji, N.; Wang, M; Fan, J; Chesnut, E.; Wudl, F.; Moser, J.; *J. Mater. Chem.* **2012**, *22*, 13286

Banerji, N.; Seifter, J.; Wang, M.; Vauthey, E.; Wudl, F.; Heeger, A. *Phys. Rev. B* **2011**, *84*, 075206

13.
Zeng, L.; Blanton, T.N.; Chen, S. H. *Langmuir* **2010**, *26*, 12877

Escosura, A.; Martínez-Díaz, M. V.; Barbera, J.; Torres, T. *J. Org. Chem.* **2008**, *73*, 1475

Bottari, G.; Torre, G.; Guldi, D. M.; Torres, T. *Chem. Rev.* **2010**, *110*, 6768

Lemmetyinen, H.; Tkachenko, N. V.; Efimov, A.; Niemi, M. *Phys. Chem. Chem. Phys.,* **2011**, *13*, 397

Matino, F.; Arima, V.; Piacenza, M.; Sala, F. D.; Maruccio, G.; Phaneuf, R. J.; Sole, R.; Mele, G.; Vasapollo, G.; Gigli, G.; Cingolani, R.; Rinaldi, R. *Chem. Phys. Chem.* **2009**, *10*, 2633

Geerts, Y. H.; Debever, O.; Amato, C.; Sergeyev, S. *Beilstein J. Org. Chem.* **2009,** *5, No.* 49

D'Souza, F.; Chitta, R.; Ohkubo, K.; Tasior, M.; Subbaiyan, N. K.; Zandler, M. E.; Rogacki, M. K.; Gryko, D. T.; Fukuzumi, S. *JACS* **2008**, *130*, 14263

Molina-Ontoria, A.; Fernández, G.; Wielopolski, M.; Atienza, C.; Sánchez, L.; Gouloumis, A.; Clark, T.; Martín, N.; Guldi, D. M. *JACS* **2009**, *131*, 12218

Schuster, D. I.; MacMahon, S.; Guldi, D. M.; Echegoyen, L.; Braslavsky, S. E.; *Tetrahedron* **2006**, *62*,1928

Iehl, J.; Nierengarten, J.-F.; Harriman, A.; Bura, T.; Ziessel, R.; *JACS* **2012**, *134*, 988

14.
Kroon, R.; Lenes, M.; Hummelen, J. C.; Blom, P. W. M.; Boer, B. *Poly. Rev.* **2008**, *48*, 531

15.
Anslyn, E. V.; Dougherty, D. A. *Modern Physical Organic Chemistry*. Sausalito, CA: University Science Books **2006**, *Ch 17*, 1001

16.
Chochos, C. L.; Choulis, S. A. *Prog. Poly. Sci.* **2011**, *36, 1326*

18.
Kirchartz, T.; Taretto, K.; Rau, U. *J. Phys. Chem. C* **2009,** *113,* 17958

20.
Thilgen, C.; Sergeyev, S.; Diederich, F. Topics in Current Chem. **2004**, *248*, 1

21.
Wudl, F. *J. Mater. Chem.*, **2002**, *12*, 1959

22.
Martín, N.; Altable, M.; Filippone, S.; Martín-Domenech, A. *Synlett* **2007**, *20*, 3077

23.
Troshin, P. A. ; Peregudov, A. S.; Troyanov, S. I.; Lyubovskaya, R. N. Russ. Chem. Bull., Int. Ed. **2008***, 57,* 887

24.
Sternfeld, T.; Thilgen, C.; Hoffman, R.; Heras, M. R. C.; Diederich, F.; Wudl, F.; Scott, L. T.; Mack, J.; Rabinovitz, M. *JACS* **2002**, *124*, 5734

Knight, B.; Martín, N.; Ohno, T.; Ortí, E.; Rovira, C.; Veciana, J.; Vidal-Gancedo, J.; Viruela, P.; Viruela, R.; Wudl, F.; *JACS* **1997**, *119*, 9871

25.
Corey, E. J.; Nicolaou, K. C. *Strategic Applications of Named Reactions in Organic Synthesis* Burlington, MA:Elsevier Academic Press, **2005**, 468

26.
Kitamura, C.; Tanaka, S.; Yamashita, Y. *Chem. Mater.* **1996,** *8,* 570

28.
Hummelen, J. C.; Knight, B. W.; LePeq, F.; Wudl, F. *J. Org. Chem.* **1995,** 60**,** 532

Zhao, G.; He, Y.; Xu, Z.; Hou, J.; Zhang, M.; Min, J.; Chen, H.-Y.; Ye, M.; Hong, Z.; Yang, Y.; Li, Y. *Adv. Funct. Mater.* **2010**, *20*, 1480

29.
Hummelen, J. C.; Knight, B. W.; LePeq, F.; Wudl, F. *J. Org. Chem.* **1995,** 60**,** 532

30.
Tamayo, A. B.; Tantiwiwat, M.; Walker, B.; Nguyen, T.-Q.; *J. Phys. Chem. C* **2008,** *112,* 15543

31.
Bélanger, G.; Larouche-Gauthier, R.; Ménard, F.; Nantel, M.; Barabé, F. *J. Org. Chem.* **2006**, *71*, 704

32.
Downie, I. M.; Earle, M. J.; Heaney, H.; Shuhaibar, K.; *Tetrahedron* **1993**, 49, 4015

33.
Kumar, A. S.; Nagarajan, R. *Org. Lett.* **2011**, *13*, 1398

Ermilia, A.; Castro, A. J.; Westfall, P. A. *J. Org. Chem.*, **1965**, 30, 339

34.
Echegoyen, L.; Echegoyen, L. E. *Acc. Chem. Res*. **1998,** *31*, 593

35.
Echegoyen, L.; Echegoyen, L. E. *Acc. Chem. Res*. **1998,** *31*, 593

37.
Verploegen, E.; Mondal, R.; Bettinger, C. J.; Sok, S.; Toney, M. F.; Bao, Z. *Adv. Funct. Mater.* **2010**, *20*, 3519

Chapter 3

Investigation of Fullerene-Dye Adduct Blends

3.1 Introduction

The previous chapter presented the synthesis of four fullerene-dye adducts and a study of their physical properties. This chapter will build upon the investigation of these fullerenes (**Figure 3.1**) through examination of their optoelectronic and morphological behavior in blended systems. Interpretation of their bulk behavior in mixed material assemblies will be based upon the prior analysis of their pristine molecular behavior. Therefore, data previously collected from the pristine fullerene-dye adducts will be referenced, when appropriate, to aid assessment of their influence on the collective properties of the blends.
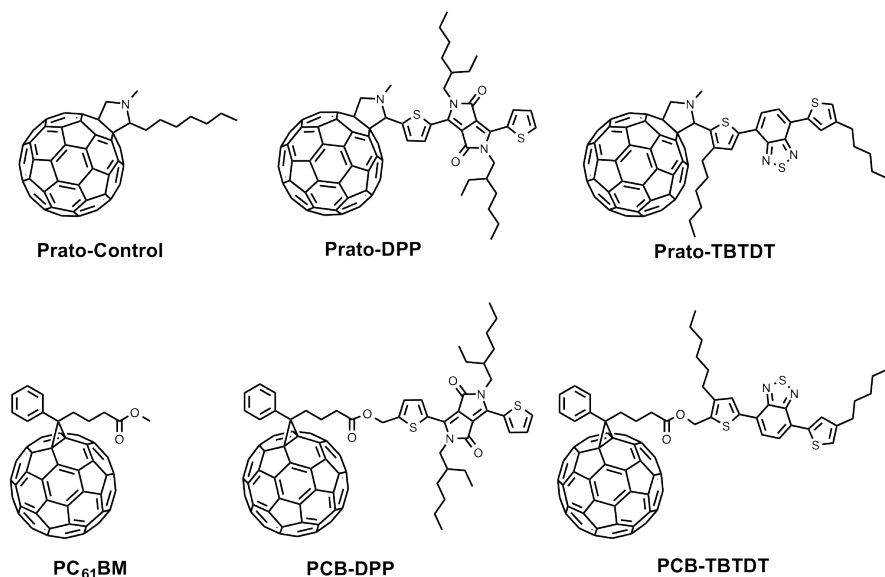
Figure 3.1: Chemical Structures of the Fullerene-Dye Adducts and Their Controls

Investigations of donor:fullerene-dye adduct thin films are instrumental for elucidating the potential of this class of fullerenes to perform as *n-type* materials with enhanced photon absorption relative to $PC_{61}BM$.[1] With this in mind, several broad guidelines were useful in the selection of the *p-type* materials to be blended with the fullerenes. Blends incorporating *p-type* materials that allowed the influence of complementary optical profiles on photocurrent generation to be examined were of particular interest. In addition, to facilitate exploration of electronic compatibility with the various fullerene-dye adducts, donors with contrasting frontier orbital values were ideal. As the influence of thin film morphology is known to have a significant affect on the performance of organic electronic devices, materials with distinct morphological features would also prove useful for deriving a general sense of the correlation between the given fullerenes and the resulting heterojunction microstructures. On the basis of these characteristics, the fullerene-dye adducts were blended with the following organic donors: P3HT, PDPP2FT, and Benzoporphyrin (**Figure 3.2**).[2] These three donors are distinguished by contrasting optical, electronic, and morphological features and are therefore expected to interact differently with each of the fullerene-dye adducts. This broad collection of blends will allow the influence of fullerene-dye adduct structure on bulk behavior to be thoroughly surveyed.
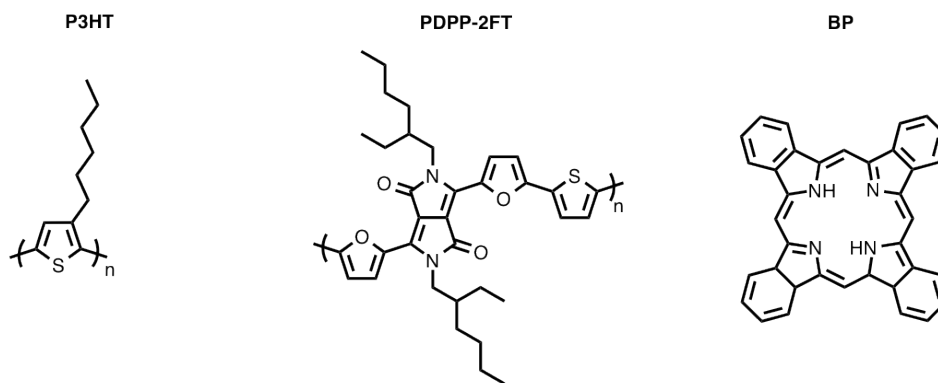
Figure 3.2: Chemical Structures of P3HT, PDPP2FT, and BP

This chapter will present an investigation of the thin films prepared from fullerene-dye adducts blended with donors P3HT, PDPP2FT, and BP; with each donor:acceptor system analyzed independently in the order described. To begin, the optical behavior of each donor:fullerene-dye adduct system will be examined to assess their potential as optical complements. The frontier orbital energies of each blend will then be outlined to illustrate the electronic alignment of these systems and their capacity for cascade charge transfer. Following, the processing conditions of these blends will be described, and the consequent morphologies of their thin films will be discussed. The electronic behavior of the donor:fullerene-dye adduct blends will then be analyzed via examination of the current-voltage (JV) plots and device parameters obtained from their OSCs. To investigate the general effectiveness of covalently anchoring dyes onto fullerene as a strategy for enhancing photon absorption, the external quantum efficiency (EQE) measurements performed on each donor:fullerene-dye adduct blend will also be presented and evaluated. Subsequently, the opto-electronic and morphological behavior of each blend will be summarized to help identify the global trends present in these systems. The results of these experiments are expected to clarify the structure-function relationships of fullerene-dye adducts as pristine

materials and in blends, and are ultimately intended to improve upon the ability to rationally design fullerenes for blended systems with application in organic photovoltaic devices.

3.2 P3HT Blends

3.2.1 Optical Absorption

Analysis of the absorption spectra for P3HT, $PC_{61}BM$, Prato-Control, and the four fullerene-dye adducts is presented below in **Figures 3.3 – 3.5**. The molar extinction coefficients were collected from solution absorption measurements conducted in toluene. Although the P3HT used in this study is high molecular weight (50-70k), P3HT is not considered to be a low band-gap polymer. Low band-gap polymers typically have a band gap < 1.5 eV.[3] Conversely, P3HT has a band gap of 2.2 eV.[4] An effect of P3HT's band-gap can be observed in its absorption profile (**Figure 3.3a**). In solution, the main absorption band of P3HT exists between 300 nm – 550 nm with a ε = 7.91 x 10^3 $M^{-1}cm^{-1}$ at λ_{max} = 450 nm. Therefore, P3HT is not a strong absorber of low energy photons (ie. λ > 600 nm).
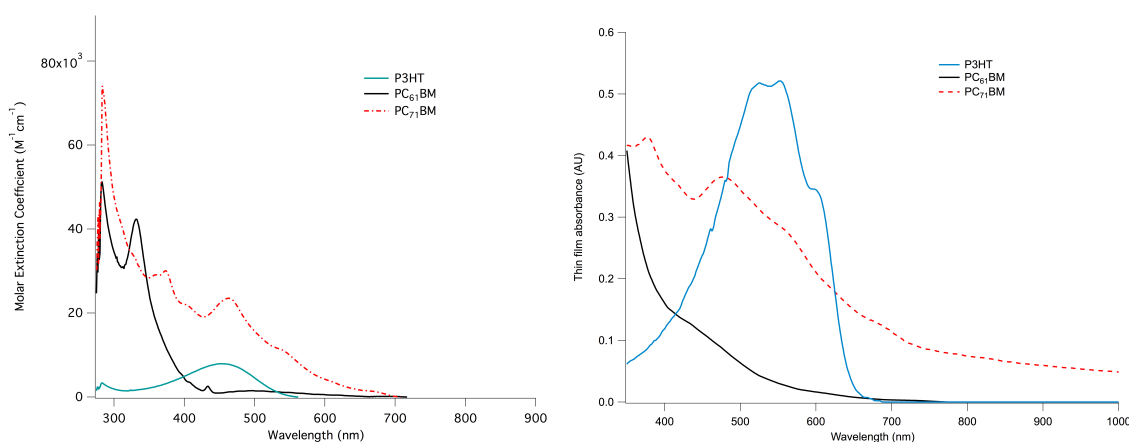
Figure 3.3: Absorption Spectra of P3HT, $PC_{61}BM$, and $PC_{71}BM$

a. molar extinction coefficients measured in toluene **b**. thin film absorbance

While the solution absorption was necessary to assess P3HT's molar absorptivity, the thin film absorption shown in **Figure 3.3b** is also relevant because it illustrates the absorption behavior as a solid-state system, similar to that found in an OSC. In contrast to solution measurements, the n-π* transition of P3HT is found between 350 nm – 650 nm, representing a significant red-shift in absorption on account of the aggregation of P3HT in the solid state.[5]

In solution, the primary absorption of P3HT (300 nm – 550 nm) overlaps with that of the TBTDT series (400 nm – 550 nm) as shown in **Figure 3.4**. However, the molar extinction coefficients for PCB-TBTDT and Prato-TBTDT from $\lambda = 400$ nm – 550 nm are larger than that of P3HT, respectively. In addition, the solution absorption of the DPP series also overlaps slightly with P3HT from 430 nm – 550 nm. Incidentally, the molar extinction coefficients of Prato-DPP and PCB-DPP from $\lambda = 430$ nm – 600 nm are larger than that of P3HT.
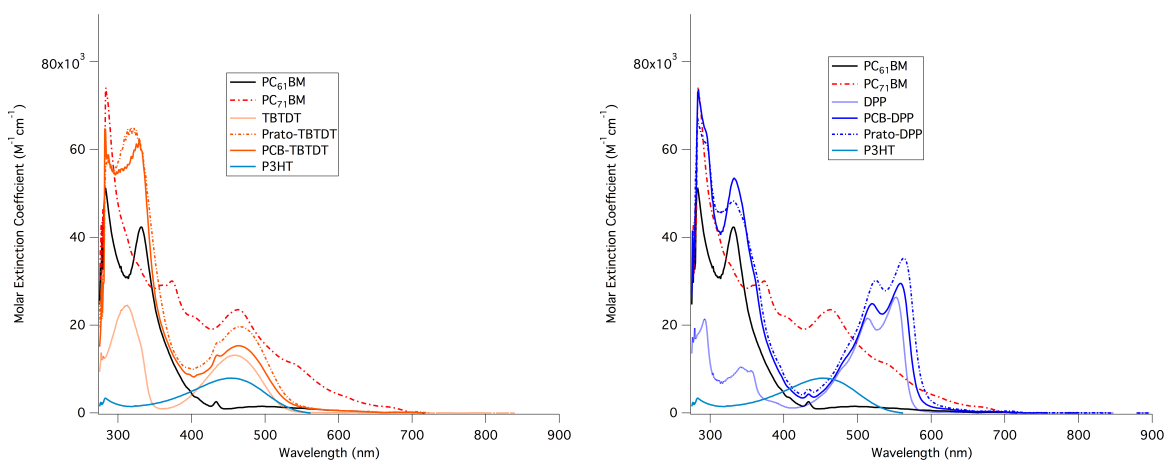
Figure 3.4: Comparison of Molar Extinction Coefficients of P3HT and the Fullerene-Dye Adducts **a.** P3HT and the TBTDT series **b.** P3HT and the DPP series

P3HT's absorption continues to overlap the absorption profiles of the TBTDT adducts in UV-vis measurements taken of their thin films (**Figure 3.5a**). Moreover, P3HT's thin film absorption overlaps the thin film absorption profiles of the DPP adducts (**Figure 3.5b**) more completely than was seen for their solution absorptions. The degree to which the molar absorptivity coefficients collected in solution correlate with the thin film absorptions is unclear. However, as P3HT's absorption profile offers no clear optical window between 400 nm – 650 nm, the additional absorption from the fullerene-dye adducts does not readily complement P3HT. The optical benefit of a P3HT:fullerene-dye adduct blend is therefore expected to be limited.
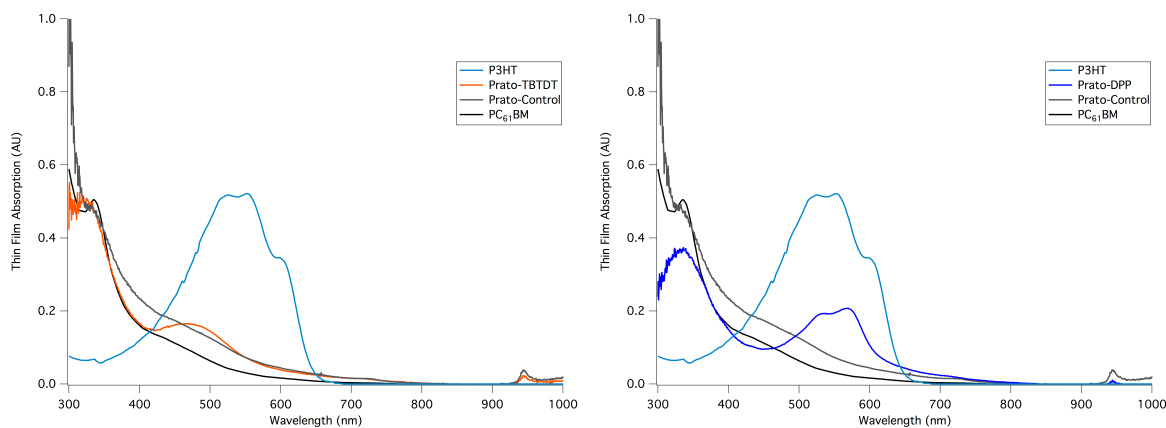
Figure 3.5: Thin Film Absorption Spectra for P3HT and the Fullerene-Dye Adducts

a. P3HT and the TBTDT series **b.** P3HT and the DPP series

Note: thin films were not measured on the same absorptivity scale

3.2.2   Frontier Orbital Alignment of the P3HT:Fullerene-Dye Adduct Blends
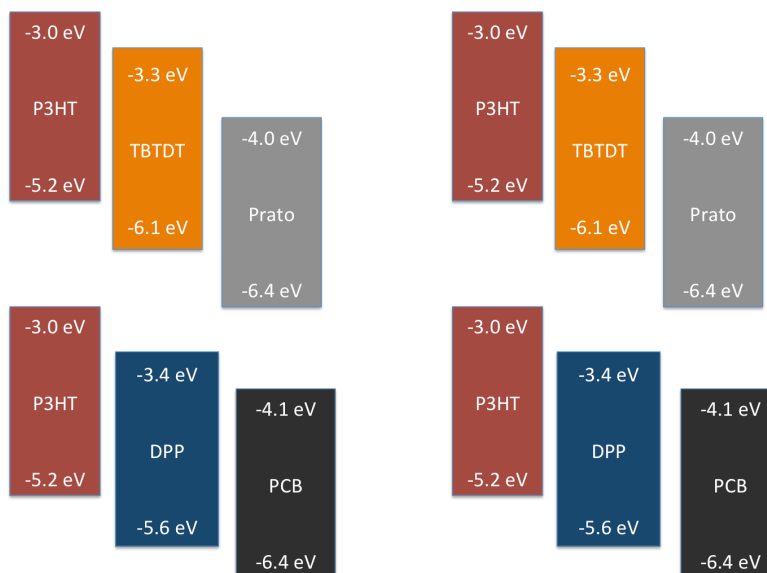
Figure 3.6: Frontier Orbital Alignment of P3HT and the Fullerene-Dye Adducts

Figure 3.6 illustrates the frontier orbital alignment (registered to vacuum) for each P3HT:fullerene-dye adduct blend. P3HT's LUMO of -3.0 eV favors the possibility of single electron transfer into the LUMOs of the pendant dyes, as each of their LUMOs is deeper than that of P3HT. Charge-transfer from P3HT's LUMO directly into the LUMOs of both Prato and PCB fullerenes is also favored. As described in Chapter 2, charge-transfer from the dyes' LUMO into the fullerene core is also energetically favored. In addition, P3HT's HOMO of -5.2 eV provides a driving force to accept holes transferred from the HOMOs of the pendant dyes and fullerenes. The dyes' HOMO can also mediate hole transfer from fullerene's HOMO.

In principle, the frontier orbital alignment of the P3HT:fullerene-dye adducts offers an electronically compatible system with the capacity to promote cascade charge transfer between the polymer and fullerene vis-à-vis the pendant dye. This feature is anticipated to provide a strong internal driving force for separating excitons and delivering free-charge

carriers to the fullerene and P3HT phases, while minimizing energetic traps. Therefore, exclusively on the basis of compatible orbital alignment, the P3HT:fullerene-dye adduct blends are, in principle, expected to produce working devices. The compatible energetics of this system contrasted by the non-complementary optics, however, presents an interesting dichotomy for P3HT:fullerene-dye adduct blends and will be explored in the sections below.

3.2.3 Device Fabrication of P3HT:Fullerene-Dye Adduct Blends

The P3HT:fullerene blends were prepared from stock solution mixtures of 36 mg/mL P3HT and 36 mg/mL fullerene-dye adduct in o-dichlorobenzene. The blend mixtures stirred overnight at 80 ˚C. All devices were prepared in an inert oxygen/water free atmosphere. The active layers were deposited onto PEDOT:PSS treated ITO using the following spin coater conditions: 550rpm 60s, 2000rpm 1s. Devices were made from as cast and solvent annealed-thermal annealed films. Following deposition, the annealed films were prepared by placing the substrate under a petri dish for 20 minutes. These films were subsequently thermally annealed at 150 ˚C for 5 mins. Devices were fabricated with the following configuration. ITO/PEDOT:PSS /P3HT:Fullerene/Ca/Al

3.2.4 Morphology

P3HT is a polycrystalline material with coexisting regions of crystalline and amorphous polymer. [6] Thin films of P3HT are generally characterized by a periodicity of out-of-plane peaks, which signal its crystalline regions have a degree of long range ordering perpendicular to the substrate. [7] In addition, π-π stacking peaks can be observed in plane, meaning on average, P3HT interacts with the substrate in an edge-on fashion. Upon annealing, the out-of-

plane peaks sharpen and grown in intensity, indicating growth of P3HT crystallites and improved preferential ordering. Higher hole mobilities are generally observed following this improvement in the anisotropy of P3HT molecular assemblies. [8] Furthermore, P3HT:acceptor OSCs commonly witness enhancements to their J_{sc} and FFs on account of this morphological change. [9]

Several interesting features are noted in the morphologies of the fullerene-dye adducts as pristine films. Each of the four fullerene-dye adducts are characterized by amorphous behavior in their as cast and annealed pristine films spun from ortho-dichlorobenzene (**Figure 3.7**). Prato-Control is also amorphous as cast, but shows higher long-range order upon annealing, as indicated by the periodic rings structure and its intensity, relative to background. $PC_{61}BM$ is also amorphous as cast, with some improvements in ordering upon annealing as well. In general, the glassy amorphous behavior of the four pristine fullerene-dye adducts is consistent with the amorphous morphology widely acknowledged to be preferential for high performance solar cells. [10]

As Cast

Ann 150 ˚C 5 mins

Prato-Control

Prato-TBTDT

Prato-DPP

PCB-TBTDT

PCB-DPP
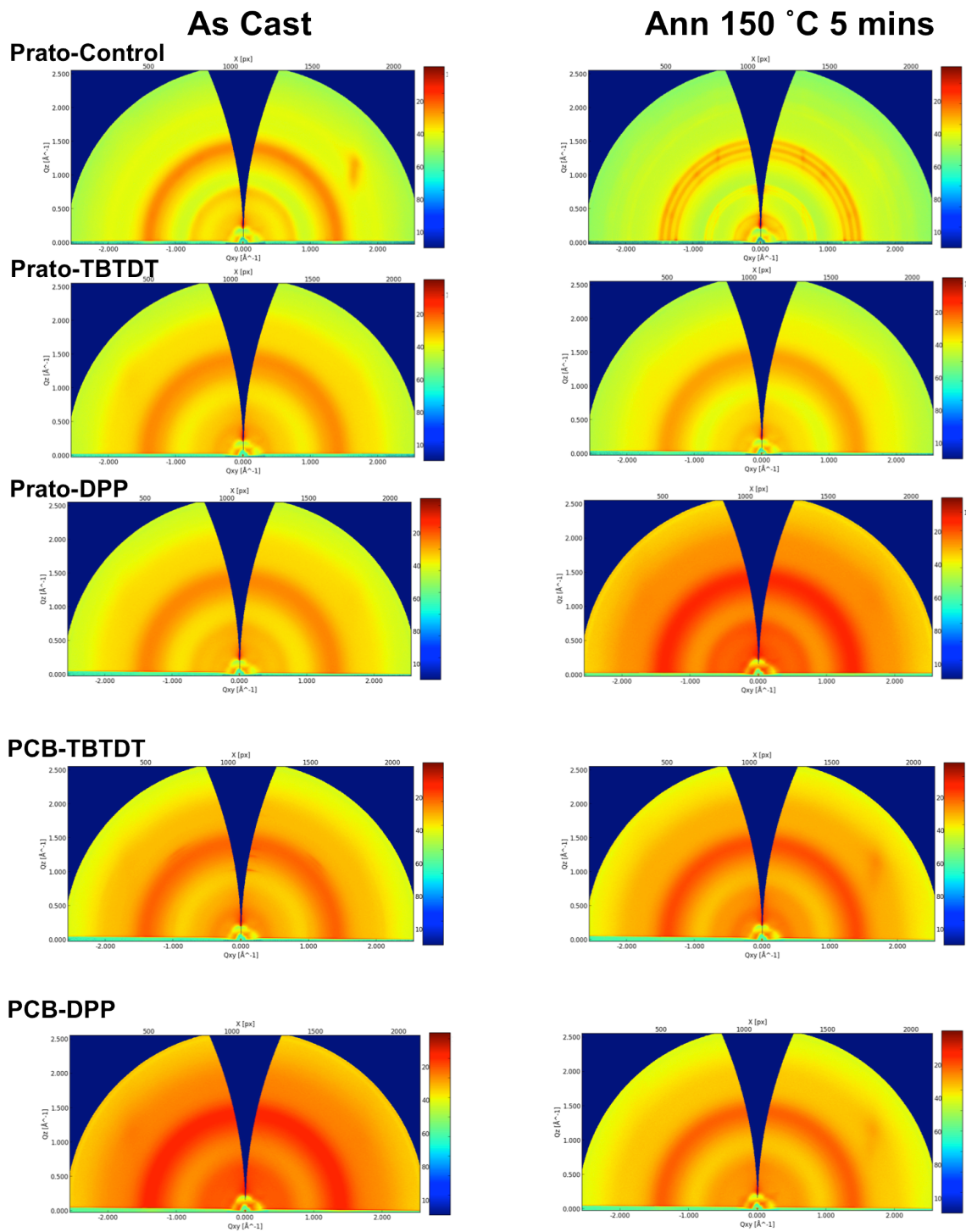
Figure 3.7: GIWAXS Images of the Fullerene-Dye Adducts and Their Controls

90

Figure 3.8 depicts the as cast and annealed P3HT:Prato-TBTDT devices that were prepared from chlorobenzene and o-dichlorobenzene and their correlating GIWAXS images. For P3HT:Prato-TBTDT blends, processing conditions which accelerate drying (ie. use of chlorobenzene as a deposition solvent) afford structures that are more highly textured, showing a distinct out-of-plane peak that correlates to the Prato-TBTDT species. This is not observed in systems that are processed from o-dichlorobenzene because the solvent evaporates more slowly. The affect of processing conditions on morphology would appear to influence device efficiencies by a substantial degree in P3HT:Prato-TBTDT blends, as indicated in **Table 3.1** below. This feature suggests that in P3HT blends Prato-TBTDT performs better as an *n-type* material when allowed to self-assemble into a more isotropic network. It is anticipated that processing conditions which extend the timescale of the fullerene-dye adducts miscibility with P3HT would continue to improve the thermodynamic compatibility of the two materials. However, the extent to which further optimization of processing conditions can be expected to enhance device efficiency is unclear.

System	D:A Molar Ratio	Solvent	V_{oc} (V)	J_{sc} (mA/cm^2)	FF	PCE (%)
P3HT:Prato-TBTDT	6.8:1	CB	0.39	-2.81	0.23	0.24
P3HT:Prato-TBTDT	6.8:1	CB	0.39	-0.58	0.19	0.04
P3HT:Prato-TBTDT	6.8:1	ODCB	0.50	-5.71	0.39	1.13
P3HT:Prato-TBTDT	6.8:1	ODCB	0.63	-6.17	0.39	1.53

Table 3.1: Device Results of P3HT:Prato-TBTDT Blends Deposited From Different

Solvents
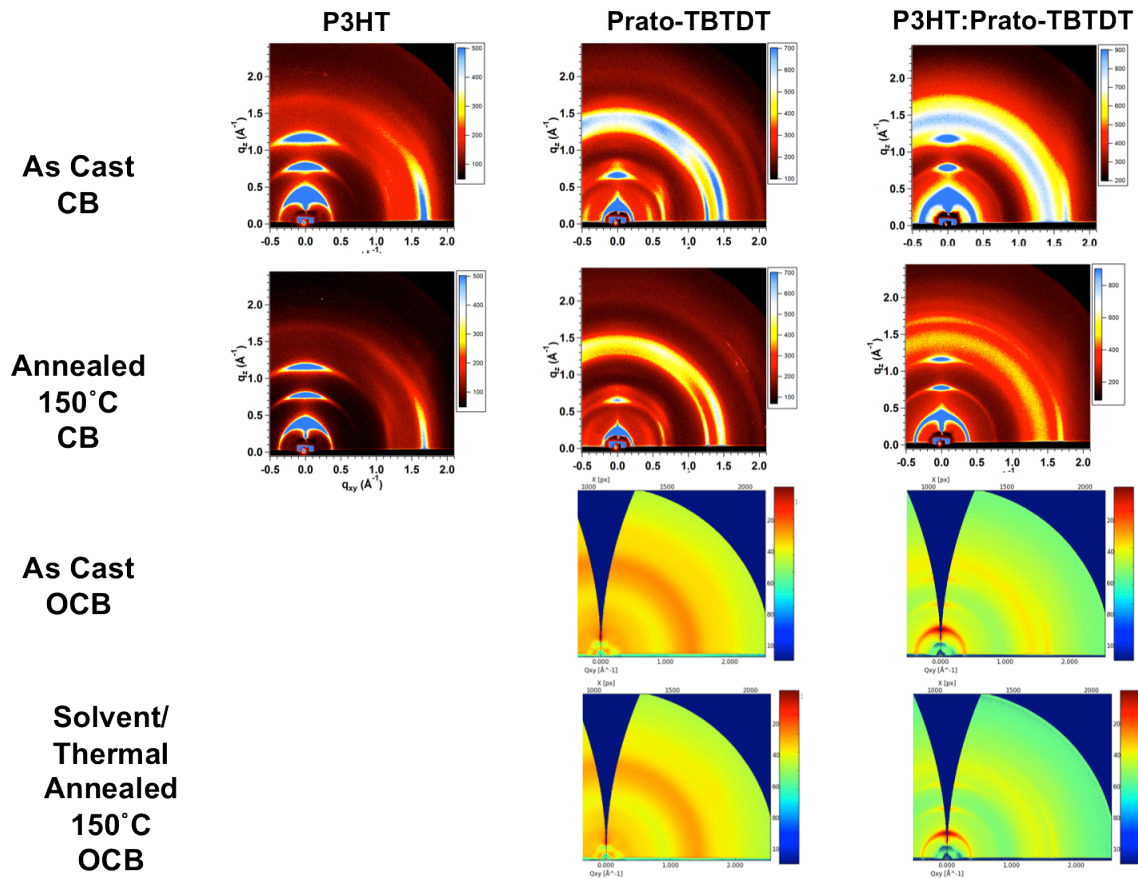
Figure 3.8: GIWAXS Images Highlighting the Affect of Processing Conditions on the

Morphology of P3HT:Prato-TBTDT Blends

3.2.5 Solar Cell Results of the P3HT:Fullerene-Dye Adduct Blends

A summary of the device results for the P3HT:fullerene-dye adduct blends and their controls is presented below in **Table 3.2**. The results provided for each blend ratio were averaged from 2 cells with 5 pixels each. The JV plots for the as cast and solvent annealed-thermal annealed blends are also presented in **Figure 3.9**. A more comprehensive table summarizing the device results collected from investigations of various processing conditions for the P3HT:fullerene-dye adduct blends is presented in the **Appendix**. In all cases, the

solvent annealed - thermal annealed devices were characterized by significant improvements in solar power conversion efficiency relative to the devices utilizing as cast films.
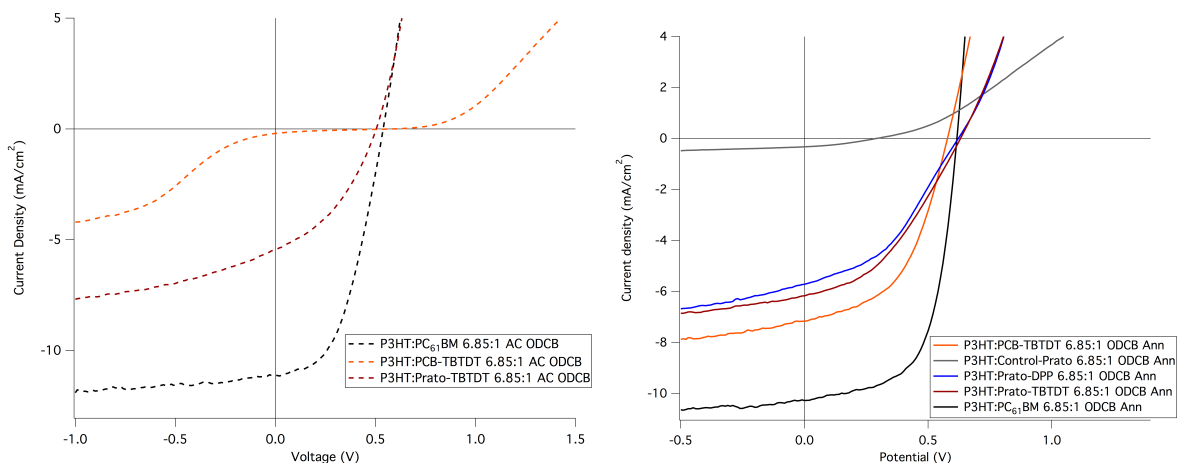
Figure 3.9: IV plots P3HT:Fullerene-Dye Adduct Blends

a. as cast devices **b.** solvent annealed - thermal annealed devices

Note: films prepared from o-DCB solutions with a molar ratio of 6.85:1

donor:acceptor

Among devices investigated from the P3HT:Prato blends, Prato-TBTDT yielded the highest performance (PCE = 1.5%), followed by Prato-DPP (PCE = 1.4%), and Prato-Control (PCE = 0.030%). Under the given processing conditions, incorporation of the dye onto the Prato anchor yielded an improvement for Prato-TBTDT and Prato-DPP relative to the 'dye-free' Prato-Control. Further comparison of the Prato series underscores that the Prato-dye adducts outperformed Prato-Control in V_{oc}, J_{sc}, and FF. The marginal difference in the V_{oc}'s of Prato-TBTDT and Prato-DPP suggests that for P3HT:Prato blends, the general presence of a dye has stronger influence over the internal cell bias than the identity of the dye itself. The absence of the dye may also be implicated in the especially low J_{sc} and FF of

Prato-Control, suggesting transport and extraction of free-charge carriers is problematic for this system. The higher long-range ordering observed in pristine Prato-Control (**Figure 3.7**) points to a physical origin for the especially poor performance of this material, although further exploration of the blend morphology would be needed to assert this claim definitively.

System	D:A Molar Ratio	V_{oc} (V)	J_{sc} (mA/cm^2)	FF	PCE (%)
P3HT:PC$_{61}$BM*	6.85:1	0.54	-11.13	0.48	2.9
P3HT:PC$_{61}$BM	6.85:1	0.61	-10.19	0.62	3.9
P3HT:PCB-TBTDT*	6.85:1	0.61	-0.17	0.18	0.020
P3HT:PCB-TBTDT	6.85:1	0.58	-7.17	0.50	2.1
P3HT:Prato-Control	6.85:1	0.29	-0.32	0.34	0.030
P3HT:Prato-TBTDT*	6.85:1	0.50	-5.71	0.39	1.1
P3HT:Prato-TBTDT	6.85:1	0.63	-6.17	0.39	1.5
P3HT:Prato-DPP	6.85:1	0.62	-5.49	0.41	1.4

Table 3.2: Summary of Device Results Obtained from P3HT:Fullerene-Dye Adduct Blends

Devices screened in the P3HT:PCB series yielded PC$_{61}$BM as the champion device (PCE = 3.9%), followed by PCB-TBTDT (PCE = 2.1%). As the V_{oc}'s measured from the PCB series show little deviation from one another, it is reasonable to infer that in binary P3HT:PCB blends, the internal cell bias is not significantly affected by the presence of the pendant dye. Incidentally, the marked decrease in J_{sc} and FF of the P3HT:PCB adduct blends relative to P3HT:PC$_{61}$BM draws attention to the dyes' affect on charge transport and extraction. It is also possible, however, that this observation is not an accurate reflection of the intrinsic capacity of the dye, but rather an affect of processing. Certain processing conditions can yield defects that are physical in nature, presenting geometric obstacles which alter the electronic behavior of the devices (ie. grain boundaries that preclude efficient charge transport). It is also likely that the dye-adducts do not have a thermodynamic or kinetic

driving force strong enough to adopt a more ideal morphology than that of P3HT:PC$_{61}$BM, despite inclusion of a solvent annealing step. This result implies that under the given processing conditions, the presence of the pendant dye may be problematic for the active layer microstructure of binary P3HT:PCB adduct blends. However, it is also possible that further optimization of the processing conditions could render morphologies that are more favorable to efficient charge transport and extraction, improving the PCEs of these blends as a consequence.

Closer comparison of Prato-TBTDT and PCB-TBTDT highlights that while there is only an 8% difference in the V$_{oc}$'s of PCB-TBTDT (0.58 V) and Prato-TBTDT (0.63 V), PCB-TBTDT shows a 16% improvement in its J$_{sc}$ (7.17 mA/cm^2, 6.17 mA/cm^2 respectively) and a 28% improvement in its FF (0.50, 0.39 respectively) relative its Prato homologue. Two important molecular distinctions exist between the two anchors, and are believed to be the source of this anomaly. First, the Prato anchor locks the dye into a closer spatial orientation with C$_{60}$, with less rotational freedom than its PCB analogue. Second, the Prato anchor has a heterocyclic pyrrolidine ring.

The structural differences associated with the lower J$_{sc}$ and FF of the Prato adducts relative to the PCB adducts suggest two probable rationales. On one hand, it could be reasoned that the PCB anchor allows the heterojunction to adopt a superior microstructure over the Prato anchor, with little affect to the energetic alignment of the blend components since the internal bias of the cell appears unaffected. In principle, the Prato anchor separates the dye from C$_{60}$ by about 3 angstroms while the PCB adduct separates the dye from C$_{60}$ by about 12 angstroms. It is therefore reasonable to infer the additional distance between fullerene and dye in PCB-TBTDT affords sufficient molecular flexibility to adopt a

morphology more favorable to the solar cell's capacity for charge transport and extraction. Conversely, it could be rationalized (as described in Chapter 2) that since the Prato anchor's pyrrolidine nitrogen is capable of being quarternized by trace acid in the chlorinated deposition solvents, the Prato anchor may support charged electronic obstacles which inhibit charge transport.

3.2.6   EQE of the P3HT:Fullerene-Dye Adduct Blends

Several noteworthy observations can be made from analysis of the EQEs measured for the P3HT:fullerene-dye adduct blends (**Figure 3.10**). First, for each of the fullerene-dye adduct blends including Prato-Control, the EQE is shown to be lower than that of P3HT:PC$_{61}$BM. This observation indicates the P3HT:PC$_{61}$BM active layer generates photocurrent more efficiently than the active layers utilizing fullerene-dye adducts. As was reasoned from the stability in V$_{oc}$'s and distinct reductions in J$_{sc}$'s and FF's of the fullerene-dye adduct blends relative to PC$_{61}$BM, this feature speaks to the reduced ability of these systems to transport and extract charge effectively. The optical advantage gained via the pendant dye's additional light harvesting capacity could be counter balanced by molecular assemblies that reduce the efficiency of converting absorbed photons into photocurrent.
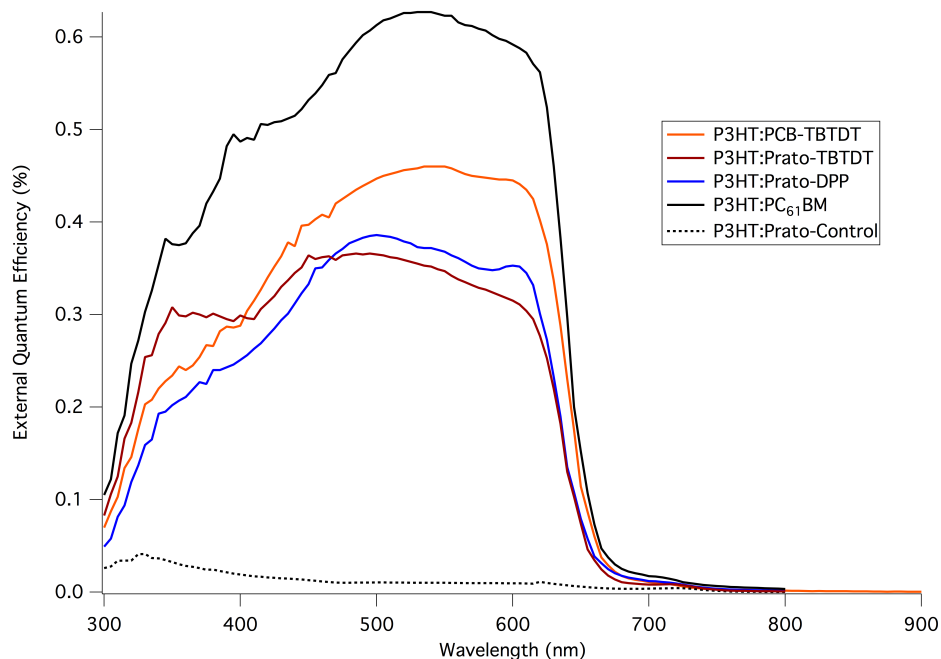
Figure 3.10: EQE of the P3HT:Fullerene-Dye Adduct Blends

Furthermore, because of overlapping absorptions and substantial decreases in photocurrent intensity across the visible spectrum for the P3HT:fullerene-dye adduct blends, it is difficult to directly attribute contributions from the pendant dye's additional photon harvesting capacity to the EQE (**Figure 3.11**). This phenomenon was seen in each of the P3HT:fullerene-dye adduct blends. As previously noted, while the electronic orbitals of P3HT and the pendant TBTDT and DPP dyes complement one another, their optical absorptions do not. The ultimate consequence of this detail is that photocurrent generated from the dye's absorption cannot be independently quantified from P3HT's absorption.

3.2.7 P3HT:PC$_{61}$BM:Prato-TBTDT Ternary Blends

In an effort to further analyze the affect of fullerene-dye adducts on device performance and EQE, a series of ternary blend P3HT:PC$_{61}$BM:Prato-TBTDT devices were investigated. The total molar concentration of P3HT:fullerene was held constant while the molar feed ratios of PC$_{61}$BM:Prato-TBTDT were varied. The IV curves of these experiments are presented below in **Figure 3.12**. The results of these experiments are also summarized in **Table 3.3** and **Figure 3.13** for clarity.
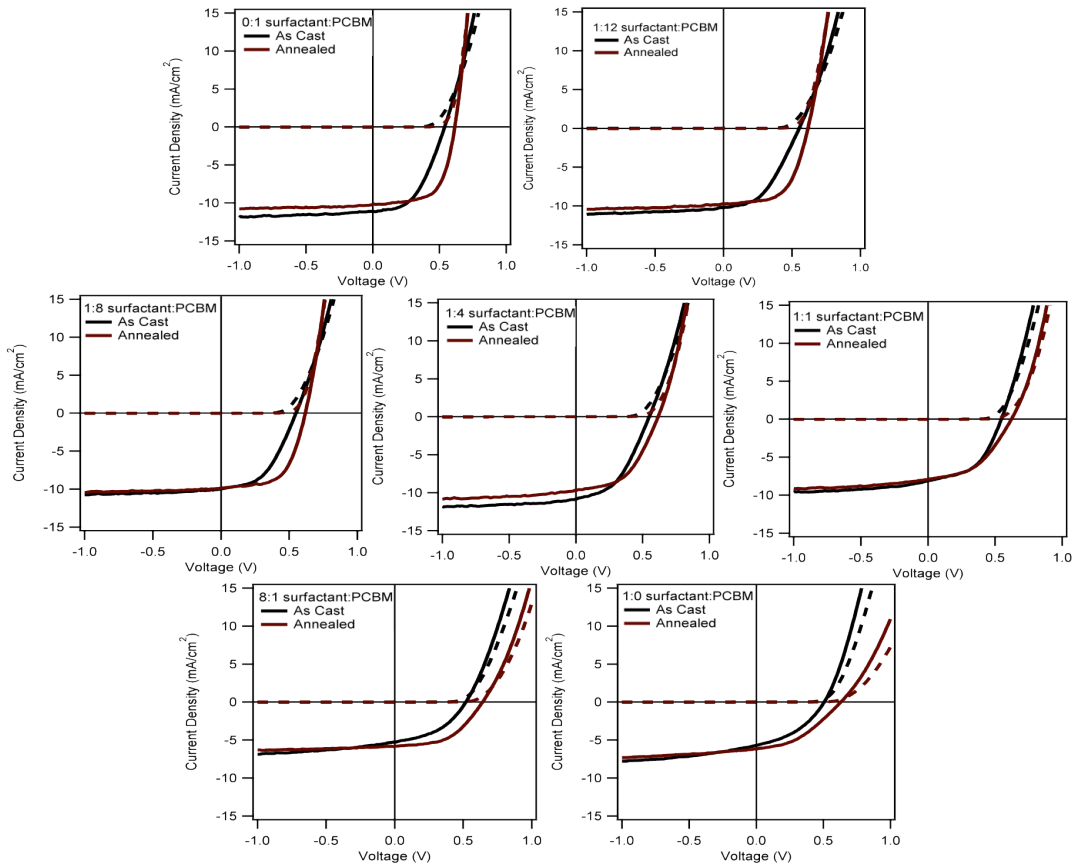
Figure 3.12: IV Plots of the P3HT:PC$_{61}$BM:Prato-TBTDT Ternary Blends.

Note: molar ratio of P3HT:fullerene is held constant, while the relative ratios of the two fullerenes are varied.

The principle trend in these ternary blend devices was a decrease in PCE with increasing molar concentration of Prato-TBTDT. Interestingly, deviations in V_{oc} were found to be minimal, with only a slight increase in V_{oc} for the annealed blends and a small decrease for the as cast blends noted with increasing Prato-TBTDT content. In both cases, the largest deviations in V_{oc} fell within 6% of the parent P3HT:PC$_{61}$BM blend. However, these fluctuations did not significantly affect the global trend in PCEs, lending further support to arguments that the internal cell bias of P3HT:fullerene-dye adduct blends is largely unaffected by the presence of the dye. In contrast, a stronger correlation was registered between the decrease in J_{sc} and increasing feed ratio of Prato-TBTDT for both as cast and annealed blends. In particular, a 40% loss in J_{sc} and 38% decrease in FF was measured from P3HT:PC$_{61}$BM to P3HT:Prato-TBTDT for the annealed cells.

PC$_{61}$BM:Prato-TBTDT	V_{oc} (V)	J_{sc} (mA/cm^2)	FF	PCE (%)
1:0*	0.54	-11.13	0.48	2.9
1:0	0.61	-10.19	0.63	3.9
12:1*	0.55	-10.20	0.44	2.5
12:1	0.62	-9.74	0.59	3.5
8:1*	0.52	-5.28	0.43	1.2
8:1	0.64	-5.82	0.50	1.9
4:1*	0.55	-10.83	0.44	2.6
4:1	0.62	-9.67	0.49	2.9
1:1*	0.55	-8.12	0.49	2.2
1:1	0.62	-7.93	0.45	2.2
1:8*	0.52	-5.28	0.43	1.2
1:8	0.64	-5.82	0.50	1.9
0:1*	0.51	-5.71	0.39	1.1
0:1	0.63	-6.17	0.39	1.5

Table 3.3: Device Results for the P3HT:PC$_{61}$BM:Prato-TBTDT Ternary Blends.
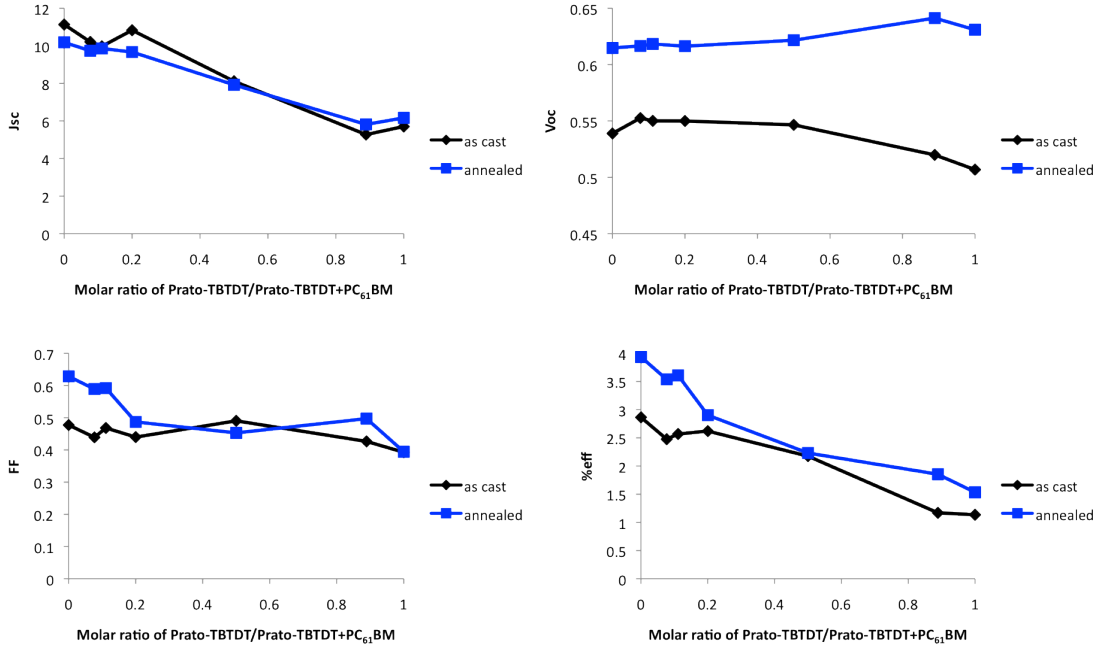
Figure 3.13: Device Parameters from the P3HT:PC$_{61}$BM:Prato-TBTDT Ternary Blends

The prominent reductions measured in J$_{sc}$ and FF, as a function of increasing Prato-TBTDT feed ratios, provide convincing evidence that the recorded decreases in PCE are principally rooted in the introduction of Prato-TBTDT. The evolution of this trend indicates an emergence of barriers in the active layer that are increasingly disruptive to effective charge transport and extraction. Had the basis of this observation been purely electronic in nature, absent of any physical origin, it would be expected that the V$_{oc}$'s of these blends would have likewise suffered as a consequence. However, due to the relative stability of V$_{oc}$'s across blend ratios, the salient trend in PCEs suggests that while incorporation of Prato-

TBTDT does not compromise the cell's internal bias, it does introduce physical features into the active layer that are problematic for device performance nonetheless.

Examination of the EQEs measured for P3HT:PC$_{61}$BM:Prato-TBTDT ternary blends offers an interesting piece of evidence. The central observable trend in EQE is an overall decrease in photocurrent with increasing Prato-TBTDT content; again discarding the plausibility of a direct correlation between enhanced dye absorption and improved photocurrent (**Figure 3.14a**). However, analysis of the mean normalized EQE is compelling (**Figure 3.14b**). As the relative ratio of Prato-TBTDT increases, a boost in EQE is noted from 325 nm - 400 nm relative to the 400 nm – 650 nm range. The molar extinction coefficient for Prato-TBTDT is larger than PC$_{61}$BM in the 325 nm – 400 nm range. This data suggests the relative contribution to the photocurrent from the π-π* transition of Prato-TBTDT scales with the amount of the fullerene-dye adduct incorporated into the blend. Although this transition does not represent the n-π* transition of TBTDT initially targeted, it nevertheless indicates that the fullerene-dye adduct was responsible for generating photocurrent, with the effect increasingly pronounced as the feed ratio of PC$_{61}$BM is decreased. Ultimately, higher EQEs were observed as the ratio of PC$_{61}$BM increased. This data further confirms the importance of PC$_{61}$BM's ability to facilitate charge transport, despite its modest contribution to photon absorption.
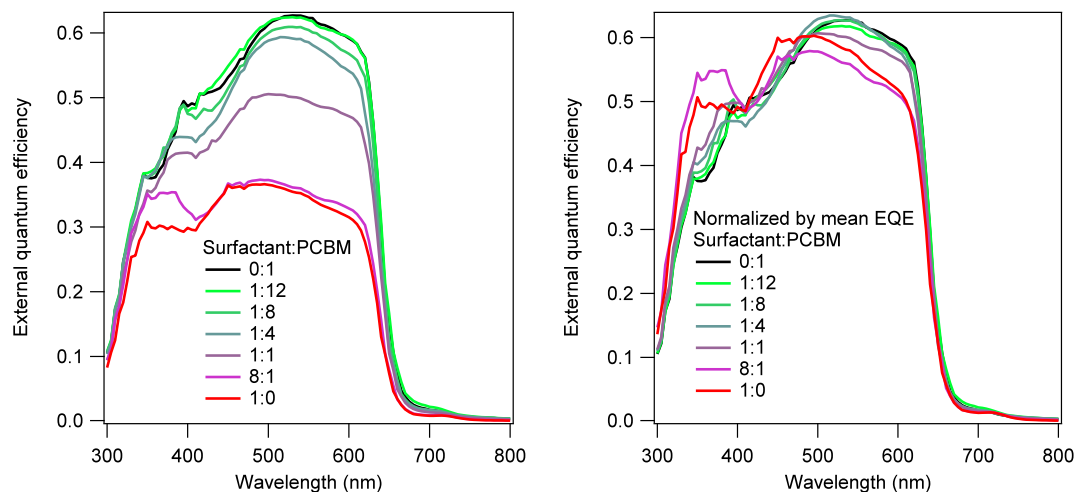
Figure 3.14: EQE of P3HT:Prato-TBTDT:PC_{61}BM Ternary Blends

a. non-normalized **b.** mean normalized

3.2.8 Summary of P3HT:Fullerene-Dye Adduct Blends

The P3HT:fullerene-dye adduct blends present a system where the optical profiles of both materials largely overlap. The electronic alignment of these blends is complementary, however, and their frontier orbitals provide a driving force for the pendant dye to mediate cascade charge-transfer between P3HT and fullerene. The thermally driven growth and preferential ordering of P3HT crystallites is not significantly affected by the presence of the fullerene-dye adduct. In addition, film deposition from higher boiling point solvents affords microstructures that decrease the texturing of fullerene-dye adducts within the blend. A strong correlation between PCE and fullerene texturing was observed.

3.3 PDPP2FT:Fullerene-Dye Adduct Blends

3.3.1 Optical Absorption of PDPP2FT and the Fullerene-Dye Adducts

Figure 3.15 provides a comparison of the molar extinction coefficients and thin film absorption of PDPP2FT, P3HT, $PC_{61}BM$, and $PC_{71}BM$. In contrast to P3HT, PDPP2FT is a low band gap polymer with an absorption profile that extends into the near IR. In solution, the n-π* transition for this polymer falls between 500 nm - 900 nm, with ε = 9.09 x 10^4 M$^-$ ^{1}cm^{-1} at λ_{max} = 814 nm. However, similar to $PC_{61}BM$, the molar absorptivity of PDPP2FT from 400 nm – 600 nm is quite low (ε < 1.00 x 10^4 M^{-1}cm^{-1}). In contrast, $PC_{71}BM$'s absorptivity in this region is substantially larger than $PC_{61}BM$'s, which is the primary rational cited for inclusion of $PC_{71}BM$ in OSCs prepared with low band-gap blend.[11] Comparison of the EQEs of PDPP2FT:$PC_{61}BM$ (**Figure 3.21)** vs. PDPP2FT:$PC_{71}BM$[12] highlight the additional photocurrent generated from capturing more photons in this optical region.
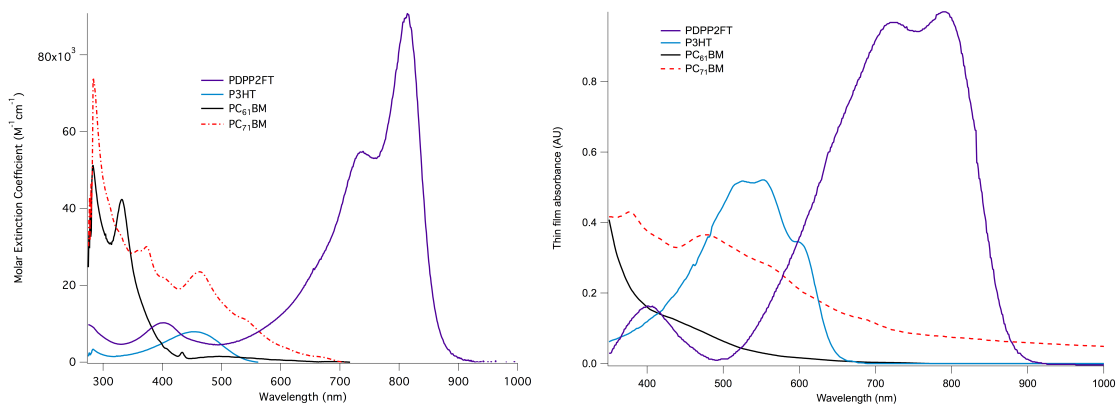
Figure 3.15. Absorption Spectra of PDPP2FT, P3HT, $PC_{61}BM$, and $PC_{71}BM$

a. molar extinction coefficients measured in toluene **b.** thin film absorption

A comparison of the molar extinction coefficients of the fullerene-dye adducts and PDPP2FT is provided in **Figure 3.16**. Prato-TBTDT and PCB-TBTDT show enhanced

absorption relative to PDPP2FT from 275 nm – 515 nm with a slight deviation from this trend noted around 400 nm. In addition, PCB-TBTDT and Prato-TBTDT outperform $PC_{61}BM$ from 275 nm – 550 nm. It is therefore reasonable to assume that if the system's molar absorptivity were the primary factor for generation of EQE photocurrent, enhancements in EQE from 275 nm – 515 nm would be expected in PDPP2FT:TBTDT adduct blends, relative to PDPP2FT:$PC_{61}BM$.
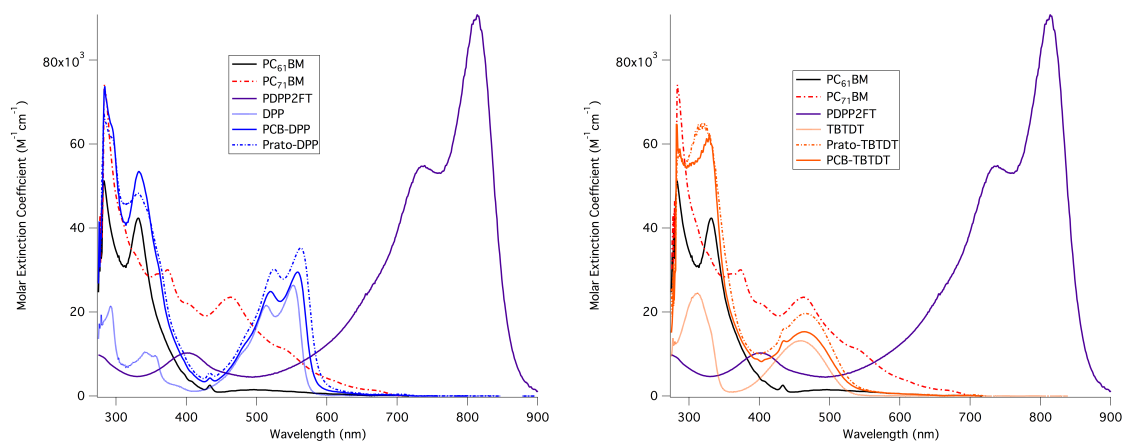
Figure 3.16: Molar Extinction Coefficients of the Fullerene-Dye Adducts with PDPP2FT

a. PDPP2FT & DPP series **b.** PDPP2FT & TBTDT series

Prato-DPP and PCB-DPP also show enhanced absorption relative to PDPP2FT from 275 nm – 585 nm, with a slight deviation from this trend noted from 400 nm - 450 nm. Moreover, the DPP adducts show enhanced optical absorption over $PC_{61}BM$ from 275 nm to 600 nm. Therefore, on the basis of molar absorptivity, relative to PDPP2FT:$PC_{61}BM$, enhancements in the EQE from 275 nm – 400 nm and 450 nm – 585 nm would be expected for solar cells made from blends of PDPP2FT:DPP adducts.
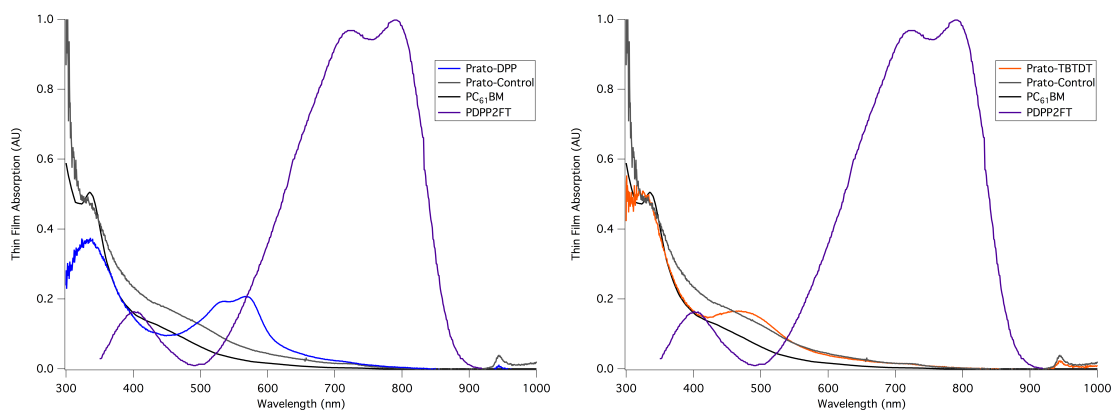
Figure 3.17: Thin Film Absorption of PDPP2FT and the Fullerene-Dye Adducts

a. PDPP2FT and the DPP series **b.** PDPP2FT and the TBTDT series

Note: thin films were not measured on the same absorptivity scale

3.3.2 Frontier Orbital Alignment of PDPP2FT and the Fullerene-Dye Adducts

Figure 3.18 illustrates the frontier orbital alignment of PDPP2FT and the fullerene-dye adducts. PDPP2FT has a LUMO of -3.5 eV and a HOMO of -5.2 eV.[13] Cyclic voltammetry measurements presented in chapter 2 register the LUMOs of the pendant TBTDT and DPP dyes at -3.3 eV and -3.4 eV respectively. Due to the higher LUMOs of the pendant dyes, it is expected that charge transfer from the lower lying LUMO of PDPP2FT into the dyes' LUMO will not proceed under normal conditions. PDPP2FT does, however, have the capacity to transfer electrons into the fullerene LUMOs, as do each of the dyes.

Conversely, holes from fullerene's HOMO have an energetic driving force for charge transfer into the HOMOs of the pendant dyes and PDPP2FT. In principle, holes from both dyes could also charge transfer into PDPP2FT, though this scenario could be complicated by the polymer's inability to neutralize the exchange through electron transfer into the dye's LUMO. An internal morphology that physically locks the pendant dyes into immediate contact with the polymer, at the exclusion of fullerene, could favor energetic barriers

105

impeding charge transport as a consequence. In comparison to the P3HT system detailed in **Section 3.2**, solar cells made from PDPP2FT blends present a divergent materials system for the analysis of fullerene-dye adducts. In the case of PDPP2FT:Fullerene-dye adduct blends, the pendant dyes complement the optical absorption of PDPP2FT, but their energy levels are less compatible for cascade charge transfer from polymer to fullerene vis-à-vis the dye. The consequences of this system will be explored in the sections that follow.
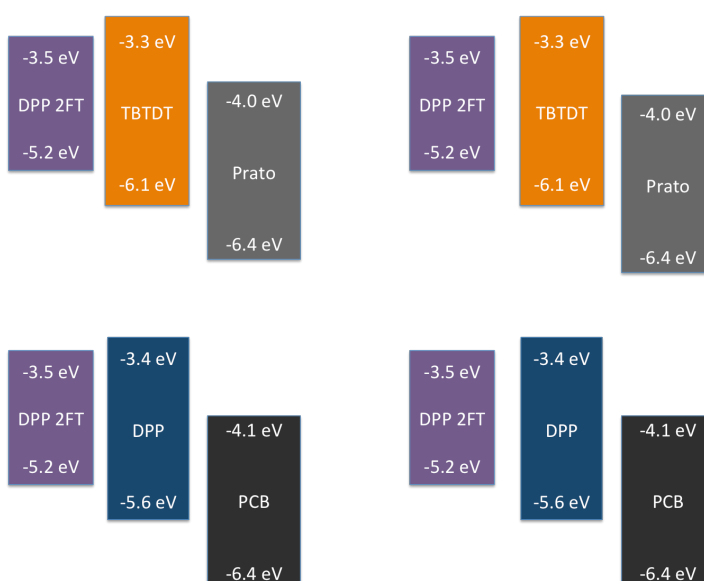
Figure 3.18: Frontier Orbital Alignment of PDPP2FT and the Fullerene-Dye Adducts

3.3.3   Device Fabrication

The PDPP2FT blend devices were prepared based on the protocol used by Frechet et al.[14] The PDPP2FT:Fullerene blends were prepared from stock solution mixtures of 36 mg/mL P3HT and 36 mg/mL fullerene-dye adduct in chlorobenzene and o-dichlorobenzene. Analogous solutions containing 9 vol% chloronaphthalene were also prepared. The blend mixtures stirred overnight at 80 ˚C. All devices were prepared in an inert oxygen-free

atmosphere. The active layers were deposited onto PEDOT:PSS treated ITO using the following spin coater conditions: 2000 rpm 60 s. Devices were made from as cast and thermally annealed films. Following deposition, the annealed films were prepared under the following conditions; 150 °C for 5 mins. Devices were fabricated with the following configuration, ITO/PEDOT:PSS /PDPP2FT:Fullerene/LiF/Al

3.3.4   Morphology of PDPP2FT:Fullerene-Dye Adduct Thin Films

The ethyl hexyl derivative of PDPP2FT used in these studies is known to self-assemble into a disordered isotropic network in thin films.[15] It was therefore of interest to examine the structural interactions of fullerene-dye adducts with an amorphous polymer in thin films to facilitate future interpretation of their device results. GIWAXS images of the PDPP2FT:PCB-TBTDT and PDPP2FT:Prato-TBTDT bulk heterojunction thin films are provided below in **Figure 3.19**. Notably, these images are absent of features consistent with long-range ordering and crystalline domains, indicating an amorphous morphology for the PDPP2FT:fullerene-dye adduct blends in both as cast and annealed films.

The PDPP2FT:fullerene-dye adduct microstructures contrast those observed in the P3HT blends, since the annealing step offers no clear improvements to the molecular anisotropy of either blend component. Furthermore, these images suggest a homogenous blend of donor and acceptor. Such a morphology may increase the number of donor:acceptor interfaces and could favor charge separation. However, if the homogeneity of the blend precludes formation of donor or acceptor rich domains, broadly acknowledged as an important features for charge transport, a corresponding increase in exciton recombination

and charge trapping could handicap device performance as a result. The affects of this morphology on device performance will be discussed in the sections that follow.
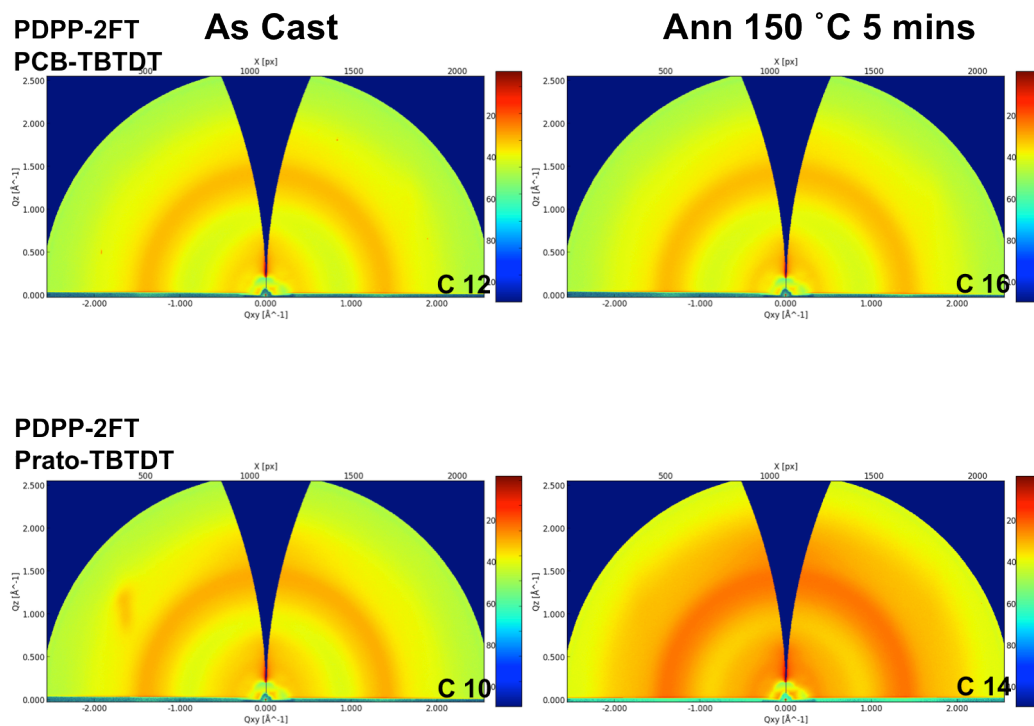
Figure 3.19: GIWAXS of PDPP2FT:Fullerene-Dye Adduct Thin Films

3.3.5 Device Results of the PDPP2FT:Fullerene-Dye Adduct Blends

The results for devices prepared from the PDPP2FT:fullerene-dye adduct blends are presented below in **Figure 3.20** and **Table 3.4**. The results provided for each blend ratio were averaged from two cells, each containing five pixels. A more comprehensive device table summarizing the various parameters modified during optimization of the PDPP2FT blend processing conditions is also provided in the **Appendix**. In general, devices made from as cast blends performed better than their annealed analogues. In addition, molar ratios of 0.53:1 PDPP2FT:fullerene were found to produce higher PCE's for the PCB series, while molar

ratios of 1:1 PDPP2FT:fullerene yielded the higher PCEs for the Prato series. A PDPP2FT:PC$_{61}$BM blend was used for the control device and yielded a substantially higher PCE (3.2%) relative to the fullerene-dye adducts.

Overall, the V$_{oc}$'s recorded from the PDPP2FT:fullerene-dye adduct blends were high, with the majority of devices registering V$_{oc}$'s between 0.7 V - 0.8 V. In opposition to this trend of high V$_{oc}$'s, J$_{sc}$ and FF values were consistently low; with the majority of devices having J$_{sc}$'s < 1 mA/cm^2 and FF's < 0.40. The low J$_{sc}$ and FF values highlight the inability of these systems to transport and extract charge effectively. Moreover, the S-shaped appearance of many of the IV curves indicates an accumulation of charge within the device, modulating the device's internal potential and disrupting its capacity to dissociate excitons and extract charge.[16] An absence of contiguous polymer and fullerene domains may have precluded balanced carrier mobilities, leading to the emergence of the S-shaped curves.[17]

The general observation of low J$_{sc}$'s, low FFs, and S-shaped IV curves is symptomatic of blends that promote over-mixing of polymer and fullerene domains, with poor carrier transport and unbalanced charge extraction. The amorphous PDPP2FT:fullerene-dye adduct GIWAXS images are consistent with a homogenous blend microstructure devoid of donor and acceptor rich domains needed for efficient charge transport. Additionally, the electronic misalignment between PDPP2FT and the pendant dyes could have limited cascade electron transfer from the polymer to the fullerene via the dye, therein reducing charge generation and transport.
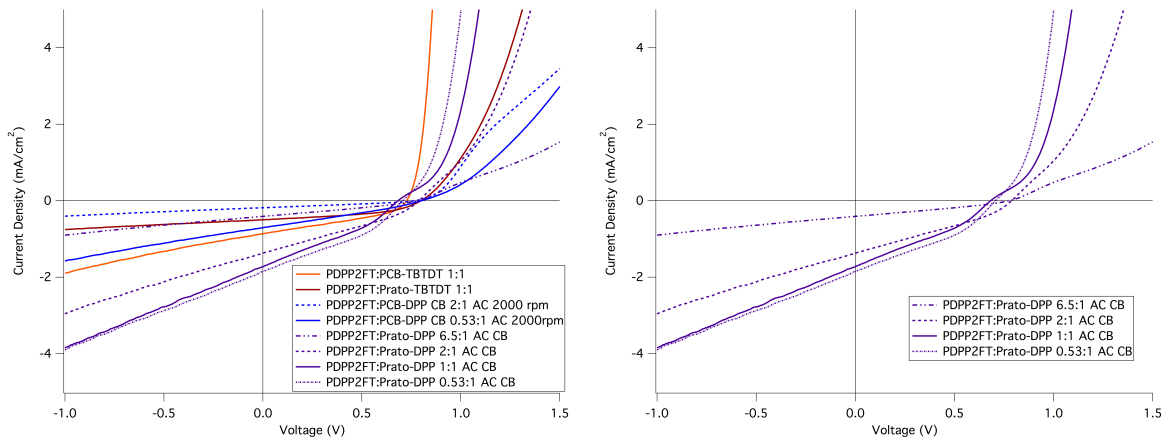
Figure 3.20: IV curves for the PDPP2FT:Fullerene-Dye Adduct Blends

System	D:A Molar Ratio	V_{oc} (V)	J_{sc} (mA/cm^2)	FF	PCE (%)
PDPP2FT:PC$_{61}$BM*	0.53:1	0.73	-7.52	0.58	3.2
PDPP2FT:PC$_{61}$BM	0.53:1	0.74	-5.86	0.56	2.5
PDPP2FT:PCB-TBTDT*	0.53:1	0.71	-0.89	0.36	0.23
PDPP2FT:PCB-TBTDT	0.53:1	0.75	-0.36	0.37	0.10
PDPP2FT:PCB-DPP*	0.53:1	0.77	-0.37	0.28	0.080
PDPP2FT:PCB-DPP	0.53:1	0.79	-0.45	0.28	0.10
PDPP2FT:Prato-TBTDT*	0.53:1	0.75	-0.44	0.40	0.14
PDPP2FT:Prato-TBTDT	0.53:1	0.65	-0.34	0.38	0.09
PDPP2FT:Prato-DPP*	0.53:1	0.72	-2.03	0.33	0.49
PDPP2FT:Prato-DPP	0.53:1	0.60	-1.17	0.32	0.22
PDPP2FT:PCB-TBTDT*	1:1	0.71	-0.92	0.37	0.24
PDPP2FT:PCB-TBTDT	1:1	0.72	-0.51	0.37	0.13
PDPP2FT:PCB-DPP*	1:1	0.76	-0.44	0.26	0.09
PDPP2FT:PCB-DPP	1:1	0.75	-0.32	0.26	0.06
PDPP2FT:Prato-TBTDT*	1:1	0.81	-0.49	0.45	0.18
PDPP2FT:Prato-TBTDT	1:1	0.78	-0.54	0.46	0.19
PDPP2FT:Prato-DPP*	1:1	0.74	-2.10	0.32	0.49
PDPP2FT:Prato-DPP	1:1	0.70	-1.83	0.33	0.43

Table 3.4: Summary of the PDPP2FT:Fullerene-Dye Adduct Device Results

* denotes devices made from as cast blends

3.3.6   EQE

An EQE of the PDPP2FT:PC$_{61}$BM blend is provided below in **Figure 3.21**. A reduction in photocurrent is observed from 400 nm – 650 nm, the basis of which is rooted in the low

absorptivity of the blend in said region. Relative to $PC_{61}BM$ and PDPP2FT, each of the four fullerene-dye adducts shows enhanced molar absorptivity between 400 nm – 650 nm and would therefore be expected to help compensate the parent blends inability to harvest photons in this region.
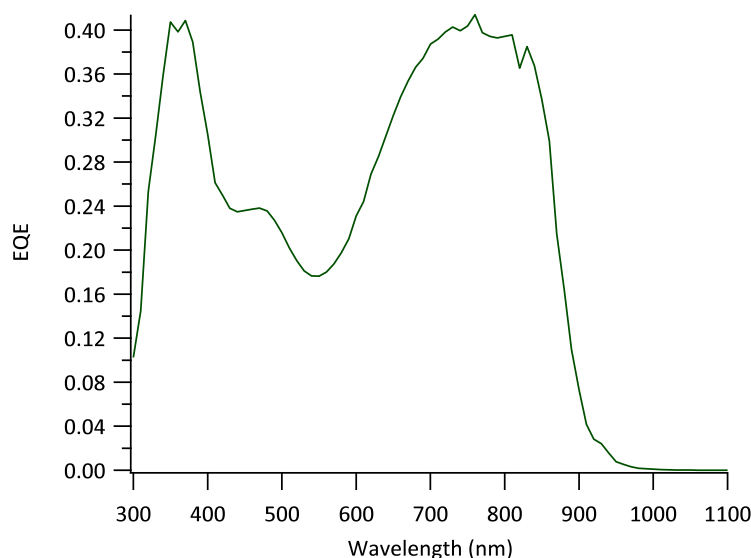
Figure 3.21: EQE of PDPP2FT:$PC_{61}BM$

Several EQEs obtained from various blend ratios of PDPP2FT:fullerene-dye adducts are present below in **Figure 3.22**. In comparison to the PDPP2FT:$PC_{61}BM$ control, the PDPP2FT:fullerne-dye adduct devices have markedly lower photocurrent. Notably, however, EQEs measured for the Prato-TBTDT, Prato-DPP, and PCB-DPP blends each show higher photocurrent in the regions corresponding to fullerene's π-π^* and dye's n-π^* transition relative to PDPP2FT's n-π^* transition. This result is telling because the molar absorptivity of PDPP2FT's n-π^* band is comparatively larger ($\varepsilon = 9.09 \times 10^4 \ M^{-1}cm^{-1}$ at $\lambda_{max} = 814$ nm) than that of either dye or fullerene. Therefore, despite inclusion of a strongly absorbing low band-

gap polymer into the active layer, under the given processing conditions, these blends nevertheless handicap PDPP2FT's capacity to generate photocurrent; with a majority of the measured current ascribed to the fullerene and pendant dye rather than PDPP2FT. The low J_{sc}'s of these systems highlight their inability to efficiently shuttle separated charges to the electrodes, a phenomenon which likely plays a role in observations of low efficiency photocurrent generation.
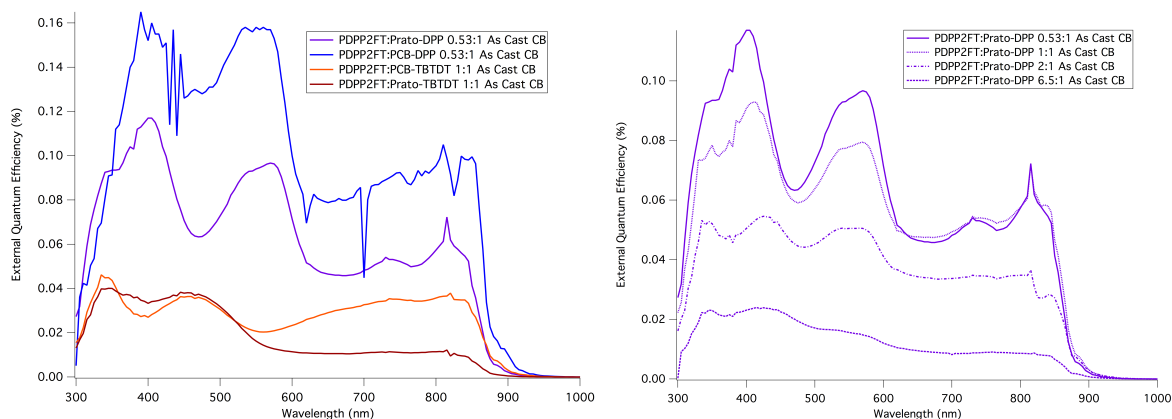
Figure 3.22: EQEs of PDPP2FT:Fullerene-Dye Adduct Blends

a. EQEs of the champion device for each adduct **b.** EQEs of the Prato-DPP blends with varying molar ratios

Interestingly, while the EQE measured for the PDPP2FT:PCB-TBTDT blend is quite low, it nevertheless indicates that the fullerene, dye, and polymer made relatively equal contributions to the photocurrent (**Figure 3.23**). This observation is noteworthy in light of the equimolar ratios of fullerene, dye, and polymer that belie their relative differences in molar absorptivity. The PDPP2FT:PCB-TBTDT blend also registered a high V_{oc}, low J_{sc}, and low

FF; suggesting again that its low PCE stems from problematic charge transport and extraction.

Another interesting observation noted with the Prato-DPP series was a decrease in EQE as the relative ratio of PDPP-2FT was increased (**Figure 3.22b**). This observation suggests that increasing the ratio of polymer to fullerene prevents the formation of domains needed for efficient charge transport.
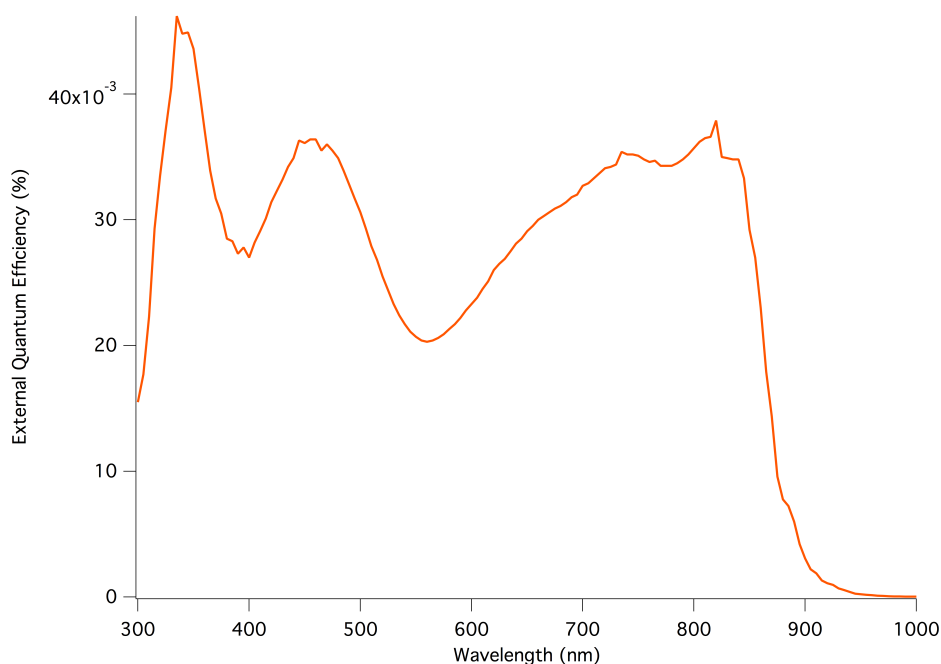
Figure 3.23: EQE of the PDPP2FT:PCB-TBTDT Blend

3.3.7   Summary of PDPP2FT:Fullerene-dye Adduct Blends

The PDPP2FT:fullerene-dye adduct blends represent an optically complementary system with the pendant dye filling the 400 nm - 650 nm optical gap in the absorption profile of the low band-gap PDPP2FT. The frontier orbital energies of this system indicate electron transfer from the polymer to the fullerene is possible, although the dyes' LUMO may

preclude it from mediating this process. Hole transfer from the fullerene to PDPP2FT vis-à-vis the dye is energetically favored, however. Bulk heterojunctions of the PDPP2FT:fullerene-dye adduct blends show no preferential ordering of their molecular assemblies in their as cast or annealed thin films and suggest a largely homogenous mixture with little evidence of donor or acceptor rich domains.

As previously mentioned in the sections detailing the P3HT blends, the problematic charge transport observed in the PDPP2FT:fullerene-dye adduct systems could be rooted in morphological phenomena. If the blends are unable to adopt morphologies favoring balanced carrier transport and uninhibited extraction, device performance could suffer. It can further be reasoned that if the amorphous PDPP2FT mixes more readily with the pendant dye of the fullerene-dye adduct than the fullerene to which its attached, the blend is likely to have interfaces where the polymer is prevented from direct contact with the fullerene core and is instead physically separated from the fullerene by the presence of the dye. Were electron transfer from PDPP2FT's LUMO to that of the dye energetically favored, it is likely that charges generated from the polymer's absorption of low energy photons would yield noticeable enhancements in the photocurrent corresponding to that region.

In spite of the possible morphological shortcomings of this system, in all cases it was observed that the pendant dyes from the fullerene-dye adducts were responsible for generating current in the regions corresponding to their n-π* transitions. PCEs notwithstanding, this result is important because it demonstrates that fullerene-dye adducts can indeed harvest photons which are inaccessible to certain low band-gap polymers. Further optimization of the processing conditions in the PDPP2FT blends could potentially render improvements in the PCEs and EQEs. A better understanding of how the processing

114

conditions affect the morphology of these systems could facilitate this objective. Conversely, this study may also highlight that PDPP2FT may not be an appropriate match for these dye adducts. A *p-type* material with a higher LUMO and a more controlled D:A interface could provide a viable alternative.

3.4 Benzoporphyrin:Fullerene-Dye Adducts

3.4.1 Optical Absorption of BP and the Fullerene Dye Adducts

A comparison of the optical absorption profiles of BP, PDPP2FT, P3HT, $PC_{71}BM$ and $PC_{61}BM$ is presented below in **Figure 3.24**. Because BP is insoluble in most organic solvents[18] its molar absorptivity could not be measured in solution. The molar extinction coefficient of BP was instead obtained via conversion of the linear extinction coefficient measured from its thin film absorption. BP's main absorption lies between 380 nm – 525 nm with $\varepsilon = 1.50 \times 10^5$ $M^{-1}cm^{-1}$ at $\lambda_{max} = 431$ nm. A smaller, lower energy band exists between 550 nm – 725 nm with a local maximum at $\lambda = 686$ nm with $\varepsilon = 8.06 \times 10^4$ $M^{-1}cm^{-1}$. In addition, BP's molar absorptivity is never lower than 1.50×10^4 $M^{-1}cm^{-1}$ from 300 nm – 700 nm, underscoring its strength as an absorber of visible light.
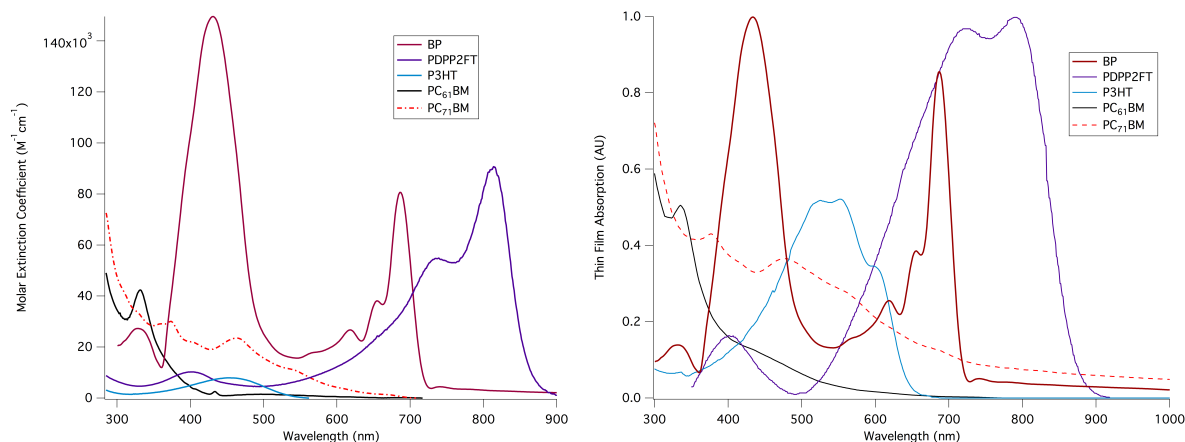
As illustrated in **Figure 3.25**, the π-π* transition of the TBTDT and DPP fullerene-dye adducts outperforms BP from 300 nm – 350 nm. Conversely, BP overwhelms the absorption of the TBTDT adducts n-π* transition from 400 nm – 550 nm. BP's absorptivity is also much higher than that of the DPP adducts' from 350 nm – 500 nm and 580 nm – 600 nm. However, the molar absorptivity of each DPP analogue is larger than that of BP for the optical window from 510 nm – 570 nm. Therefore, it is expected that among the BP:fullerene-dye adducts blends, PCB-DPP and Prato-DPP should show a measurable improvement in the photocurrent generated in this region.
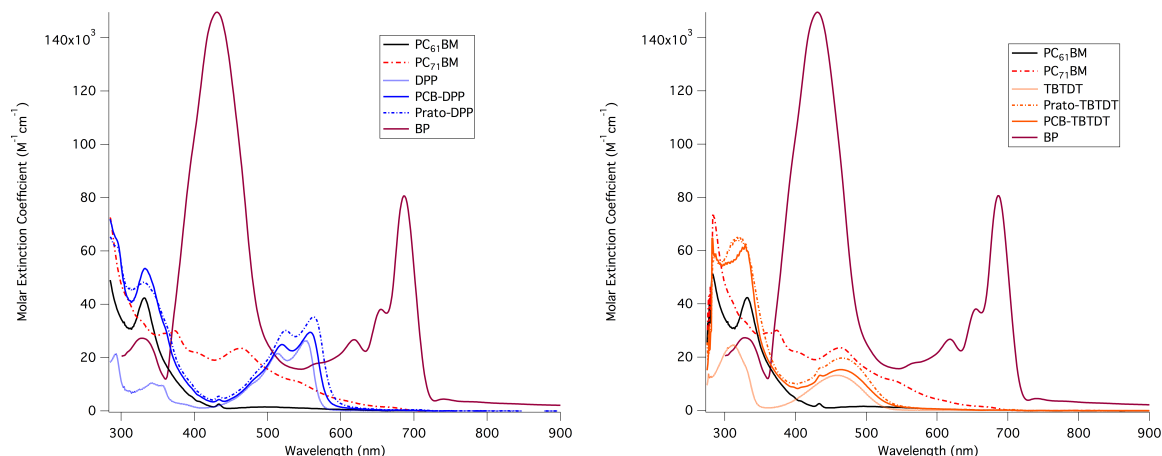
Figure 3.25: Molar Absorptivity of BP and the Fullerene-Dye Adducts

a. BP and the DPP series **b.** BP and the TBTDT series
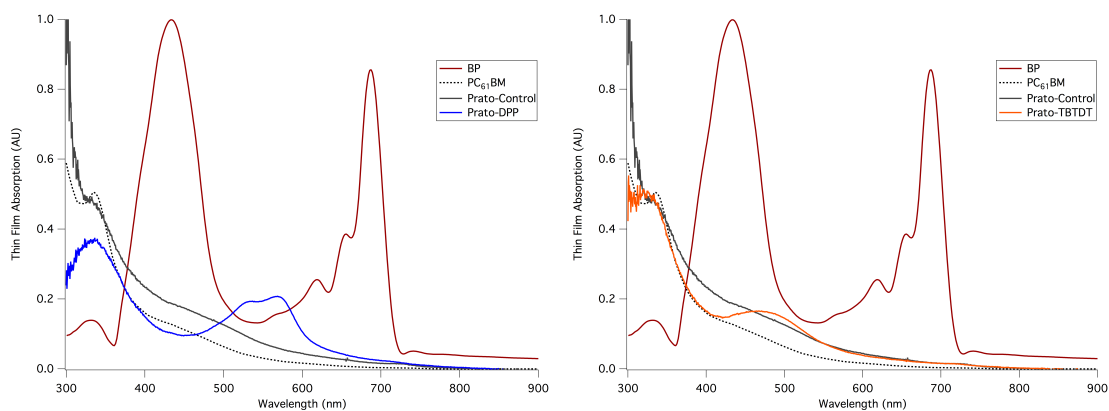
Figure 3.26: Thin Film Absorption of BP and the Fullerene-Dye Adducts

a. BP and the DPP series **b.** BP and the TBTDT series

Note: thin films were not measured on the same absorptivity scale

3.4.2 Frontier Orbital Alignment of BP and the Fullerene-Dye Adducts

The frontier orbital alignment of the BP:fullerene-dye adduct systems is depicted below in **Figure 3.27**. BP has a LUMO of -3.2 eV and a HOMO of -4.9 eV. The LUMO energy of BP provides a driving force for electron transfer to the LUMOs of both the dye and fullerene. In addition, BP can accept holes from both fullerene and pendant dye. In principle, the molecular electronics of this system should promote cascade electron and hole transfer between BP and the fullerene vis-à-vis the pendant dye. In contrast to the P3HT and PDPP2FT blends, BP offers a system that is optically complementary to the DPP adducts and electronically complementary to each of the fullerene-dye adducts. The results of their pairing will be described in the following sections.

117
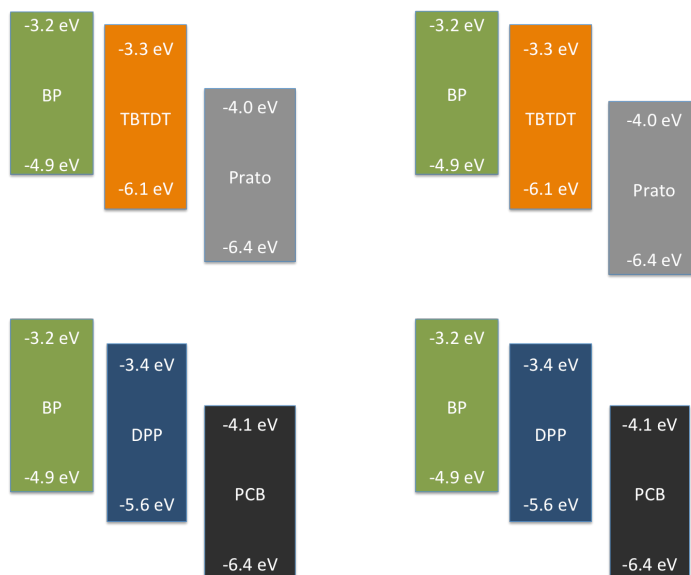
Figure 3.27: Frontier Orbital Alignment of BP:Fullerene-Dye Adduct Systems

3.4.3 Device Fabrication

Devices were fabricated via the following conditions: A solution of 2 wt. % CP, the soluble precursor to BP,[19] was prepared in 1:2 chloroform:chlorobenzene. The solution was filtered with a 0.2 um PTFE filter and 3 – 4 drops of solution were drop-cast onto PEDOT:PSS treated ITO. The BP film was spun cast at 1500 rpm for 30 sec. Subsequently, the substrates were annealed for 20 mins at 180˚C directly on a hotplate.

Following deposition of the donor layer, the acceptor layer was deposited. A 1.2 wt. % solution (12 mg/mL) in chlorobenzene was prepared for each fullerene and stirred for several minutes at 100˚C until solid particles of fullerene were no longer observable to the naked eye.

The solution was batch filtered using a 0.2 um PTFE filter. 3 - 4 drops were placed on the BP layer and the sample was spun cast at 1500 rpm for 60 seconds. The devices were made with the following configuration: ITO/PEDOT:PSS/BP/Fullerene/Al. The aluminum contacts

were deposited at 0.3 A/s for the first 10 nm and then gradually ramped to 2.3 A/s for the remaining 90 nm.

3.4.4 Morphology of BP:Fullerene-Dye Adduct thin films

The use of BP bilayer devices is a unique asset to investigations wishing to isolate the affects of morphology from device performance. Upon annealing, CP, the soluble precursor to BP, is converted into a rigid film of BP that can no longer be dissolved in common organic solvents. However, because the surface of BP is especially rough it affords more donor:acceptor interfaces than would be expected from a planar film. In this sense, BP's sawtooth bilayers serve as quasi-bulk heterojunctions with consistent microstructures for the *p-type* material and high thermal stability. This feature allows multiple fullerenes to be screened against BP, with the influence of morphology effectively decoupled from evaluations of their performance.
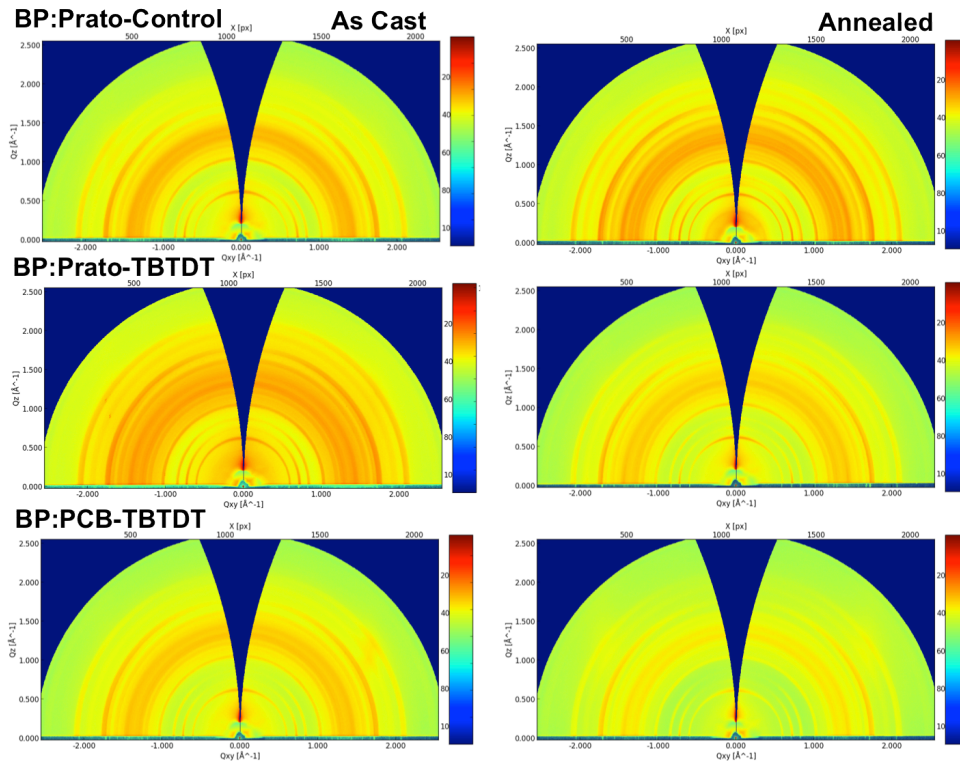
Figure 3.28: GIWAXS Images of BP:Fullerene-Dye Adduct Bilayers

3.4.5 Device results for BP:Fullerene-Dye Adduct Blends

Figure 3.29 depicts the JV plots of the BP:fullerene-dye adduct bi-layer devices. The results provided for each device were averaged from 2 cells with 5 pixels each. **Table 3.5** summarizes the device results for the thick and thin layers of the fullerene-dye adducts. As indicated above, a chief advantage of BP:fullerene bilayers is that they allow fullerenes to be analyzed independent of morphology. Therefore it is noteworthy that the $PC_{61}BM$ control device was the only device shown to perform better with a thicker layer of fullerene. The Prato-Control and TBTDT adduct devices all yielded better performing devices when thinner layers of fullerene were used. Bilayer devices showing a correlation between decreased performance and increased layer thickness, signal the PCE may have been limited by the carrier mobility through the modified film layer.[20]
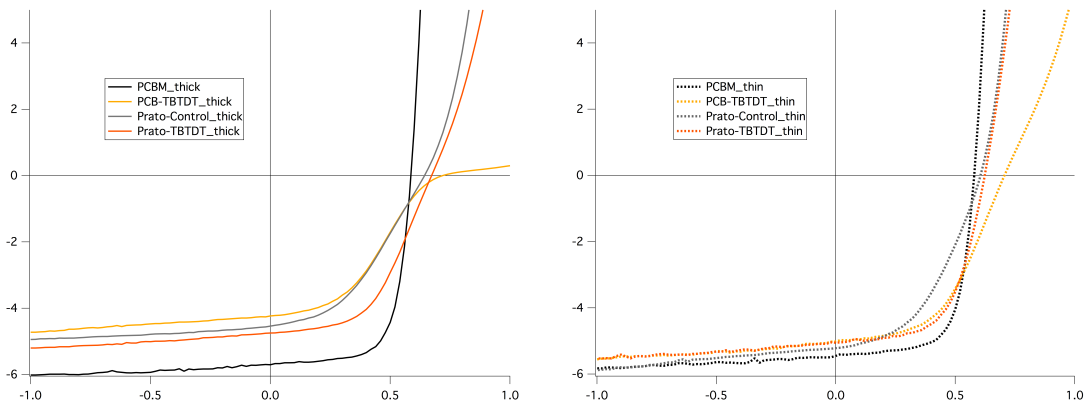
Figure 3.29: IV Plots for BP:Fullerene-Dye Adduct Bilayers.

a. bilayer OSCs with thicker fullerene layer. **b.** bilayer OSCs with thinner fullerene

layer.

System	V_{oc} (V)	J_{sc} (mA/cm^2)	FF	PCE
PC$_{61}$BM	0.58	-5.45	0.68	2.1%
PC$_{61}$BM*	0.58	-5.70	0.69	2.3%
PCB-TBTDT	0.70	-5.02	0.51	1.8%
PCB-TBTDT*	0.72	-4.23	0.38	1.2%
Prato-Control	0.60	-5.22	0.46	1.4%
Prato-Control*	0.64	-4.54	0.41	1.2%
Prato-TBTDT	0.62	-5.05	0.59	1.9%
Prato-TBTDT*	0.68	-4.75	0.51	1.6%

Table 3.5: Summary of the Device Results Obtained from the BP Bilayer Devices

(* denotes devices made with thicker fullerene layers)

It is also interesting that while the V_{oc}'s of the Prato adducts are equivalent within

experimental error (~0.60 V), the V_{oc} of PCB-TBTDT (0.70 V) is significantly larger than

that of PC$_{61}$BM (0.58 V). This result would suggest that given a uniform microstructure, the

V_{oc} of the Prato adduct is dictated by the Prato anchor itself rather than the dye. Under

analogous morphological constraints, however, the significant difference in V_{oc}'s measured for the BP:PCB bilayers indicates their internal cell bias is strongly influenced by the identity of the ester. In addition, the J_{sc} and FF of the BP:PC$_{61}$BM bilayers were higher than their counterparts. This observation implies that PC$_{61}$BM is better at transporting and extracting free-charge carriers than either the Prato-Control or the fullerene-dye adducts; further corroborating the assumption of mobility being the limiting factor in the Prato-Control and fullerene-dye adduct devices.

When the fullerene-dye adducts are assessed independent of morphology, relative to BP:PC$_{61}$BM bilayers, the PCEs of PCB-TBTDT and Prato-TBTDT are 78% and 81% of the PC$_{61}$BM control, respectively.

3.4.6 EQE of BP:Fullerene-Dye Adduct Blends

The EQEs and mean normalized EQEs of the bi-layer devices are shown below in **Figure 3.30**. The EQE of BP:PC$_{61}$BM was obtained from the thicker device, all others were obtained from the thinner devices. Although the photocurrents measured for Prato-Control, Prato-TBTDT, and PCB-TBTDT devices were lower than those of both PC$_{61}$BM devices, an interesting observation can be made with respect to the TBTDT adducts. In the region between 480 nm − 530 nm, the fullerene-dye adducts both show a relative enhancement in EQE that is not observed in the fullerenes without dyes.
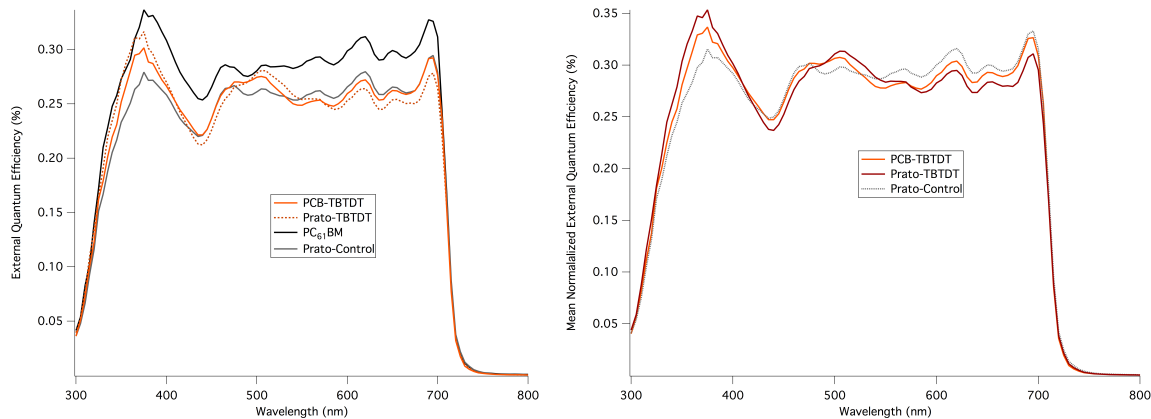
Figure 3.30: EQEs of BP:Fullerene-Dye Adduct Devices

a. unnormalized EQE **b.** mean normalized EQE

3.4.7 Summary of BP:Fullerene-Dye Adduct Bilayers

The BP:fullerene-dye adduct bilayers represent a system that is optically complementary for the DPP adducts, with the pendant DPP partially filling the optical gap in BP's absorption from $500-600$ nm. The BP:TBTDT adducts are not optical complements to BP, as their molar absorptivities are shadowed by BP's visible absorption. The frontier orbital energies of the BP:fullerene-dye adduct systems are compatible, indicating charge transfer from BP to the fullerene may be mediated vis-à-vis the dye. Use of BP bilayers allowed the fullerenes to be examined in a quasi-bulk heterojunction where the self-assembly of the donor layer was unaffected by the assembly behavior of the fullerene-dye adduct. This feature allows the fullerene-dye adducts to be investigated independent of their influence on microstructure.

Apart from the BP:PC_{61}BM control device, all other BP:fullerene-dye adduct bilayers were found to show better performance in devices with thinner layers of fullerene. This observation indicates that the mobility of the fullerene-dye adducts is a limiting factor and

becomes increasingly problematic as the thickness of the fullerene layer is increased. The geometric obstacle precluding pi-stacking of the pendant dyes may inhibit the hole mobility through the fullerene layer and could offer one plausible explanation to this behavior. In addition, the presence of the pendant dye significantly affected the V_{oc} of the PCB series more than the Prato series. It is currently unclear why the identity of the anchoring unit would influence the internal cell bias to this extent. Nevertheless, the PCEs of the BP:fullerene-dye bilayers were closer to the PCEs of the BP:PC$_{61}$BM control devices than observed in the P3HT or PDPP2FT systems.

EQEs of the BP bilayers showed an enhancement in the photocurrent from 480 nm – 530 nm for the TBTDT adducts. It is further believed that the DPP adducts would show yield a greater improvement in photocurrent, although the hole mobility through the fullerene layer could limit this effect.

3.6 References

1.

Wang, M.; Chesnut, E.; Sun, Y.; Tong, M.; Guide, M.; Zhang, Y.; Treat, N. D.; Varotto, A.; Mayer, A.; Chabinyc, M. L.; Nguyen, T.-Q.; Wudl, F.; *J. Phys. Chem*. C **2012**, *116*, 1313

2.

Guide, M.; Pla, S.; Sharenko, A.; Zalar, P.; Fernández-Lázaro, F.; Sastre-Santos, Á.; Nguyen, T.-Q.; *Phys. Chem. Chem. Phys.,* **2013**, *15*, 18894

Woo, C. H.; Beaujuge, P. M.; Holcombe, T. W.; Lee, O. P.; Fréchet, J. M. J.; *JACS* **2010**, *132*, 15547

3.

Bundgaard, E.; Krebs, F. C. *Solar Energy Materials & Solar Cells* **2007**, *91*, 954

4.

Koch, F. P. V. Silva, C.; Salleo, A.; Nelson, J., Smith, P., Stingelin, N.; *Progress in Polymer Science* **2013**, *38,* 1978

5.

Gao, Y.; Martin, T. P.; Niles, E. T.; Wise, A. J.; Thomas, A. K.; Grey, J. K.; *J. Phys. Chem. C,* **2010***, 114,* 15121

6.

Treat, N. D.; Varotto, A.; Takacs, C. J.; Batara, N.; Al-Hashimi, M.; Heeney, M. J.; Heeger, A. J.; Wudl, F.; Hawker, C. J.; Chabinyc, M. L.; *JACS* **2012**, *134*, 15869

7.

Treat, N. D.; Brady, M. A.; Smith, G.; Toney, M. F.; Kramer, E. J.; Hawker, C. J.; Chabinyc, M. L.; *Adv. Energy Mater.* **2011**, *1*, 82

8.

Savenije, T. J.; Kroeze, J. E.; Yang, X.; Loos, J.; *Thin Solid Films* **2006**, 2-6, 512

Turner, S. T.; Pingel, P.; Steyrleuthner, R.; Crossland, E. J. W.; Ludwigs, S.; Neher, D.*; Adv. Funct. Mater.* **2011**, *21*, 4640

Kniepert, J.; Lange, I.; Kaap, N. J.; Koster, L. J. A.; Neher, D.; *Adv. Energy Mater.* **2014**, *4*, 1301401

Bagui, A.; Iyer, S. S. K.; *Organic Electronics*, **2014**, *15*, 1387

9.

Treat, N. D.; Shuttle, C. G.; Toney, M. F.; Hawker, C. J.; Chabinyc, M. L.; *J. Mater. Chem.*, **2011**, *21*, 15224

Treat, N. D.; Brady, M. A.; Smith, G.; Toney, M. F.; Kramer, E. J.; Hawker, C. J.; Chabinyc, M. L.; *Adv. Energy Mater.* **2011**, *1*, 82

11.

Wienk, M.; Kroon, J. M.; Verhees, W. J. H.; Knol, J.; Hummelen, J. C.; Hal, P.A.; Janssen, R. A. J. *Angew. Chem. Int. Ed.* **2003**, *42*, 3371

12.

Woo, C. H.; Beaujuge, P. M.; Holcombe, T. W.; Lee, O. P.; Fréchet, J. M. J.; *J. AM. CHEM. SOC.* **2010**, *132*, 15547

13.

Robb, M. J.; Montarnal, D. M.; Eisenmenger, N. D.; Ku, S.-Y.; Chabinyc, M. L.; Hawker, C. J.; *Macromolecules* **2013**, *46*, 6431

Woo, C. H.; Beaujuge, P. M.; Holcombe, T. W.; Lee, O. P.; Fréchet, J. M. J.; *JACS* **2010**, *132*, 15547

14.

Woo, C. H.; Beaujuge, P. M.; Holcombe, T. W.; Lee, O. P.; Fréchet, J. M. J.; *JACS* **2010**, *132*, 15547

15.

Li, W.; Hendriks, K. H.; Furlan, A.; Roelofs, W. S. C.; Meskers, S. C. J.; Wienk, M. M. W.; Janssen, R. A. A. J.; *Adv. Mater.* **2014**, *26*, 1565

Chen, M. S.; Lee, O. P.; Niskala, J. R.; Yiu, A. T.; Tassone, C. J.; Schmidt, K. S.; Beaujuge, P. M.; Onishi, S. S.; Toney, M. F.; Zettl, A.; Fréchet, J. M. J.; *J. Am. Chem. Soc*. 2013, *135*, 19229

16.

Qi, B.; Wang, J.; *Phys. Chem. Chem. Phys.* **2013**, *15*, 8972

17.

Günes, S.; Neugebauer, H.; Sariciftci, N. S.; *Chem. Rev*. **2007**, *107*, 1324

18.

Ku, S.-Y.; Liman, C. D.; Cochran, J. E.; Toney, M. F.; Chabinyc, M. L.; Hawker, C. J.; Adv. Mater. **2011**, *23*, 2289

19.

Guide, M.; Pla, S.; Sharenko, A.; Zalar, P.; Fernández-Lázaro, F.; Sastre-Santos, Á.; Nguyen, T.-Q.; *Phys. Chem. Chem. Phys.* **2013**, *15*, 18894

20.

Wang, M.; Chesnut, E.; Sun, Y.; Tong, M.; Guide, M.; Zhang, Y.; Treat, N. D.; Varotto, A.; Mayer, A.; Chabinyc, M. L.; Nguyen, T.-Q.; Wudl, F.; *J. Phys. Chem. C* **2012**, 116, 1313

Chapter 4

Investigation of the Thermal Behavior, Morphological Stability, and Operational Lifetime of

Organic Solar Cells Prepared from P3HT:PC$_{61}$BM:PCB-F Mixed Fullerene Ternary Blends

4.1 Introduction

Recent progress in organic photovoltaics (**OPVs**) has spurred the development of organic solar cells (**OSCs**) surpassing the 10% power conversion efficiency (**PCE**) benchmark commonly cited as their threshold for commercially viability.[1] As a result of these advancements, the field has witnessed a notable shift in focus beyond simply improving efficiency, towards exploring deeper issues in OPVs which pose additional barriers to market entry.[2] Notably, challenges associated with extending the operational lifetime of OSCs have received particular attention because of their commercial implications. A solar cell which experiences a rapid decline from 10% PCE after only several hours of operation would be impractical for use in consumer products. The importance of overcoming this obstacle cannot be undervalued, and it remains a principle topic for the organic electronics community to tackle moving forward.[3] Therefore, efforts in pursuit of clarifying the root causes of device instability and improving upon the ability to rationally prolong the lifespan of OSCs are paramount.

A number of underlying issues within OSCs have been linked to PCE degradation. For example, several studies have shown that the intrusion of trace oxygen and water may accelerate PCE losses.[4] A correlation between stressors to the top contacts and lowered operational lifetimes has also been observed.[5] In addition, the intrinsic instability of

PEDOT:PSS has proven to be problematic for long-term device stability.[6] Interestingly, in some cases even extended light irradiation has been implicated in accelerated degredation.[7] However, it is especially well documented that changes within the active layer's microstructure, which evolve over time, play a central role in observations of reduced efficiency as OSCs age.[8]

An evolution in bulk morphology over time is especially evident in OSCs which utilize bulk heterojunctions (**BHJs**). Possessing polycrystalline and amorphous materials that self-assemble into interpenetrating networks of donor rich domains, acceptor rich domains, and homogeneously mixed donor/acceptor domains, these active layers are inherently disordered and less stable as a result.[9] In addition, solar cells incorporating organic semiconductors with low thermal transitions present an extra layer of complexity. Blends with T_gs and T_ms below ceiling temperatures utilized for device processing or practical operation are particularly problematic, as their thin films are more susceptible to morphological changes that may occur at elevated temperatures. For example, roll-to-roll printing techniques adopted to remove excess processing solvents typically employ multiple annealing steps, each of which can induce transformations in the active layer's morphology.[10] By the same logic, low T_g polycrystalline active layers share a capacity to reorganize in OSCs operating outside on a hot summer day. In many cases, observations of decreased device performance as a function of time trace their origin to the physical consequences of transient bulk microstructures. Furthermore, declines in PCE are often noted within minutes of initial measurements of device performance.[11]

Numerous investigations exploring the relationship between device performance and morphology changes have identified fullerene acceptors as a primary antagonist.[12] A general

observation emerging from several independent studies is that fullerenes are prone to diffuse over time, leading to growth of large fullerene crystallites; a physical phenomenon that tends to coincide with decreased device performance.[13] There are several rational reasons for this behavior. X-ray analysis of unannealed thin films prepared from binary polymer/fullerene blends confirm that upon deposition, these blends typically assemble into morphologies where fullerenes reside within disordered, amorphous regions.[14] These initial morphologies are not necessarily permanent, however. In comparison to conjugated polymers, the small size of fullerenes affords them molecular mobility throughout disordered bulk systems. On account of their capacity for diffusion through amorphous domains, thermal treatment of these thin films may accelerate transformations in fullerene assembly within the bulk.[15] These structural evolutions may also occur at lower temperatures; although the timescale for said changes would be longer.[16] A general correlation can therefore be drawn between fullerene diffusion and the microstructural evolution of the active layer.

Aggressive annealing conditions mimicking the effects of accelerated aging further substantiate the culpability of transient fullerene aggregates in observations of time-dependent PCE degradation. A typical consequence of fullerene diffusion is an increase in the number of nucleation sites that initiate the propagation of fullerene crystallization.[17] Binary P3HT:PC$_{61}$BM BHJs clearly show the emergence of large fullerene crystallites, even within 10 minutes of heating.[18] In fact, many of the crystallites that form are macroscopic in size and can be observed with the naked eye. In addition, despite evidence of elevated annealing procedures encouraging the assembly of donor polymers into morphologies more optimal for charge transport, OPV processing protocols typically limit annealing to five minutes at 150 ˚C to avoid fullerene crystallization and its associated drawbacks.[19]

Several research efforts have explored various methods aimed at stabilizing the microstructure of bulk heterojunctions. For example, conjugated polymers decorated with crosslinking pendants have been investigated as an approach for cementing favorable bulk morphologies via UV irradiation.[20] Polymers with acid and thermocleavable side chains have also been examined for their potential to enhance morphological stability post-processing.[21] Studies exploring the use of block copolymers to template self-assembly and control morphology have been reported as well.[22] Recently, however, several novel OPV studies have emerged which exploit the behavior of fullerenes to address problems associated with morphological instability.

In an investigation motivated by the ability of chemical impurities to modify crystallization behavior, Pozzo and coworkers demonstrated that inclusion of C_{60} into P3HT:$PC_{61}BM$ blends could arrest $PC_{61}BM$ crystallization at feed ratios of 50 wt.% C_{60}.[23] Inspired by these results, research efforts led by the Müller group confirmed the potential of mixed fullerene ternary blends to prevent premature crystallization, hypothesizing their observations stemmed from the capacity of mixed fullerenes to impede fullerene nucleation events.[24] The McCulloch and Chabinyc groups also showed that use of multifullerene ternary blends could lengthen the lifespan of an OSC.[25] Furthermore, their studies illustrated the enhanced stability was attributed to suppression of fullerene crystallization rather than differences in fullerene miscibility.

To date, reports demonstrating the advantages of ternary blends in extending OSC operational stability have chiefly employed fullerenes that were similar in chemical structure and behavior; yielding marginal influence over bulk morphology beyond suppression of fullerene crystallization. Although this strategy has its merits, it is also of interest to explore

131

systems which program additional handles of control over molecular self-assembly. The incorporation of chemically distinct fullerenes with orthogonal blending behaviors is an approach, which, in principle, could be utilized to enhance the ability to direct ternary blend self-assembly towards thin film architectures consistent with reports of prolonged OSC lifetime. This method could prove useful for investigations of ternary blends; establishing the degree to which trends in morphological and device stability hold true for blending strategies which advance the capacity for rational influence over bulk microstructure.

Numerous reports of organic semiconducting systems incorporating perfluorinated materials have highlighted the general utility of their inclusion as a vehicle for enhancing self-assembly.[30] The basis for this behavior can be traced to the propensity of perfluorinated groups to migrate towards the air interface, on account of fluorine's characteristically low surface energy with air. The subsequent influence of this migration on the anisotropy of bulk molecular assemblies has proven beneficial in a number of cases.[31] For instance, this strategy has led to observations of improved efficiency in inverted solar cells using perfluorinated materials as a substitute for PEDOT:PSS.[32] These examples underscore how phase-segregation of perfluorinated groups towards the air-interface yields a surface dipole which may induce favorable modifications to the work functions of certain contact electrodes, improving upon an otherwise limited capacity for injection of appropriate free-charge carriers.[33] Incorporation of perfluorinated fullerenes into standard solar cell architectures has also been explored as an approach for inducing self-assembled, de-facto electron transporting layers.[34] Evidence of favorable bulk morphologies stemming from perfluorinated phase-segregation is generally noted via tangible benefits to charge transport and extraction; empirically observed as statistically significant improvements in J_{sc}, FF, and R_s. The use of

fullerenes modified with perfluorinated groups therefore presents a viable approach for screening the affects of enhanced self-assembly on the operational lifetime of OSCs prepared from ternary blends.

To investigate the morphological and electronic stability of ternary blend devices utilizing two chemically distinct fullerenes with enhanced phase-segregation, a series of ternary blends based on P3HT:$PC_{61}BM$:PCB-F were prepared (**Figure 4.1**). The absolute ratio of P3HT:fullerene was held constant in these devices, while the relative ratios of each fullerene were systematically varied. As indicated above, reports detailing the tendency of perfluorinated fullerenes to phase-segregate from $PC_{61}BM$ suggested PCB-F would be an optimal material for introducing greater influence over the bulk morphology of ternary blends.[35] Moreover, because PCB-F has identical frontier orbital energies as $PC_{61}BM$, its use presented a control for molecular electron affinity. In principle, this feature would allow the interpretation of emerging trends in the electronic behavior of the blends to be simplified and unambiguously attributed to the chemical identity of the perfluorinated tail rather than the LUMO of the fullerene core itself. It was therefore of interest to explore the general applicability of ternary blends for prolonging the morphological stability and device lifetime of OSCs through use of a blending strategy where enhancements in self-assembly could be rationally dialed-in.
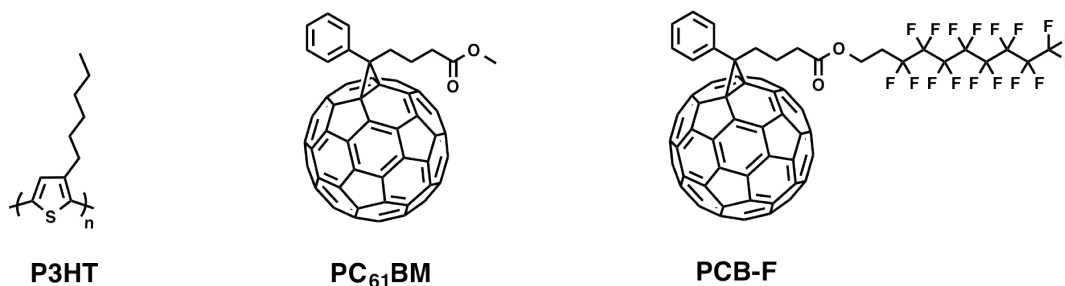
Figure 4.1: Chemical structures of P3HT, PC$_{61}$BM, and PCB-F

This chapter will investigate the thermal behavior and self-assembly of P3HT:PC$_{61}$BM:PCB-F ternary blends, systematically varying the relative ratios of PC$_{61}$BM:PCB-F to rationalize the influence of their chemical identity and blending properties on trends observed in the morphological stability and operational lifetime of their corresponding OSCs. First, a study contrasting the thermal behavior of PC$_{61}$BM:PCB-F binary blends with P3HT:PC$_{61}$BM:PCB-F ternary blends will be presented. Analysis of these two systems will clarify the chemical origin of thermal trends emerging from the introduction of perfluorinated pendants. The effects of thermal processing on the self-assembly of P3HT:PC$_{61}$BM:PCB-F blends will then be described through analysis of their thin film morphologies via optical microscopy and GIWAXS measurements. This behavior will in turn be discussed through the context of DSIMS measurements collected to analyze their vertical molecular profiles. Finally, a device study of these ternary blends will be presented to rationalize the influence of blend composition, self-assembly, and thermal processing on the electrical behavior and operational lifetime of OSCs. The results of this investigation are anticipated to shed light on the potential for ternary blends with enhanced self-assembly to extend morphological and electronic stability to OPV devices. The global objectives of this study are to add clarity to future decisions in choice of fullerenes for ternary blends, and to

further improve upon the ability to rationally design fullerenes which target desirable materials properties in blended bulk systems.

4.2 Differential Scanning Calorimetry of Binary and Ternary Blends

4.2.1 Sample Preparation

The thermal behavior of binary $PC_{61}BM:PCB-F$ and ternary $P3HT:PC_{61}BM:PCB-F$ blends was analyzed via DSC. The samples were prepared by drop-casting solutions of each blend into the center of a dimpled petri dish, where they were allowed to slowly evaporate in air until thoroughly dry. The resulting glassy films were removed from the petri dish with a spatula, weighed, and transferred to T-zero pans for analysis. On average, 3-7 mg of the drop cast films were recovered by this method: note, each solution was prepared using 10 mg of fullerene. The samples were subjected to three sequential heat-cool scans from 25 ˚C to 325 ˚C at a temperature ramp of 10 ˚C/min with a three minute isothermal step included at each end point. Analysis was performed under an inert N_2/He atmosphere. The second heat-cool scan is depicted in the thermograms detailed below.

4.2.2 Thermal Behavior of the PC$_{61}$BM:PCB-F Binary Blends

PC$_{61}$BM (mg)	PCBF (mg)	PC$_{61}$BM Cold Cryst.	PC$_{61}$BM Melt	Hybrid Melt 1	Hybrid Melt 2	Hybrid Cryst.
10	0	182.5	284.5	-	-	-
9	1	179	266.5	275	-	-
8	2	174.5	264.5	279.5	298	-
7	3	172.5	265	280	301	-
6	4	-	-	283	304	241
5	5	-	-	-	304	250
4	6	-	-	-	305	254
3	7	-	-	-	303	270
2	8	-	-	-	303	242.5
1	9	-	-	-	-	-
0	10	-	-	-	-	-

Table 4.1: Thermal Transitions of the PC$_{61}$BM:PCB-F Binary Blends

Analysis of the binary blend heating cycles highlights several interesting thermal features (**Table 4.1, Figures 4.2 – 4.3**). In the given thermal window, pristine PC$_{61}$BM shows a cold crystallization endotherm during heating while pristine PCB-F sample does not demonstrate such behavior. Cold crystallization of PC$_{61}$BM is a well documented phenomenon that refers to an endothermic rearrangement of PC$_{61}$BM at elevated temperatures that coincides with the formation of a periodic crystal structure.[36] This cold crystallization is observed in the blends from 10:0 PC$_{61}$BM:PCB-F to 7:3 PC$_{61}$BM:PCB-F. Moreover, a decrease in cold crystallization temperature from 182.5 ˚C to 172.5 ˚C is noted as the feed ratio of PCB-F is increased. This behavior indicates that as the fraction of PCB-F is increased, PC$_{61}$BM achieves this endothermic structural rearrangement at increasingly lower temperatures. Interestingly, the cold crystallization of PC$_{61}$BM is no longer observed at ratios of 6:4 PC$_{61}$BM:PCB-F to 0:10 PC$_{61}$BM:PCB-F.

Following cold crystallization, pristine $PC_{61}BM$ shows an exothermic melt at 284 ˚C. The small fraction of PCB-F in the 9:1 $PC_{61}BM$:PCB-F blend is enough to disrupt this behavior, and the emergence of two lower temperature melts is observed at 266.5 ˚C and 275 ˚C, respectively. Neither of these peaks are directly attributed to PCB-F, as the pristine PCB-F heat scan exhibits no identifiable exothermic behavior; indicating either a lack of PCB-F crystals to melt or a T_m that falls outside of the measured thermal window. However, the temperature and sharpness of the first exotherm strongly suggests it correlates to pristine $PC_{61}BM$ crystallites that have been reduced in size. Analysis of the 9:1 $PC_{61}BM$:PCB-F heat scan therefore indicates that inclusion of PCB-F prompts the formation of an independent domain that may be distinguished from pristine $PC_{61}BM$. The fact that there are two distinguishable exotherms suggests that while the original $PC_{61}BM$ crystal structure is preserved to a degree, it coexists with a distinct, ordered hybrid-fullerene domain that forms separately.

At ratios of 8:2 and 7:3 $PC_{61}BM$:PCB-F, this first melt (attributed to $PC_{61}BM$) remains stationary as the second melt appears to shift toward higher temperatures, with both exotherms broadening in appearance. Moreover, beyond 7:3 $PC_{61}BM$:PCB-F, $PC_{61}BM$'s cold crystallization and melt disappear while the second hybrid-exotherm continues to broaden. This thermal behavior indicates that while the presence of distinct ordered fullerene domains may originate from the inclusion of PCB-F, beyond a certain PCB-F wt.% threshold, their boundaries may become indistinguishable. In addition, between 7:3 and 2:8 $PC_{61}BM$:PCB-F, a second hybrid melt appears to remain stationary, noticeably sharpening in appearance at 4:6 and 3:7 $PC_{61}BM$:PCB-F before completely disappearing after 2:8 $PC_{61}BM$:PCB-F. This

feature seems to indicate an equilibrium has been reached between 4:6 and 3:7 PC$_{61}$BM:PCB-F, which allows another separate and distinct hybrid-fullerene domain to exist.

The cooling cycles of the binary blends are also telling. From 10:0 to 7:3 PC$_{61}$BM:PCB-F, a broad indistinct exotherm is observed. This thermal behavior is suggestive of a disorganized process of fullerene self-assembly that yields energetically frustrated isotropic domains. Between 6:4 and 2:8 PC$_{61}$BM:PCB-F, sharper exotherms are noted on the cooling cycle. Incidentally, the emergence of these exotherms coincides with the disappearance of PC$_{61}$BM's cold crystallization and melt after 7:3 PC$_{61}$BM:PCB-F. This lends further weight to the hypothesis of emerging PC$_{61}$BM:PCB-F hybrid-fullerene domains that reaches equilibrium between 4:6 and 3:7 PC$_{61}$BM:PCB-F. Pristine PCB-F is observed to remain completely amorphous in the thermal windows of examined.
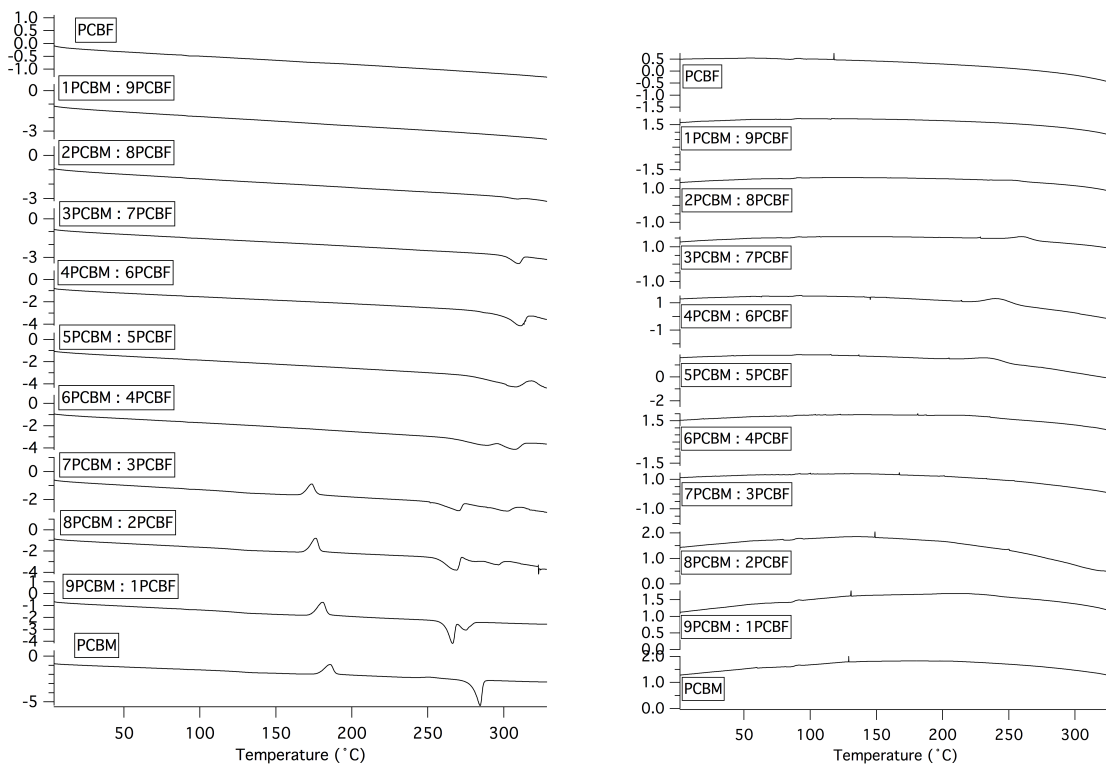
Figure 4.2: Second Cycle Thermograms of PC$_{61}$BM:PCB-F Binary Blends.

138
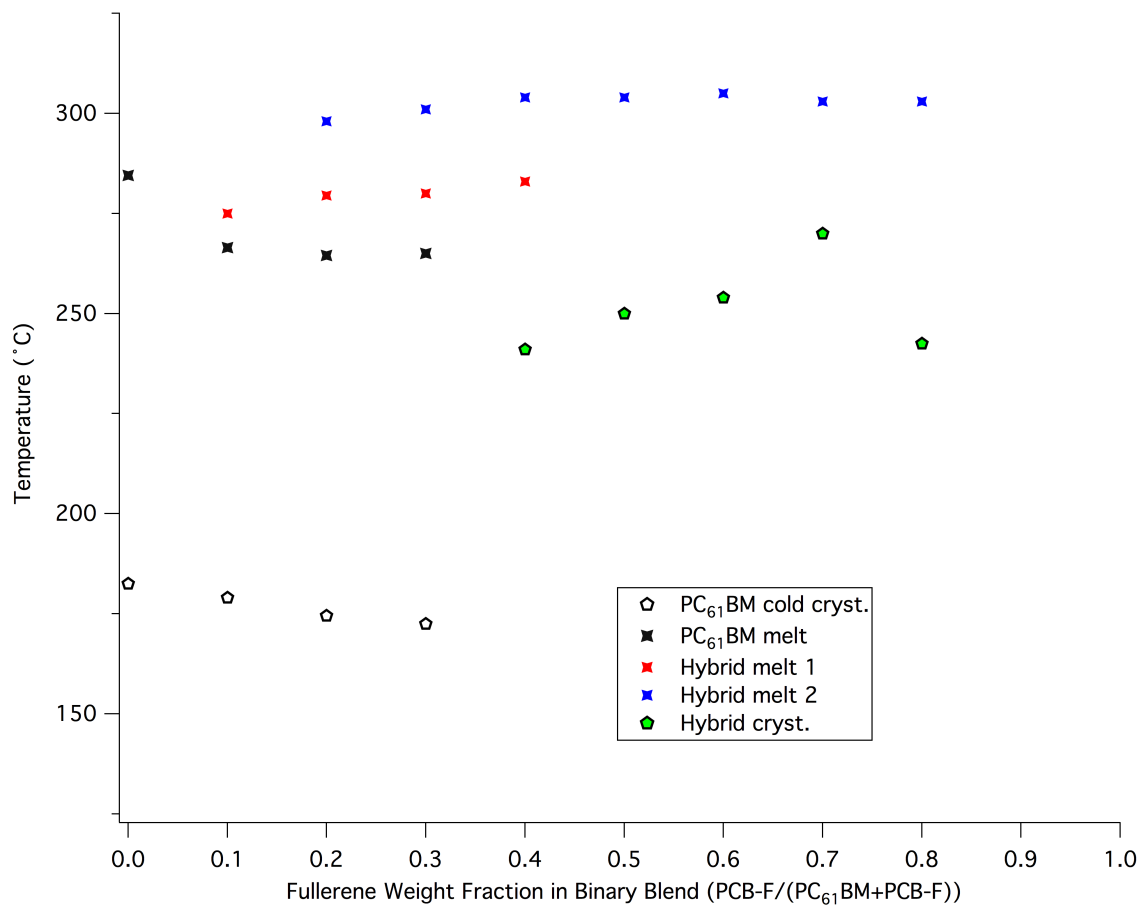
Figure 4.3: Thermal Transitions of $PC_{61}BM$:PCB-F Binary Fullerene Blends

4.2.3 Thermal Behavior of the P3HT:PC$_{61}$BM:PCB-F Ternary Blends

P3HT (mg)	PC$_{61}$BM (mg)	PCB-F (mg)	P3HT Melt	Melt 2	P3HT Cryst	Blend Cryst
9	0	0	235	-	195	-
5	4	0	-	200	-	-
5	3.6	0.4	-	200	-	-
5	3.2	0.8	-	200	-	-
5	2.8	1.2	-	210	-	155
5	2.4	1.6	-	200	-	-
5	2	2.0	-	200	-	-
5	1.6	2.4	-	200	-	-
5	1.2	2.8	-	202	-	-
5	0.8	3.2	-	200	-	-
5	0.4	3.6	-	200	-	-
10	0	4	-	202	-	-

Table 4.2: Thermal Transitions of the PC$_{61}$BM:PCB-F Binary Fullerene Blends

Examination of the thermal behavior of the ternary blends underscores a number of interesting interactions (**Table 4.2, Figures 4.4 – 4.5**). Pristine P3HT produces a sharp exotherm at 235 ˚C on the heating scan and a sharp endotherm at 195 ˚C on the cooling scan corresponding to its melt and crystallization, respectively. However, P3HT's melt shifts to cooler temperatures in each of the blends, a result which indicates P3HT's crystallization process is frustrated by the presence of fullerene. In addition, the cold crystallization and melt typically associated with PC$_{61}$BM are no longer observed in any of the blends, suggesting P3HT chains induce an equally disruptive effect on PC$_{61}$BM nucleation, therein retarding the onset of its crystallization.

The cooling scan of binary P3HT:PC$_{61}$BM shows a large broad endotherm, suggesting many arrangements of P3HT:PC$_{61}$BM aggregates exist and that their assembly into lower energy macromolecular conformations is frustrated by the global disorder of the system. Similar behavior is observed for binary P3HT:PCB-F. In general, these thermal profiles speak to the inherent disorder of conjugated polymer/fullerene blends and their interpenetrating networks.

Each of the P3HT:PC$_{61}$BM:PCB-F ternary blends show broadening of P3HT's melt as well as a down-shift in its temperature. This phenonenon is believed to indicate the presence of smaller P3HT crystalline domains within the blend, relative to pristine P3HT. Broad endothermic behavior is also observed on the cooling cycles across the majority of ternary blend compositions; a feature that is consistent with the molecular disorder of bulk heterojunction systems. Interestingly, however, the P3HT:PC$_{61}$BM:PCB-F blend with 7:3 PC$_{61}$BM:PCB-F maintains a more distinct melting exotherm (210 ˚C) than the other blend ratios. In addition, its cooling scan also shows a sharper crystallization endotherm than either of the blends, including binary P3HT:PC$_{61}$BM and P3HT:PCB-F. Although this DSC experiment leaves room for interpreting the source of this particular thermal transition, it is reasonable to assume this particular blend composition induces the assemblage of P3HT domains with a higher degree of long range ordering. The other ternary blend compositions do not suggest a similar level of molecular ordering is achieved, as their broad endotherms lack a comparable level of definition.
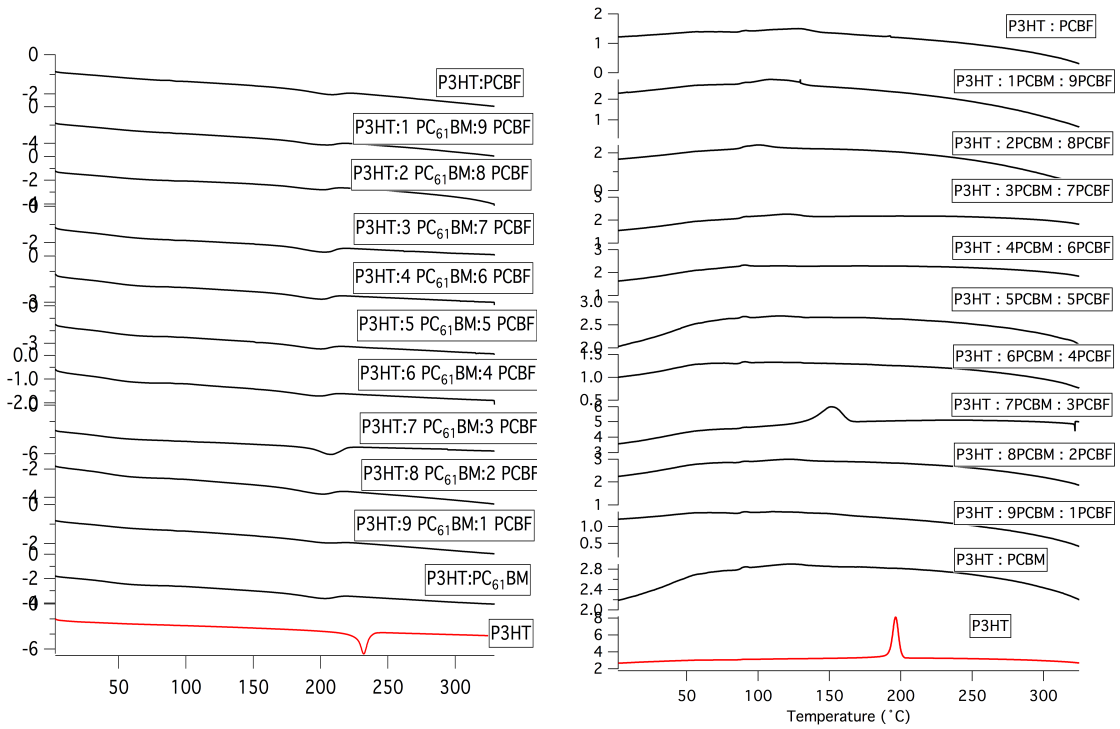
Figure 4.4: Second Cycle Thermograms of P3HT:PC$_{61}$BM:PCB-F Ternary Blends

a. heating scan **b.** cooling scan
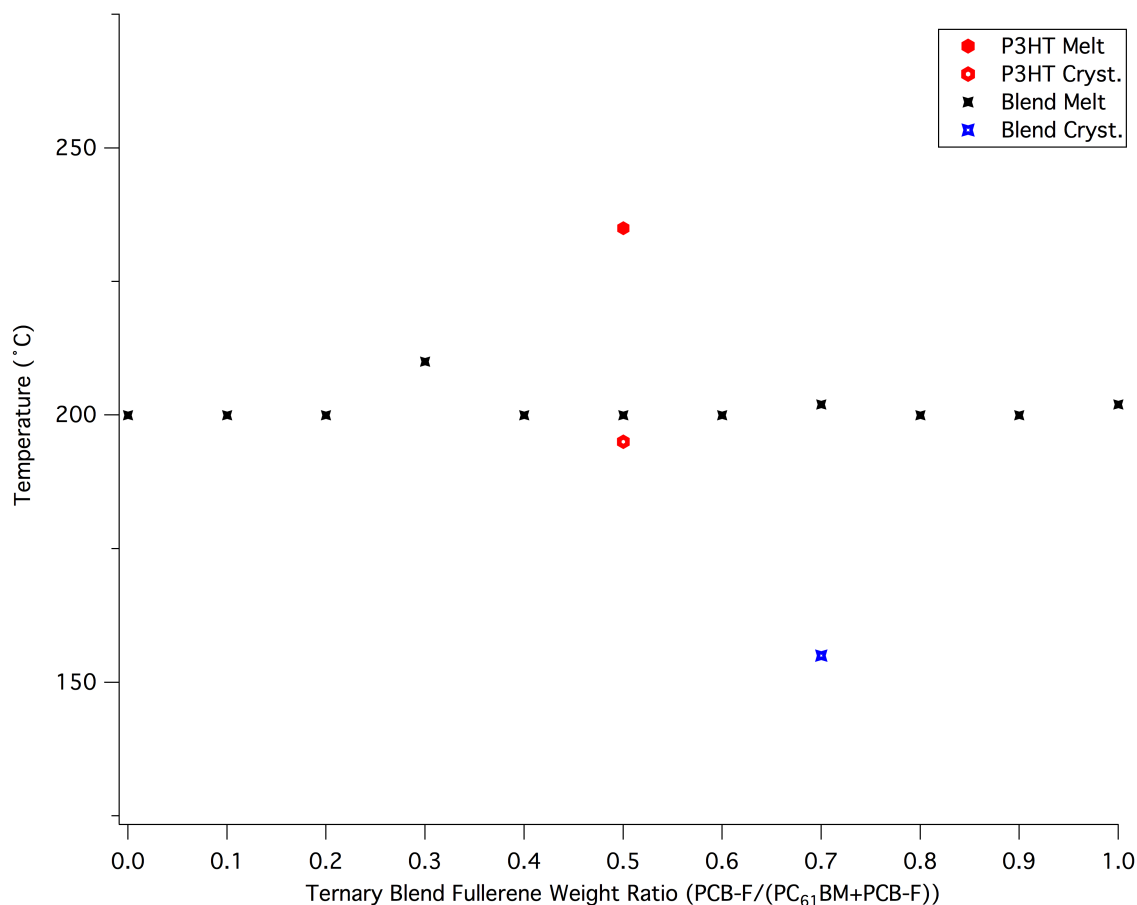
Figure 4.5: Thermal Transitions of P3HT:PC$_{61}$BM:PCB-F Ternary Blends

4.3 Optical Microscopy of Binary and Ternary Blends

4.3.1 Sample Preparation

Doped native oxide silica substrates (1.5 cm x 1.5 cm) were sonicated sequentially in acetone, 5% soap/deionized water (**DI water**) solution, DI water, and 2-isopropyl alcohol (**IPA**) for 30 minutes each and dried with N$_2$ airgun. The silica substrates were then plasma cleaned for 2-3 minutes using O$_2$ as the flow gas immediately prior to deposition of PEDOT:PSS. PEDOT:PSS (Clevios PVP Al 4083) was spun-cast at 4000 rpm for 1 minute

and annealed at 155 ˚C for 30 minutes. Annealed Silica/PEDOT:PSS films were then transferred into the glovebox.

The ternary blend solutions were prepared in a N_2 atmosphere glovebox with 0.3 mL of *ortho*-dichlorobenzene (**o-DCB**), heated to 80 ˚C, and stirred overnight. The ternary blends were filtered with 0.45 μm PTFE filters prior to their deposition onto the ITO/PEDOT:PSS substrates. The ternary blend active layers were then were spun-cast in two sequential steps; 550 rpm for 1 minute, 2000 rpm for 1 second. The substrates were subsequently annealed on a hotplate at 150 ˚C in air for the time periods indicated.

4.3.2 Annealing Study of Ternary Blend Thin Films

In order to examine the effects of annealing on the surface morphologies of the various blend compositions, the P3HT:PC$_{61}$BM:PCB-F ternary blend thin films were periodically monitored via reflection microscopy at the time intervals indicated. As previously described, the process of fullerene diffusion through disordered blends typically coincides with the formation of fullerene crystalline domains.[37] **Figure 4.6** depicts images of P3HT:PC$_{61}$BM binary blends under extended annealing conditions which clearly confirm the formation of such crystals. Within 10 minutes of annealing at 150 ˚C, crystallites nearly 50 microns in length are readily observed. After an hour of annealing, fullerene crystallites measuring over 1 millimeter in length are recorded. Absent of any external factors to suppress the fullerene crystallization, the process of fullerene crystallization begins quite rapidly in binary P3HT:PC$_{61}$BM and, in principle, continues until all non-nucleated fullerene is depleted.
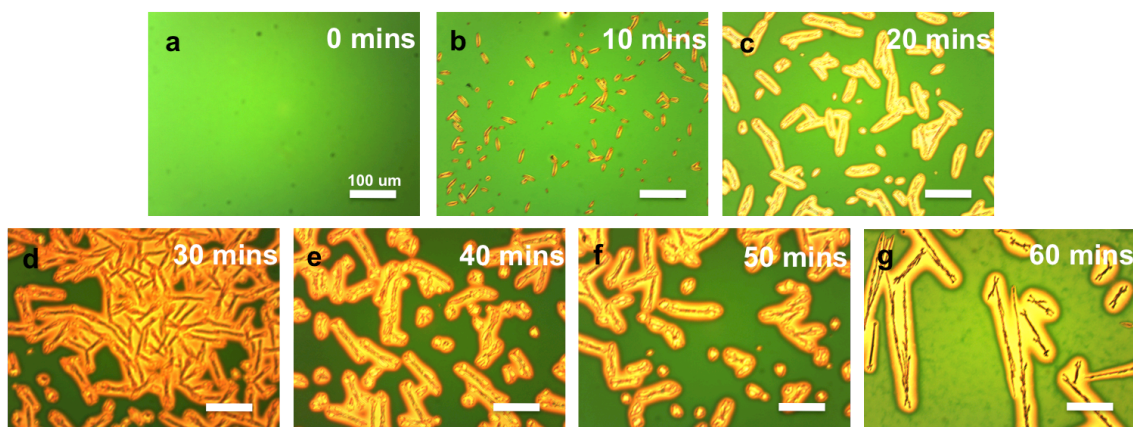
Figure 4.6: Optical Micrographs Showing the Influence of Annealing Time on P3HT:PC$_{61}$BM Binary Blend Thin Films Annealed at 150 ˚C

Binary P3HT:PCB-F blends are also observed to yield fullerene crystallites (**Figure 4.7**). However, these crystallites differ in size and shape from those seen in the P3HT:PC$_{61}$BM binary blends. Moreover, the formation of PCB-F crystallites are not readily observed until 1 hour of annealing. In contrast, P3HT:PC$_{61}$BM blends show fullerene crystallization within 10 minutes of heating. At 60 minutes of annealing, the emergence of 4-micron diameter, star-shaped fullerene crystallites are noted. Additionally, the spatial density of these crystallites is particularly high.
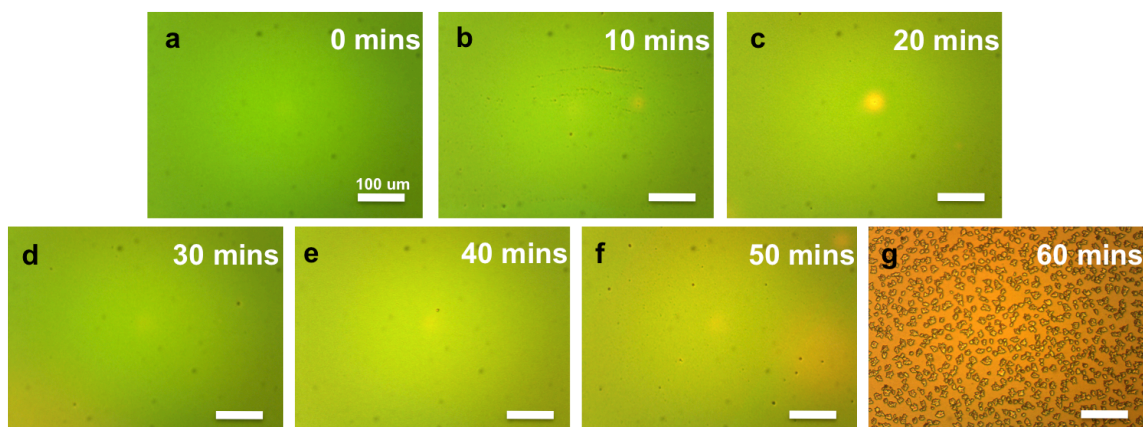
Figure 4.8 depicts optical micrographs of the 0.9:0.1 $PC_{61}BM$:PCB-F wt. ratio P3HT:$PC_{61}BM$:PCB-F ternary blend thin films. Extended annealing conditions of these blends also leads to the formation of fullerene crystallites. However, this particular blend composition yields fullerene crystallites which appear to be much smaller and more spherical in shape than those of binary P3HT:$PC_{61}BM$. At 10 minutes of annealing, the emergence of crystallites less than 10 microns in diameter are noted. At 50 minutes of annealing, clusters of these crystallites are observed. Importantly, the diameter of the fullerene crystallites does not appear to increase significantly as a function of annealing time. In comparison to the binary P3HT:$PC_{61}BM$ blend, it can therefore be reasoned that the inclusion of the small fraction of PCB-F resulted in suppression of fullerene crystallization.
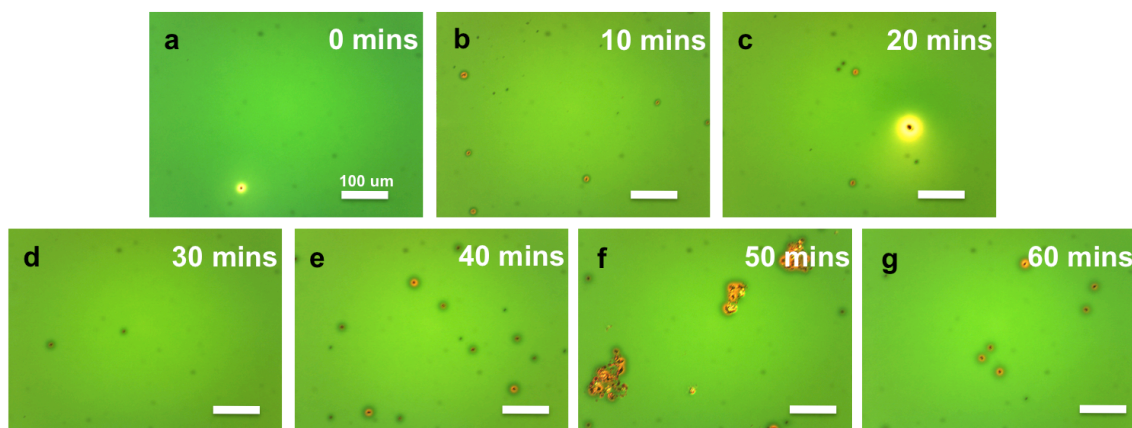
Figure 4.8: Optical Micrographs Showing the Influence of Annealing Time on

P3HT:0.9$PC_{61}BM$:0.1PCB-F Ternary Blend Thin Films Annealed at 150 ˚C

The optical micrographs of 0.8:0.2 $PC_{61}BM$:PCB-F P3HT:$PC_{61}BM$:PCB-F ternary blend thin films are presented below in **Figure 4.9**. Similar to the 0.9:0.1 $PC_{61}BM$:PCB-F ternary blends, these aggregates are small and spherical (diameter < 10 microns). One clear distinction between the 0.9:0.1 and 0.8:0.2 $PC_{61}BM$:PCB-F wt. ratio P3HT:$PC_{61}BM$:PCB-F ternary blends is the absence of large aggregate clusters of fullerene crystallites. The larger weight fraction of PCB-F in the 0.8:0.2 $PC_{61}BM$:PCB-F blend likely enhances the suppression of fullerene crystallization seen in this thin film and further reduces their aggregation.
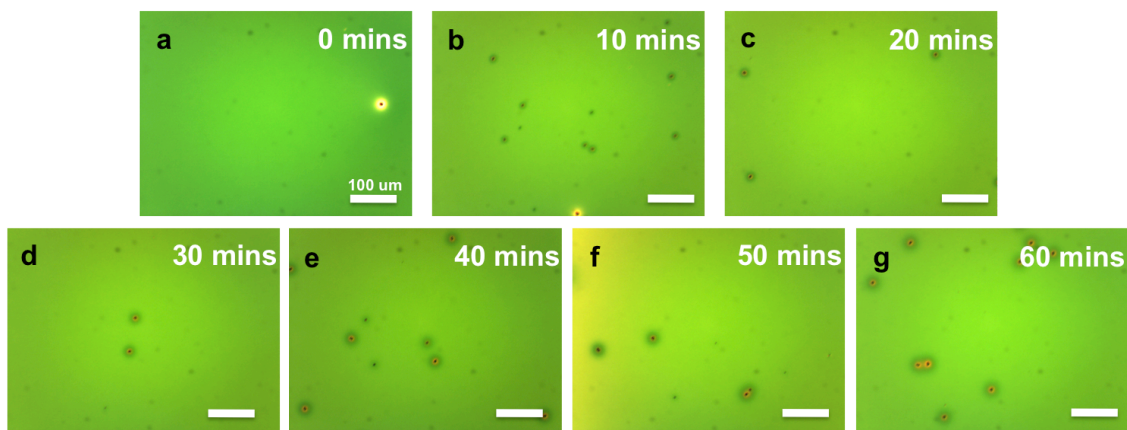
Figure 4.9: Optical Micrographs Showing the Influence of Annealing Time on P3HT:0.8$PC_{61}BM$:0.2PCB-F Ternary Blend Thin Films Annealed at 150 ˚C

Interestingly, no fullerene crystallites are observed at wt. ratios of 0.2:0.8 and 0.1:0.9 $PC_{61}BM$:PCB-F in the P3HT:$PC_{61}BM$:PCB-F ternary blends, even after 1 hour of annealing (**Figure 4.10, 4.11**). In fact, as can be observed in the optical micrographs shown in **Figure 4.12**, ternary blends with $PC_{61}BM$:PCB-F wt. ratios from 0.75:0.25 to 0.1:0.9 also show complete suppression of fullerene crystallization up to 1 hour of annealing. This observation

suggests the strategy of utilizing mixed fullerenes to suppress fullerene crystallization extends to P3HT:PC$_{61}$BM:PCB-F ternary blends, despite significant differences in chemical composition. Moreover, it suggests a highly amorphous fullerene such as PCB-F can further enhance the suppression of fullerene crystallization.
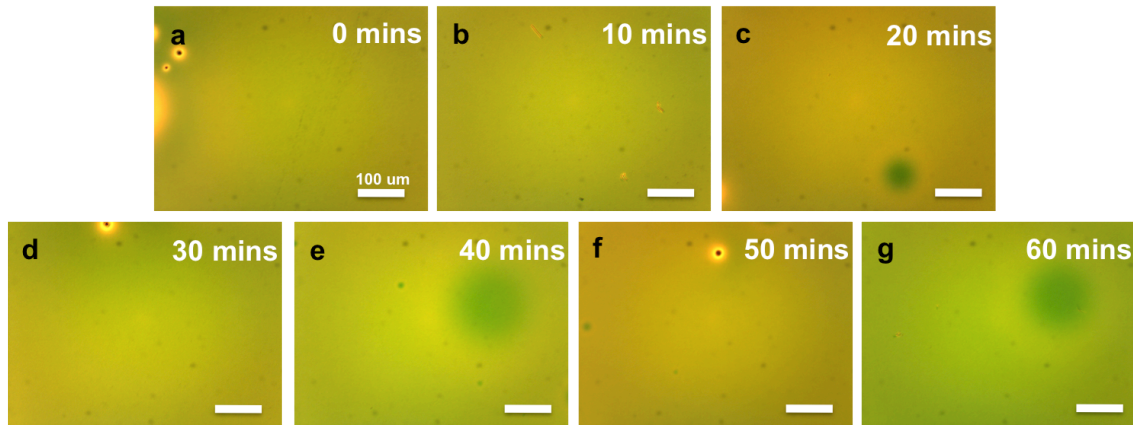
Figure 4.10: Optical Micrographs Showing the Influence of Annealing Time on P3HT:0.2PC$_{61}$BM:0.8PCB-F Ternary Blend Thin Films Annealed at 150 ˚C
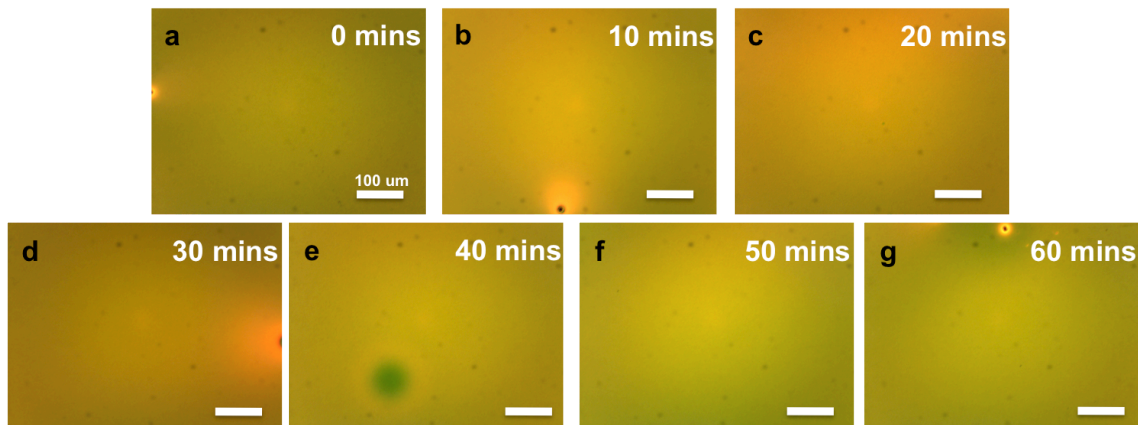
Figure 4.11: Optical Micrographs Showing the Influence of Annealing Time on P3HT:0.1PC$_{61}$BM:0.9PCB-F Ternary Blend Thin Films Annealed at 150 ˚C
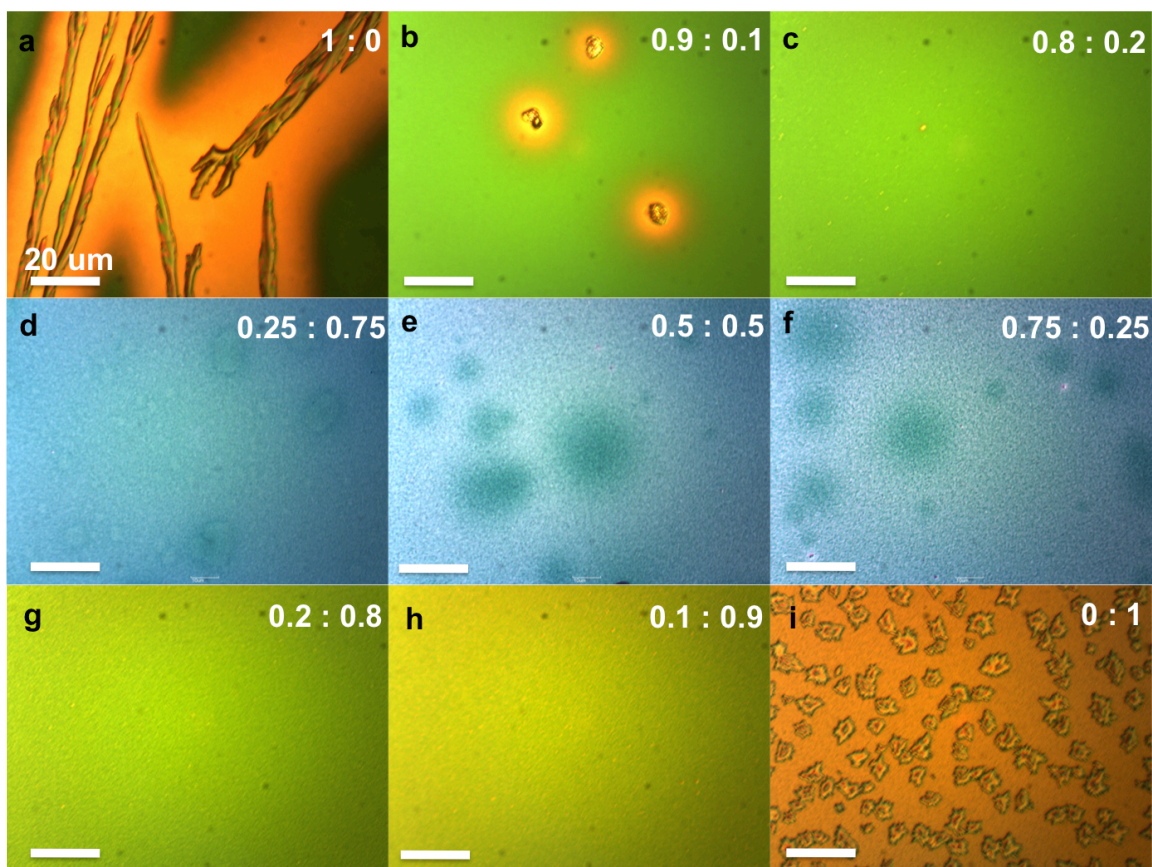
Figure 4.12: Comparison of the Optical Micrographs of P3HT:PC$_{61}$BM:PCB-F Ternary

Blend Thin Films Annealed at 150 ˚C for 1 Hr.

Note: the PC$_{61}$BM:PCB-F ratio is given in the top right corner of each image.

4.4 Grazing Incidence Wide Angle X-Ray Scattering of Ternary Blends

4.4.1 Sample Preparation

Doped native oxide silica substrates (1.5 cm x 1.5 cm) were sonicated sequentially in acetone, 5% soap/ DI water solution, DI water, and IPA for 30 minutes each and dried with N_2 airgun. The silica substrates were then plasma cleaned for 2-3 minutes using O_2 as the flow gas immediately prior to deposition of PEDOT:PSS. PEDOT:PSS (Clevios PVP Al 4083) was spun-cast at 4000 rpm for 1 minute and annealed at 155 ˚C for more than 30 minutes. The ternary blend solutions were prepared in a N_2 atmosphere glovebox with 0.3 mL of oDCB, heated to 80 ˚C, and stirred overnight. Annealed Silica/PEDOT:PSS films were transferred into the glovebox. Ternary blends were filtered with 0.45 μm PTFE filters prior to spin-coating onto ITO/PEDOT:PSS substrates. The ternary blend active layers were then were spun-cast in two sequential steps; 550 rpm for 1 minute, 2000 rpm for 1 second. The films were annealed on a hotplate in a N_2 atmosphere. Note: films annealed at 200 ˚C were annealed directly from their as cast substrates and received no prior thermal treatment.

4.4.2 Pristine PC$_{61}$BM and PCB-F Thin Films
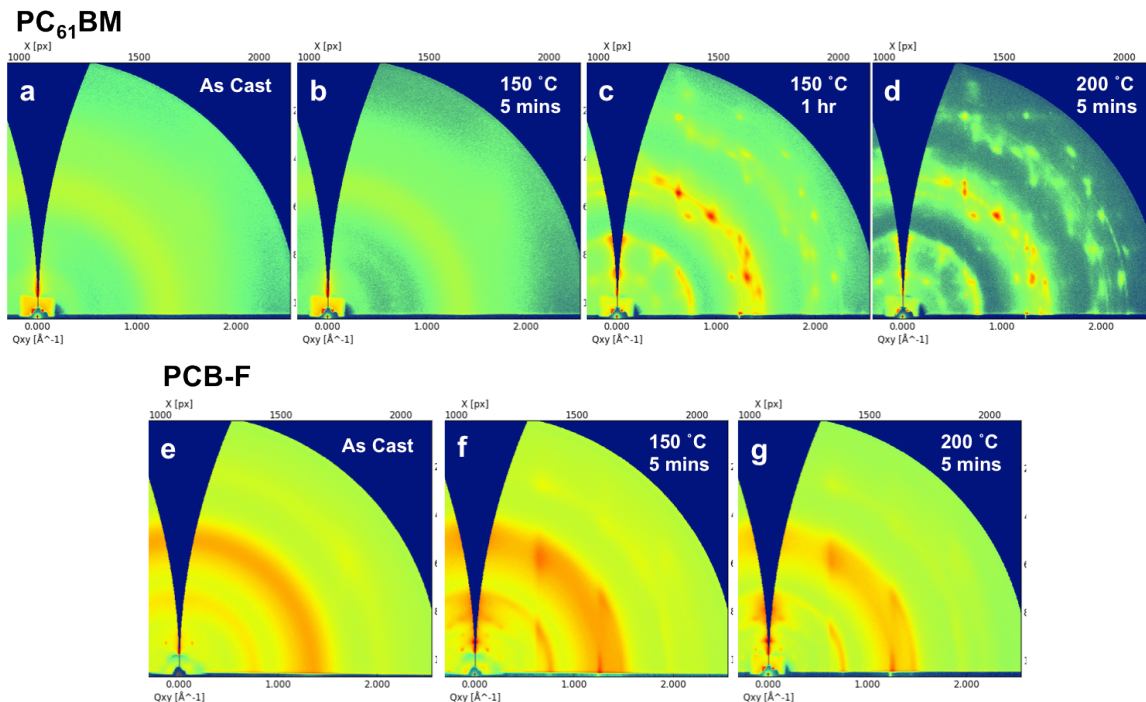
Figure 4.13: GIWAXS Images Showing the Effects of Thermal Annealing on

Pristine PC$_{61}$BM and PCB-F Thin Films

Figure 4.13 depicts GIWAXS images that highlight the morphological changes that occur in pristine PC$_{61}$BM and PCB-F as a result of thermal annealing. The as cast images of PC$_{61}$BM and PCB-F indicate that prior to thermal treatment, both materials initially form amorphous assemblies in their respective thin films. PCB-F does show a higher degree of long range ordering in comparison to PC$_{61}$BM, however, as witnessed by the periodic ring structure. Annealing at 150 ˚C induces crystallization in PCB-F after 5 minutes, evidenced by the emergence of distinct peaks. In contrast, similar treatment of PC$_{61}$BM does not yield the formation of distinct crystallites. This result highlights the capacity of the perfluorinated chain to direct molecular self-assembly and the time scale for such transformations. One hour of annealing does, however, lead to the observation of many distinct PC$_{61}$BM crystalline

peaks. Annealing at 200 ˚C for 5 minutes also leads to the emergence of crystalline peaks in both materials.

4.4.3 P3HT:PC$_{61}$BM:PCB-F Ternary Blend Thin Films
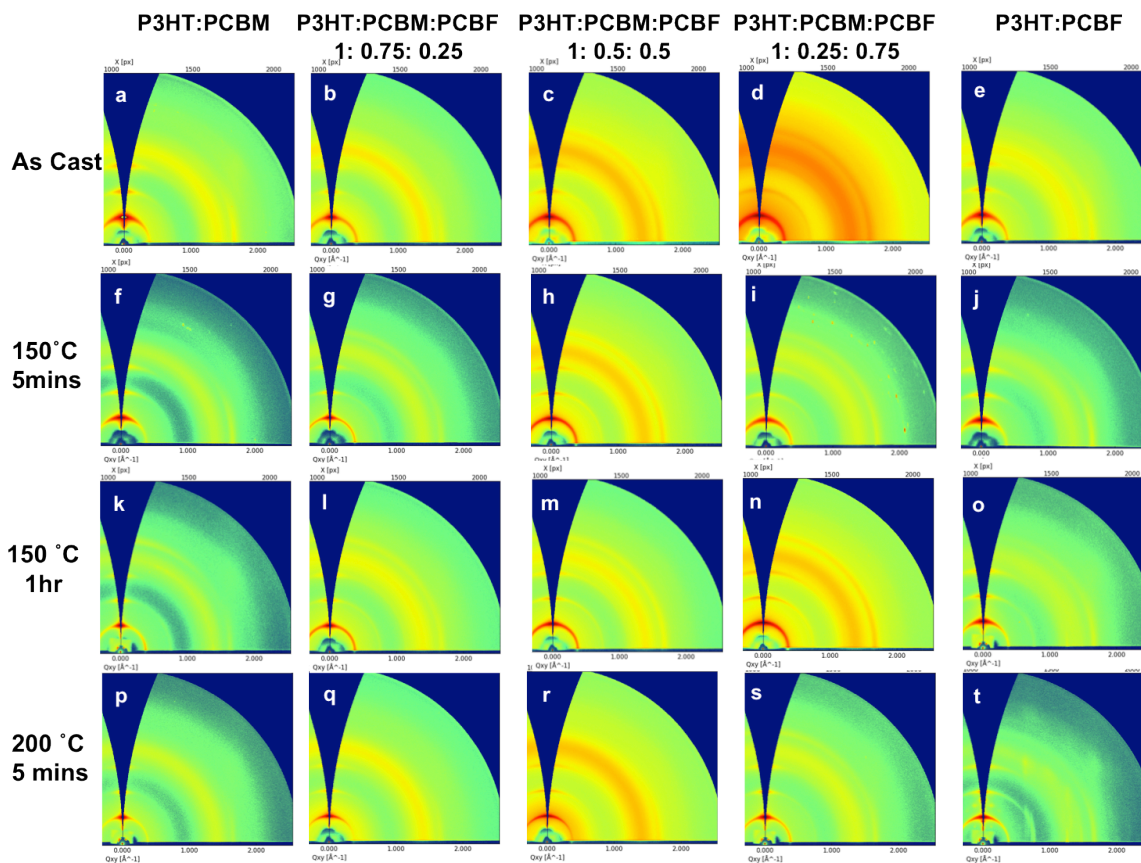
Figure 4.14: GIWAXS Images of the P3HT:PC$_{61}$BM:PCBF Ternary Blends and Their Binary Controls Following Thermal Treatment

The effects of thermal annealing on the P3HT:PC$_{61}$BM:PCB-F ternary blend thin films can be observed in the GIWAXS images provided above in **Figure 4.14**. Comparison of the P3HT:PC$_{61}$BM and P3HT:PCB-F binary blends as the relative metrics of this series

underscores several key features. The as cast P3HT:PC$_{61}$BM and P3HT:PCB-F binary blends both show a periodicity of out-of-plane (**oop**) scattering, a feature consistent with long-range ordering of P3HT perpendicular to the substrate. In addition, both blends show some arching in their oop peaks, indicating that while there is a degree of vertical ordering, the preferential directional alignment in these crystallites is weak. One contrasting feature is that P3HT's in-plane (**ip**) pi-stacking peak shows broader arching in the P3HT:PCB-F blend. This observation indicates that P3HT does not strictly assume an edge-on conformation relative to the substrate. The P3HT:PC$_{61}$BM device, however, does demonstrate less arching in P3HT's pi-stacking peak, signaling a stronger preference for edge-on alignment under the given processing conditions.

Upon annealing at 150 ˚C for 5 minutes, the P3HT:PC$_{61}$BM blend shows decreased arching and higher intensity in its oop peaks, denoting improved vertical ordering. The P3HT:PCB-F blend also shows higher intensity in its oop peaks as well as a decrease in their arching, also pointing to an overall improvement in the vertical alignment of P3HT. However, relative to binary P3HT:PC$_{61}$BM, the P3HT:PCB-F blend still has more arching in its P3HT oop peaks and ip pi-stacking peak, which indicates the P3HT in this blend is still less ordered in comparison.

Annealing at 150 ˚C for 1 hour further improves the vertical ordering of P3HT in the binary P3HT:PC$_{61}$BM blend, as evidenced by the sharpening of its oop peaks. The bandwith of the fullerene arch in the P3HT:PC$_{61}$BM blend also appears to tighten after the hour of annealing. Binary P3HT:PCB-F also shows some sharpening of its oop plane peaks under equivalent annealing conditions, although, relative to P3HT:PC$_{61}$BM, this blend continues to

show higher intensity in its arching. In contrast to the $PC_{61}BM$ blend, the fullerene arch of P3HT:PCB-F appears to have increased in bandwidth after 1 hour of annealing.

Annealing binary $P3HT:PC_{61}BM$ films at 200 ˚C for 5 minutes leads to P3HT crystallites which are highly ordered ip and oop. Identical annealing conditions for binary P3HT:PCB-F thin films also signals improved P3HT ordering, although to a lesser degree. Interestingly, the emergence of PCB-F crystallites is also clearly observed in the GIWAXS images of this thin film.

Examination of the GIWAXS images collected for the $P3HT:PC_{61}BM:PCB$-F ternary devices highlights several important trends. In the as cast devices, a progressive increase in molecular disorder is observed as the weight fraction of PCB-F is increased from 0.25 to 0.75. This disorder is especially noted by the increasing width of the fullerene scattering peak, in addition to the arcing of the P3HT 1st, 2nd, and 3rd oop scattering peak and its ip pi-stacking peak. An increase in vertical P3HT ordering is observed in each of the ternary blends upon annealing for 5 mins at 150 ˚C, though less than the binary blends. Despite this improvement, the general trend of a decrease in P3HT vertical ordering with increasing PCB-F weight fraction is maintained. Annealing beyond 5 minutes does not appear to promote any significant changes in the microstructure of P3HT or either fullerene, as can be seen from the films annealed at 150 ˚C for 1 hour. Annealing for 5 mins at 200 ˚C does appear to improve the P3HT vertical ordering of the $P3HT:0.25PC_{61}BM:0.75PCB$-F ternary blend to a larger extent than observed in the other ternary blends, however.

4.5 Dynamic Secondary Ion Mass Spectrometry

4.5.1 Sample Preparation

Doped silica substrates (1.5 cm x 1.5 cm) with a thermally grown oxide layer were sonicated sequentially in acetone, 5% soap/DI water solution, DI water, and IPA for 30 minutes each and dried with N_2 airgun. The silica substrates were then plasma cleaned for 2-3 minutes using O_2 as the flow gas immediately prior to deposition of PEDOT:PSS. PEDOT:PSS (Clevios PVP Al 4083) was spun-cast at 4000 rpm for 1 minute and annealed at 155 ˚C for 30 minutes. Annealed Silica/PEDOT:PSS films were then transferred into the glovebox.

The ternary blend solutions were prepared in a N_2 atmosphere glovebox with 0.3 mL of o-DCB and heated and stirred at 80 ˚C overnight. Blends were prepared from stock solutions of 6.8:1 P3HT:fullerene molar ratios. The total P3HT:fullerene molarity was held constant at 6.83:1, while the relative molar ratios of d-PC$_{61}$BM:d-PCB-F were varied from 0:1 − 1:0 mol. Ternary blends were filtered with 0.45 μm PTFE filters prior to deposition onto ITO/PEDOT:PSS substrates. The ternary blend active layers were then were spun-cast in two sequential steps; 550 rpm for 1 minute, 2000 rpm for 1 second.

The annealed films were solvent annealed on a petri dish for 10 minutes and then thermally annealed at 150 ˚C for 5 minutes on a hotplate in a N_2 atmosphere. Following thermal processing, a polystyrene standard layer was floated on top of the ternary blend in dilute HF. The films were subsequently dried under vacuum overnight. **Table 4.3** summarizes the blend ratios that were studied.

#	P3HT molar ratio	d-PC$_{61}$BM molar ratio	d-PCB-F molar ratio	Processing
1	6.83	1	0	AC
2	6.83	0.9	0.1	AC
3	6.83	0.8	0.2	AC
4	6.83	0.6	0.4	AC
5	6.83	0.4	0.6	AC
6	6.83	0.2	0.8	AC
7	6.83	0	1	AC
8	6.83	1	0	Ann
9	6.83	0.9	0.1	Ann
10	6.83	0.8	0.2	Ann
11	6.83	0.6	0.4	Ann
12	6.83	0.4	0.6	Ann
13	6.83	0.2	0.8	Ann
14	6.83	0	1	Ann

Table 4.3: Blend Ratios of P3HT:d-PC$_{61}$BM:d-PCB-F Ternary Blend Thin Films

4.5.2 Depth Profiling Measurements

The P3HT:d-PC$_{61}$BM:d-PCB-F ternary blends were examined via DSIMS to evaluate the influence of their molecular composition on vertical self-assembly (**Figure 4.15**). To enhance molecular contrast against P3HT, deuterated analogues of PC$_{61}$BM and PCB-F were used in these measurements. Moreover, a deuterated analogue of PCB-F was employed to mitigate any false positives of fluorine ions. Notably, as d-PCB-F has 48% more mass than d-PC$_{61}$BM, the total mass in the thin films would be anticipated to increase as the relative ratio of PCB-F is increased because the P3HT:fullerene molar ratio is held constant. The films were rastered with Ar$^+$ to produce a 300 um^2 crater from which the analysis was

156

conducted. Note, the limit of vertical molecular resolution afforded by the instrumentation used in this experiment is 10 nm.
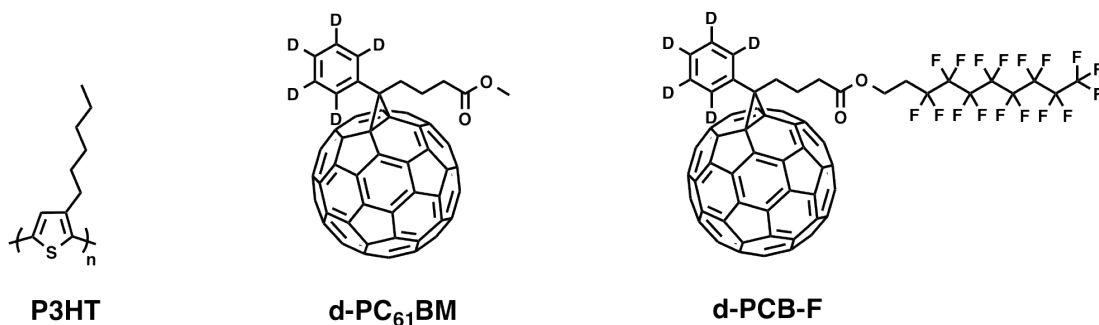
Figure 4.15: Chemical Structures of P3HT, d-PC$_{61}$BM, d-PCB-F

In principle, each representative thin film contains an equal amount of P3HT and deuterium. Therefore, within the bounds of experimental error, films consisting of completely homogenous mixtures of the ternary blends would be expected to yield identical traces of sulfur and deuterium for each blend ratio. In addition, if the two fullerenes were completely mixed, the shape of the deuterium and fluorine traces for each specific blend would be expected to be congruent, while the total fluorine counts would be anticipated to scale with the relative molar ratio of d-PCB-F. Deviations from homogeneity, however, would result in significantly different looking traces from those described above.

As the GIWAXS measurements discussed in **Section 4.4.3** indicated, crystalline P3HT domains were present in both as cast and annealed thin films across all blend ratios. In addition, although the degree to which the two fullerene species were mixed could not be conclusively established, the fullerenes were observed to be amorphous in the as cast and annealed thin films of all blends. These features signal that the blends are not homogeneous

157

mixtures of P3HT and fullerenes, but rather mixtures of crystalline P3HT, amorphous P3HT, and amorphous fullerenes. Assuming the average size and frequency/unit volume of the P3HT and fullerene domains were unaffected by the inclusion of the perfluorinated fullerene tail, the measurements would be expected to yield sulfur and deuterium traces that integrated to the same value or maintained the same shape. However, if the shape of the sulfur and deuterium traces were found to differ significantly with the amount of PCB-F, such findings would indicate the perfluorinated tails strongly influences the size and self-assembly of the P3HT and fullerene domains.

DSIMS analysis of the vertical ordering of sulfur shows strong differences between the as cast and annealed thin films (**Figure 4.16**). A prominent feature in the as cast blends is the concave "U" shape of the sulfur counts for all the blend ratios; although less exaggerated in the 0% PCB-F and 80% PCB-F blends. This behavior indicates that P3HT tends to aggregate towards the air interface and PEDOT:PSS prior to thermal treatment, an affect which seems to be amplified by the presence of a perfluorinated subunits.

In general, the vertical distribution of sulfur appears to become more uniform upon annealing. Interestingly, however, comparatively higher sulfur counts in the 0% and 10% PCB-F traces for both as cast and annealed substrates, indicate the presence of larger amounts of P3HT in the volumes probed for these films. Because the total amount of P3HT is unchanged each the films, this observation could possibly suggest the average size and/or frequency of P3HT domains is affected by the presence of PCBF. In contrast, this affect could also, in principle, reflect changes in ionization efficiency as a result of drifts in the instrumentation's ion beam. Note: the increase in sulfur counts after 1500s is attributed to the emergence of the thermal oxide layer and does not indicate the presence of P3HT.
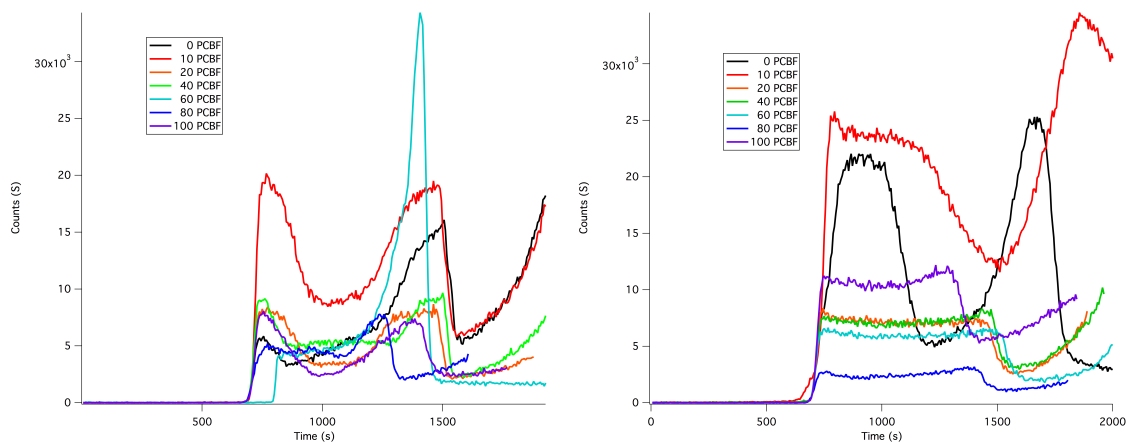
Figure 4.16: DSIMS of the Sulfur in the Ternary Blend Thin Films

a. as cast **b.** annealed

Figure 4.17 depicts the vertical distribution of deuterium throughout the film. As previously noted, deuterated analogues of $PC_{61}BM$ and PCB-F were used for these experiments. Therefore, the vertical distribution of deuterium would correlate directly to the vertical self-assembly of fullerene throughout the films. From the deuterium trace alone, however, the distribution of d-$PC_{61}BM$ and d-PCB-F are indistinguishable.

In the as cast films, the general profiles of the deuterium traces are concave-down and quasi-parabolic in appearance. This shape appears to be somewhat of an inversion of the concave-up, quasi-parabolic as cast sulfur trace. This feature suggests the deuterated fullerenes demonstrate a tendency to aggregate toward the interior of the films in the as cast substrates.

Upon annealing, however, the deuterium counts lose their quasi-parabolic shape and assume a more uniform vertical distribution throughout the film, indicating a change in

159

fullerene self-assembly. Another interesting feature of the annealed films is that the 0% PCB-F trace, and to a lesser extent the 10% PCB-F trace, fail to reach baseline deuterium levels after their initial decline. This phenomenon indicates the Ar^+ beam has reached the silicon oxide layer more rapidly. In combination with observations of the sulfur traces previously described, this behavior is highly suggestive of crystalline defects and grain boundaries within the films of 0% and 10% PCB-F. The films with larger fractions of fluorine do not mirror this behavior, an outcome that seems to indicate PCB-F arrests and/or retards fullerene vitrification, a conclusion further substantiated by evidence from microscopy and GIWAXS.
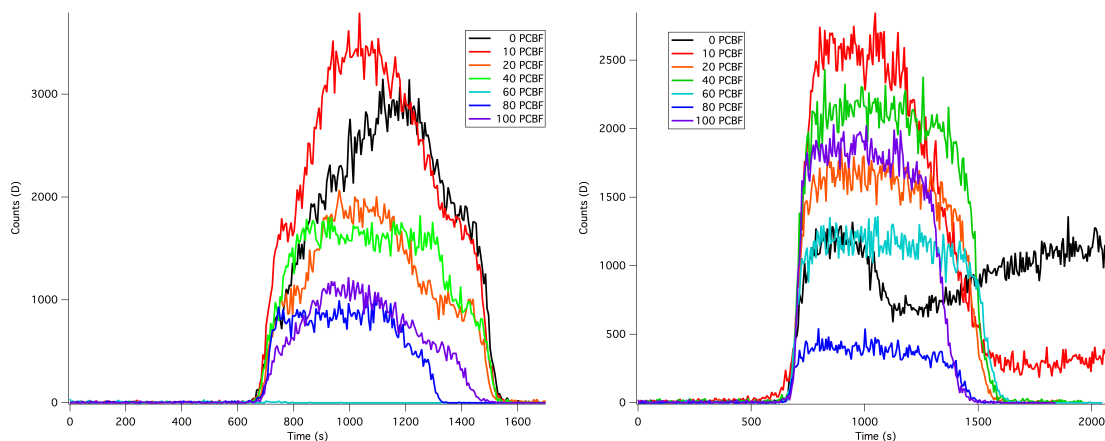
Figure 4.17: DSIMS of the Deuterium in the Ternary Blend Thin Films

a. as cast **b.** annealed

Examination of the fluorine counts (**Figure 4.18**) offers additional insight into the vertical distribution of these ternary blends. As previously described, deuterated analogues of $PC_{61}BM$ and the perfluorinated fullerene PCB-F were used to enhance molecular contrast against P3HT. Therefore, if the two fullerenes were completely mixed, the shape of the deuterium and fluorine traces would be expected to be congruent for each blend composition,

160

while the total fluorine counts would be anticipated to scale linearly with the relative molar ratio of d-PCB-F. In contrast, significant differences in the shape of the fluorine and deuterium traces would indicate the fullerene materials are not homogenously mixed. Such behavior would suggest self-assembly of the fullerene domains within the ternary blends may be influenced by the chemical composition of each fullerene.

A salient feature observed in the as cast films is the initial sharp spike in fluorine counts. Although reports detailing the tendency of perfluorinated groups to self-assemble at the air-interface would suggest similar behavior could be anticipated from these blends, the width of this spike is not within the instrument's capacity for vertical resolution. The fact that the shape of this spike may be an instrumental artifact limits its physical interpretation. Therefore, the appearance of this shape cannot explicitly substantiate the occurrence of any preferential vertical ordering of the perfluorinated tails at the air-interface. Moreover, due to the absence of a parallel spike in the deuterium trace, this initial spike and decline in fluorine cannot unambiguously confirm that larger amounts of d-PCB-F are assembled at the surface of the film. As an addendum, the high ionization efficiency of fluorine could potentially provide a reasonable explanation for the sharp burst in fluorine counts recorded.

Interestingly, the amount of fluorine in the first spike seems to stabilize at 80% d-PCB-F. This observation could perhaps suggest the saturation limit of d-PCB-F on the surface has been reached at 80% d-PCB-F, although the limits to vertical resolution also leave room open for interpretation of this behavior. Above 80% d-PCB-F, it can be observed that a larger proportion of d-PCB-F is situated in the interior of the film.

A similar sharp spike in fluorine counts is again noted near the end of the fluorine traces for the as cast substrates. The width of this spike also falls outside of the instrument's

limits for molecular depth resolution. However, because analogous behavior is not observed in the annealed thin films, the spike in fluorine counts likely indicates a modification in the molecular self-assembly of d-PCB-F at the PEDOT:PSS interface during thermal treatment.

Apart from the spikes in fluorine described, the general concave-down, quasi-parabolic appearance of the fluorine trace suggests that the majority of d-PCB-F lies within the interior of the as cast thin films. With the exception of these spikes, the general profile of the fluorine trace appears to mirror that of the deuterium, suggesting d-PCB-F is not more preferentially stratified toward the air interface than d-PC$_{61}$BM and that the two fullerenes are perhaps homogeneously mixed. However, it should also be noted that in the as cast films, the fluorine counts of each trace do not scale linearly with the relative ratio of incorporated d-PCB-F. This observation could possibly contradict conclusions of fullerene homogeneity, suggesting instead that d-PCB-F is not uniformly distributed throughout the film, but rather isolated in certain domains.

Analysis of the vertical molecular composition of the annealed substrates indicates thermal treatment has a strong influence on the vertical self-assembly of d-PCB-F within the films. Across all blend ratios, thermal treatment diminishes the quasi-parabolic concave-down shape of the fluorine trace, indicating a more uniform vertical distribution of d-PCB-F has occurred within the bulk. The prominent spike in fluorine counts recorded in the as cast films is also observed at the air-interface of the annealed films. In contrast, no spike in fluorine counts is measured at the PEDOT:PSS interface, underscoring the change in molecular self-assembly that has taken place as a result of thermal treatment. Notably, the binary P3HT:d-PCB-F film shows a much larger fluorine spike, relative to the other blend compositions. This feature could imply a larger migration of perfluorinated units to the air-

interface has occurred upon annealing of this binary blend, as this behavior is substantially less pronounced for the other blends.

Incidentally, the fluorine counts of the annealed blends do not scale linearly with d-PCB-F molar feed ratios. Similar to the as cast blends, this observation could signal the domains of amorphous d-PCB-F are not uniformly distributed; suggesting that while d-PC$_{61}$BM and d-PCB-F reside within amorphous domains, there is a possibility that these domains are nonetheless distinct.
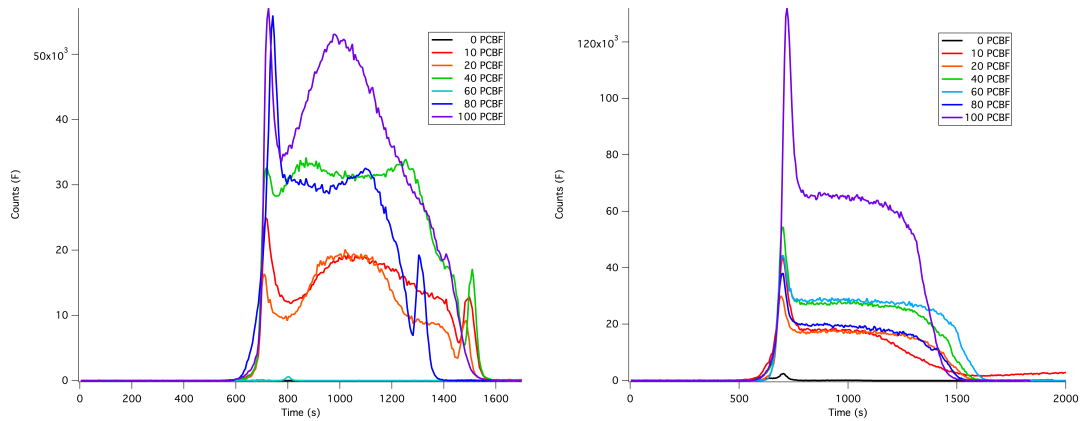
Figure 4.18: DSIMS of the Fluorine in the Ternary Blend Thin Films
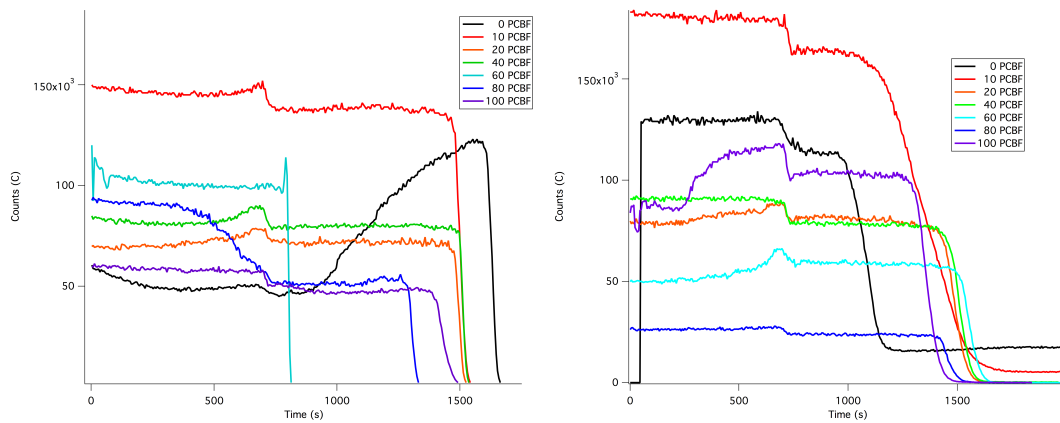
a. as cast **b.** annealed

Figure 4.19: DSIMS of the Carbon in the Ternary Blend Thin Films **a.** as cast **b.** annealed
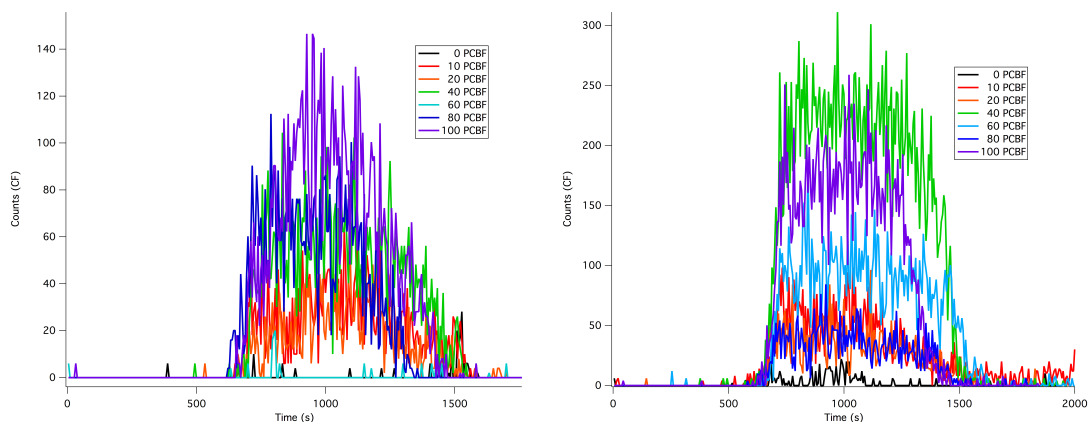
Figure 4.20: DSIMS of the C-F Bond in the Ternary Blend Thin Films **a.** as cast **b.** annealed

4.6 Optoelectronic Characterization of Solar Cells

4.6.1 Sample Preparation

Tin-doped indium oxide substrates (**ITO**) (1.5 x 1.5 cm with a 4 mm ITO-free stripe at the top) were sonicated sequentially in acetone, 5% soap/DI water solution, DI water, and IPA for 30 minutes each and dried with N_2 airgun. ITO substrates were plasma cleaned for 2-3 minutes using air as the flow gas immediately prior to deposition of PEDOT:PSS. PEDOT:PSS (Clevios PVP Al 4083) was spun-cast at 4000 rpm for 1 minute and annealed at 155 °C for more than 30 minutes. Annealed ITO/PEDOT:PSS devices were then transferred into the glovebox.

The ternary blend solutions were prepared in a N_2 atmosphere glovebox with 0.3 mL of o-DCB, heated to 80 °C, and left to stir overnight. Ternary blends were filtered with 0.45 μm PTFE filters prior to their deposition onto the ITO/PEDOT:PSS substrates. Active layer ternary blends were spun-cast in two sequential steps; 550 rpm for 1 minute and 2000 rpm

for 1 second. Top-contact electrodes were deposited via thermal vapor deposition onto the ITO/PEDOT:PSS/ternary blend substrates under vacuum. The top-contact electrodes consisted of calcium/aluminum (Ca/Al) and were thermally deposited at rates of 0.2 and 3 Å/s for final thicknesses of 10 and 70 nm respectively. The ITO size and mask design allowed for five OPV pixels per substrate with an area of 0.06 cm^2. The finished devices (ITO/PEDOT:PSS/ternary blend/Ca/Al) were measured using a solar simulator with AM1.5 G irradiation in a N_2 atmosphere.

The substrates were annealed prior to contact deposition for either 5 minutes or 1 hour, as indicated. Following contact deposition and initial device measurements, the films were subsequently annealed at 150 ˚C in 1 hour intervals and retested to mimic the affects of accelerated aging. The films were annealed under ambient light, not AM 1.5 G irradiation.

4.6.2   Lifetime Study of Ternary Blend Devices Pre-Annealed for 5 mins at 150 ˚C

The following P3HT:PC_{61}BM:PCB-F ternary blend devices were initially annealed at 150 ˚C for 5 minutes and subsequently annealed at 150 ˚C for 1 hour intervals. The results provided for each blend ratio were averaged from five pixels on a single substrate. Graphs depicting the averaged device results as a function of fullerene weight ratios and annealing time are also presented.
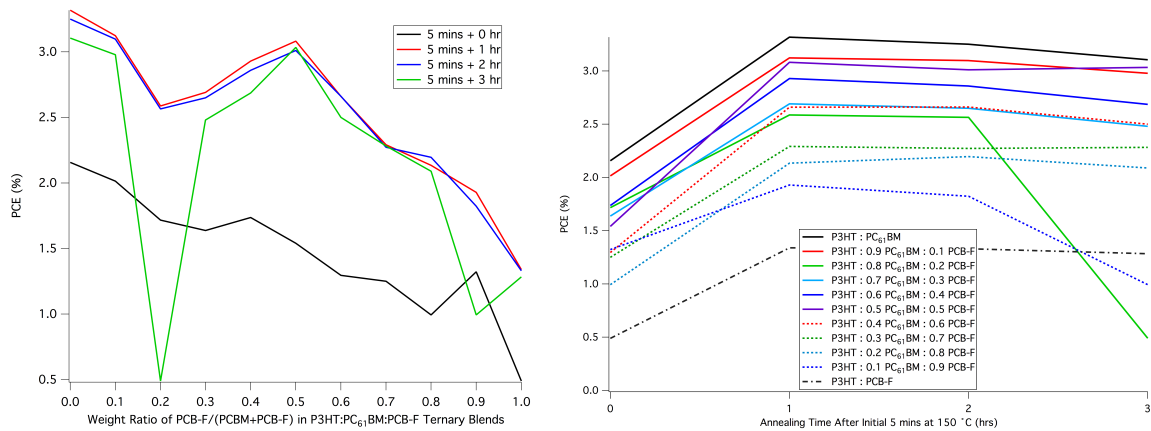
Figure 4.21: Plots Showing the Effects of Post-Annealing Treatment on the PCEs of the Various P3HT:PC$_{61}$BM:PCB-F Ternary Blends Substrates Pre-Annealed at 150 ˚C for 5 mins. **a.** emphasizes the effect of blend composition on PCE **b.** emphasizes the effect of aging on PCE

The effects of accelerated aging and molecular composition on PCE are highlighted in **Figure 4.21**. The most salient trend in the PCEs of these devices is the unanimous improvement in efficiency of the post-annealed substrates, relative to those that were exclusively pre-annealed. A general decrease in PCE with increasing PCB-F content is also observed, although a slight local minimum and maximum are noted around 20 and 50 wt.% PCB-F, respectively.
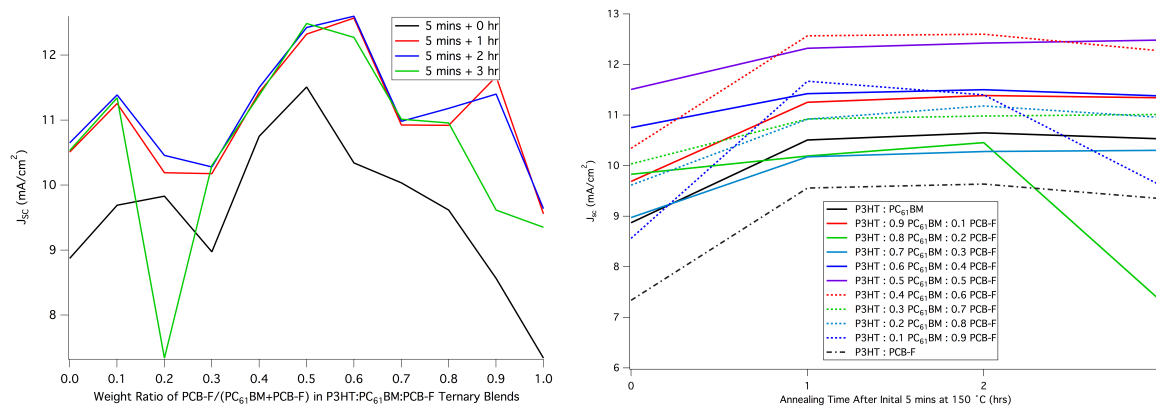
Figure 4.22: Plots Showing the Effects of Post-Annealing Treatment on the J_{sc}'s of the Various P3HT:PC$_{61}$BM:PCB-F Ternary Blends Substrates Pre-Annealed at 150 ˚C for 5 mins. **a.** emphasizes the effect of blend composition on J_{sc} **b.** emphasizes the effect of aging on J_{sc}

Similar to the trend observed in PCEs, post-annealing treatment improves the J_{sc} across all blends ratios, relative to the substrates that were only pre-annealed for 5 minutes (**Figure 4.22**). In contrast to trends in PCE, however, the increasing weight fraction of PCB-F has several divergent effects on J_{sc}. For example, with the exception of the devices exclusively pre-annealed, the increase in PCB-F wt.% does not appear to cause a major decrease in J_{sc}. In fact, global maximums in J_{sc} are observed between 50 - 60 wt.% PCB-F, indicating an improvement to charge transport that originates from the introduction of PCB-F. Additionally, a local minimum is also observed near 30 wt.% PCB-F for each of these devices, a feature that appears to cause the dip in PCEs located at this wt.% of PCB-F. Incidentally, the blend composition of the global maximum in J_{sc} appears to correlate with similar features in the PCE graphs, although the behavior is less pronounced at these ratios in the PCE graphs. It can therefore be reasoned that the changes in chemical composition, which evolve as a function of PCB-F incorporation, modify the molecular self-assembly of each blend and its

167

capacity for charge transport. In turn, the resulting microstructures that emerge from the self-assembly of these ternary blends directly influence global trends in PCE.
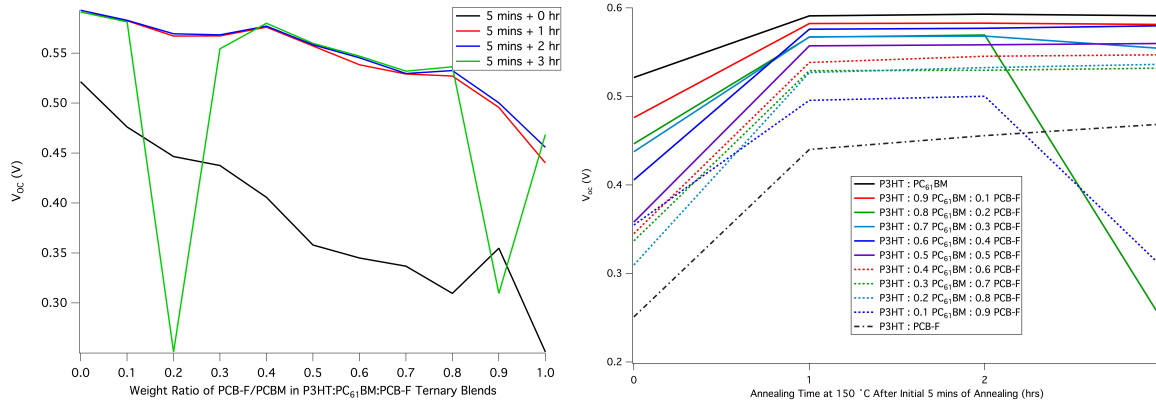
Figure 4.23: Plots Showing the Effects of Post-Annealing Treatment on the V_{oc}'s of the Various P3HT:PC$_{61}$BM:PCB-F Ternary Blends Substrates Pre-Annealed at 150 ˚C for 5 mins. **a.** emphasizes the effect of blend composition on V_{oc} **b.** emphasizes the effect of aging on V_{oc}

In agreement with trends observed in J_{sc} and PCE, significant improvements to V_{oc} were measured in the post-annealed devices, relative to those that were only pre-annealed (**Figure 4.23**). This affect is especially pronounced for blends with a higher wt.% PCB-F. However, in general, these devices are also marked by a continuous and approximately linear decrease in V_{oc} with increasing wt.% PCB-F. The decrease in V_{oc} as a function of PCB-F wt.% indicates that the presence of PCB-F leads to a drop in internal cell bias. Moreover, the linear appearance of this feature suggests this condition is additive.

Because PCB-F and PC$_{61}$BM have identical electron affinities, the origin of this behavior cannot be reasoned to arise from differences in the molecular electronic levels of the two fullerenes. Notably, PCB-F has 48% more mass than PC$_{61}$BM, the bulk of which

168

exists in its perfluorinated ester tail. Because the total weight ratio of fullerene is held constant across the array of ternary blends, the overall number of fullerene molecules per blend decreases as the wt.% of PCB-F is increased. While maintaining a constant P3HT:fullerene weight ratio allows the morphologies of each ternary blend to be more systematically compared, it also means the mass differences of these molecules alters the P3HT:fullerene molar ratio, which could influence charge transport in the cell. It can also be reasoned that the molecular dipole of the perfluorinated tail has a strong influence on the internal cell bias, with a composition dependent effect on emerging trends in V_{oc}.
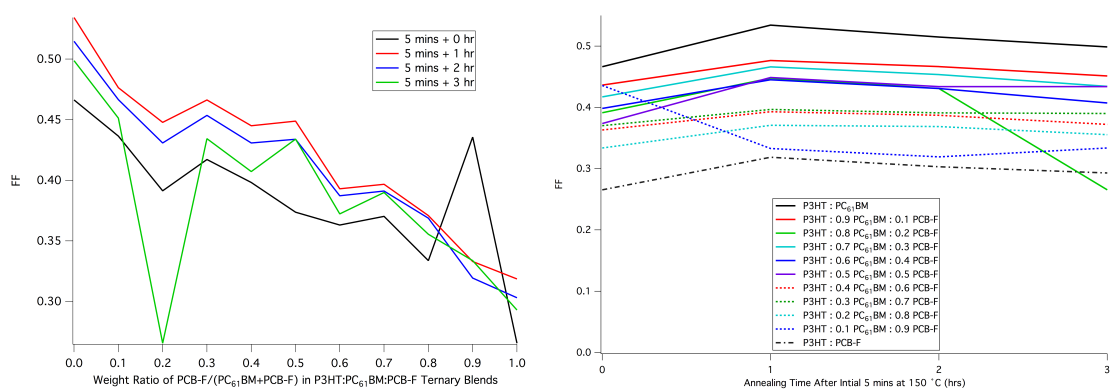
Figure 4.24: Plots Showing the Effects of Post-Annealing Treatment on the FFs of the Various P3HT:PC$_{61}$BM:PCB-F Ternary Blends Substrates Pre-Annealed at 150 ˚C for 5 mins. **a.** emphasizes the effect of blend composition on FF **b.** emphasizes the effect of aging on FF

Relative to devices that were only pre-annealed for 5 minutes, post-annealing treatment also lead to an increase in FF (**Figure 4.24**). The general trend of a decreasing FF with increasing wt.% PCB-F was largely unaffected by annealing, although minor deviations are noted at 30, 50, and 70 wt.% PCB-F. This behavior suggests that charge extraction is increasingly inhibited as a consequence of PCB-F incorporation.
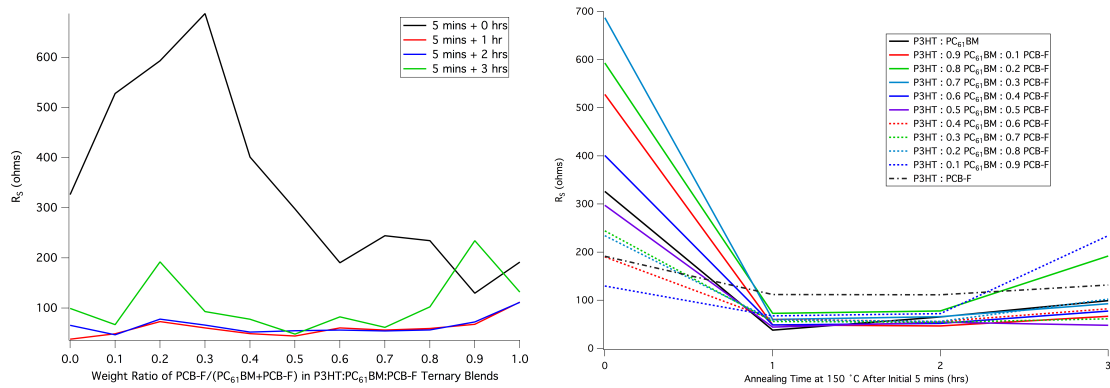
Figure 4.25: Plots Showing the Effects of Post-Annealing Treatment on the R_S of the Various P3HT:PC$_{61}$BM:PCB-F Ternary Blends Substrates Pre-Annealed at 150 ˚C for 5 mins. **a.** emphasizes the effect of blend composition on R_S **b.** emphasizes the effect of aging on R_S
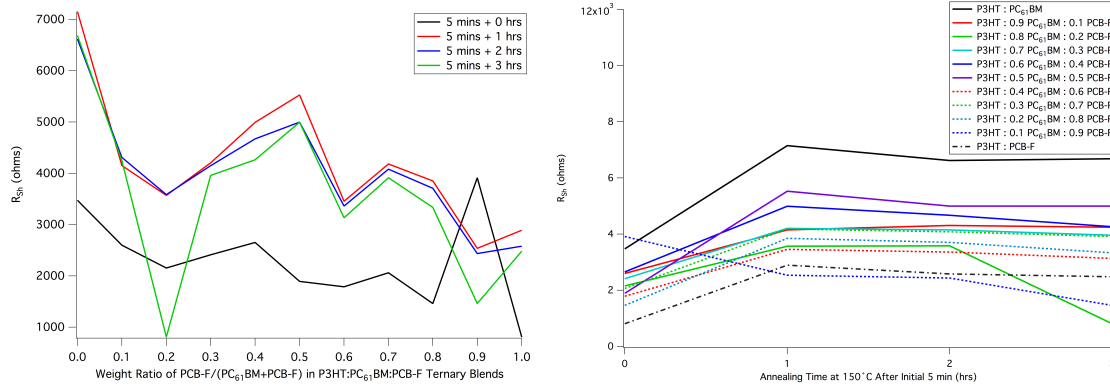
Figure 4.26: Plots Showing the Effects of Post-Annealing Treatment on the R_{Sh} of the Various P3HT:PC$_{61}$BM:PCB-F Ternary Blends Substrates Pre-Annealed at 150 ˚C for 5 mins. **a.** emphasizes the effect of blend composition on R_{Sh} **b.** emphasizes the effect of aging on R_{Sh}

4.6.3 Lifetime Study of Ternary Blend Devices Pre-Annealed for 1 hr at 150 ˚C

170

The following P3HT:PC$_{61}$BM:PCB-F ternary blend devices were annealed for 1 hour prior to contact deposition and subsequently annealed for 1 hour intervals following deposition. The results provided for each blend ratio were averaged from five pixels on a single substrate. Graphs depicting the average device results as a function of fullerene wt. ratios and post-contact deposition annealing time are also presented.
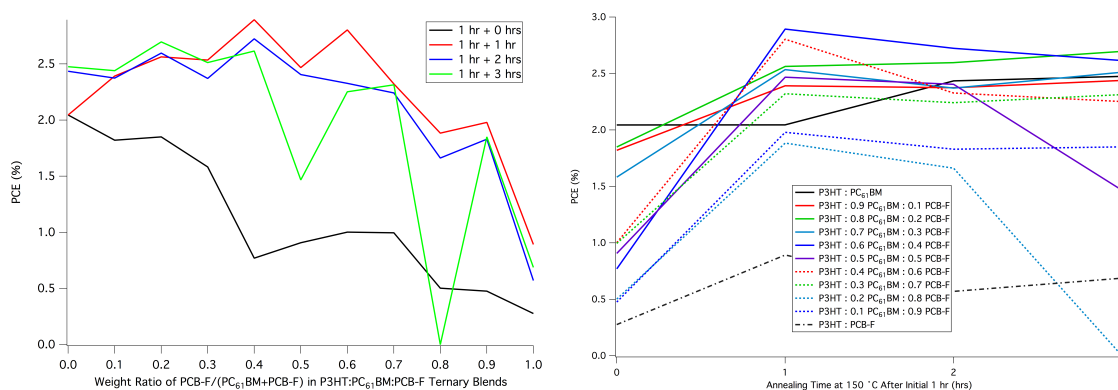
Figure 4.27: Plots Showing the Effects of Post-Annealing Treatment on the PCEs of the Various P3HT:PC$_{61}$BM:PCB-F Ternary Blends Substrates Pre-Annealed at 150 ˚C for 1 hr. **a.** emphasizes the effect of blend composition on PCE **b.** emphasizes the effect of aging on PCE

Annealing for 1 hour post-contact deposition was generally observed to increase the PCEs of these devices, relative to the substrates that received no post-annealing treatment (**Figure 4.27**). One interesting divergence from this trend occurs with the binary P3HT:PC$_{61}$BM substrate, however. With this particular device, two hours of post-annealing were needed before an increase in PCE could be noted. Another salient feature of these devices is the general decrease in efficiency with increasing wt.% PCB-F for the substrates that were not post-annealed. A similar trend was observed in the devices exclusively pre-

171

annealed for 5 minutes described in **Section 4.6.2**. Interestingly, the post-annealed devices show a general increase in efficiency as the blend ratios approach median mixtures, with local maximums observed at 40 and 60 wt% PCB-F. In addition small local minimums are noted at 30 and 50 wt% PCB-F. This behavior indicates that at certain blend ratios, incorporation of PCB-F may be favorable for extending the operational lifetime of OSCs.
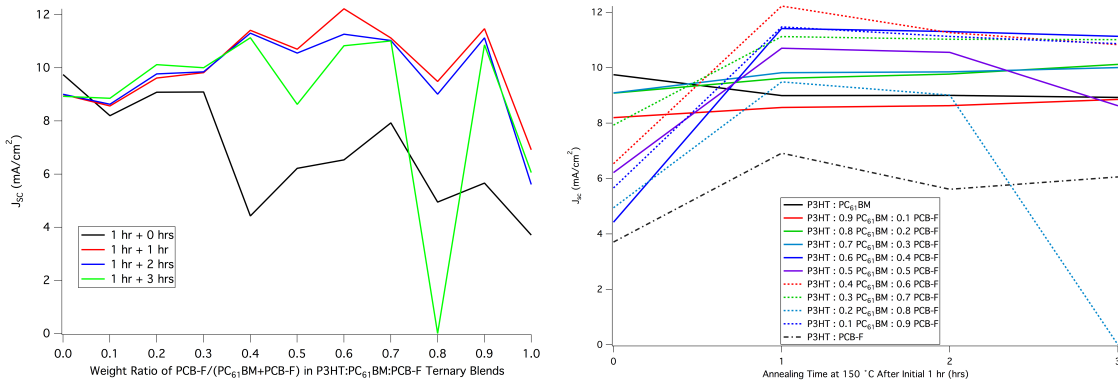
Figure 4.28: Plots Showing the Effects of Post-Annealing Treatment on the J_{sc}'s of the Various P3HT:PC$_{61}$BM:PCB-F Ternary Blends Substrates Pre-Annealed at 150 ˚C for 1 hr. **a.** emphasizes the effect of blend composition on J_{sc} **b.** emphasizes the effect of aging on J_{sc}

The J_{sc}'s of the devices show a general increase in current with post-annealing treatment (**Figure 4.28**). Local maxima are observed at 40, 60, and 90 wt.% PCB-F, and a sharp decrease in J_{sc} is measured in the binary P3HT:PCB-F blend. These results suggest that while incorporation of PCB-F at certain blend ratios can favor enhanced charged transport, some amount of PC$_{61}$BM may still be needed to maximize the benefit. The improvements in charge transport likely originate from morphological features.
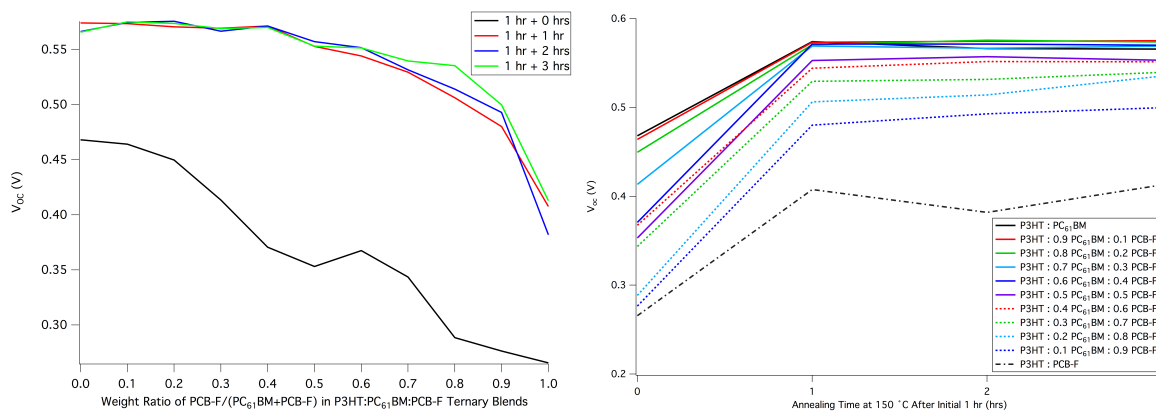
Figure 4.29: Plots Showing the Effects of Post-Annealing Treatment on the V_{oc}'s of the Various P3HT:PC$_{61}$BM:PCB-F Ternary Blends Substrates Pre-Annealed at 150 ˚C for 1 hr. **a.** emphasizes the effect of blend composition on V_{oc} **b.** emphasizes the effect of aging on V_{oc}

In agreement with the principle trend observed in post-contact deposition annealing treatment, the V_{oc}'s of these devices also witness a large increase in voltage following post-annealing. Despite this increase, a general trend of decreasing V_{oc} as a function of increasing wt.% PCB-F is also measured. Interestingly, across all annealing conditions, an acceleration of this decrease is observed at blend ratios approaching binary P3HT:PCB-F. This behavior contrasts the phenomena seen in the devices outlined in **Section 4.6.2**, as their decrease in V_{oc} was more linear in appearance. While the decrease in V_{oc} indicates the incorporation of PCB-F is destructive to the internal bias of the cell as a whole, the effect appears to be amplified at longer pre-annealing times. Again, this behavior could trace its roots to the increasingly fewer fullerenes available as the weight ratio of PCB-F is increased. It could also point to a disruptive change in the internal bias of the cell that stems from the molecular dipole of the perfluorinated pendants.
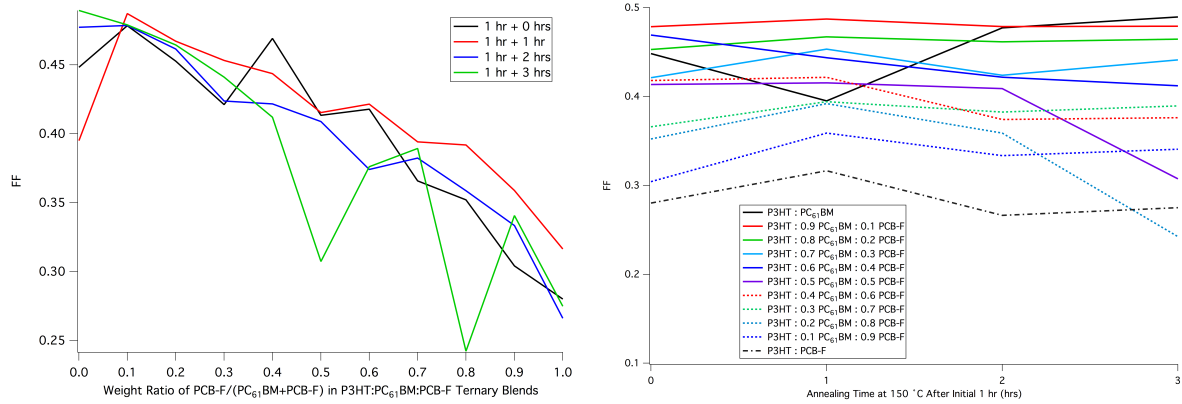
Figure 4.30: Plots Showing the Effects of Post-Annealing Treatment on the FFs of the Various P3HT:PC$_{61}$BM:PCB-F Ternary Blends Substrates Pre-Annealed at 150 ˚C for 1 hr. **a.** emphasizes the effect of blend composition on FF **b.** emphasizes the effect of aging on FF

Following the first post-contact annealing treatment, the FFs of these devices show modest improvement, with slight deviations from this trend noted at 0 and 40 wt.% PCB-F (**Figure 4.30**). Across each of the annealing conditions, the general feature of decreasing FFs with increasing wt.% PCB-F is observed. This behavior suggests the inclusion of PCB-F is problematic to the extraction of charge. It is possible that the decrease in total fullerene molecules has a detrimental affect on the FF as well.
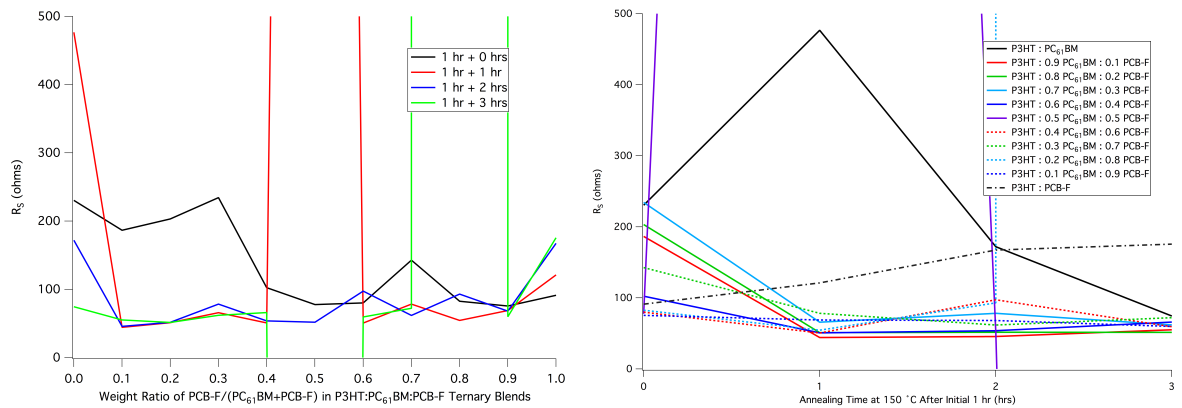
Figure 4.31: Plots Showing the Effects of Post-Annealing Treatment on the R_S of the Various P3HT:PC$_{61}$BM:PCB-F Ternary Blends Substrates Pre-Annealed at 150 ˚C for 1 hr. **a.** emphasizes the effect of blend composition on R_S **b.** emphasizes the effect of aging on R_S
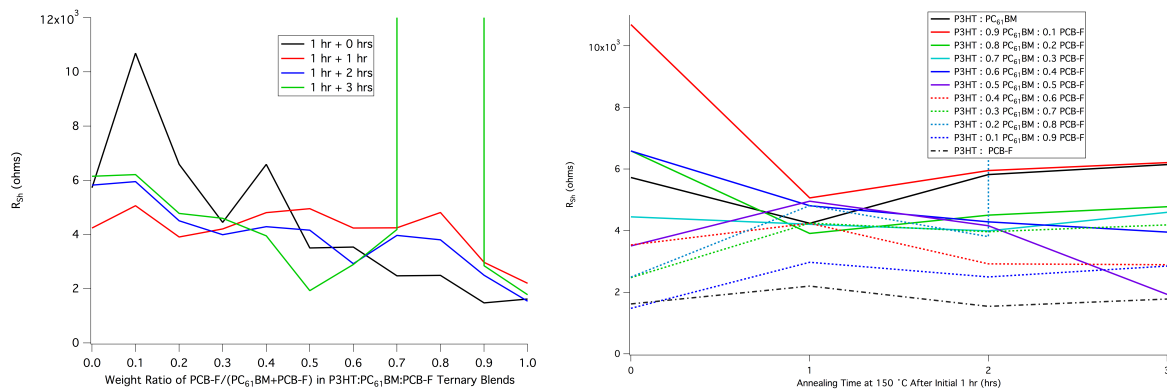
Figure 4.32: Plots Showing the Effects of Post-Annealing Treatment on the R_{Sh} of the Various P3HT:PC$_{61}$BM:PCB-F Ternary Blends Substrates Pre-Annealed at 150 ˚C for 1 hr. **a.** emphasizes the effect of blend composition on R_{Sh} **b.** emphasizes the effect of aging on R_{Sh}

4.6.4 Study of the Influence of Annealing Temperature on Ternary Blend Devices

The following series of P3HT:PC$_{61}$BM:PCB-F ternary blend devices were annealed for 5 minutes at the indicated temperatures prior to contact deposition. The results shown in the figures below represent the values obtained by averaging the 5 pixels across a singular substrate.

Graphs depicting the average device results as a function of fullerene wt. ratios and annealing temperature are also presented.

175
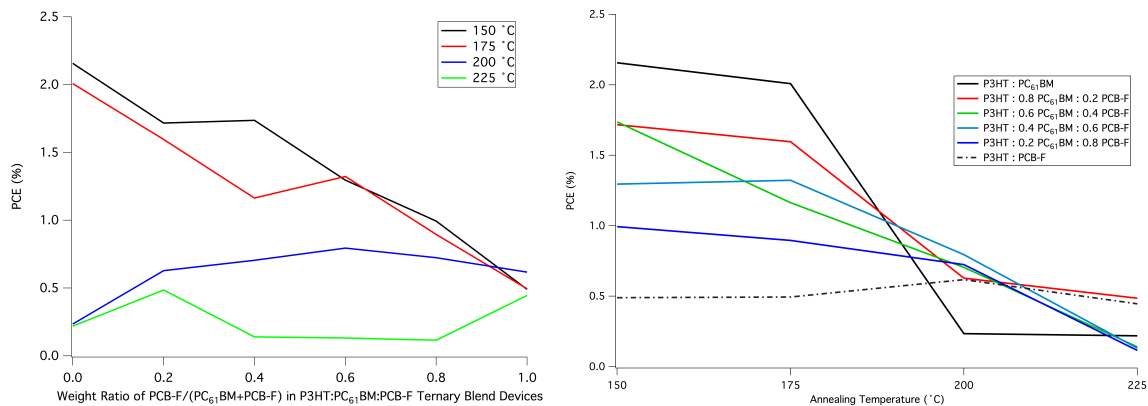
Figure 4.33: Plots Showing the Effects of Annealing Temperature on the PCEs of the Various P3HT:PC$_{61}$BM:PCB-F Ternary Blends Substrates Pre-Annealed at for 5 mins **a.** emphasizes the effect of blend composition **b.** emphasizes the effect of annealing temperature

A general decrease in PCE with increasing wt.% PCB-F is observed for the substrates annealed at 150 ˚C (**Figure 4.33**). A slight divergence from this trend is noted for the devices annealed at higher temperatures, however. For the substrates annealed at 175 ˚C, a small local maximum in PCE was noted at 60 wt.% PCB-F, indicating an improved thermal resilience on account of the inclusion of PCB-F. Blends incorporating PCB-F also showed enhanced thermal stability, relative to binary P3HT:PC$_{61}$BM, in devices annealed at 200 ˚C. Devices annealed at 225 ˚C further demonstrated that inclusion of PCB-F could enhance thermal stability, as substrates prepared with 20 wt.% PCB-F and 100 wt.% PCB-F held higher PCEs relative to PC$_{61}$BM. Notably, devices prepared from blends with 40 – 80 wt% PCB-F showed less thermal stability in comparison to PC$_{61}$BM when annealed at 225 ˚C.
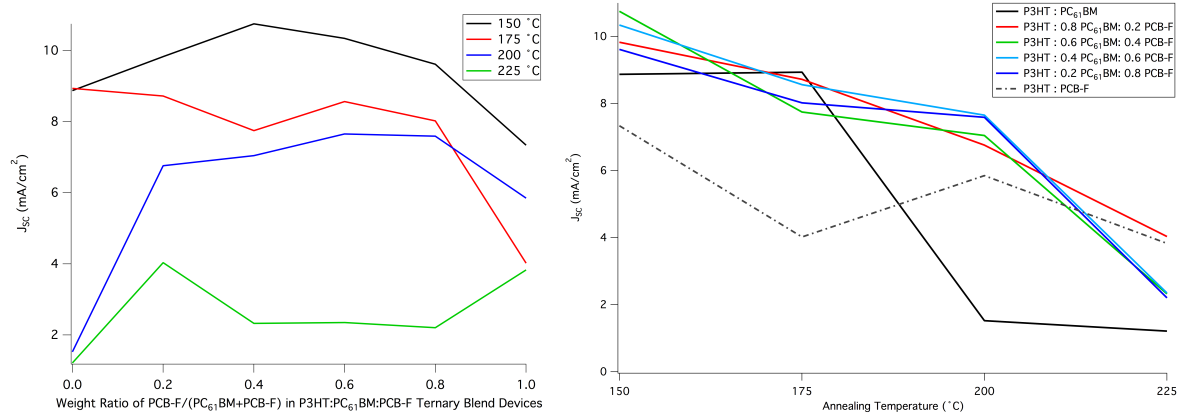
Figure 4.34: Plots Showing the Effects of Annealing Temperature on the J_{sc}'s of the Various

P3HT:PC$_{61}$BM:PCB-F Ternary Blends Substrates Pre-Annealed at for 5 mins

a. emphasizes the effect of blend composition **b.** emphasizes the effect of annealing temperature

Several prominent changes in the J_{sc}'s of these blends are noted with increasing annealing temperature (**Figure 4.34**). In devices annealed at 150 °C, an increase in J_{sc} is observed as the blend ratios approach equal weight mixtures of each fullerene. This trend does not hold for substrates annealed at 175 °C, however, and a slight minimum at 40 wt.% PCB-F is noted. With the exception of P3HT:PCB-F, substrates annealed at 200 °C experience an additional drop in J_{sc} relative to those annealed at 175 °C. In particular, a marked decrease in current from 9 mA/cm^2 to 1 mA/cm^2 is measured for binary P3HT:PC$_{61}$BM, while J_{sc}'s from the PCB-F blends show enhanced thermal resistance. Annealing at 225 °C lead to additional declines in J_{sc}, although devices prepared from PCB-F blends continue to show enhanced thermal stability relative to the binary P3HT:PC$_{61}$BM substrate.
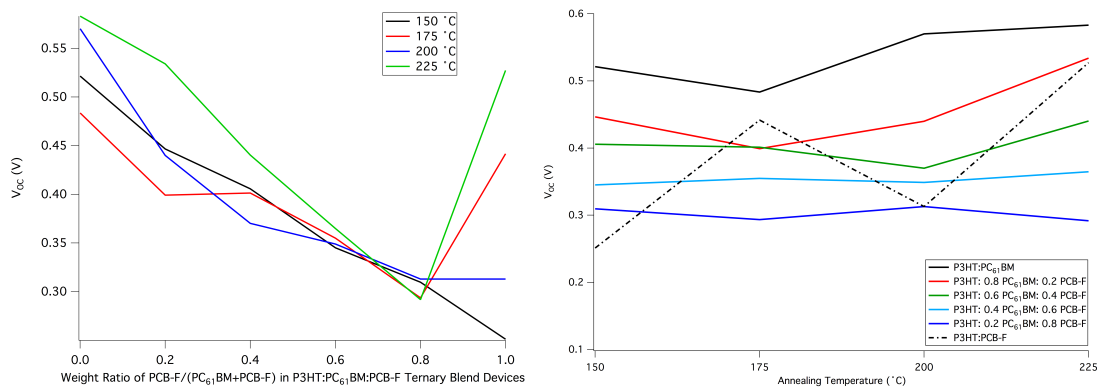
Figure 4.35: Plots Showing the Effects of Annealing Temperature on the V_{oc}'s of the Various P3HT:PC$_{61}$BM:PCB-F Ternary Blends Substrates Pre-Annealed at for 5 mins **a.** emphasizes the effect of blend composition **b.** emphasizes the effect of annealing temperature

The V_{oc} data for the ternary blends shows more complex behavior (**Figure 4.35**). For the substrates annealed at 150 ˚C, a steady drop in V_{oc} is noted with increasing PCB-F wt%. A noticeable deviation from this pattern is observed in devices annealed at 175 ˚C, with the V_{oc} of binary P3HT:PCB-F increasing drastically from 0.25 V to 0.45 V. Apart from the P3HT:PCB-F device, a general decrease in V_{oc} was measured for devices annealed at 175 ˚C relative to those annealed at 150 ˚C. The substrates annealed at 200 ˚C experienced a decline in V_{oc} as a function of PCB-F wt.%, similar to their homologues annealed at 150 ˚C. However, while the binary P3HT:PC$_{61}$BM blend annealed at 200 ˚C recorded a higher V_{oc} than its counterpart annealed at 150 ˚C and 175 ˚C, the binary P3HT:PCB-F substrate annealed at 200 ˚C experienced a decrease in voltage relative to its homologue annealed at 175 ˚C. Interestingly, for all blend ratios except that of 80 wt.% PCB-F, annealing the substrates at 225 ˚C led to higher V_{oc}'s than for any other annealing temperature. In

178

particular, the V_{oc} of binary P3HT:PCB-F shows the highest improvement as it's V_{oc} more

than doubles from 150 ˚C to 225 ˚C.
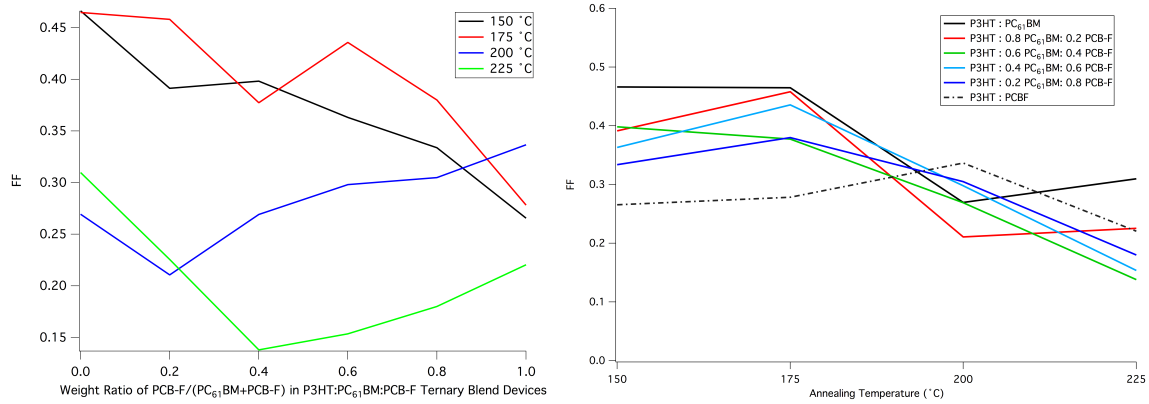
Figure 4.36: Plots Showing the Effects of Annealing Temperature on the FFs of the Various

P3HT:PC$_{61}$BM:PCB-F Ternary Blends Substrates Pre-Annealed at for 5 mins

a. emphasizes the effect of blend composition **b.** emphasizes the effect of annealing

temperature

The FFs of these devices also point to a complex relationship between ternary blend

composition and annealing temperature (**Figure 4.36**). In devices annealed at 150 ˚C, a

general decrease in FF with increasing wt.% PCB-F is noted, with the slight exception of a

small local maximum at 40 wt.% PCB-F. Annealing at 175 ˚C tends to raise the FF's relative

to 150 ˚C except for binary P3HT:PC$_{61}$BM, which experienced no change, and 40 wt.%

PCB-F, which resulted in a modest decrease in FF. In comparison to substrates annealed at

175 ˚C, annealing at 200 ˚C led to a significant decrease in FF for all blend compositions

apart from binary P3HT:PCB-F. In addition, an increase in FF as a function of PCB-F wt.%

is noted between 20 – 100 wt.% PCB-F at this processing temperature. Substrates annealed at

225 ˚C saw an improvement in FF for 0 and 20 wt.% PCB-F over those measured for devices

annealed 200 ˚C devices, while 40 – 100 wt.% PCB-F blends experienced a drop in FF. Interestingly, a global minimum was observed at 40 wt.% PCB-F for devices prepared at this annealing temperature.
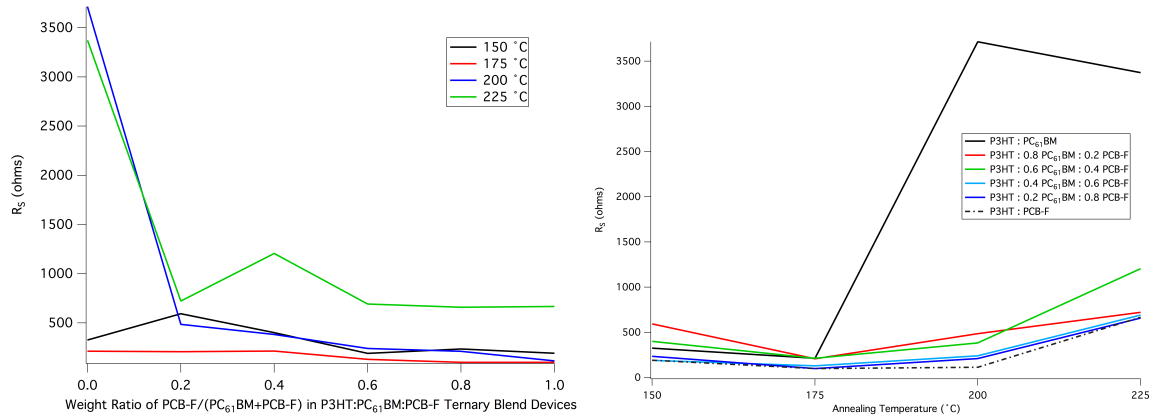
Figure 4.37: Plots Showing the Effects of Annealing Temperature on the R_S of the Various

P3HT:PC_{61}BM:PCB-F Ternary Blends Substrates Pre-Annealed at for 5 mins

a. emphasizes the effect of blend composition **b.** emphasizes the effect of annealing temperature
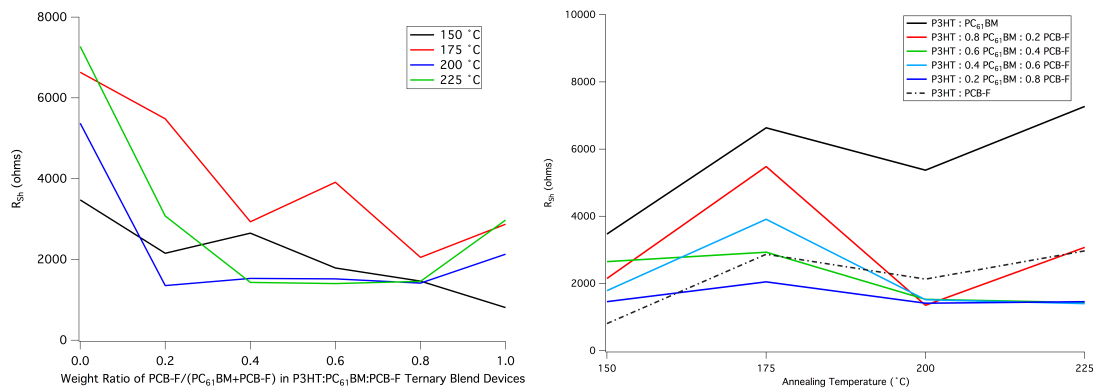
Figure 4.38: Plots Showing the Effects of Annealing Temperature on the R_{Sh} of the Various

P3HT:PC_{61}BM:PCB-F Ternary Blends Substrates Pre-Annealed at for 5 mins

180

a. emphasizes the effect of blend composition **b.** emphasizes the effect of annealing temperature

4.7 Conclusion

A study evaluating the potential of P3HT:PC$_{61}$BM:PCB-F ternary blends to enhance the morphological stability and operational lifetime of OSCs was presented. To isolate the impact of the fullerene's chemical identity from the complex behavior of the ternary blends, in all cases, the absolute ratio of P3HT:fullerene was held constant while the relative ratios of PC$_{61}$BM:PCB-F were systematically varied. Characterization techniques were selected on the basis of their ability to help elucidate the impact of fullerene composition on blending behavior, molecular self-assembly, and PCE degradation in mixed fullerene systems. In addition, a general emphasis on thermally driven processes and accelerated aging was central to these studies. The results of these experiments are summarized below.

DSC analysis of the thermal transitions of binary PC$_{61}$BM:PCB-F and ternary P3HT:PC$_{61}$BM:PCB-F blends highlighted several interesting features. In general, the incorporation of PCB-F was observed to have a distinct influence on the thermal behavior and blending properties of the mixed fullerene binary blends. While the binary blends from 9:1 to 7:3 PC$_{61}$BM:PCB-F were found to retain thermal characteristics consistent with pure PC$_{61}$BM domains, inclusion of as little as 10 wt.% PCB-F additionally promoted the formation of distinct hybrid domains with thermal behavior that could be distinguished from either of the pristine parent fullerenes. In addition, the disappearance of PC$_{61}$BM's cold crystallization and melt at 6:4 PC$_{61}$BM:PCB-F indicated the emergence of a more

181

homogenous mixture of the two fullerenes, with $PC_{61}BM$ likely sufficiently dispersed within a matrix of PCB-F such that nucleation of its crystallites was suppressed.

The ternary $P3HT:PC_{61}BM:PCB-F$ blends were found to modify the thermal properties of P3HT, disrupting its crystallization in addition to broadening its melt and shifting it to lower temperatures. The changes observed in P3HT's thermal behavior are consistent with the assembly of smaller P3HT domains with decreased macromolecular anisotropy. The thermal transitions of pristine $PC_{61}BM$ and hybrid fullerene domains recorded in the mixed fullerene binary blends were not clearly registered in any of the ternary blends, indicating that the presence of P3HT mutually affected the self-assembly of both fullerenes. The possibility that pristine and/or hybrid fullerene domains formed within the ternary blends cannot be completely eliminated, however. It could also be rationalized that analogous fullerene domains with reduced size and spatial frequency formed, with direct observation of their thermal behavior instead precluded by heat transfers falling below the detection limit of the instrumentation on account of their smaller size.

Optical microscopy was used to qualitatively assess the extent to which fullerene composition influenced the morphological stability of thin films prepared from $P3HT:PC_{61}BM:PCB-F$ ternary blends. In particular, changes in the surface features of the films, which emerged as a result of aggressive annealing conditions, were of interest. In addition, these experiments illustrated how observations of molecular self-assembly in the ternary blend thin films could facilitate interpretation of their DSC thermograms.

The binary $P3HT:PC_{61}BM$ and P3HT:PCB-F thin films were each observed to form crystalline fullerene domains, although several interesting differences were recorded. Notably, $PC_{61}BM$ crystallization was initiated within 10 minutes of annealing the binary

182

P3HT:PC$_{61}$BM thin film; culminating in the formation of elongated, rod-like helical domains after 1 hour. In contrast, PCB-F took longer to crystallize. Smaller, star-like PCB-F crystallites were only observed after 1 hour of annealing the binary P3HT:PCB-F thin film.

The DSC profiles of the pristine parent fullerenes can be extended to interpret the crystallization phenomena of their thin films. Although pristine PC$_{61}$BM was observed to reversibly cold-crystallize, this behavior was not observed in the thermogram of binary P3HT:PC$_{61}$BM. However, microscopy images illustrating the rapid formation of PC$_{61}$BM domains suggest the absence of observable PC$_{61}$BM thermal transitions in the binary P3HT:PC$_{61}$BM thermograms was a consequence of P3HT retarding and/or reducing the self-assembly of PC$_{61}$BM crystallization rather than impeding it altogether. Likewise, given the distinct shape and protracted formation of PCB-F crystallites within thermally annealed P3HT:PCB-F thin films, the lack of an observable PCB-F melt and/or crystallization in the DSCs of pristine PCB-F and binary P3HT:PCB-F speaks to differences in the time-scale and mechanism of its assembly, relative to PC$_{61}$BM. This behavior could suggest that PCB-F domains are initially smaller and more isotropically dispersed than PC$_{61}$BM, the affect of which retards formation of their crystallites and limits their size. It should also be noted that differences in sample size, film formation, and substrate interactions could have led to the discrepancies observed between the DSC thermograms and optical microscopy images.

Interestingly, incorporation of even 10 wt.% PCB-F in the ternary blend had a drastic affect on fullerene aggregation in the thin films. The formation of elongated PC$_{61}$BM crystallites was clearly disrupted in the 9:1 PC$_{61}$BM:PCB-F ternary P3HT blend, as only small spherical fullerene crystallites were observed. Extending the annealing time had no significant effect on the diameters of these crystallites; however, it did lead to an aggregation

of larger clusters of these crystallites on the surface of the film. Thin films prepared from the 8:2 $PC_{61}BM$:PCB-F ternary P3HT blend formed still fewer and more dispersed fullerene crystallites with annealing. Moreover, at 30 – 90 wt.% PCB-F, no fullerene crystallization was observed, even with an hour of annealing. This result supports DSC evidence of PCB-F's ability to modify fullerene crystallization in mixed fullerene blends and further suggests that at certain weight fractions, PCB-F can arrest fullerene crystallization altogether.

Analysis of the ternary blend thin films via GIWAXS further elucidated the behavior of these mixed fullerene systems. In general, annealing for 1 hour at 150 ˚C did not lead to an observation of periodic fullerene diffraction peaks in the thin films of binary P3HT:$PC_{61}BM$, binary P3HT:PCB-F, or any of the ternary P3HT:$PC_{61}BM$:PCB-F blends. Observations of $PC_{61}BM$ and PCB-F crystallites noted in the optical micrographs of homologous binary P3HT blend substrates seem to contradict the absence of distinct, crystalline fullerene diffraction peaks in their GIWAXS images. However, this result may instead indicate an extremely disorganized mechanism of fullerene nucleation that propagates the formation of highly isotropic, crystalline fullerene assemblies with a nominal lack of preferential long-range ordering ip and oop. In addition, the absence of fullerene diffraction and increased bandwidth of the fullerene pi-stacking ring, suggests an additional decrease in the molecular ordering of fullerenes in ternary blend thin films, relative to their binary P3HT controls. This interpretation is consistent with observations from DSC and optical microscopy, which equally demonstrate the capacity of mixed fullerene systems to suppress fullerene crystallization.

The arcing of P3HT's oop and ip diffraction was also observed to increase as the weight fraction of PCB-F increased. This behavior signals that the long-range ordering of

P3HT crystallites and their preference for edge-on assembly, relative to the substrate, is increasingly compromised by the presence of PCB-F. This effect may also shed light on the mechanism(s) suppressing fullerene crystallization in parallel.

Analysis of the vertical molecular distribution of sulfur, deuterium, and fluorine via DSIMS revealed important aspects in the self-assembly P3HT:d-PC$_{61}$BM:d-PCB-F thin films. In general, the as cast films were observed to have higher concentrations of sulfur and lower concentrations of deuterium at both interfaces, indicating a preferential assembly of P3HT toward the interfaces. In turn, the congruently lower concentrations of sulfur and higher concentrations of deuterium toward the interior of the film, indicated the fullerenes were largely aggregated within the interior of the as cast films.

Annealing for 5 minutes at 150 ˚C afforded a more uniform vertical molecular distribution of P3HT, d-PC$_{61}$BM, and d-PCB-F; evidenced by a flattening of the sulfur and deuterium traces. Interestingly, the deuterium counts in the annealed binary P3HT:PC$_{61}$BM and 10% PCB-F ternary blend thin films failed to reach baseline. This behavior is consistent with what would be anticipated from a rough, polycrystalline material with multiple grain boundaries. Deuterium traces of the annealed films prepared from ternary blends with 20% PCB-F and higher did reach baseline, however, a result that is generally consistent with the reduced crystallinity of these systems observed via DSC, microscopy, and GIWAXS.

Notably, interpretation of the self-assembly of d-PCB-F in the as cast and annealed films was limited by the presence of sharp spikes in the fluorine counts which fell below the instrument's threshold detection limit for vertical resolution. The shape of the fluorine peaks at the interface is therefore assumed to be an instrumental artifact. As a result, the self-assembly of d-PCB-F at the interfaces is not well understood. However, it can generally be

concluded that d-PCB-F is present throughout the depths of the film in its entirety. With little evidence of any stratification of perfluorinated groups within the film, the collected data does not support the hypothesis of perfluorinated fullerenes preferentially directing the self-assembly of d-PCB-F towards the air-interface. This result seems to contradict previous reports detailing the ability of perfluorinated pendants to induce migration of perfluorinated fullerenes towards the air-interface.[39]

Analysis of the OSCs fabricated from the P3HT:PC_{61}BM:PCB-F ternary blends provided insight into how the molecular composition of the ternary blends affected the device parameters and operational lifetime. In the devices pre-annealed for 5 minutes, the PCEs were found to decrease with increasing wt.% PCB-F. This decline in efficiency was largely ruled by a decrease in V_{oc} which occurred as a function of increasing PCB-F wt.%. This result challenged the expectation of a V_{oc} unaffected by fullerene blend ratios hypothesized by the identical frontier orbital energies of PC_{61}BM and PCB-F. In addition, the linear decline in V_{oc} with increasing PCB-F incorporation suggested the effect was additive. This phenomenon could possibly be rationalized by changes to the ternary blend's dipole induced by the perfluorinated tail. It could also be reasoned that the origin of this behavior stems from the progressive decrease in fullerene units emerging from higher wt.% PCB-F blends. On account of the fixed P3HT:fullerene weight ratios and PCB-F's larger mass, relative to PC_{61}BM, the molar ratio of fullerene to P3HT is gradually decreased as the weight fraction of PCB-F is increased.

Interestingly, the maximum J_{sc}'s were observed near median mixtures of the fullerenes. This result suggests that for certain blend ratios, PCB-F can have a favorable effect on the

films ability to transport charge. This observation likely correlates to physical features within the microstructure which better support charge transport.

Accelerated aging experiments indicate a general improvement in the device parameters across all blend ratios for substrates annealed post-contact deposition, relative to the substrates that received no post-annealing treatment. The influence of molecular composition on operational lifetime remains unclear, however. The timescale of these experiments did not conclusively support observations of an unambiguous benefit to device performance stemming from the suppression of fullerene crystallization by mixed fullerene ternary blends.

In conclusion, investigation of P3HT:PC$_{61}$BM:PCB-F mixed fullerene ternary blends yielded important insight into their potential for use in OSCs. Notably, analysis of their bulk behavior via DSC, optical microscopy, GIWAXS, and DSIMS unanimously corroborated the ability of PCB-F to disrupt PC$_{61}$BM crystallinity. Observations of reduced fullerene crystallization lend further support to the use of mixed fullerene blends as a broadly applicable strategy for suppression of fullerene crystallization, even in systems characterized by significant differences in the chemical identity and mixing behavior of the component fullerenes. Evidence of improved morphological stability and reduced fullerene crystallization in P3HT:PC$_{61}$BM:PCB-F ternary blends could not be extended to conclusively validate their ability to arrest PCE degradation. However, at certain weight incorporations of PCB-F, improvements to the J$_{sc}$ were noted. This preliminary device data demonstrates the capacity of P3HT:PC$_{61}$BM:PCB-F ternary blends to encourage morphological features which enhance device performance in OSCs. In light of these results, continued exploration of these

systems is warranted, as further optimization of ternary blend processing protocols could lead to additional benefits in morphology and device performance as a consequence.

4.8 References

1.

http://www.nrel.gov/ncpv/images/efficiency_chart.jpg

2.

Schlenker, C. W.; Thompson, M. E. *Top Curr Chem* **2012**, *312*, 175

Gaudiana, R. *J. P. S. B: Poly. Phys*. **2012**, *50*, 1014

Kumar, P.; Chand, S. *Prog.Photovolt:Res.Appl.* **2012**, *20*, 377

3.

Cao, H.; He, W.; Mao, Y.; Lin, X.; Ishikawa, K.; Dickerson, J. H.; Hess, W. P. *J. of Power Sources* **2014**, *264*, 168

Bundgaard, E.; Helgesen, M.; Carlé, J. E.; Krebs, K. C.; Jørgensen, M. *Macromol. Chem. Phys.* **2013**, *214*, 1546

8.

Verploegen, E.; Mondal, R.; Bettinger, C. J.; Sok, S.; Toney, M. F.; Bao, Z. *Adv. Funct. Mater.* **2010**, *20*, 3519

9.

Treat, N. D.; Chabinyc, M. L. *Annu. Rev. Phys. Chem*. **2014**, *65*, 59

Thompson, B. C.; Fréchet, J. M. J. *Angew. Chem. Int. Ed*. **2008**, *47*, 58

10.

Koidis, C.; Logothetidis, S.; Kassavetis, S.; Kapnopoulos, C.; Karagiannidis, P. G.;

Georgiou, D.; Laskarakis, A. Solar Energy Mater. & Solar Cells 112, **2013,** 36

 11.

Verploegen, E.; Mondal, R.; Bettinger, C. J.; Sok, S.; Toney, M. F.; Bao, Z. *Adv. Funct.*

Mater. **2010**, *20*, 3519

Richards, J. J.; Rice, A. H.; Nelson, R. D.; Kim, F. S.; Jenekhe, S. A.; Luscombe, C. K.;

Pozzo, D. C. *Adv. Funct. Mater.* **2013**, *23*, 514

15.

Treat, N. D.; Mates, T. E.; Hawker, C. J.; Kramer, E. J.; Chabinyc, M. L. *Macromolecules*

2013, *46*, 1002

17.

Richards, J. J.; Rice, A. H.; Nelson, R. D.; Kim, F. S.; Jenekhe, S. A.; Luscombe, C. K.;

Pozzo, D. C. *Adv. Funct. Mater.* **2013**, *23*, 514

18.

Verploegen, E.; Mondal, R.; Bettinger, C. J.; Sok, S.; Toney, M. F.; Bao, Z. *Adv. Funct.*

Mater. **2010**, *20*, 3519